Università degli studi di Modena e Reggio Emila

Dipartimento di Ingegneria “Enzo Ferrari”

Corso di Dottorato di Ricerca in

Tecnologia Industriale e del territorio “Enzo Ferrari” - XXXIII Ciclo

Development and Industrialization of PBF machine and validation by
process parameters optimization of
Brass CuZn42 and Harmonic Steel C67

Relatore: Prof. Andrea Gatto

Correlatore: Prof.ssa Elena Bassoli

Candidato: Riccardo Groppo

Sommario

Il detto *nomen est omen* difficilmente può essere applicato in tecnologia specie per processi innovativi. Nel caso della presente tesi si evidenzia che negli ambienti industriali che si occupano di lavorazioni meccaniche più tradizionali e consolidate, le persone sono propense ad usare il termine stampa 3D o prototipazione rapida. Nell'ambiente tecnico il personale e gli ingegneri parlano invece di "Additive Manufacturing", perché questo termine rappresenta totalmente tutte le tecnologie basate sullo stesso concetto: tecnologie con movimentazione elettrica in grado di combinare materiali sfusi per la produzione di prodotti complessi massivi in un'unica fase di processo controllata digitalmente e senza stampi o altri utensili. [1]

Le tecnologie di costruzione additiva, dalla loro nascita alle prime applicazioni industriali, hanno fatto un grande salto in termini di sviluppo di hardware e materiali.

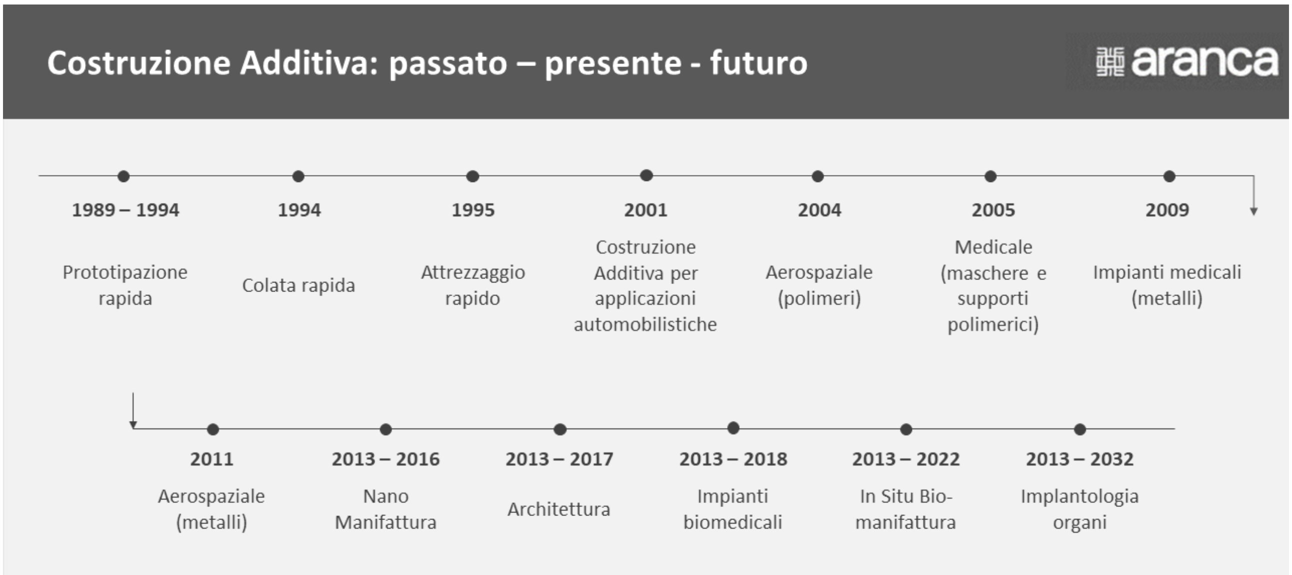

Figura 1: Passato – Presente - Futuro delle applicazioni per mezzo della costruzione additiva - www.aranca.com

La continua ricerca di nuovi mercati e l'offerta che tenta di inseguire la crescente domanda hanno indotto la nascita di nuovi competitori che con politiche commerciali aggressive hanno reso più accessibili i costi di tali tecnologie. Dall'uso dei polimeri per fare prototipi alle polveri metalliche per fare parti meccaniche reali il concetto fondamentale è sempre lo stesso, la parte strato per strato. In termini di fatturato dagli anni Ottanta ad oggi il processo di stampa 3D mantiene un trend di crescita positivo particolarmente promettente anche per il futuro. [1]

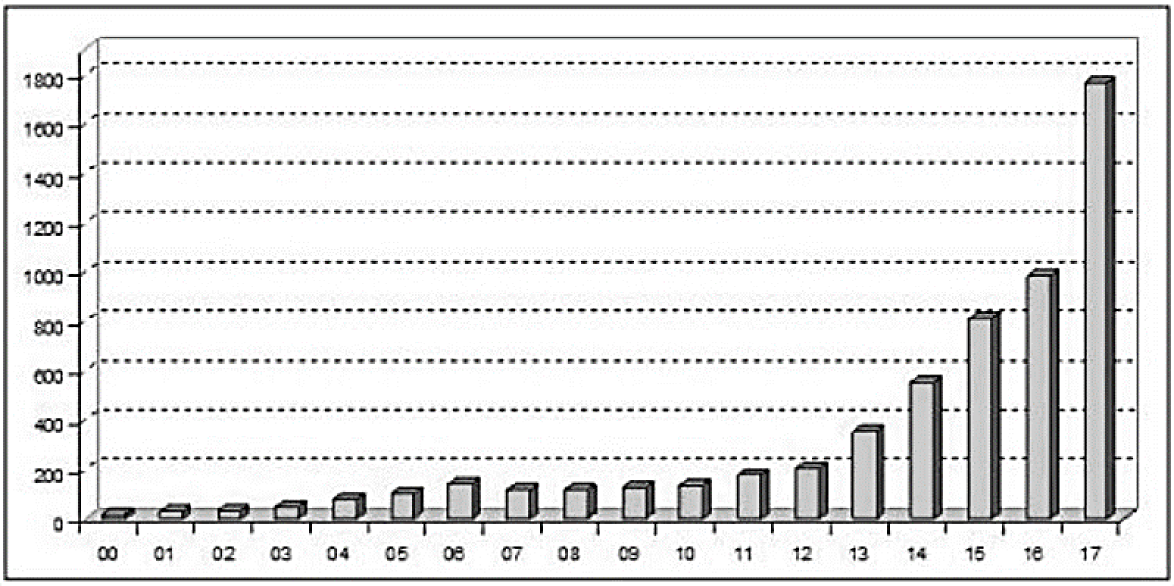

Figura 2: Imponente crescita delle vendite in campo Additive Manufacturing - Wohlers Reports 2018

Le tecnologie di costruzione additiva possono avere effetti positivi, in termini di impatto sui costi monetari ed energetici, nella produzione di parti complesse. Per una corretta valutazione delle tecnologie di costruzione additiva, in termini di lifecycle management, è necessario considerare il consumo energetico di produzione [2], aspetto che, molto spesso, viene trascurato, determinando una perdita di consapevolezza sulle reali potenzialità della tecnologia.

In molte catene di produzione tradizionali, dove stime affidabili del consumo energetico potrebbero non essere disponibili, l'adozione della tecnologia per costruzione additiva consente ai produttori di fornire ai propri clienti dati affidabili sull'energia incorporata nei prodotti o nei componenti durante la fase di produzione. [2]

È stato dimostrato che la selezione della configurazione dei costi minimi in Additive Manufacturing potrebbe portare all'effetto secondario della riduzione al minimo del consumo energetico di processo. [2]

La tesi di dottorato discuterà una specifica tecnologia di produzione additiva, basata sul processo di fusione del letto in polvere utilizzando un LASER come fonte di fusione.

Verranno analizzate le principali componenti costruttive presenti nella macchina prototipo, cercandone le principali criticità individuate in:

- (sistema di filtraggio e recupero delle polveri;
- abbattimento polvere nera;
- flusso del gas in camera;
- misura delle perdite di carico nei tratti caratteristici dell’impianto;
- sistema di raccolta delle polveri;
- sistema di distribuzione e di deposizione delle polveri sul piatto di stampa;

e, nel caso queste causino un arresto anomalo oppure un'irregolarità nella qualità nel componente stampato, se ne svilupperà una modifica oppure una sostituzione radicale del componente in esame.

Verificata la stabilità di processo e garantite le condizioni di ripetibilità sono state analizzate le proprietà meccaniche dei campioni ottenuti con acciaio inossidabile X2CrNiMo17-12-2 - AISI316L, polvere di ottone CuZn42 e acciaio C67 – dopo Tempra. Le principali proprietà richieste a un componente costruito per costruzione additiva sono espresse in termini di resistenza meccanica porosità, densità, durezza, carico a rottura e tensione di snervamento.

In particolare, sono stati effettuati dei rilevamenti della densità del provino mediante misurazione della densità volumetrica relativa con metodo di Archimede. Successivamente è stata valutata la rugosità superficiale attraverso acquisizione di mappe per mezzo di un microscopio conoscopico e attraverso un software per l'analisi d'immagine per ottenere la rugosità superficiale media. Lo stesso campione è stato poi utilizzato per misurare la durezza media del materiale per mezzo di un durometro.

Per testare il carico a rottura e il limite di snervamento sono stati prodotti dei campioni con geometria ad osso di cane a sezione circolare su cui è stato montato un estensimetro analogico. Per l'elaborazione della curva sforzo – deformazione si è ricorso ad un apposito software di elaborazione dei dati.

Riassunto

Il presente elaborato di tesi riguarda il periodo di tre anni trascorso presso l'Università di Modena e Reggio Emilia, in particolare sono state approfondite quelle che sono le tecnologie tradizionali e non in ambito produttivo. Nello specifico è stato oggetto di studio l'ottimizzazione e successivamente l'industrializzazione di una stampante 3d LASER a letto di polvere, in particolare utilizzando polveri metalliche. Le polveri metalliche che sono state testate per questa tecnologia sono state acciaio inox X2CrNiMo17-12-2 - AISI 316L e una la lega di ottone ad alto contenuto di zinco CuZn42, utilizzata in particolare nell'industria alimentare e per condutture idriche, e polvere di acciaio C67, che è prossimo per composizione all'acciaio armonico per lo sviluppo di molle.

La tesi inizia con una panoramica su quello che è il processo di costruzione additiva; il componente viene elaborato attraverso l'utilizzo di software dedicati, che ne semplificano la geometria convertendoli in file discretizzati (il formato più comunemente utilizzato è quello STL); questi vengono poi elaborati da altri software adibiti all'ottimizzazione dell'orientazione per ridurre il più possibile la presenza di strutture supplementari, definiti supporti, che devono essere eliminati a fine processo.

Create le strutture necessarie all'ottenimento del componente, lo stesso software elabora le sezioni del componente in base allo spessore dello strato di polvere con cui si vuole procedere alla stampa e calcola il percorso del LASER (o i percorsi, se i LASER sono più di uno), in modo da comporre lo strato relativo al componente. Costruito strato per strato il componente, questo deve essere rimosso e pulito dai residui. Infine, il componente attraversa una fase di post processo per poi essere effettivamente impiegato (figura 1).

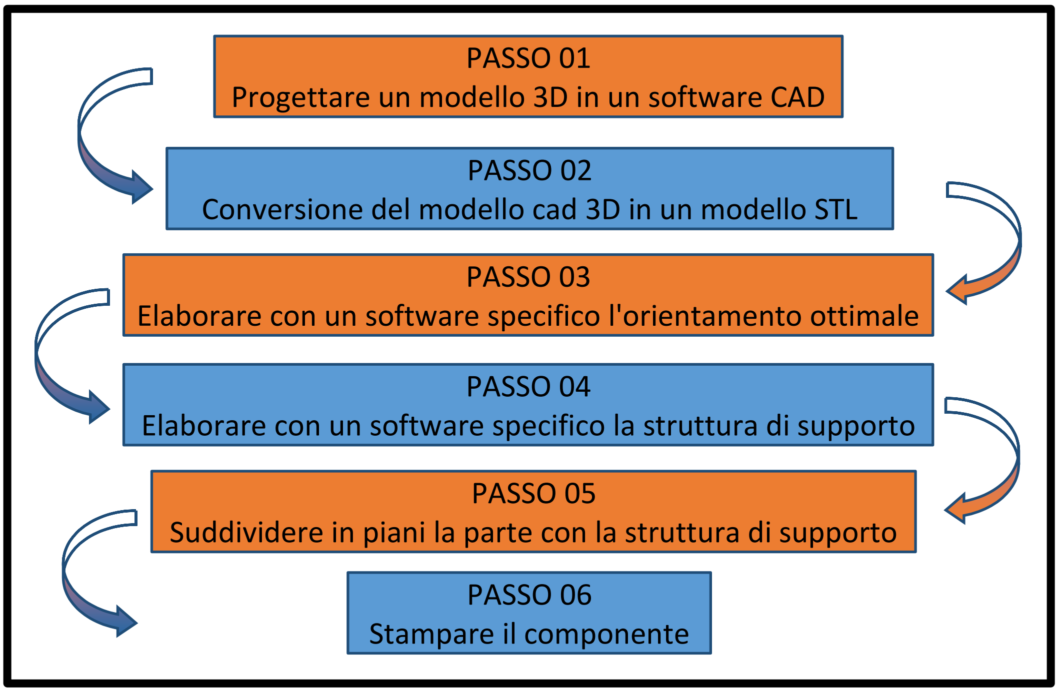

Figura 1: fasi della progettazione: dal design alla stampa del componente

Nel secondo capito la tesi tratta delle tecnologie disponibili sul mercato attuale, approfondendo le particolarità costruttive e operative dei macchinari commerciali: i LASER, i volumi di stampa, i sistemi di setacciatura e recupero polveri e i sistemi di filtraggio. La sezione dedicata ai LASER discute criticamente le sorgenti ad oggi maggiormente utilizzate: LASER CO_2, LASER fibra, LASER Nd-Yag oppure sorgenti a fascio di elettroni. Viene altresì analizzato il range delle polveri metalliche presenti attualmente sul mercato globale.

Le sezioni successive riguardano lo sviluppo di una macchina prototipale progettata e realizzata in collaborazione con l'azienda 3D4Mec di Sasso Marconi, Bologna. L'attività di dottorato ha implicato anche le fasi di raccordo e coordinamento e collaborazione diretta tra l'azienda e il gruppo di ricerca in Tecnologia Meccanica e Sistemi di Lavorazione del Dipartimento di Ingegneria Enzo Ferrari, guidato dal professor Andrea Gatto. L'attività ha incluso una analisi critica delle peculiarità costruttive e operative della macchina, finalizzata all'individuazione di criticità specifiche e allo sviluppo di opportune soluzioni.

La prima criticità è stata riscontrata nelle dimensioni della camera di stampa, all'interno della quale si creano volumi morti, che causano la formazione di flussi vorticosi. Questi, andando ad interagire con il volume di flusso che serve ad espellere i residui da fusione, generano a loro volta turbolenze anomale, che vanno ad inficiare tutto il sistema di aspirazione dei residui. La polvere di scarto, pertanto non essendo rimossa nella maniera più opportuna, andava ad inquinare polvere stesa sugli strati ma ancora riutilizzabili per processi successivi.

Un'altra criticità è stata riscontrata sulla geometria del distributore della polvere; è stato misurato che il tempo utile per far sì che il distributore erogasse il quantitativo di polvere necessario a ricoprire il piatto di stampa risultava eccessivamente elevato e, soprattutto nel caso in cui si dovessero stampare pezzi di piccole dimensioni, risultava preponderante rispetto al tempo di azione del LASER, con una ricaduta eccessiva sulla produttività. Inoltre, la geometria del distributore non era ottimizzata per prevenire grippaggi dei cuscinetti a causa di un eccessivo deposito di polvere. È stata conseguentemente ottimizzata la geometria del distributore.

Un terzo intervento ha riguardato la standardizzazione della procedura di calibrazione del LASER in modo da ottimizzare lo spot sul piano relativo alla stampa, garantendo sempre una corretta messa a fuoco.

È stato poi realizzato un impianto pilota (figura 2A) per la misura delle perdite di carico in ogni sezione dell'impianto di ricircolo, determinando la pressione necessaria a garantire il corretto funzionamento di un ciclone appositamente dimensionato per aumentare la durata di utilizzo dei filtri. Dalle stesse misurazioni si è riscontrato che la presenza di soffiatori che garantiscono il flusso lineare del gas in realtà causa un'eccessiva caduta di pressione, vanificando gli sforzi della pompa. I soffiatori sono stati giudicati del tutto incompatibili con il presente sistema. La loro rimozione permette alla pompa di lavorare in un range doppio rispetto al set up originale. Da questo punto sono state ottimizzate le bocchette di ingresso ed uscita partendo sia nel numero sia nella loro geometria per eliminare l'effetto Coandă presente in tali sistemi. L'effetto Coandă è la tendenza di un getto di fluido a seguire il contorno di una superficie solida prossima alle linee di flusso originali (vedi figura 2B).

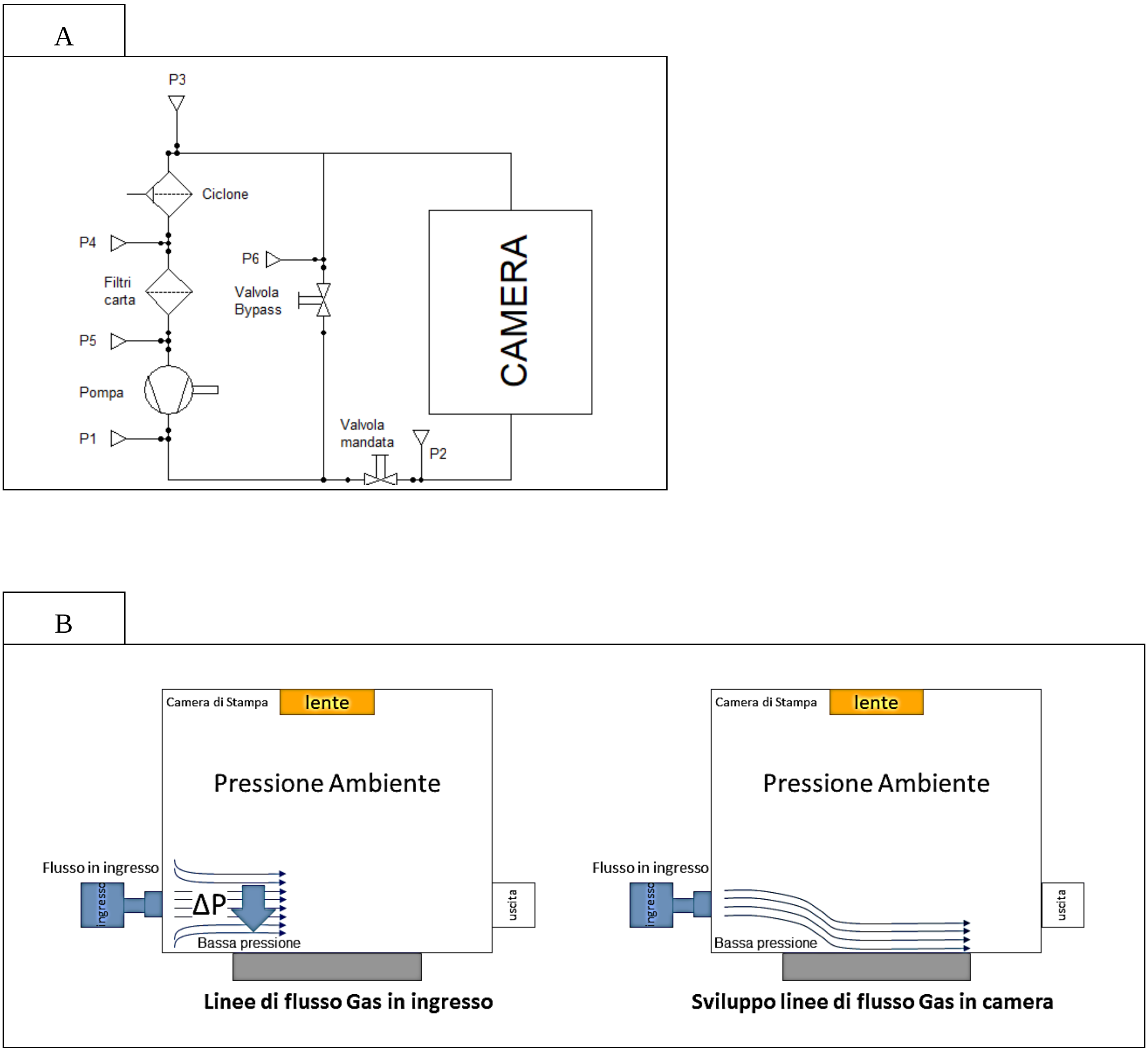

Figura 2: A) schema impianto, B) effetto Coandă

Una ulteriore ottimizzazione della camera di stampa ha riguardato le posizioni dei motori atti alla movimentazione del distributore e del caricatore. La prima versione della macchina prevedeva la presenza di una trasmissione a cinghia che movimentava il distributore della polvere. Per la presenza di polvere volatile all'interno della camera di stampa si è progettato un sistema di rinvio delle pulegge interne alla camera con delle pulegge esterne, in modo da garantire il moto lineare del distributore, preservando il motore. La modifica riguardante questo sistema è la sua sostituzione con l'inserimento di una guida a ricircolo di sfere con sensori di fine corsa incorporati; tutto il blocco viene inserito internamente alla camera; in questo modo, l'albero di trasmissione risulta l'unico elemento uscente dalla parete della camera. Questa modifica porta molteplici vantaggi: la riduzione del numero di componenti, l'inserimento di un componente completamente integrato e commerciale (quindi facile nella sostituzione in caso di guasto), riduzione di molteplici punti di trafilamento del gas dalla camera.

Altro aspetto sotto esame è la sostituzione del monitor con sistema basculante con l'inserimento di un monitor con sistema a bracci snodati per garantire una migliore ergonomia all'operatore.

Ultimo aspetto valutato più per fini commerciali che funzionali, è il rinnovo del design della macchina.

Parallelamente alle ottimizzazioni della macchina, l'attività di ricerca ha riguardato anche lo sviluppo dei parametri di processo con relativo piano sperimentale per le polveri metalliche. In particolare, si sono sviluppati i parametri relativi alla potenza del LASER e alla velocità di scansione per ottenere componenti meccanici con densità superiore al 99%. L'elaborato prende in considerazione per primo l'acciaio inox AISI316L, segue poi la lega di ottone ad alto contenuto di zinco CuZn42 e infine si conclude con l'acciaio armonico C67.

Il piano sperimentale è un piano definito 'full factorial', cioè un esperimento fattoriale completo. È stata inizialmente identificata l'energia specifica necessaria a fondere ciascun materiale. La seconda fase del piano sperimentale ha riguardato la variazione di potenza e velocità cercando di mantenere costante la densità di energia volumetrica, questo per ridurre il più possibile il tempo di stampa, con conseguente vantaggio in termini di tempo macchina e di costi.

Lo sviluppo dei parametri è stato condotto attraverso procedimenti ricorsivi di costruzione e caratterizzazione di campioni, sui quali è stata rilevata la densità con una bilancia idrostatica, passando attraverso l'analisi di immagine per la morfologia delle porosità, finendo con test meccanici di prove di trazione.

Il capitolo cinque è dedicato all'analisi dei dati e alle conclusioni.

Abstract

In the common uses of the additive manufacturing technologies, people tend to use the term 3D printing or rapid prototyping. In the technical ambient the technicians and the engineers speak about “Additive Manufacturing”, because this term represent totally all the technologies based on the same concept: electricity-driven technologies capable of combining materials to manufacture complex products in a single digitally controlled process step, entirely without molds, dies, or other tooling. [1]

The additive manufacturing technologies, from their birth to the first industrial applications, made a big jump in terms of hardware and material development.

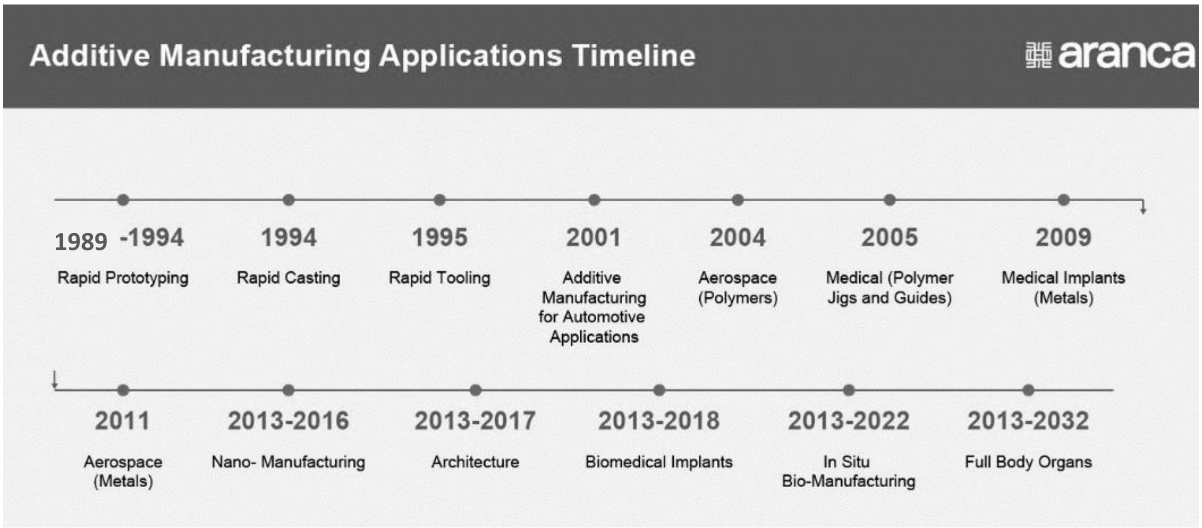

Figure 1: Timeline of Additive Manufacturing applications - *www.aranca.com*

The continuing research for new markets along with a growing demand have made sure that the costs of such technologies have become more accessible. Both the prototyping of polymer components and the manufacturing of metal part are based on the same concepts are always the same, building the part layer by layer.

the 3D printing market maintains a positive trend with much more increases for the future.[1]

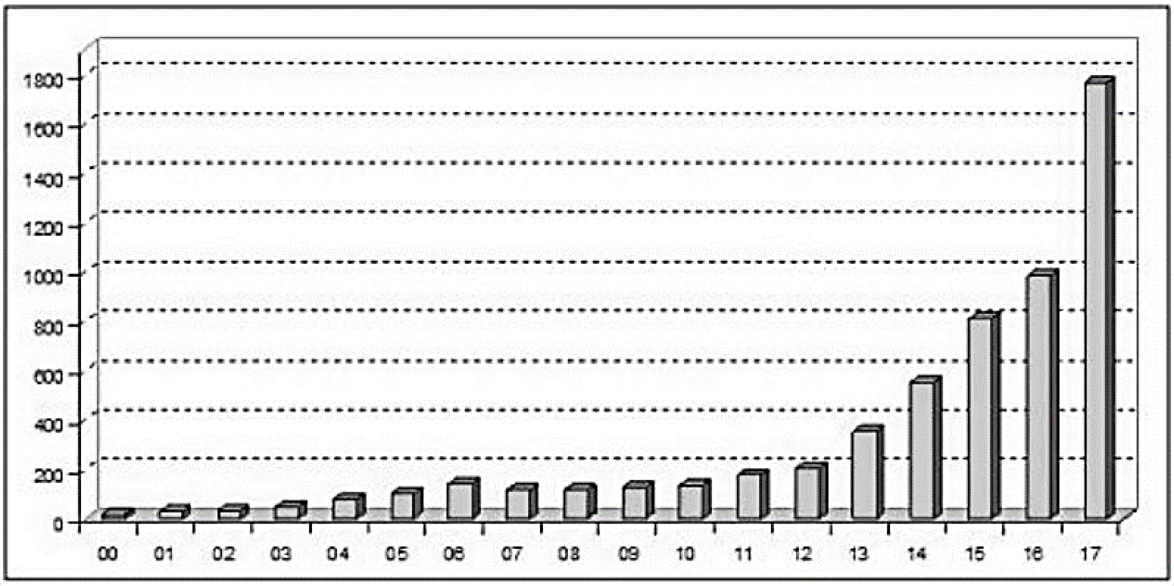

Figure 2: Dramatic rise in metal AM system sales - Wohlers Reports 2018

In terms of monetary and energy flows during the production of complex parts by the additive manufacturing technologies can have positive effects. Thus the adoption of Additive Manufacturing also simplifies measurement of the manufacturing energy consumption for life cycle inventory assessments. [2]

In many traditional supply chains, where reliable estimates of cumulative energy consumption may be unavailable, the adoption of AM allows producers to provide their customers reliable data on the energy embedded into products or component during the manufacturing stage.[2]

It has been shown that selecting the minimum cost configuration in Additive Manufacturing is likely to lead to the secondary effect of minimizing process energy consumption. [2]

The PhD thesis will discuss a specific additive manufacturing technology, based on the powder bed fusion process using a LASER as a melting source.

The main construction components present in the prototype machine will be analysed, looking for the main critical issues:

- filtering and powder recovery system;
- black powder abatement system;
- in-chamber gas flow;
- measurement of load losses in the characteristic sections of the plant;
- powder collection system;
- distribution and powder deposition system on the printing plate;

If these critical aspects cause the manufacturing process crash or irregularities in the printed component, a radical modification or replacement of this component will develop.

Once the mechanical stability of the entire machine has been verified, the mechanical properties of the samples obtained with stainless steel X2CrNiMo17-12-2 - AISI316L, CuZn42 brass powder and C67 steel - Tempered steel will be analyzed. The main mechanical properties required for a component built by additive manufacturing are the mechanical strength; porosity, density, hardness, ultimate tensile strength, and yield tension.

Specimen density measurements will be carried out by measuring the relative volumetric density by Archimedes method. Subsequently, the quality of surface roughness will be measured through the acquisition of maps by means of an optical microscope and through an image analysis software the average surface roughness will then be measured. The same sample will then be used to measure the average hardness of the material by means of a durometer.

the ultimate tensile strength and the yield strength samples were built with circular section to allow the use of an analog extensometer. Data processing software processes the strain -strain curve.

1: Backgrounds

The 3D Printing or Rapid Prototyping (RP) concept was born in 1981, when a Japanese inventor named Hideo Kodama created a product using an ultraviolet light to harden polymers and create the first 3d printed solid part. That was the milestone of the actual process called Stereolithography (SLA). [3]

Three years later, in 1984, the US inventor Charles Hull deposited the patent of the printing process Stereolithography. The process was similar as the Kodama's process, but he printed the objects layer by layer, rinsed with a solvent, and hardened with an ultraviolet light. The process used Computer Aided Design to create 3d models. Two years later he and his cofounder Raymond Freed founded the 3DSystems Inc. Company.[,1, 3]

After, 3D Systems commercialized SL in the U.S. (1988), many other companies tried to investigate and implement of the additive manufacturing technology. In two years many companies became competitors producing quite similar technologies. [1]

In the following five years the companies as EOS or Soligen commercialized new 3D printing systems; EOS commercialized a LASER sintering system and Soligen developed a solid shell production casting (DSPC). With the research of new systems many other companies developed new materials; for example, ModelMaker in 1994 commercialized new wax materials using an inkjet print head. [1]

In 1999 Dr. Matthias Fockele and Dr. Dieter Schwarze, two Germans physics , started a collaboration WITH the Fraunhofer Institute for LASER Technology, and implemented the first steel powder-based selective LASER-melting system. [1]

From the 2000 as of today many industries (e.g., EOS, SLM and Renishaw) implemented the powder bed fusion concept with some commercial machines and at the same time developed the use of new metal powders such as Cobalt-Chrome, Titanium, Aluminium or Stainless Steel. We do not forget the plastic's developments too; ABS, Polycarbonate, Polyphenylsulfone or PLA. From the 2011, when some Stratasysis patents expired, many open source systems based on the RepRap open-source project, became available. [1]

In 2009, seventy experts from around the world met at the ASTM International headquarter near Philadelphia, Pennsylvania to establish ASTM Committee F42 on Additive Manufacturing Technologies. The roundtable established the standards on testing, processes, material, design (including file format) and terminology. Two years later, in October 2011, ASTM and International Organization of Standardization (ISO) announced a cooperative agreement; this cooperation reduced the risks of a duplication of effort. [1]

In the last ten years additive manufacturing techniques based on the LASER powder bed fusion process are becoming increasingly viable for industrial applications. In the powder bed fusion technology, the component is built by exposing sequential layers of metal powder to a LASER beam that causes the melting of the metal powder. The consolidated part is formed from layer by layer and the LASER beam scan over predefined path based on 2D slices of a 3D CAD files. [4]

There are many companies which make commercially available LASER-based systems for direct melting and sintering of metal powders: EOS (Germany), Renishaw (UK), Concept LASER (Germany), Selective LASER Melting (SLM) Solutions (Germany), Realizer (Germany), and 3D Systems (France/USA The terminology is often misleading and in any case unclear- The term selective LASER melting (SLM) is used by numerous companies; however, the terms LASER Cusing and DMLS are also used by certain manufacturers. [5]

In general, speaking about PBF process it is necessary to specify exactly which energy source and manufacturing strategies the technology uses to consolidate the powder: LASER beam melting (LBM), electron beam melting (EBM) and selective LASER sintering (SLS). [6]

In addition to the LASER source the machines have other several components that concurrent to the printing of the sliced part. The other main parts are involved in the working volume and the powder loading system.

The process begins with choosing the component to print. Once the structural and mechanical constraints of the component have been established, this undergoes a topological optimization (see Figure 3). Topological optimization is the phase of the process where the component is emptied from all parts not strictly necessary to meet the operating constraints.

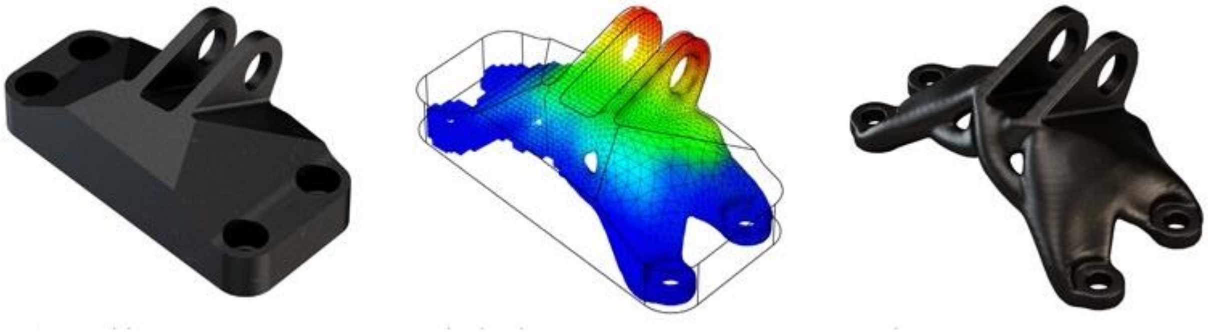

Figure 3: example of topology optimization

The finite elements method validates the new geometry, the components digital model undergoes a formatting, it moves from a continuous structure to a discretized one: the discretization takes place by breaking down the surface into many triangles, the number of whose depend on the definition need. An STL format represents the surface geometry of an object in three dimensions. However, this format does not define the texture, color, or other parameters that i can find in a CAD) model. Therefore, a 3D mosaic of triangles represents the digital model, each triangle has a known position of its three vertices (see Figure 4). The quality of 3D printing is linked to the number of triangles that make up the surface. Most CAD programs convert any 3D model to STL format. The processor slices the STL model and it translates each layer in G-code commands or like start printing. Improving the resolution and size of a file will increase the number of triangles on the surface of the 3D model accordingly (see Figure 4).

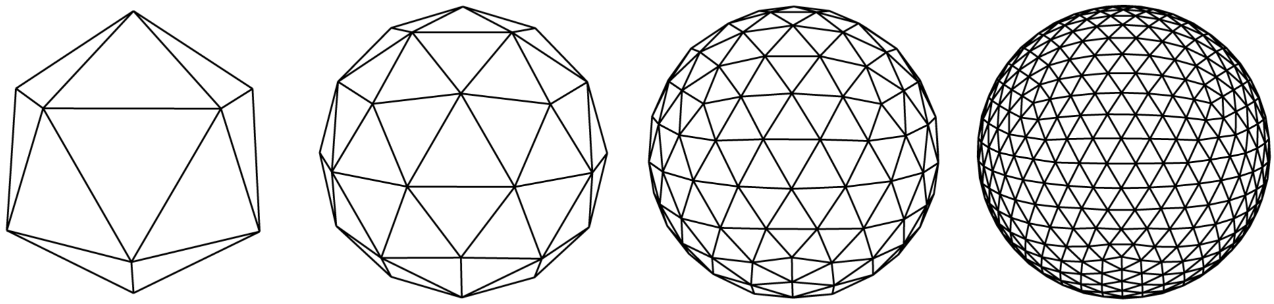

Figure 4:effects of the increasing of the resolution.

In most of the CAD systems, the settings of STL export depend on following parameters:

- Chordal Tolerance: Chordal tolerance numerically describes the maximum distance between the actual part surface and the tessellated surface of the STL file, as it is shown in Figure 5.

- Angle Control: Setting the angle control influences the tessellation of curves with relatively small radii in comparison to the overall size of the CAD model. [7]

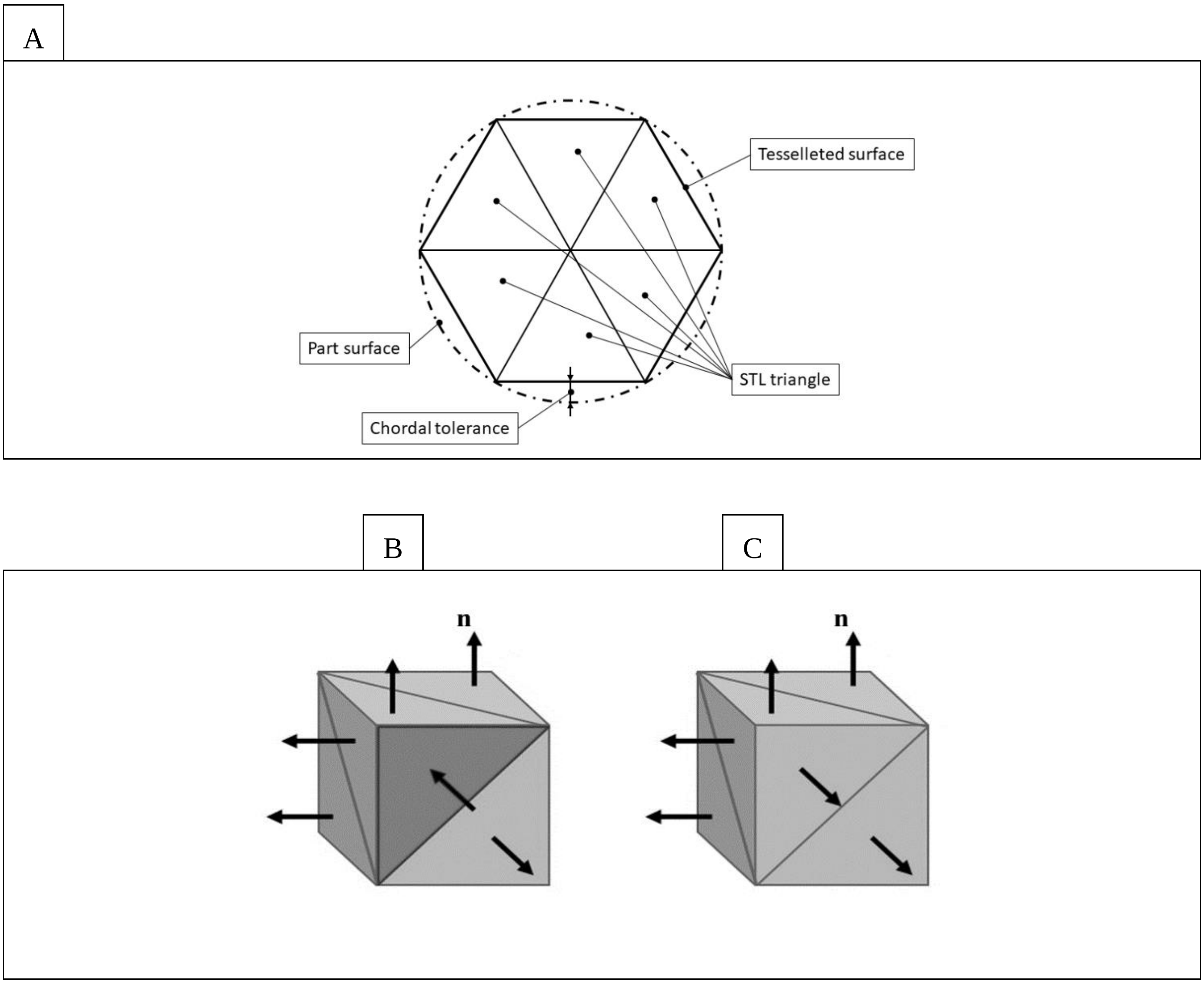

Figure 5: STL file: Figure A) example of a mesh, Figure B) normal inverted, Figure C) normal fixed

After the CAD model transformation in the discretized one (see Figure 5A), it is necessary to ensure that the new component has no errors, such as holes, inverted normal (see Figure 5B), or overlapping triangles. The correction of these errors is done using some algorithms, but these systems are effective if the missing parts have the defined contours. In many cases the designer tends to consider flat and thin surfaces as zero-thickness elements, so this causes holes inside the model.[8]

After the new component architecture validation, it is placed in the machine. If the If the working area is greater than the component projected area the component is printed in one piece, otherwise it is necessary to use dedicated software to break down the component into several parts to reduce the size of the elements, reducing the working area need.

The positioning of the piece on the building platform can never take place with direct contact on the printing plate for obvious problems related to the detachment of the component from the building platform, but always requires the presence of structures that supports it. The supports also serve for all surfaces that do not respect the condition of self-supporting. This condition is different for each powder material, since the materials have different weights, mechanical performances, and size distribution. After dividing the shape into layers, one of the slices contains one or more islands—solid regions that appear while not being supported from below. During additive fabrication from bottom to top, the material forming the island will not attach to already solidified material. For technologies using material deposition, the material forming the island will fall. The most common consequence, material deposited onto the following growth layer will also fall, and this will cause a catastrophic failure. Powder bed Fusion technologies usually are able to support the island—however weight increases in accordance with layers number and a heavy disconnected component may start to sink down. Also overhangs parts require support structures. The material is added and melted progressively along deposition paths therefore during the layering, for some overhangs the last consolidated layer (area) longer has any reinforcement under it (e.g., the top of an arc), so it just collapses. It is interesting to note that below a certain threshold the construction of the overhang can self-sustain without requiring supports (see Figure 6).

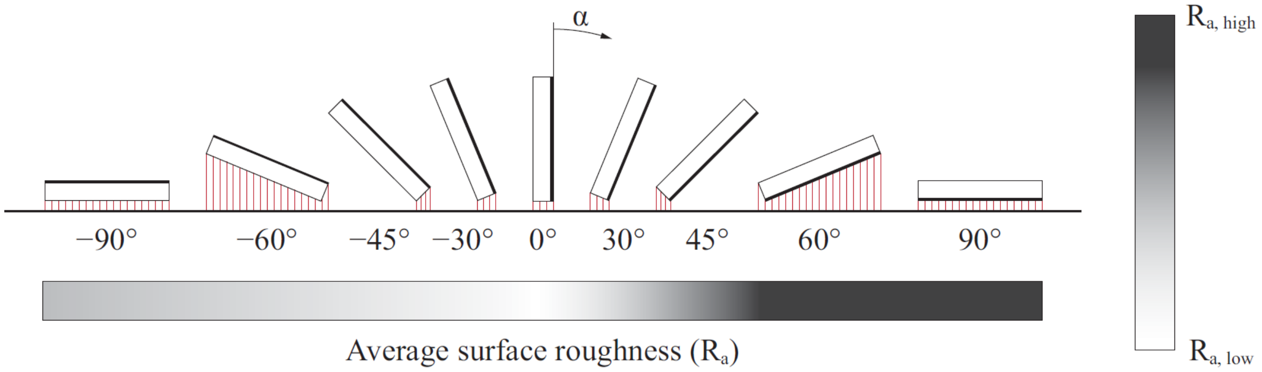

Figure 6: different overhang angles vs Average surface roughness

There are two groups of support structures: external structures, which govern the component structure externally, and internal structures, which are an integral part of the component. Support structures embedded in the component are used to reduce the volume of material used, decrease the cost, increase its lightness: this type of geometric changes should not reduce the physical properties of the component. [8]

Each Additive Manufacturing software with supports generation script, foresees various categories of supports, from the simplest to the most complex geometries. [8]

For example, in Autodesk Netfabb it can choose from a wide range of solutions: some solutions allow to support only the edges, others can cover an entire area. In other cases, the support structure makes a lattice one or a tree trunk. They support all those surfaces that fail to self-support.

The slicing phase follows the orientation and type of support choice step.

During the slicing, the software divides the component into layers and for each layer it processes the path that the LASER will have to repeat. Both of the results of slicing and the parameters entered by the operator dictate the final LASER path:

- type of scan (one-way, chess board);
- numbers of contours;
- distance between the contours;
- distance between contour and infill;
- power, and scanning speed.

For example, in Autodesk Netfabb these parameters are handled within the process toolpath. Before the conversion of the slicing in a CLI file (Command-line interface), the operator can simulate if the choices are correct or they need some adjusts. If the process is right, the operator can start the conversion and than to lunch the print (see Figure 7).

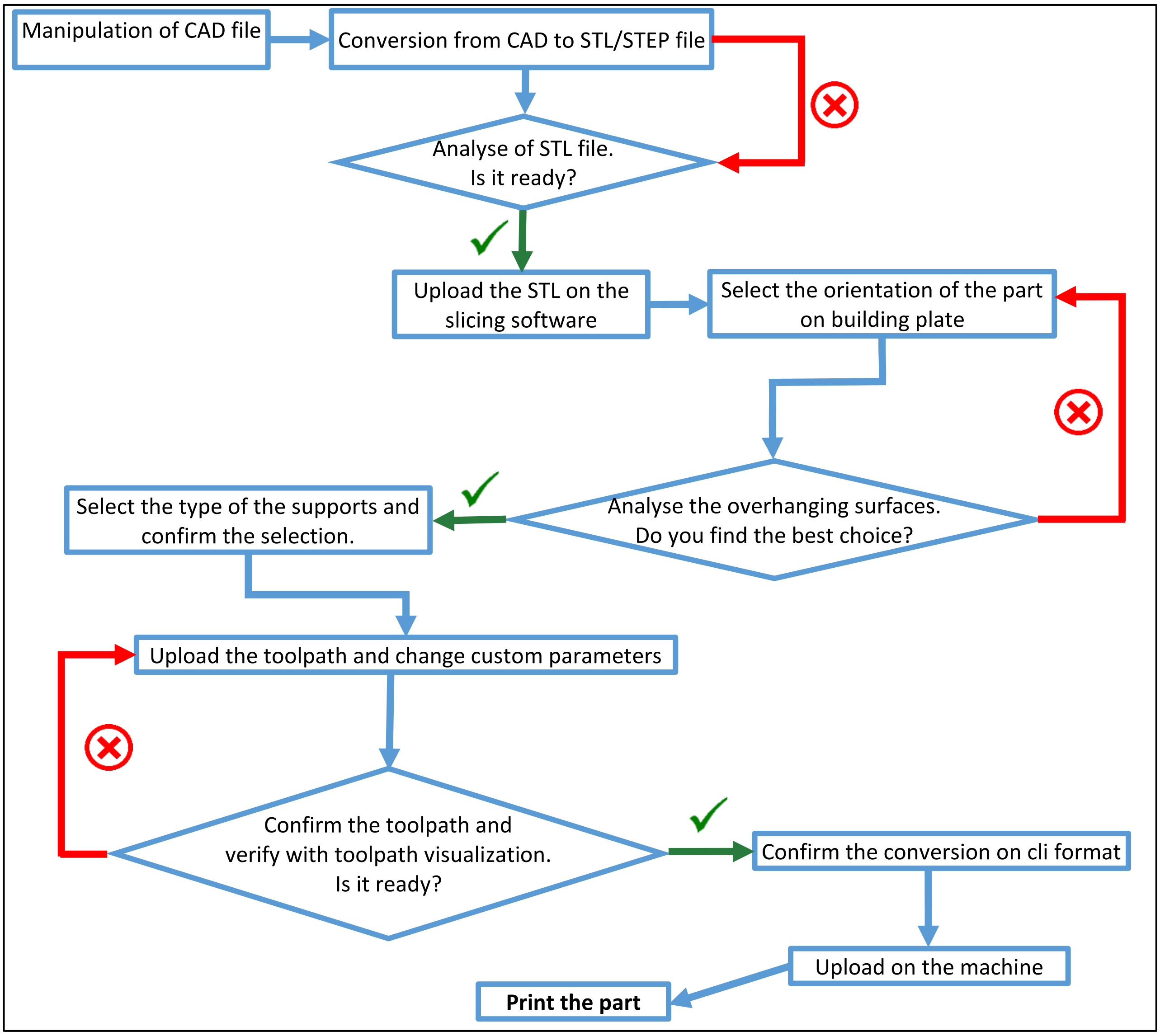

Figure 7: flowchart of printable part step by step

1.1: LASER sources for LPBF – LASER Powder Bed Fusion

A LASER generally consists of a gain medium, a pumping energy source, and an optical resonator. The gain medium placed inside the optical resonator amplifies the light beam by stimulated emission using the external energy supplied by a pumping source. LASERs are usually classified by the gain medium in use – solid state, gas, excimer, dye, fiber or semiconductor ones. [9]

The acronym LASER means "Light Amplification by Stimulated Emission of Radiation", so basically light amplification caused by the stimulated emission of electromagnetic radiations.

There are two kind of emissions at atomic level: spontaneous (see Figure 8) and stimulated radiation emission (see Figure 8). In the case of spontaneous emission, the system under consideration (e.g an atom) can remain in an energy-excited state for an approximately long time (at atomic scale), depending on the delta (difference) of energy. When the system becomes unearthed and returns to the fundamental energy state, the lost energy is released in the form of electromagnetic radiation. In case of stimulated emission, the system returns to its initial energy state (stimulated) by an accident photon. The outgoing photons, however, in this case are in the same direction due to the effect of the reflective walls. In addition, crucially, the outgoing photons have the same phase and this leads to a constructive interference (see Figure 8). [10], [11]

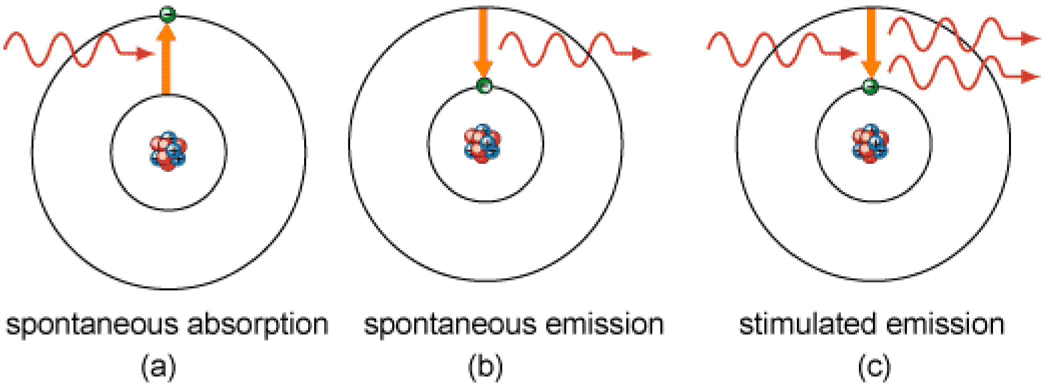

Figure 8: scheme of spontaneous absorption, emission and stimulated emission

In summary, photons emitted by stimulated emission have three important characteristics:

- the issued photon is in phase with the incident photon,
- the photon emitted has the same wavelengthλ as the incident photon,
- the issued photon travels in the same direction (beam).

at equilibrium state there are many atoms in the fundamental state and few in the excited one. The atoms are then "pumped" into the excited state, providing energy in various methods: this creates a population inversion" An incident photon, causes the returning on a stable level, resulting in the emission of other photon (always all-in phase).

The active LASER medium is the material that emits photons in phase, the simplest cavity form has two mirrors. A mirror is semi reflecting one, it allows the exit of the beam and borders the active medium. The mirrors reflect the emitted photons through the active LASER medium, and they cause the increase in the intensity of the light beam. In addition, the length cavity design depends on the wavelength of the photons emitted. The two mirrors allow the obtaining of a highly coherent beam (see Figure 9).

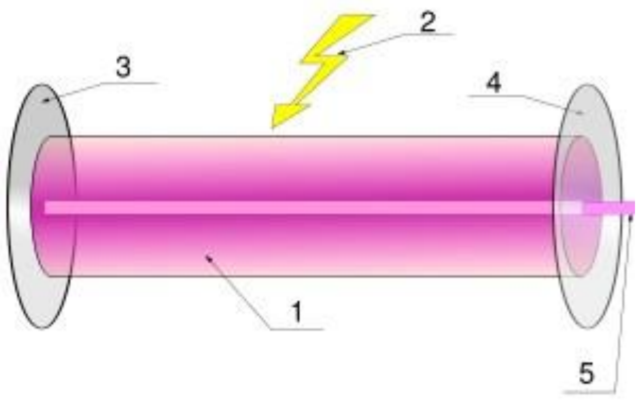

1. Active LASER medium
2. Energy from the flashlight
3. Reflecting mirror
4. Semi reflecting mirror
5. LASER beam

Figure 9: main parts of a LASER beam generator

The first LASER used in metal powders AM techniques was the CO_2 LASER. Developed in 1964 by Kumar Patel in Bell Laboratories, this type of LASER source consists of silicon-coated or molybdenum mirrors, as normal glass hit by an infrared source no longer acts as a transparent material; the lenses and exit windows are in germanium. CO_2 gas can be stimulated with continuous or alternating electrical current for population conversion. The wavelength of the outgoing LASER beam ranges from 9.0 µm to 11.0 µm. Compared to other LASER sources, the CO_2 LASER is the one with the greatest efficiency. One of the limitations of this technology is the instability of the heat diffusion process within the system, derived from the turbulence of the gas during the stimulation phase.

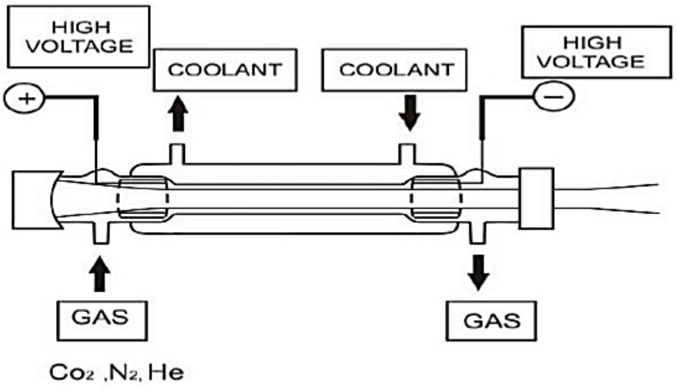

Figure 10: CO_2 LASER scheme

CO_2 LASERs require the use of free-space bulk reflective optics to drive the beam the optical fibers are anable to drive it. Therefore, in order to work with a wider range of materials or take advantage of fiber-based beam delivery, other types of LASERs have to be considered. [9]

The simplest form of CO_2 LASER consists of a gas discharge tube with a fully reflective mirror at one end and an output coupling (usually a semi-reflective selenium mirror zinc coated) at the exit end. The reflectivity of the exit mate mirror is usually 5-15%. LASER output, for high-powered applications, can have a particular coupling (edge-coupled) to reduce optical heating problems. [9]

The main CO_2 LASER competitor has been solid state LASER and more recently fiber LASER.

Fiber LASERs, are cheaper (to purchase and maintainance), more compact, energy efficient, and have better beam quality than solid state Nd:YAG LASERs. [5]

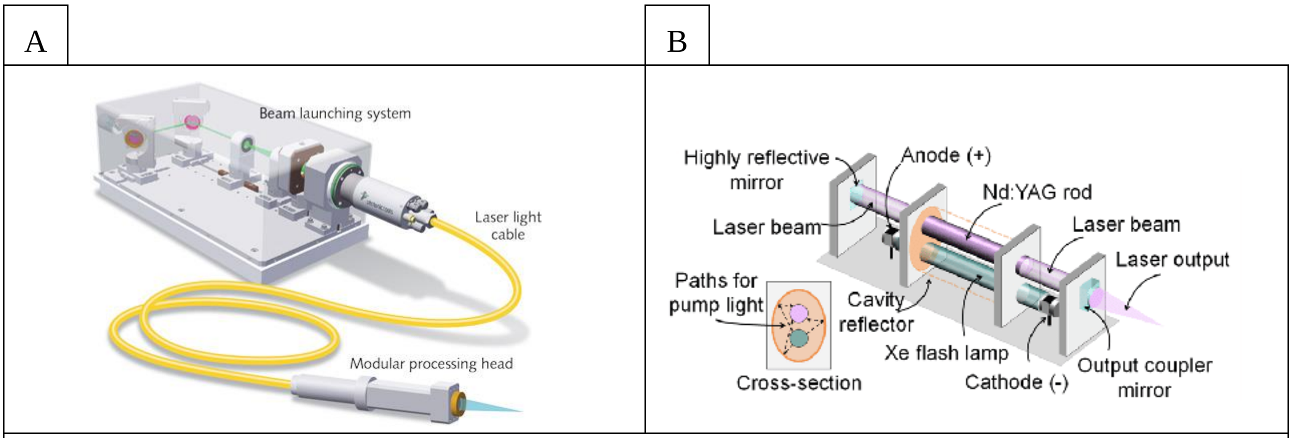

Figure 11: LASER sources - A) fiber LASER scheme, B) Nd-YAG LASER scheme

Some companies prefer to use an electron beam and not the LASER fiber. The structure of an electron beam is reported on figure 12:

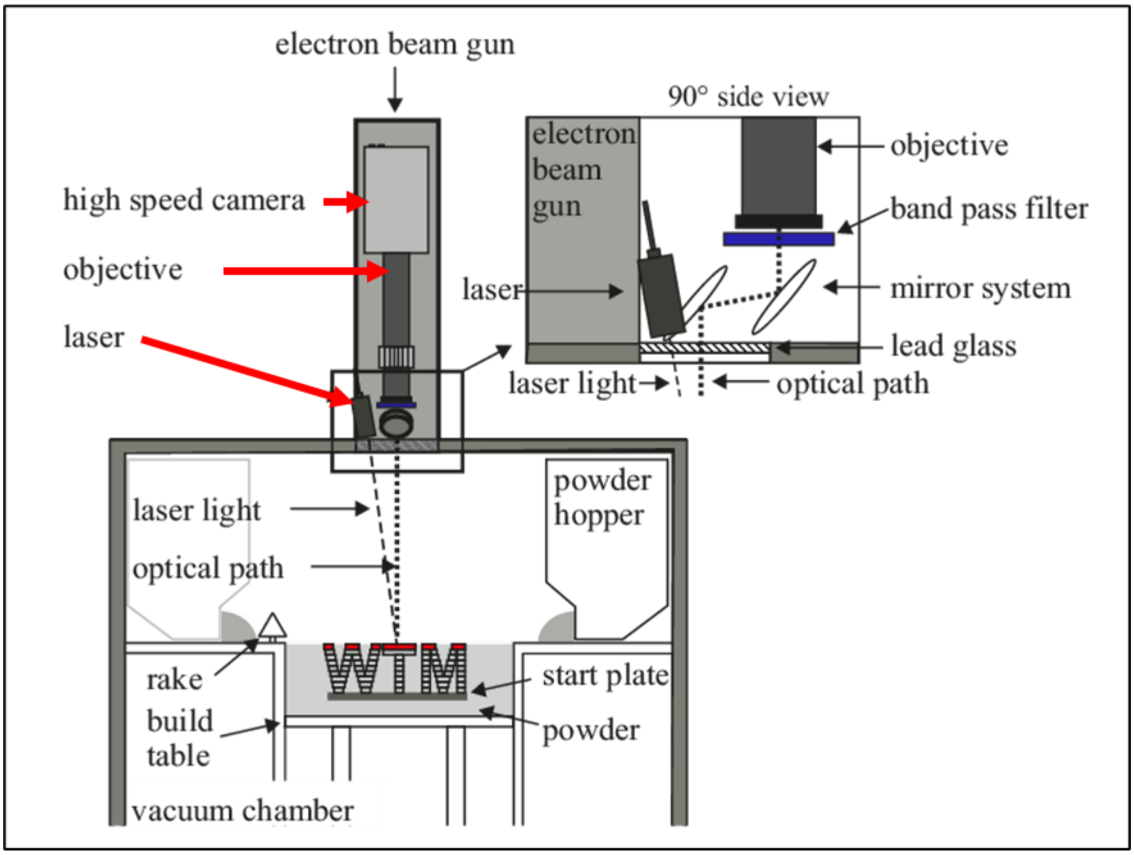

Figure 12: example of an electron beam melting system.

EBM technology uses an electron beam produced by an electron gun. The latter extracts the electrons from a tungsten filament under vacuum and projects them in an accelerated way on the metallic powder. These electrons will selectively fuse the powder. [12]

One of the most important reasons for choosing a type of laser is its wavelength. In addition to the wavelength, the average power and specific, the spot, must be considered.

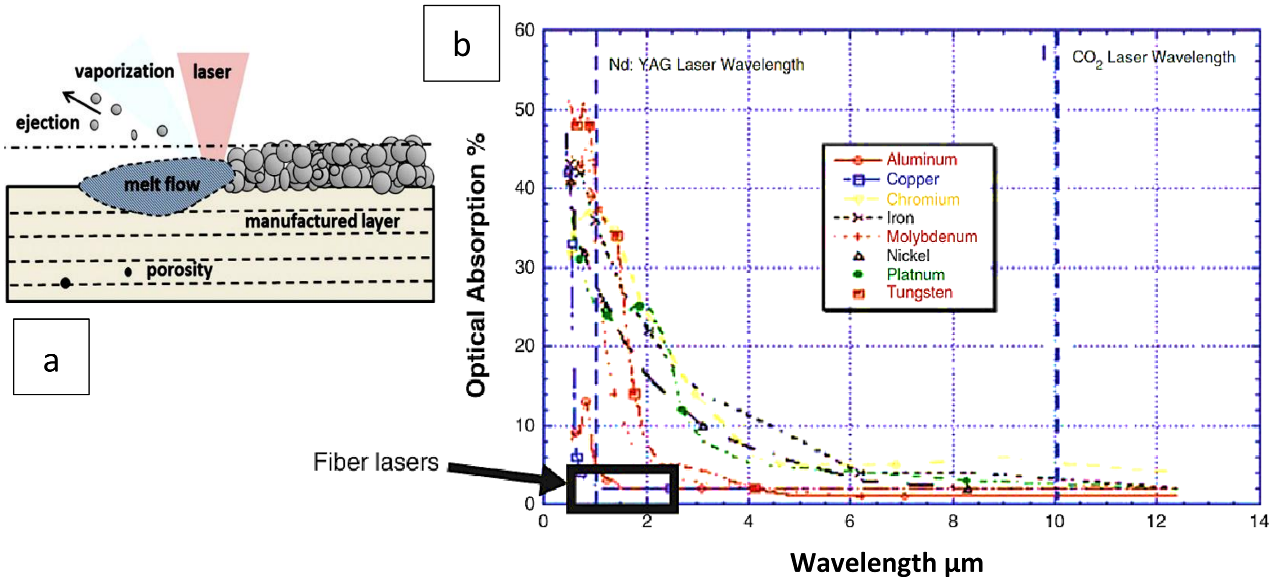

Figure 13: a) The powder bed fusion process - b) Optical Absorption % (absorptivity) of selected metals vs. wavelength (courtesy of OPTOMEC) [5], [13]

The most used LASERs in additive manufacturing are the Fiber ones. The active gain medium of a fiber LASER is a rare-earth doped optical fiber. The best rare-earth doped gain fibers are the Yb-fibers thanks to their high-power generation in order to high quantum efficiency (~94%).

Yb-fiber LASERs are widely used in material processing due to their high efficiency therefore they have mostly replaced Nd:YAG LASERs in additive manufacturing. The output is a near-infrared wavelength:1030 – 1070 nm). A diodes LASER with a 950-980 nm wavelength pumpu the LASER fiber gain. Other advantages, due to the fiber-based gain medium and optical components, are the high electrical-to-optical efficiency (~25%), excellent beam quality, robustness against environmental disturbances, and system compactness. The limitations of the Yb-fiber LASERs are due to the light propagation inside the fiber. The high peak of the power that is possible to reach with nonlinear effects, such as self-focusing, self-phase modulation, Kerr lens effect, and Raman effects are high limits of the LASER performances.

In table 1 the industrial choices are shown. The choice depends on the price on the energy source and on the quality of the beam, in terms of operating wavelength, average power, pulse energy and intensity, pulse duration. the technological obsolescence of additive construction machines occurs in about 2-3 years, this leads to rapid changes for which the description of construction solutions tends to be quickly overcome.

Table 1: LPBF companies and their main machines

VENDOR	MODEL	LASER TYPE	SPOT
Renishaw [14]			
	AM 250	200W or 400W	70 µm
	AM 400	400W	70 µm
	RenAM 500M Q/S	Q(quad) 4x500W ytterbium fiber LASER S(single) 1x500W ytterbium fiber LASER	80 µm
3D Systems [15]			
	DMP Flex 100	100W fiber LASER	
	DMP 200	300W fiber LASER	
	DMP 300	500W fiber LASER	
	DMP 350 Flex/Factory	500W fiber LASER	
Concept LASER [16]			
	Mlab	100W fiber LASER	
	Mlab 200R	200W fiber LASER	
	M2 Series 5	400W x 2	
	Xline 200R	1000W x 2 fiber LASERs	
	Mline factory	4 x 400W or 4 x 1000W fiber LASERs	
EOS [17]			
	M 100	200 W Yb fiber LASER	40 µm
	M 290	400 W fiber LASER	100 µm
	M 300	1 x 400 W or 4 x 400 W fiber LASER	100 µm
	M 400	1 x 1 kW or 4 x 1kW fiber LASER	90 µm
SLM Solutions [18]			
	SLM 125	400 W IPG fiber LASER	70 - 100 µm
	SLM 280	(1 or 2) x (400 or 700) W Dual (700 + 10 kW)	80 - 115 µm
	SLM 500	Twin (2 x 400 W or 2 x 700 W) Quad (4 x 400 W or 4 x 700 W) IPG fiber LASER	80 - 115 µm

Further feature that distinguishes one machine from another with equal building volume is the capability to use multiple LASERs; The choice to operate with multiple LASERs on a single building volume allows the machine to increase productivity; the print volume is divided by the number of LASERs reducing, the scanning times: the systems can operate simultaneously (see Table 1). The scanning time and the recoating time define the productivity.

Over time there has been a switch from CO_2 LASER to a NdYag one, increasing the absorbability range of material, even if the CO_2 LASERs are used for specific materials. The following change from solid state laser to Fiber is due to a general lower cost of the LASER source and maintenance costs; they allow a smaller footprint, better energy efficiency and a better spot quality. Both Fiber LASERs and CO_2 LASERs can use a f-theta lens called, which allows to enhance the LASER spot by minimizing distortion during scanning: the LASER beam is always almost orthogonal to the worktop (see Figure 14).

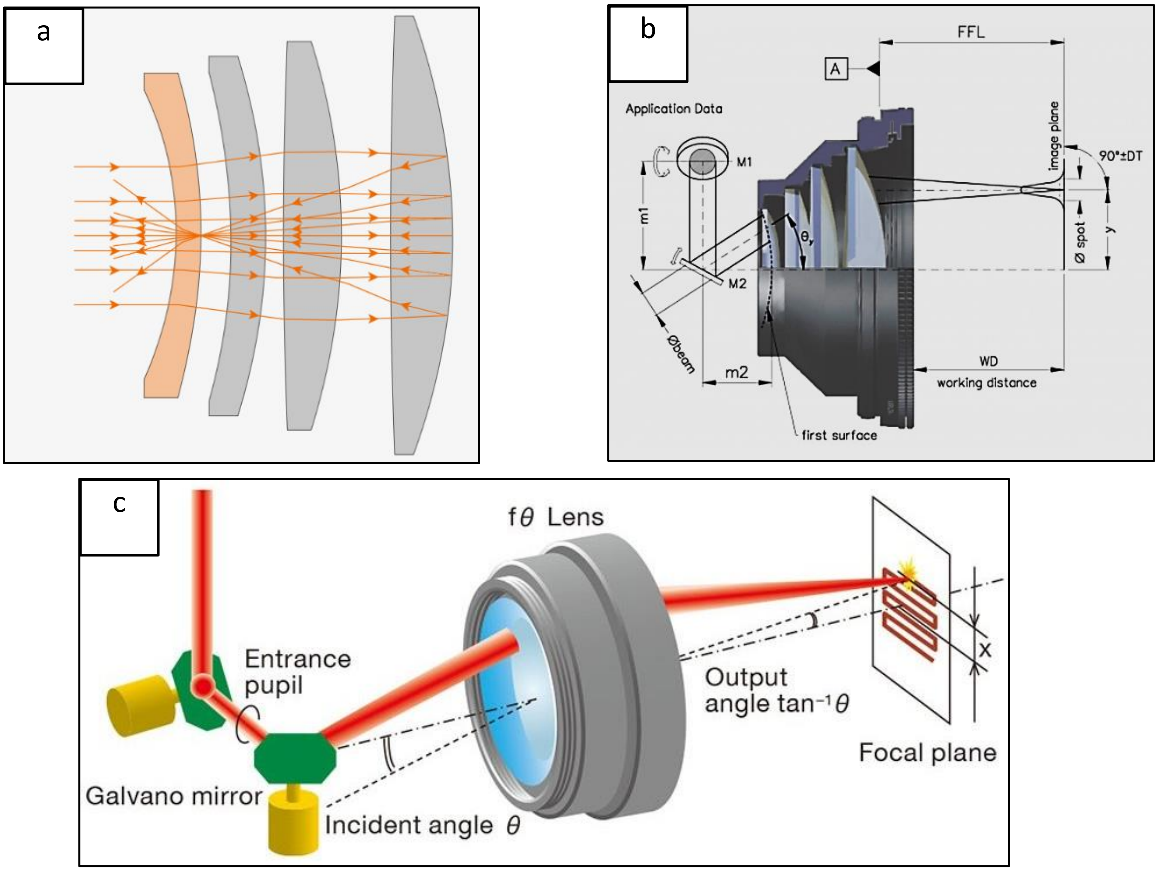

Figure 14: figures a) and b) are two schemes of how the LASER spot is focusing on the focal point and how the beam is directed on the worktop; figure c) represent a global scheme of a scanning system.

1.2: Building volumes

All AM machines manufacturers have an entry level device with relatively low print volumes. This technology was born as an aid to the prototyping, after the metal powder introduction and polymer technological consolidation became clear that the technology was suitable for the manufacturing. The evidence of manufacturing capacity required the increase of the volume, even if the increasing of the working volume generates new problems related to the thermal conductivity between the printed part and construction plate. On the AM machines market there are several working volume and plate measures to meet the needs of the expanding market and because the market itself begins to require ever larger print volumes. [14], [16], [19] some built-on-demand machine data are confidential and not available in the literature.

Table 2: Summary of the main build volume on the market the quickly technological obsolescence of these machine, the high model spare rate, with the entry of new machines and the exit of even recent machines causes any classification to be rapidly over come.

Additive Manufacturing machines and building volumes				
RENISHAW	3D SYSTEMS	CONCEPT LASER	EOS	SLM Solutions
AM 250 250x250x300 mm^3	DMP 100 100x100x80 mm^3	MLab 50/90x50/90x80 mm^3	M 100 Dia 100x95 mm^2	SLM 125 125x125x125 mm^3
AM 400 250x250x300 mm^3	ProX DMP 200 140x140x100 mm^3	MLab 200R 100x100x100 mm^3	M 290 250x250x325 mm^3	SLM 280 280x280x365 mm^3
RENAM500 250x250x350 mm^3	ProX DMP 300 250x250x300 mm^3	M2 Series 5 245x255x350 mm^3	M 300 300x300x400 mm^3	SLM 500 500x280x365 mm^3
	ProX DMP 320 275x275x380 mm^3	Xline 200R 800x400x500 mm^3	M 400 400x400x400 mm^3	
		Mline factory 500x500x400 mm^3		

All manufacturers (except 1-2 cases) selected a square working plate and not a circular one, almost certainly because a square construction plate is easier to manage in the design phase and also because the square surface is more suitable for mechanical component (Figure 15). Only EOS comes on the market with its smallest machine (EOS M100 – dia 100x95 mm^2) which has a circular printing plate. [17]

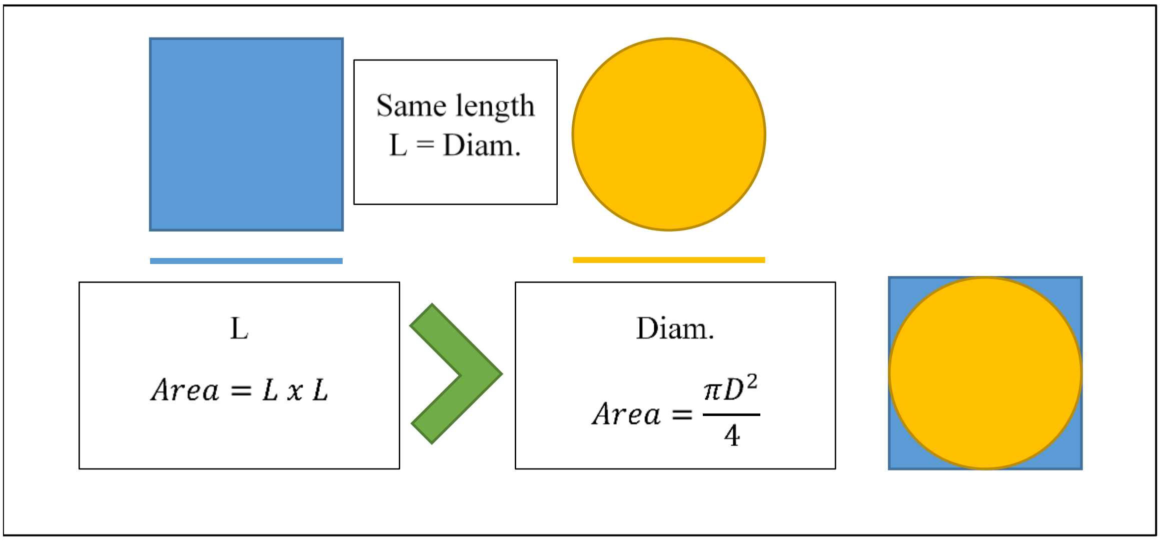

Figure 15: geometric conditions of why companies opt for a square base and not circular.

To prevent the oxidation of the powder, normally, the building volume is saturated with an inert gas (Nitrogen, Argon, a mix of them, helium). Argon can be implemented with all the materials because Argon has no chemical affinity with the most types of powders. The use of Argon is expensive and it needs high pressure cylinders to be allocated. Nitrogen is cheaper than Argon and it is easy to produce locally: it needs a Nitrogen generator that captures the atmospheric air and separates Nitrogen from the other elements.

Normally the printing chambers or building plates are heated to prevent the effects of residual stress induced by temperature gradient and heating and cooling rate that can change the part geometries. There are currently two solutions for heating the component; The first is through an infrared lamp, which radiates the entire room, the second is through the insertion of the heated plate placed under the construction plate, through electrical resistances.

The solution that uses infrared lamps allows a uniform radiation of the chamber but leads to choose materials inside the chamber that withstand significant temperatures close tor higher than 100 degrees Celsius. The solution with electrical resistance solves problems due to radiation, especially for those plastic parts inside the chamber. The electrical resistance system placed under the working plate are suitable for heating initially the part under construction but its efficiency decreases with the growing height of the component: the thermal diffusiveness decreases until it is no longer effective. This condition causes thermal stresses in the component upper this altitude. [17]

The composition and pressure and the direction of the gas inside the building chamber together with thermal diffusion of the material cause the distortions of the printed piece. The gas should be as one-way as possible to ensure the elimination of the spatter during the dust consolidation. The inadequate particles removal due to spattering cause in the component the formation of porosity, which will be a source of weakening or even grafting of fractures during the normal use of the part. [20], [21] Many studies focused on the metal AM process modelling and temperature prediction: the non-uniform temperature will cause the thermal stress in the component and the resulting tensile residual stress accelerate the crack growth. A good prediction of the temperature in metal AM is the pillar for predicting the thermal stress, residual stress, and part distortion. [20], [21]

1.3: Powder loading systems

The additive manufacturing technology is based on the concept that every component to be produced is first discretized into layers, and each section is converted into machine language that a translates software into the LASER path. The powder is first stored in a hopper than it is deposited on demand on the working plate by a recoater. By simple gravity, the powder falls into the conveyor above the recoater, which then distributes a layer on the print plate. The tank of the powder in general is located above the print chamber or sideways to the printing plate. Excess powder and dust produced during the working phase fall into a recovery tank, which in some models is disassembled at the end of printing. The recovery tank is then placed in another machine that will sieve the powder to eliminate the coarse particulate matter, which was created during the LASER consolidation (e.g M290 EOS Figure 16B). Smarter solutions involve inserting an ultrasonic sieve at the bottom of the redundant dust conveyor, which are then recharged in the upper hopper (e.g. RenAM500 Q Figure 16A).

A	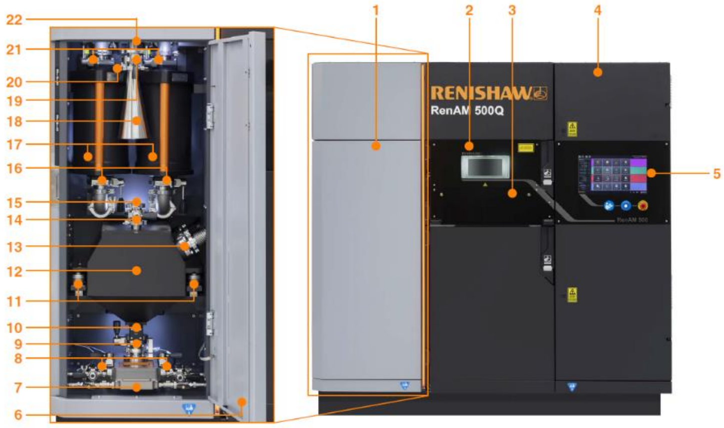	From the top of the machine with the natural gravity force (red arrow), the powder falls in front of the recoater and after that the recoater spreads the powder. The excess powder falls in a sieve (12), then with a pneumatic jet (6) the sieved powder return in the main tank on the top.
B	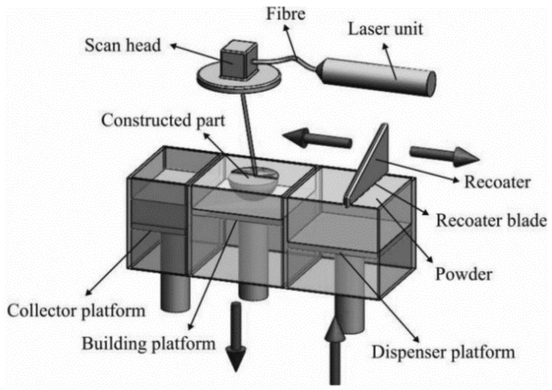	In the EOS system the main tank is near the building chamber; with a horizontal movement the recoater bring the powder from the dispenser platform and deposit the powder on the building platform. The exceeding powder goes in the collector platform.

Figure 16: different systems of powder loading

1.4: Metal powders overview

All materials that can be melted and solidified can be used in PBF processes. Thermoplastic, glass-filled polyamides, polystyrene-based materials, or elastomeric thermoplastic polymers are well-suited for power bed processing. The thesis focuses on the following metal powders: Stainless Steel 316L (Low Carbon), Brass powder with a high percentage of Zn (up to 40%) and Harmonic Steel C67.

The global market offers several material: stainless steels, Steels, Aluminium alloys (AlSi10Mg or AlSi7Mg), Maraging Steels, Titanium alloys (Ti6Al4V), Nickel-based or CoCr alloys. [5]

Steels are used for applications where high mechanical resistance is required, such as turbine spinners or, applications where high thermal exchange capacity is required. Stainless steel is used for food applications, due to their high corrosion resistance. [14], [17], [18], [22]

Aluminium powders, especially the AlSi10Mg alloy, are often used for the production of prototypes or small series in which it is necessary to have an extreme reduction of the masses; in general, the fields of application are motorsport and aeronautics. [14], [17], [18], [22]

Titanium alloys, especially the Ti6Al4V alloy, are used in cases where lightness and mechanical strength are the main objectives required. Another aspect that decides the applicability of titanium alloys is the ability being biocompatible especially in the environment like that of the human body. [14], [17], [18], [22]

Maraging steel powders are used to develop small sets of molds. [14], [17], [18], [22]

Components that require high heat resistance, corrosion and a high break threshold are produced with Nickel-based powders. An example is the paddle that makes up the high-pressure spinner of a multi-stage turbine for industrial application. [14], [17], [18], [22]

Cobalt-Chromium alloys are often used to product aeronautical components where there is required a strong thermal performance such as fuel nozzles in propulsion engines. [14], [17], [18], [22]

Figure 17 represents the comparison between hardness and resistance to the unnerving of alloys used in Additive Manufacturing. [23]

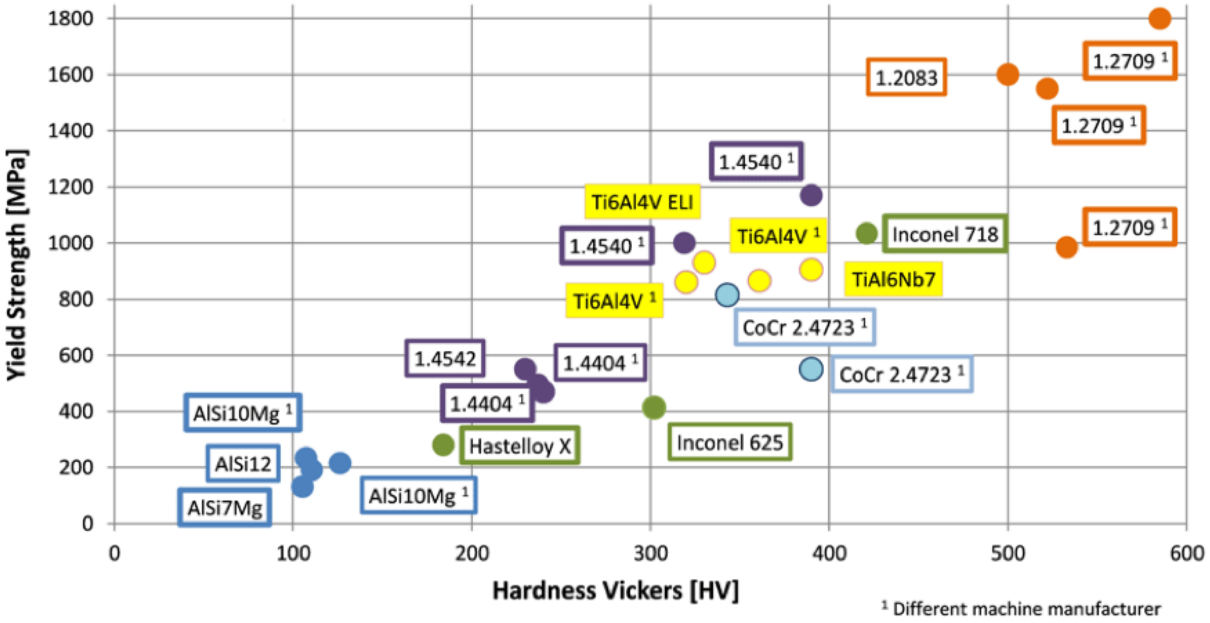

Figure 17: Yield Strength vs Hardness Vickers for additive manufacturing alloys

1.4.1: Powder Production

The main techniques suitable for the production of metal powders are:

A. Water Atomisation.
B. Gas Atomization,
C. Plasma Atomization,
D. Centrifugal Atomization,

Water Atomization is the simplest and cheapest powder production technology (Table 3 – A). The metal alloy is fused into a furnace upstream of the machine and then transferred to the crucible that is located above the atomization chamber. Thanks to the pressure environment and the presence of a nozzle that accelerates the flow, the molten material enters in the atomization chamber where the melted metal is cooled by water injections placed circularly around the metal flow, generating small droplets. The powder is collected in a container located at the base of the machine.

The shape of the metal particles is not spherical due to the high inbound speed of the molten metal along with the high thermal gradient between the water and the molten metal. The presence of oxygen during the atomization process can oxidize the surface of the metal droplets and for this reason the most suitable materials are stainless steels, nickel-based alloys, cobalt-based and copper alloys.

Due to the strong need to obtain powder with spherical particles, some manufacturers use the gas atomization technique (see Table 3 – B). The main feature for this type of atomization is the cooling gas, which is usually an inert one. Due to thermal conductivity of the gas that it is lower than that of the water, the formation of spheroid particles is more controllable. the alloys of the following base material can be gas atomized: copper, aluminium, magnesium, zinc, titanium, nickel, cobalt, precious metals.

Adjusting the speed and density of the gas allows to produce particles with dimensions in the range of 40-60 µm.

For this type of atomization there are several sub-processes divided according to the melting modes of the raw material:

- VIGA – Vacuum Inert Gas Atomization,

- EIGA – Electrode Induction Melting Gas Atomization,

- PIGA – Plasma-melting Induction-guiding Gas Atomization.

The plasma atomization (Table 3 – C) uses an ionized gas, obtaining powder with a high spherical volume and purity. The starting material is a wire, which feeds the atomization chamber where there are plasma torches melting the wire and gas jets. The torch and the gas flow provide thermal energy and mechanical energy for the transformation of the material from wire to powder. With plasma atomization, the powders are much more spherical and purer, because the presence of hot atomizing gas (instead of cold medium as for gas atomization) increases the cooling time so the transformation into spheres of the material is more controlled. For the same reason, there are little satellites and clusters on the individual spheres.

The centrifugal atomization system (Table 3 – D) as the name suggests uses centrifugal force to provide the mechanical energy needed for the atomization of the material. There are several subcategories for this technology, the most used are:

- REP – Rotating Electrode Process,

- PREP – Plasma rotating Electrode Process.

In the REP system, an electrode composed by the alloy is placed in high-speed rotation, and the free end is fused by an electric arc formed by the metal alloy electrode and a tungsten electrode. In the PREP system the fusing system is the same of the REP. As soon as the rotating bar enters the atomization chamber, plasma torches melt the end, along with the rotation the powders are produced. The flow of molten metal falls into a rotating disc or cone, which scatters the droplets under the centrifugal force.

The grain size properties of the powder are measured by sieves, XRD techniques, SEM, while the smoothness is evaluated with a flowability test, a known amount of dust is flowed through a properly calibrated funnel and the time it takes to flow through it, less is the time the powder flows, better the dust's smoothness qualities will be.

Table 3: Powder Production Processes

	Atomizing process	Atomized morphology
A	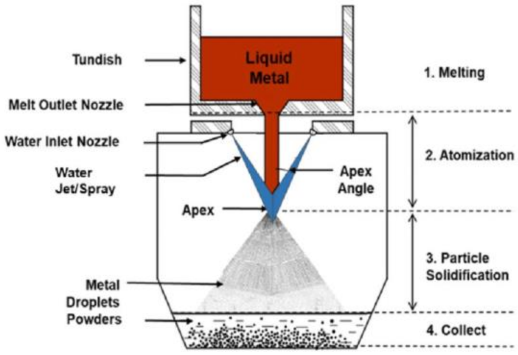	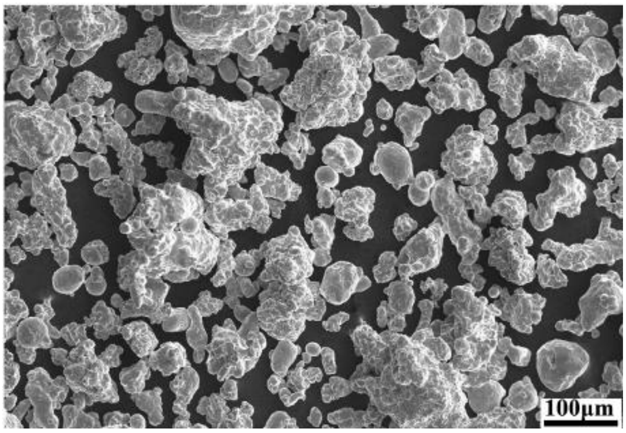
B	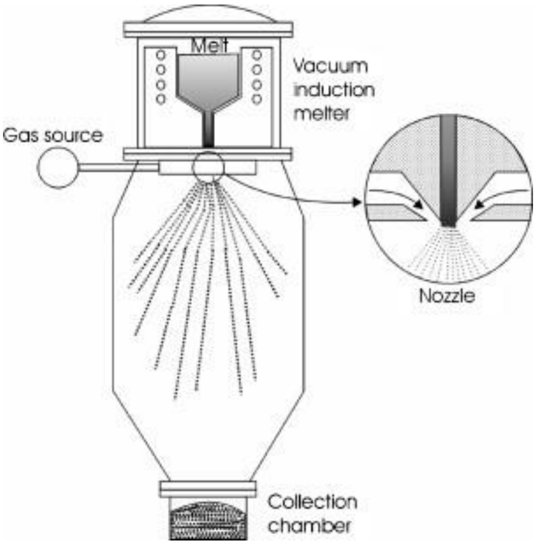	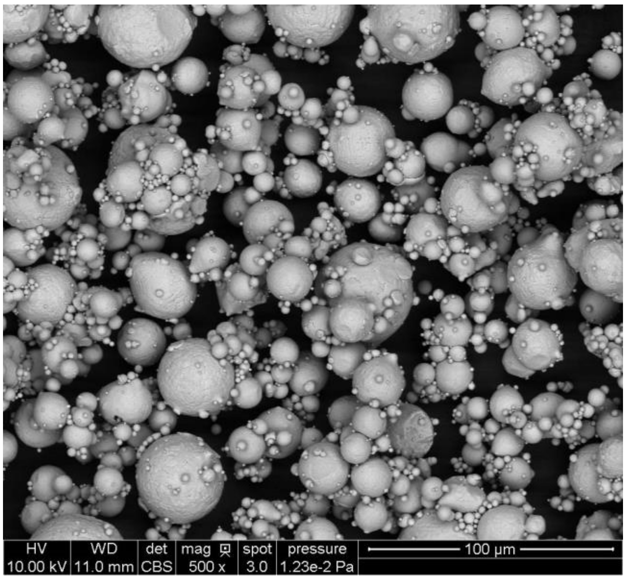
C	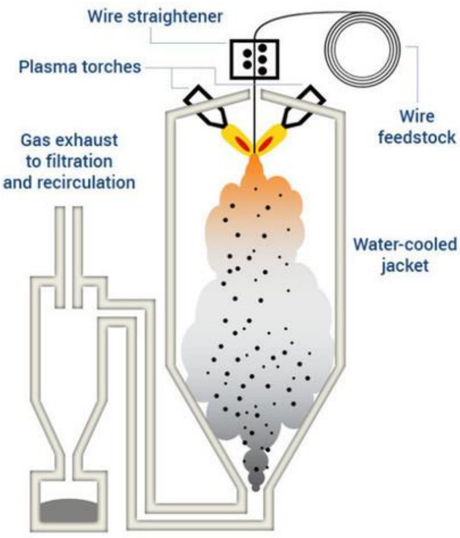	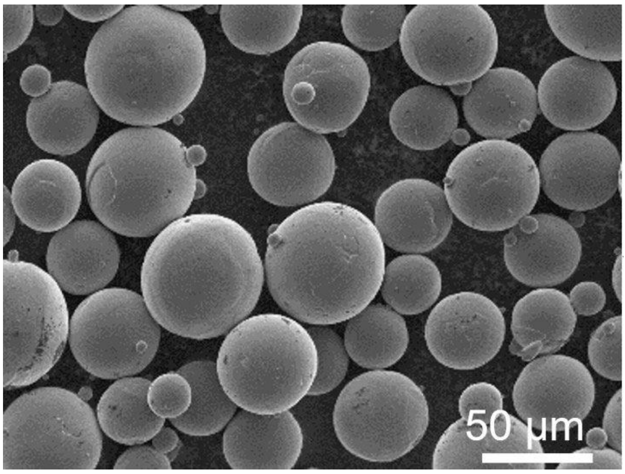

D	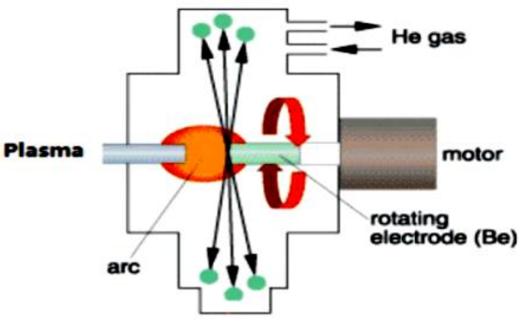	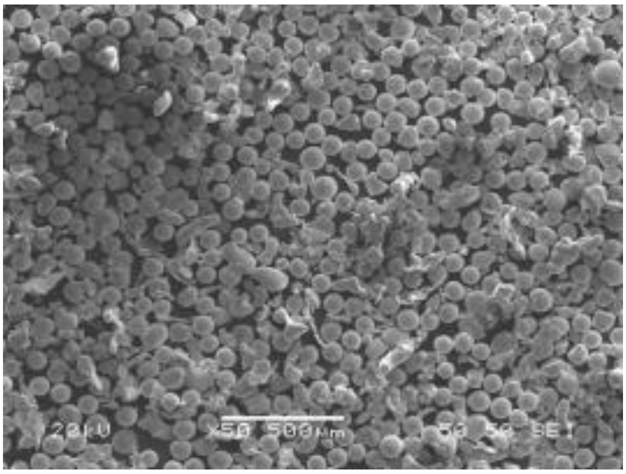

1.4.2: Powder's flowability

The flowability of the powder depends on the geometry of the particles and therefore in a system where the recoater must necessarily stretch a thin uniform layer (30 µm or 50 µm), plays a crucial role on the whole process. Since many machines use the normal gravity force for the supply of the recoater, unsuitable flowability implies a possible malfunction due to packing clogging. [24]

and the powder behaviour depends on several factors: a strongly compacted powder can behave like a continuous solid: the same material behaves like a liquid if subjected to intense cutting speeds or high cutting efforts, these working conditions common in industrial mixing processes (J. P. Seville, C.Y. Wu, 2016).

Physical interactions between particles affect mechanical properties and flowability. Figure 18 shows the variation in shear stress for a frictional powder and a Newtonian liquid. Evaluating the shear stress VS shear rate curve, it may be evidenced that if the cutting speed is constant enough, thus ensuring a continuous flow, the shear stress will be constant. However, the powder does not follow the same behaviour beyond the friction regime. The Newtonian liquids evidence a linear relationship between the shear stress and the cutting speed, called liquid viscosity.

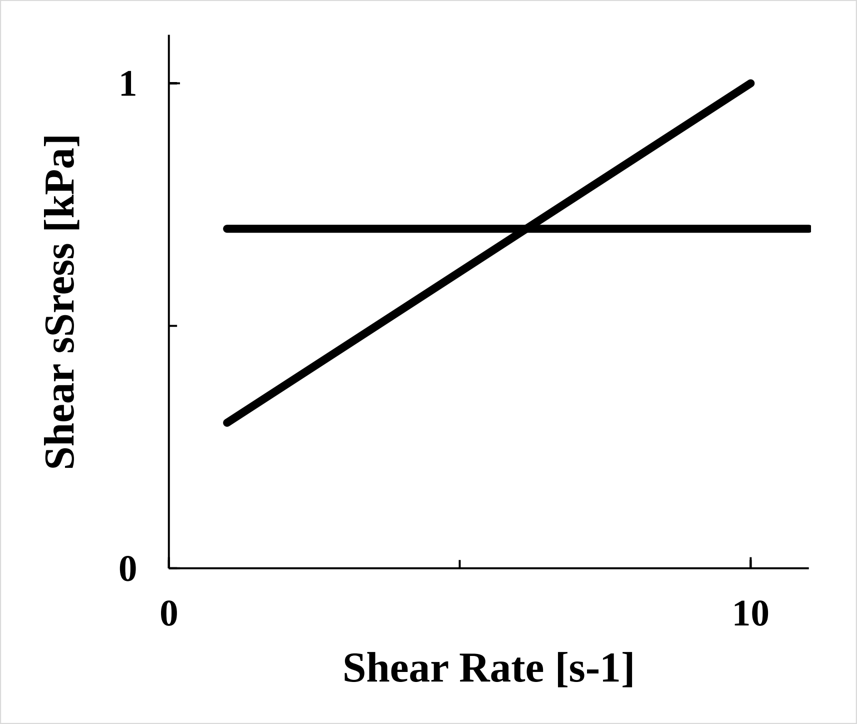

Figure 18: Shear Rate vs Shear Stress. Comparison between powders and liquids (J. P. Seville, C.Y. Wu, 2016)

Another significant difference between liquids and powders is shown in Figure 19: the initial compaction of the powder influences the behaviour of the flow (however their relationship is not always linear as represented in Figure 19). For a liquid, however, the shear stress is independent of the pressure applied, which is why the viscosity of the liquid remains constant.

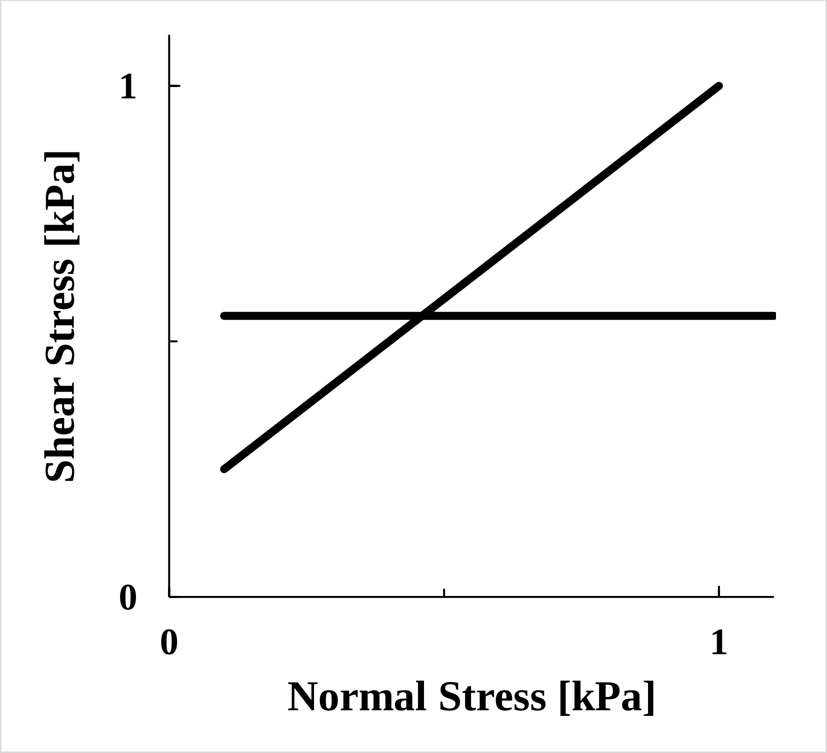

Figure 19: Shear Stress vs Normal Stress. Comparison between powders and liquids (J.P. Seville, C.Y. Wu, 2016).

According to Freeman (2000), Cain (2002), Behera et al. (2002) and Juliano et al. (2006), the cohesion of granular (or bulk) materials typically depends on certain mechanisms such as Van der Waals forces (interparticle forces), electrostatic forces or the presence of condensate liquids.

Seville et al. (1997) affirm that, cross-part forces could potentially counteract and even exceed the particle weight for granules smaller than 1 µm. Van der Waals forces are attractive forces between atoms or molecules caused by the temporary change in the dipole moment resulting from a small change in the orbit of electrons on one side of an atom or molecule, creating a similar change in adjacent atoms or molecules. Hygroscopic materials are known for their ability to form strong bonds between particles in the form of liquid bridges (the single particle is wrapped in a thin layer of water, so with an adjacent particle having the same characteristic, a liquid bridge is established). In addition, it should be noted that measuring cohesive forces in fine particulate matter is very difficult.

There are two flowability measurement methods: the direct method and the indirect one. With the direct method, it is possible to measure the flow properties at the time off the collapse from the static position; the powder is in a consolidated state that subsequently suffers a failure. These methods can fully describe the behaviour of the powder in a well-defined operating range. Shear cells, such as Jenike cells, annular cells, triaxial cells (Schewdes, 1996) belong to this group.

Indirect methods observe sizes that are supposed connected with the flow and analyse granular material in an unconsolidated or weakly packed state. Static and dynamic rest angle tests, such as fluidization and apparent density ratios, or the Hausner (HR) ratio, are techniques widely used to characterize powders. They are relatively fast and relatively simple techniques and are therefore preferred in common industrial practice. However, they do not define the state of the powder as complete as direct methods do.

Table 4 compare shear cells (cells that measure shear strain), static rest angle, and ratios between the apparent densities index. It is adapted from De Jong's work (1999) and it shows the sliding classifications and their applicability ranges of the flow factor (ff), the Hausner report (HR) and the static rest angle (α_r). Jenike's theory, based on quantifying shear strength, remains the basis for determining the flow of the powder. Shear stress is the resistance of the mass of the material to failure or flow.

Table 2 shows that the flow factor (ff) can distinguish the different behaviour to the flow of powders only for values less than 10. For higher values it loses validity and resolution. In practice it does not distinguish between various degrees of flow for powders in the weakly consolidated state. It works well for powders in the consolidated state.

Table 4: Common flowability index during application ranges

	ff	**HR**	**α_r**
Non flowing	< 2	> 1.4	> 60
Cohesive	2 – 4	> 1.4	> 60
Fairly free flowing	4 – 10	1.25 – 1.4	45 – 60
Free flowing	> 10	1 – 1.25	30 – 45
Excellent flowing	> 10	1 – 1.25	10 – 30
Aerated	> 10	1 – 1.25	< 10

The flow factor (ff) is obtained using a Shear Cell, which measures the variation in shear strain required to induce a flow with changes in normal stress for bulk (or mass) materials.

In an ideal experiment the powder sample is confined sideways and subjected in a vertical direction to a normal stress of consolidation σ_1; It may be observed that after consolidating the powder's sample, the confinement walls removal leads to its failure. The value that indicates the failure load is called the failure effort f_c. The set of tests carried out consecutively defines the so-called flow function, (FF), which is only a function of the powder's type used (see figure 20).

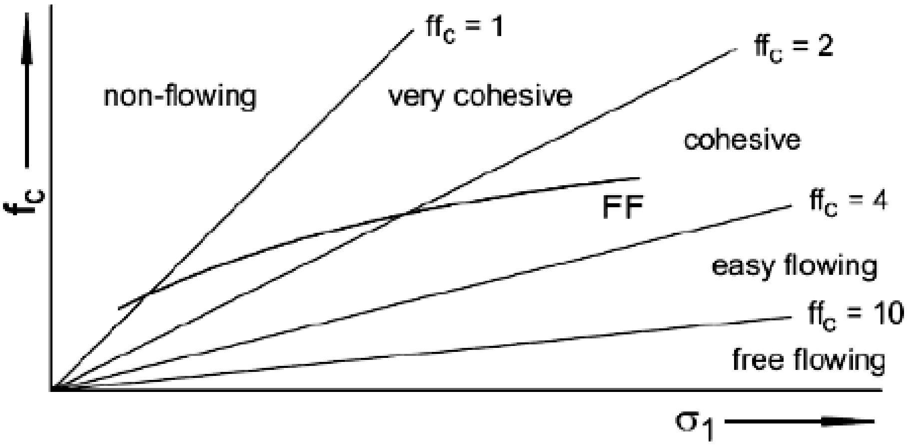

Figure 20: graphical definition of the flow factor of bulk material

The Flow Function (FF) is strictly time depending, so the same powder may have different behaviours depending on its consolidation state (see figure 20). This method can only be used if you are aware of compression stresses (consolidation σ_1) or failure stresses (f_c), and in most cases the value σ_1 and f_c are not determinable and therefore the flow factor (ff) value cannot be determined.

The flow factor (ff) unlike the flow function (FF) depends not only on the powder properties but also on the geometry of the system, so in the case of hopper containing powder, the flow factor value is indispensable to determine the inclination of the converging walls in the drain.

Another quantifying flow test identifies the rest angle. During the test, the powder is dropped by a funnel and then the powder pile is photographed, and the strip angle of the wall is measured. This parameter is the most independent of the existing parameters compared to the packing condition, because to obtain the mound from which the measurement is obtained, the powder passes from an initial packing condition constrained to the post-fall packing condition (Santomaso 2003).

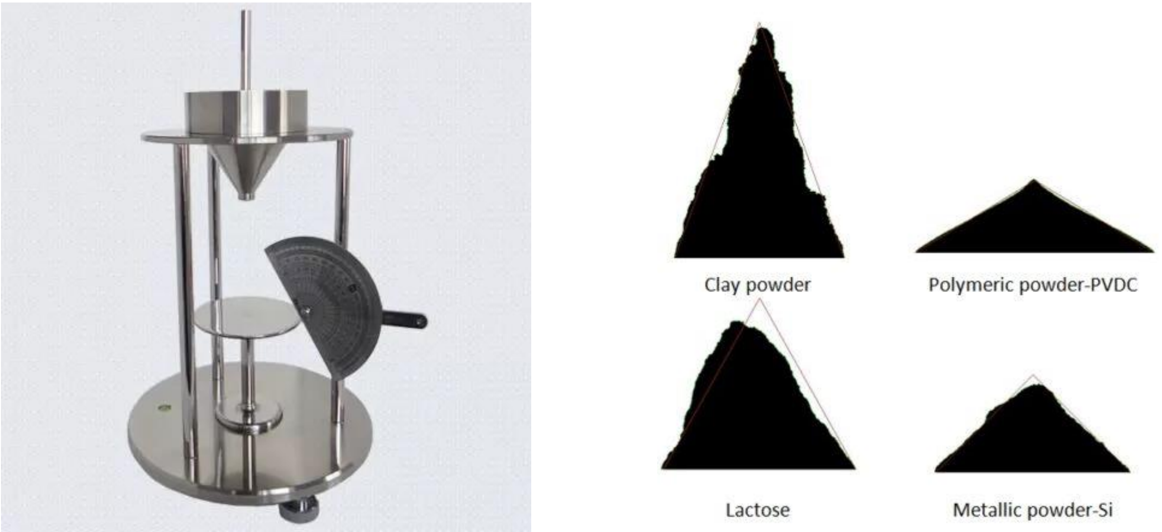

Figure 21: Repose angle testing machine and examples of repose angles

In the LASER PBF technique the flowability determines the success or the failure of the printed component. The flowability of the powder may vary due to suboptimal environmental conditions, black powder pollution or for the presence of a different kind of material (change of the printing material). [25]

The presence of moisture can cause a thin condensed layer around the particle. When two adjacent particles have the same "wet" condition, a water bridge is created by the cohesive force. If this condition is extended to a consistent volume of material, a cluster is obtained that leads to an uneven distribution on the printing plate during the passage of the recoater’s lip. [26]

In literature is possible to find some examples about powder flowability with or without moisture. In Figure 22 we can observe the case of a ceramic and metal powders. It show that the presence of moisture inside the powder significantly influence the test results [26].

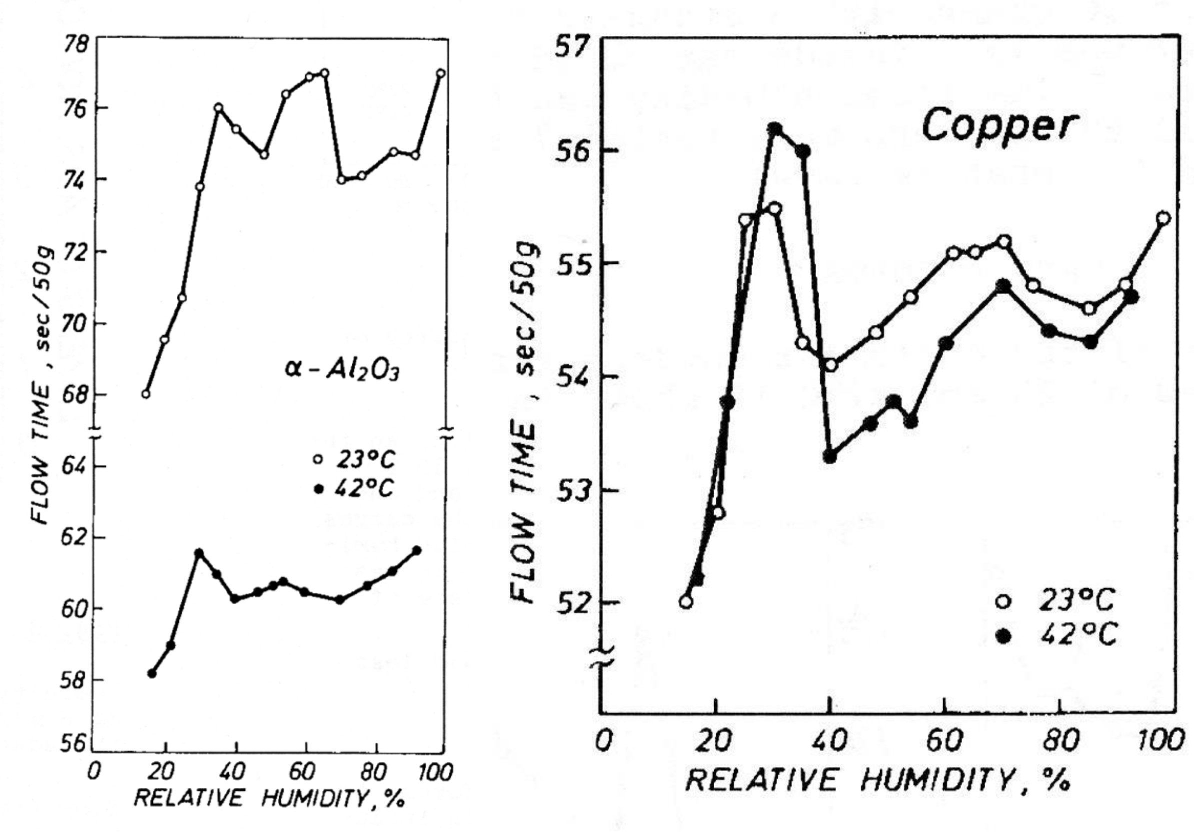

Figure 22: G.Matei , N. Claussen, H.H. Hausner : “Influence of relative humidity on flow of metal and ceramic powders”, Electronic design: circuits and systems, vol. 8, pp. 5 11, 1974

Another condition that leads to a dust packing is the type of gas used; According to studies carried out by Camille Pauzon et al, May 2019, the use of nitrogen instead of argon leads to a deterioration of the powder. The deterioration changes the geometry of the atomized material that is no longer spheroid but has all around so many satellites, which decrease the smoothness of the powder. The paper studied a 316L stainless steel. According to these studies, the degradation of powder is negligible in argon atmosphere and after a single processing in argon the powder did not present negative effects. Processed under argon atmosphere and reused for 3 cycles, the powder rarely shows the presence of darker particulate features sizing below 1 μm (see Figure 23 A and B) that were also observed for the powder exposed to the nitrogen generator atmosphere. In addition, with the nitrogen generator some particles showed a more critical oxidation with the presence of larger oxide features, covering significant area of the powder surface. [27]

If the powder surrounding the sintered part is observed, it is possible to affirm that the L-PBF process is a relatively cold process that should not lead to the oxygen pick-up through the formation of the particulate oxide features. In fact, it requires substitutional diffusion of the alloying elements, sensitive to oxygen, on the powder surface. However, local overheating of the powder close to the build part leads to a localized temperature increase of the powder particles which promotes the mass transfer of elements with high affinity to oxygen from the bulk to the surface of the particle, for example Si, Cr and Mn for 316L stainless steel. In combination with the high surface area, this explains the high reactivity and oxidation of the powder surface during the process. In Fig. 23-C, dark particulates from a few nm up to 2 μm are observed. The EDX analysis confirms that they are Cr-Mn oxides with traces of Si. Using nitrogen, the chamber temperature behaviour is comparable with the argon processing, it provides conditions for faster kinetics of powder oxidation. [27]

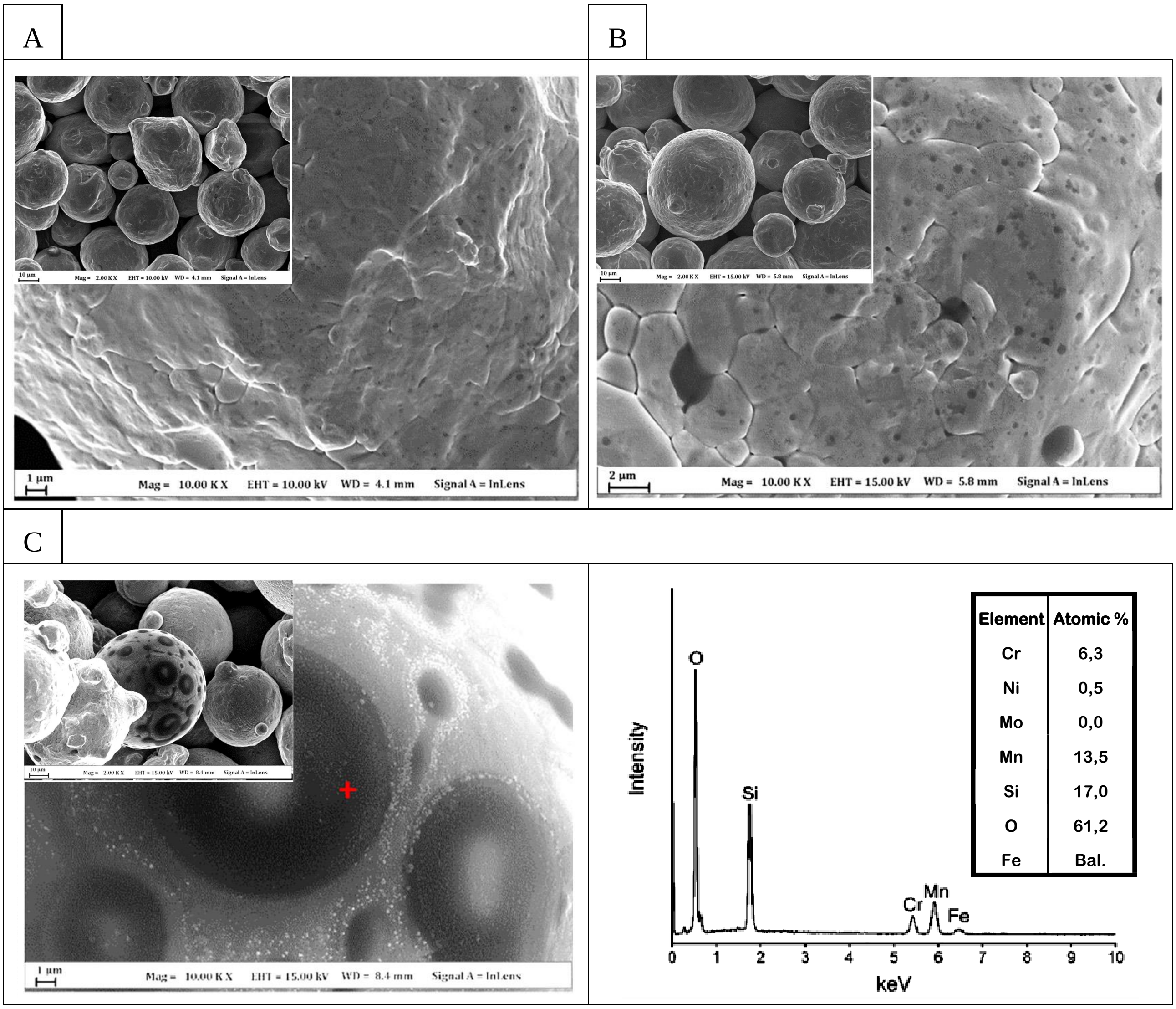

Figure 23: A) SEM micrographs of the virgin powder - B) SEM micrographs of the powder exposed to argon after three cycles – C) SEM micrographs with EDX analysis of the powder exposed to the internal nitrogen generator after one cycle. [27]

1.4.3: Powder’s spattering

During the LASER Powder Bed Fusion process, the *Spattering* causes a variation of the powder’s flowability.

The spattering phenomenon occurs during the interaction phase between the LASER beam and the metal power. The phenomenon of spattering therefore also concerns the liquid phase of the metal alloy.

Energy absorption by the feedstock materials affects the temperature profiles, deposit geometry, solidification, microstructure, and properties of the part. Energy absorption depends on the heat source characteristics. The spot radius and the power density distribution are important properties of the heat source. The power density distributions of these heat sources (TEM$_{00}$ source) follow the following axisymmetric Gaussian profiles. [28]

$$P_d = \frac{fP}{\pi r_b^2} \exp\left(-\frac{f(r^2)}{r_b^2}\right)$$

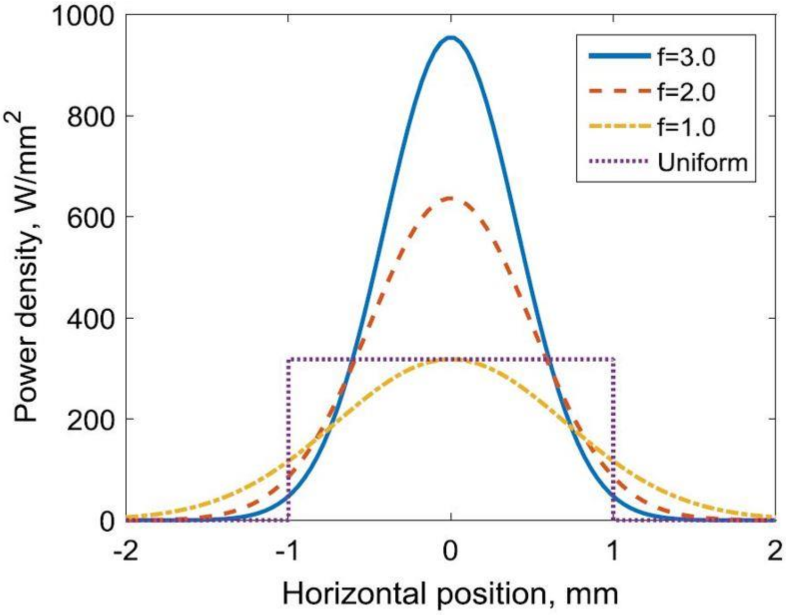

Figure 24: T. DebRoy et al. / Progress in Materials Science 92 (2018) 112–224

The Power Density equation indicates the distribution of the heat source during the melting process on the surface. The f value indicates the power density at the heat source axis, higher f value it means a higher power density. The r_b value indicates a power density along radial directions, a larger r_b indicates a lower power density on the surface. [28]

As widely described in literature a liquid is a physical system consisting of molecules held together by attractive forces called Van Der Waals forces.

Van Der Waals forces originate from weak attractions between atoms that arise from atomic or molecular dipoles. The induced dipole–dipole interaction between all atoms and molecules leads to a weak, very short-range force. The functional form of the van der Waals interaction is typically given by a hardcore repulsive interaction and the London energy of the induced dipole–dipole interaction. These interactions are often modelled by the function form.

$$Repulsion energy: be^{\alpha r} \vee \frac{b}{r^n}$$

$$Attractive potential: -\frac{a}{r^6}$$

where n is often given as 12 as in the Lennard-Jones potential (Douglas et al., 1993). Summation of all the pair-wise interatomic forces acting between the two bodies is required to calculate surface force between the two bodies. The net force (per unit area) between two flat plates is:

$$F = \frac{-A_H}{6\pi d^3}$$

where A_H is the Hamaker constant and d is the separation of two surfaces (Horn, 1990; Wan et al., 1992). The Hamaker constant depends on the medium of contact. Assuming a constant separation between two surfaces, d_0, the specific interaction energy, W_v, per unit area is given by:

$$W_V = \int_{d_0}^{\infty} \frac{A_H}{6\pi x^3} dx = \frac{A_H}{12\pi (d_0)^2}$$

Typical value of the interfacial energy due to van der Waals interaction is < 0.01 Jm^{-2}. [29]

Physical systems for example liquid-liquid interfaces or liquid-gas interfaces have interfaces that separate the two liquids of the mixture or the liquid from the gas. The molecules located at the interface are attracted to the inside of the parallel to the interface while the bulk molecules are affected by a balance state.

The result of the agent forces on a generic molecule of the bulk system is null since the forces in the various directions are balanced by those that other molecules exert on it while for a molecule located on the interface the only forces that do not remain balanced are those directed inwards of the system (see Figure 25). This means that the overall are at end to contract. The liquid molecules of the interface are also less bound than the molecules and therefore more energy, as a result ' and need to spend energy to move a molecule from the bulk to the interface. [30]

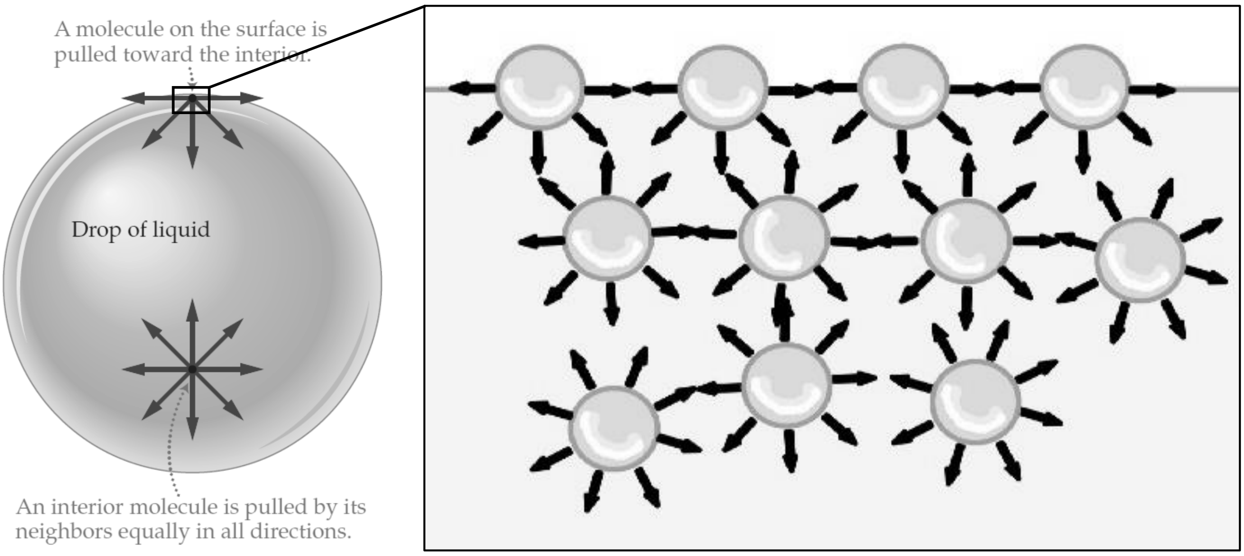

Figure 25: example of Van Der Waals resulting force, on the bulk and on the interface of a liquid drop.

Molecules forming the shell of a drop have a higher attractive charge than bulk molecules. To move a molecule from the bulk to the interface we need to spend more energy. The energy needed to achieve thermodynamic balance is called Free Energy or Free Helmholtz' Energy and is thus defined:

$$F_H = U - TS with \begin{cases} U = Internal Energy \\ T = Temperature \\ S = Entropy \end{cases}$$

$$\sigma = \frac{\partial F_H}{\partial A}$$

The dependent variable σ is known as surface tension and for liquids it is a descending monotonous function of temperature; F_H is the Free Helmholtz's Energy and A the area of which the surface contracts.

$$\frac{\partial\sigma}{\partial T} < 0$$

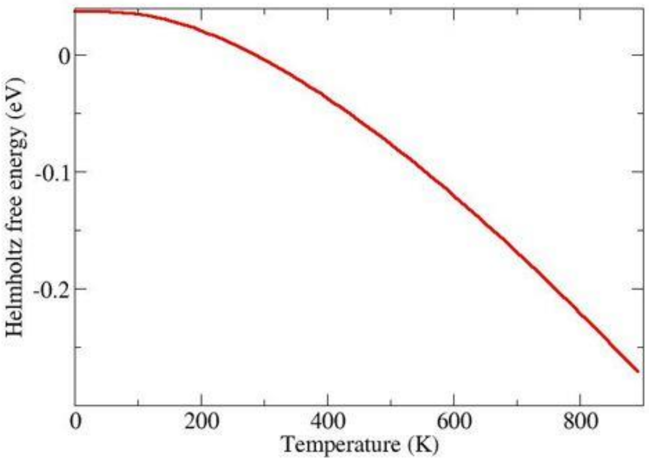

Figure 26: Free Helmholtz's energy vs Temperature; monotonous decreasing function.

The surfaces of liquids by their nature tend to contract; this natural phenomenon together with surface tension give a pressure difference between the two sides of an interface, with higher values near the concave side. Young's law – Laplace correlates the two phenomena into a single equation:

$$\Delta p = \sigma\left(\frac{1}{R_1} + \frac{1}{R_2}\right)$$

with R_1 and R_2 the respective radii of the two interfaces. For the specific case of a droplet or gas bubble the two radii are equivalent, so you get the relationship:

$$\Delta p = p_i - p_e = \frac{2\sigma}{R}.$$

This relationship is consistent with the fact that at equilibrium the sphere is the solid figure with the small minimum surface area. [30]

Another equation that governs fluid motion and affects the Marangoni effect is the Navier–Stokes equation. Velocity, pressure, temperature, density, and viscosity are the main properties that should be considered simultaneously when conducting a fluid flow examination. In accordance with the physical phenomena such as combustion, multiphase flow, turbulence, mass transport, etc., those properties diversify enormously and can be categorized into kinematic, transport, thermodynamic, and other miscellaneous properties. [30]

Thermo-fluid incidents directed by governing equations are based on the laws of conservation. The Navier-Stokes (N-S) equations is the broadly applied mathematical model to examine changes on those properties during dynamic and/or thermal interactions. These equations describe how the velocity, pressure, temperature, and density of a moving fluid are related. [30]

The equations were derived independently by G.G. Stokes, in England, and M. Navier, in France, in the early 1800's. The equations are extensions of the Euler Equations and include the effects of viscosity on the flow:

$$\partial_t(nu_\alpha)+\partial_\alpha(nu_\alpha u_\beta)=-\partial_\alpha P_{\alpha\beta}+\partial_\alpha\left[\eta\left(\partial_\alpha u_\beta+\partial_\beta u_\alpha-\frac{2\delta_{\alpha\beta}}{d}\partial_\gamma u_\gamma\right)+\xi\delta_{\alpha\beta}\partial_\gamma u_\gamma\right].$$

For an incompressible fluid (constant density in each volume portion) the relation applies:

$$\nabla\cdot u=0.$$

The Navier – Stokes equation becomes:

$$\partial_t(u_\alpha)+u_\beta\partial_\beta u_\alpha=\frac{-1}{n}\partial_\alpha P_{\alpha\beta}+\nu\nabla^2u_\alpha with \nu=\frac{\eta}{n}.$$

A spatial variation of surface tension along a liquid-liquid or liquid-gas interface results in a consequent tangential force on the same interface and therefore a motion.

This motion is known in literature as Marangoni effect, in the name of the Italian scientist Carlo Marangoni who first studied this phenomenon.

This surface tension gradient can, in turn, be induced by any inhomogeneities or anisotropies inherent in the system itself. As far as LASER powder bed fusion technology is concerned, these anisotropies and inhomogeneity can be traced back to the powder particle's size, the interaction between dust and LASER source or the interaction between molten line and powder (see Figure 27).

The interaction between a molten line and powder causes secondary phenomena such as balling effect, spattering, phenomena driven by the Plateau-Rayleigh effect. [28]

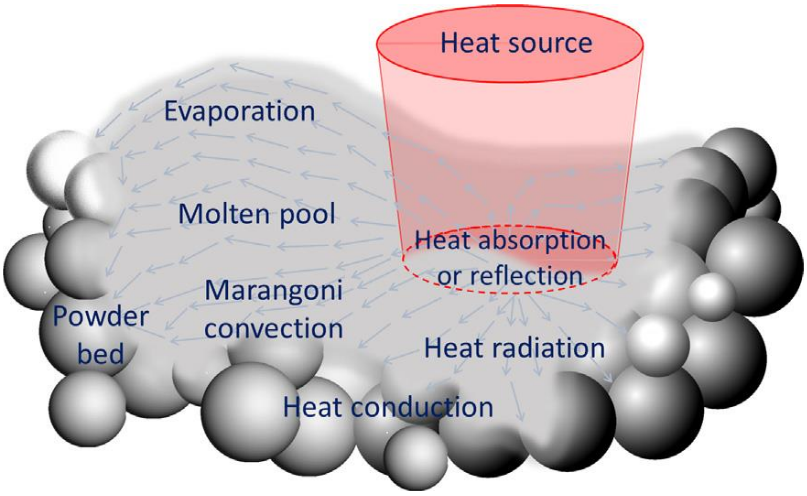

Figure 27: Heat transfer and molten pool dynamics during powder based additive manufacturing [28]

According to studies carried out by Chu Lun Alex Leung et al (2018), from the formation of the melting pool starts a Marangoni's flow opposite to the scanning direction. If the scanning speed is over 1000-1200 mm/s [31], some portions of the melting pool near the head identify localized Marangoni effects, which lead to the formation of isolated fused drops, a physical phenomenon identified as Plateau-Rayleigh instability, which generates the balling effect (see Figure 28). If these drops have no way of being incorporated into the melting pool, the gas washing flows and pressure wave that is generated at the contact interface between LASER source and dust cause the removal of the drops, which increase global spattering. [32]

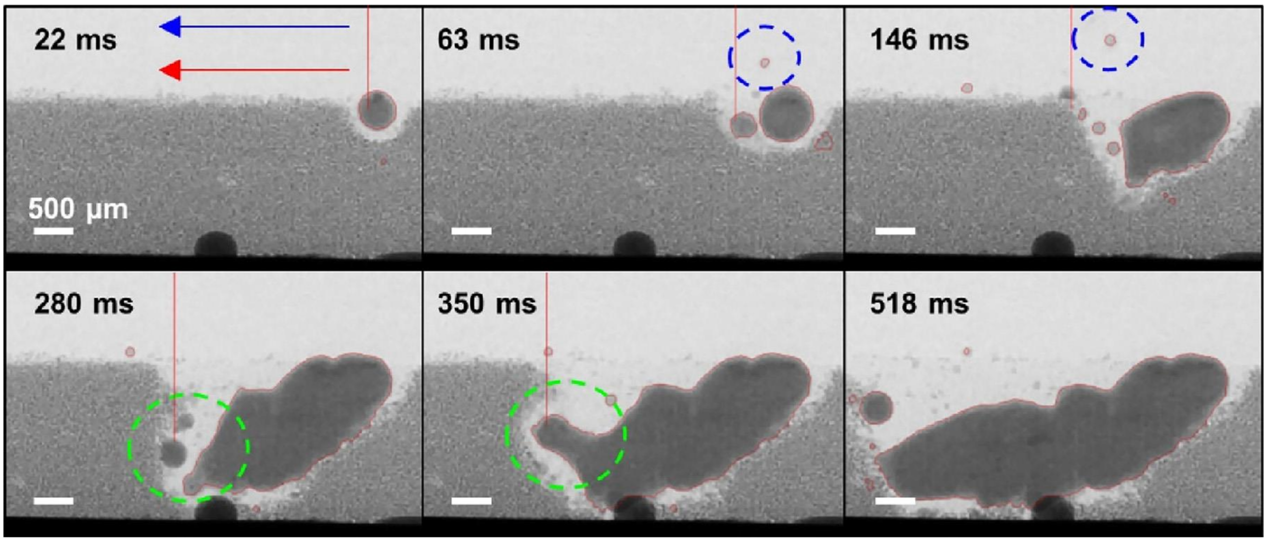

Figure 28: Typical time-series radiographs showing melt track evolution. The LASER beam direction is represented with the red arrow and the gas flow with the blue arrow. The overlaid vertical red lines indicate the LASER beam position. Blue circles highlight the droplet spatter movement. Green circles show track growth via molten pool wetting. [32]

The formation of a pore depends mainly on three factors: gas dissolution within the molten cord direction, capture of insoluble gas inside the cord, or inadequate liquid feeding upon solidification. The large open pores were formed by the coalescence of small, closed pores to minimize their surface energy which then burst open at the surface. This happens either during the final solidification stages, and hence the surface freezes, forming a surface depression or a dent at the same location, or the depression may be stabilised by an oxide thin layer. In addition to pore formation, the Marangoni-driven melt pool flow can facilitate pore migration, entraining gas pores and transporting them to different locations inside the melt track. [32]

2: Machine development and numerical characterization

The development of the machine began two years before I began the collaboration through the technology research group at the University of Modena and Reggio Emilia – Department of Mechanical Engineering Enzo Ferrari. In particular, the company that wanted, and still wants to develop a 3D printer with metal powders is called 3D4Mec, based in Sasso Marconi (BO). The company aims to develop the machine with two different print volumes; The EASY machine (110x110x250 mm^3) and the LIBERTY machine (230x230x250 mm^3); both use nitrogen as a protective gas. First, once we took over the optimization of both the machine and the process parameters, we had to look for a dedicated software for this kind of technology. The choice fell to Autodesk Netfabb. A first step was to investigate the software as much as possible so that we can understand where and how to enter the parameters we needed. The next step was to set up an experimental plan to determine the optimal parameters to ensure a good relative volumetric density around 99% with also a good surface finish. During the printing phases it was possible to analyse the operation of mechanical parts; in particular, we focused on the dust supply system, the dust dispenser, the flow of gas into the room, the filtration system, the dust sieve system.

2.1: Chamber optimization

The print chamber has a total footprint of 419x544x250 mm^3 with left-to-right gas directionality. The chamber's fabrication material is an X5CrNi18-10 (UNI EN 10088-1 – AISI 304). The choice of material depends on the fact that the company initially developed the machine for the additive production of stainless-steel mechanical parts X5CrNi18-10 – AISI 304, ensuring a high affinity between product part and manufacturer. The other important aspect in the same choice of materials depends on the wear that metal powders could cause over time to some components; a more easily processed material could be subject to erosion by volatile dust. The pollutant, over time, could lead to a little deterioration of the dust used for the construction of the printed component.

The dust spreader performs a linear movement through a belt link from the bottom of the room to the door and back. The movement of the distributor as the rotation of the dispenser is operated through brushless stepper engines. The dust inside the dispenser is loaded through a tube at the bottom of the room (see Figure 29).

GENERAL VIEW

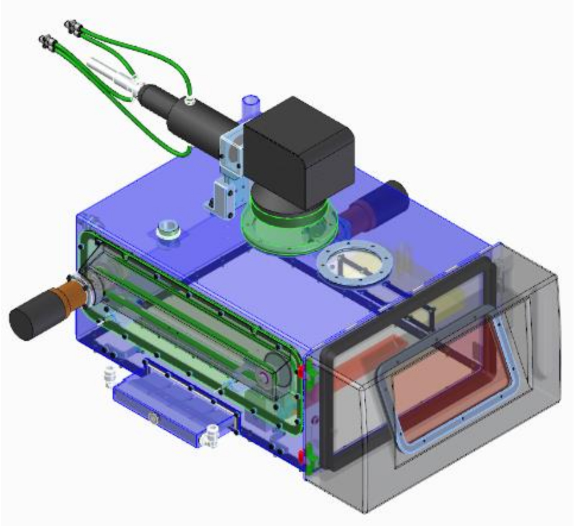

a	DIMENSIONS	b	GAS DIRECTION	c	RECOATER MOVEMENT
	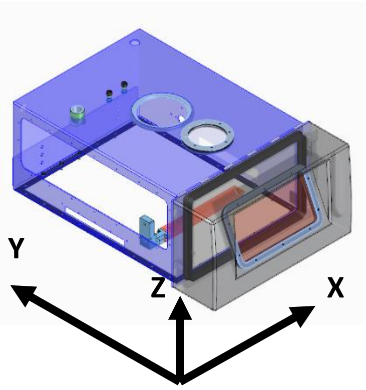 419x544x250 mm^3		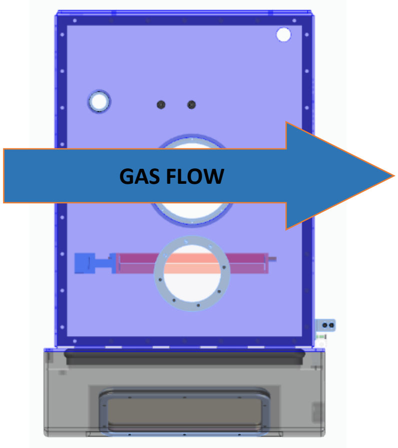		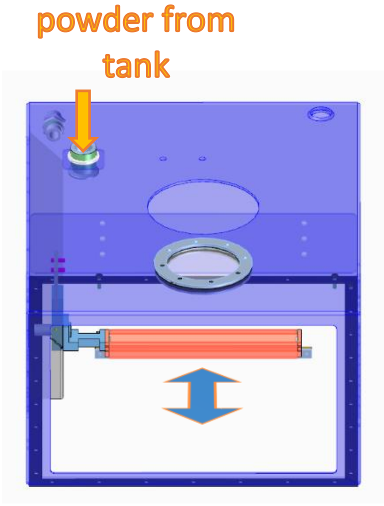

Figure 29: general view of the build chamber and view of a) dimensions, b) the gas flow and c) the recoater movement with the refill powder direction

An initial optimization of the print room was performed by reducing the volume; During the normal operation of the machine, we found that behind the dust dispenser there is a 'dead' space, which generates unwanted turbulence in the gas flow and above all turns into a dust deposit. The stagnating dust is not recovered during printing, so it removes printing capacity, and in addition, the dust is heavily polluted by the residual spatter that is not sucked in. Given the clutter of the movements and considered the clutter of the dispenser, it was possible to reduce the footprint of the room, bringing as close as possible to the effective volume.

BEFORE	AFTER
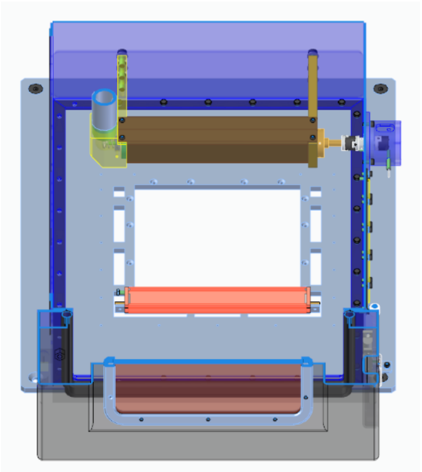 **Total volume ≈ 57 liters**	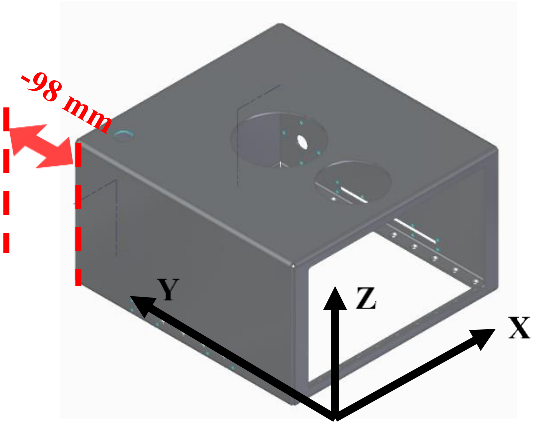 **419x446x250 mm^3** **Total volume = 46,7 liters**
VOLUME SALVAGED = 10,3 LITERS (18%)	

Figure 30: first optimization of the chamber volume

18% less volume for the print room translates into multiple benefits. From an energetic point of view, because you will need less gas in the room to saturate the environment and therefore less electricity consumption for the operation of the nitrogen generator. In addition, it will take less time to arrive at a stationary condition of complete nitrogen saturation in the printing environment (see Figure 30).

Having within the printing chamber elements that move even a few microns, it is necessary that some geometric tolerances are respected: first, it is that of flatness of the individual surfaces and then that of orthogonality between the various elements that make up the printing chamber. With the first prototype we observed through the measurement with a comparator that the chamber produced with a folded sheet of 3 mm during the flow of gas at a pressure of 0.15 MPa, producing a thrust of about 34 N turns out to deform 3 mm (see Figure 31).

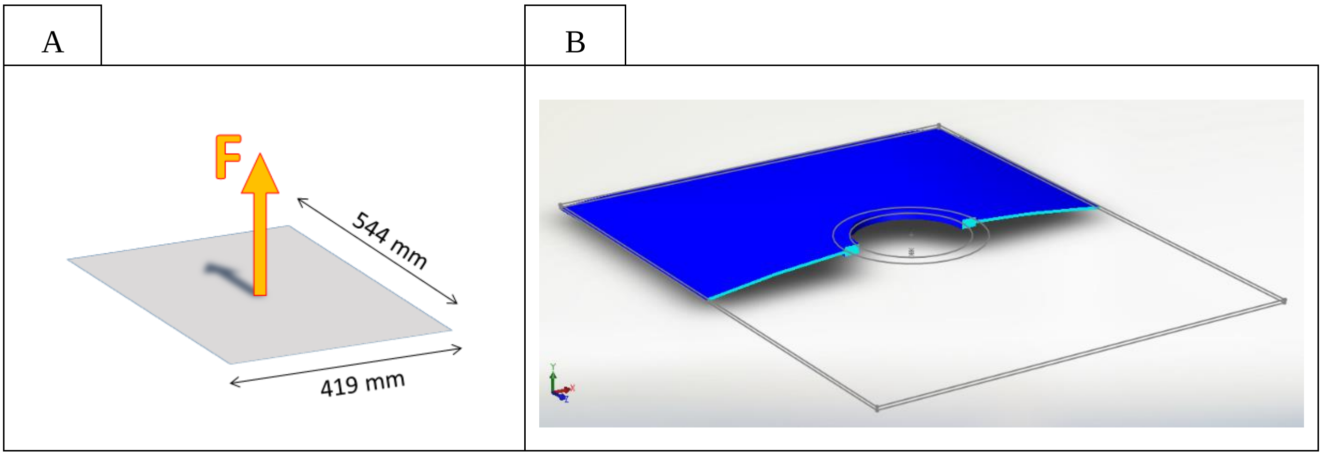

Figure 31: top of the building chamber; Figure A scheme of the applied force, Figure B representation of the curved top

For this reason, the LASER adjustment support was released from the ceiling of the room and the walls were increased in their thickness up to 9 mm. The thickening of the walls ensures, in addition to a greater rigidity, compliance with the tolerances required through small CNC processes, and also allows to consider the assembly of the chamber as an assembled set of screwed walls (see Figure 32).

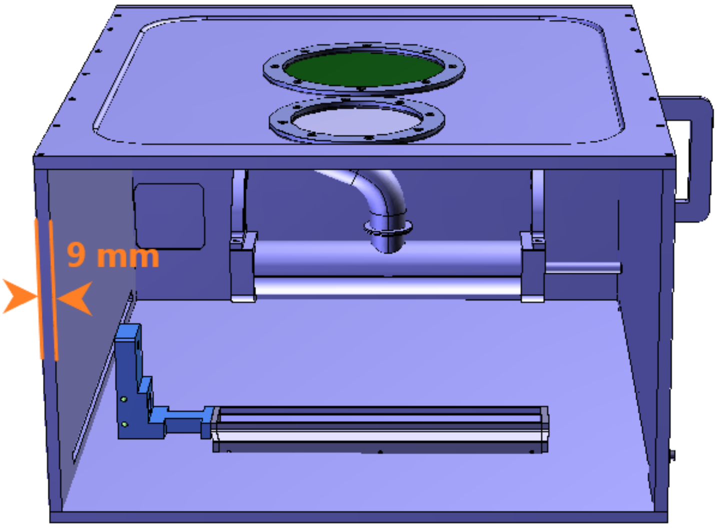

Figure 32: scheme of the optimized building chamber

One of the goals that you want to achieve in the development of the new machine is simplification: eliminating everything that is superfluous or non-functional within the machine makes everything easier both from the design point of view but also from the point of view of industrialization of the final product. By increasing the thickness on the walls, ensuring flatness and orthogonality between the wall that supports the sled and the base of the room, you can optimize the number of components that make up the distributor handling and driving system. Moving from a belt transmission to a direct coupling between the sled and the engine, the number of components and points of possible loss are reduced (particularly in the holes for the passage of trees that support the internal pulleys and pulleys outside the chamber, the holes to support the sensors, or in this case the holes for fixing the adjusted plate that supports the guide and the distributor – see Figure 33).

The presence of thick walls makes it possible to make blind punctures that guarantee perfect seals in threaded mates. The movement of the engine to the back of the camera also allows to contain the overall dimensions of the machine. The sensors for handling control are no longer external but integrated; This feature allows a lightening from an engineering point of view, but also electronically, as the controller connected to the device integrates in is all the ports for the control of micro-sensors. Mechanical and non-magnetic sensors have been used, as the material most commonly used inside the machine is an X5CrNi18-10 steel (UNI EN 10088-1, AISI 304), which has magnetic characteristics and therefore could interfere in the capture signal; In addition, the presence of black powder with low magnetic properties could in the long run affect and affect the operation of the sensors.

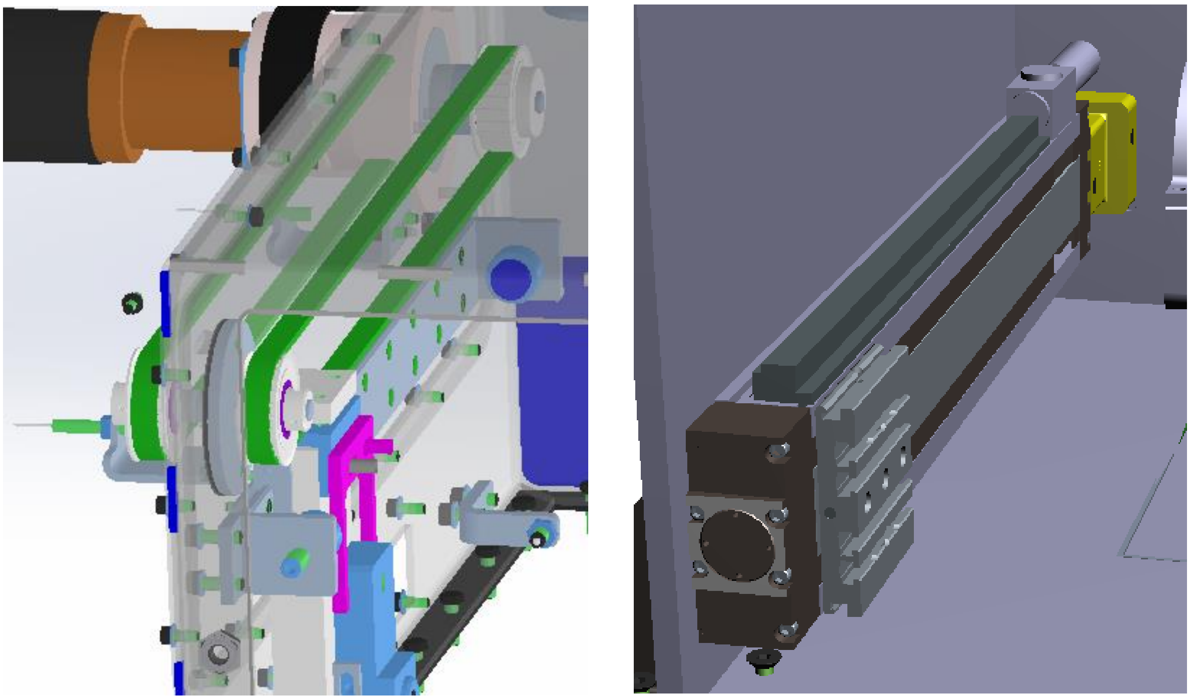

Figure 33: differences about the number of parts between the first and the second version of the machine

The engine that governs the powder dispenser is moved in a higher position compared to the position before. This is to ensure better ventilation in the room, thus also improving a correct sizing of the suction vents. The joint between the distributor and the electric step-motor is granted by an Oldham coupling to prevent the non-coaxial position of the two shafts (see Figure 34).

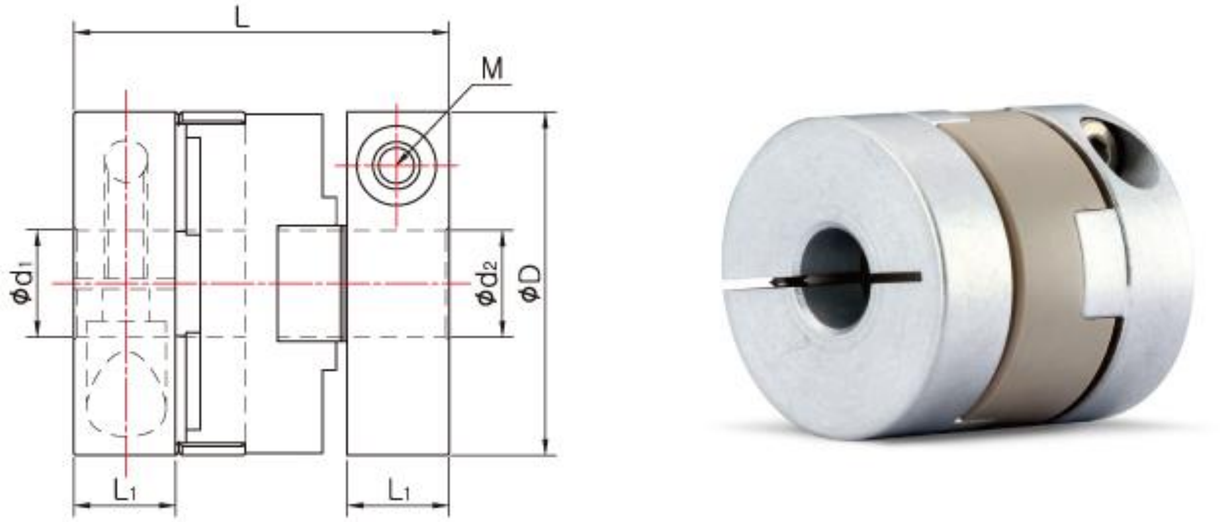

Figure 34: straight-toothed conical wheels, courtesy of www.garotti.com

The LASER source along with the galvanometer were released from the upper wall of the chamber and were fixed outside the chamber through a bracket system (see Figure 35).

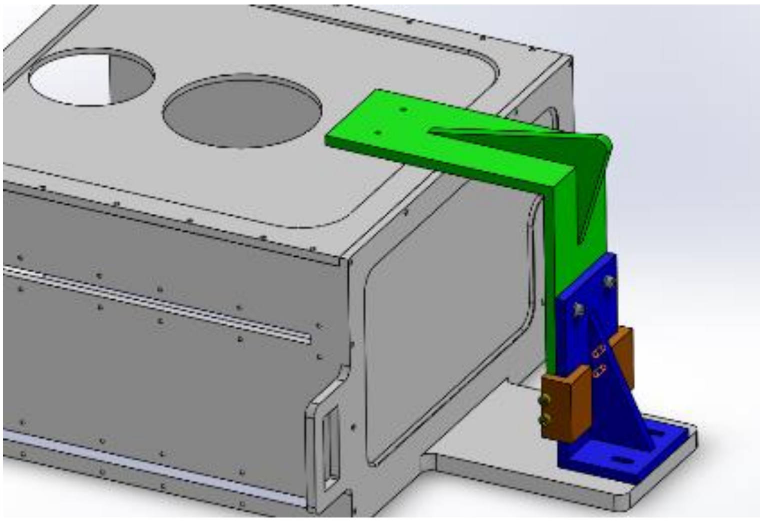

Figure 35: assembly of printing chamber and LASER support

Further space optimization led to the installation of the LASER group support in the area above the print chamber, by inserting a guide with micrometric shift control in the X and Y directions. This kind of shrewdness during LASER calibration will allow a greater focus of the LASER spot on the print plate, decreasing some LASER beam aberration effects due to the micro-defects of the focusing lenses.

2.2: Gas flow optimization with and without a cyclone

The development of the machines within the company of Sasso Marconi had to contend with a problem related to the rapid deterioration of the filtration group of the recirculation plant, with a conspicuous production of spatter inside the chamber. By analysing the suction system and consequently the send-off system, there were some critical issues. The first critical aspect was found on the type of signal with which the pump was fed. A heating effect of the gas was also found in relation to the operation of the pump, this phenomenon due to an imbalance in the flow in the room. The increase in the temperature of the gas leads to a change in the properties, the density, of the gas itself. The gas that is used to ensure that the powder does not undergo an oxidative process is nitrogen. The thermodynamic properties are:

Table 5: thermodinamic properties of Nitrogen gas

Molecular Weight	28,013
Specific Gravity, air = 1	0,967
Specific Volume (ft^3/lb, m^3/kg)	13,98 – 0,872
Density of liquid at atmospheric pressure (lb/ft^3, kg/m^3)	50,46 – 808,4
Absolute Viscosity (lbm/ft s, centipoises)	12,1*10-6 – 0,018
Sound velocity in gas (m/s)	353
Specific Heat - cp - (Btu/lb°F or cal/g°C, J/kgK)	0,249 – 1040
Specific Heat Ratio - cp/cv	1,40
Gas constant - R - (ft lb/lb°R, J/kg°C)	55,2 – 297
Thermal Conductivity (Btu/hr ft °F, W/m°C)	0,015 – 0,026
Boiling Point - at saturation pressure 14.7 psia and 760 mm Hg - (°F, °C)	-320,4 / -195,8
Latent Heat of Evaporation at boiling point (Btu/lb, J/kg)	85,5 – 199000
Freezing or Melting Point at 1 atm (°F, °C)	-346 / -210
Latent Heat of Fusion (Btu/lb, J/kg)	11,1 – 25800
Critical Temperature (°F, °C)	-232,6 / -147
Critical Pressure (psi, MN/m^2)	493 – 3,40
Critical Volume (ft^3/lb, m^3/kg)	0,051 – 0,00318
Flammable	NO

The temperature and temperature gradient of a point in the middle of fabricated tracks are presented in Figure 24 for both the use of argon and nitrogen gases during L-PBF. It may be observed that temperature and temperature gradient marginally decrease when shielding gas is changed from Argon to Nitrogen. This is due to the change in the thermal properties of Argon and Nitrogen. The thermal conductivity of Argon is lower (≈ 40%) compared to that of Nitrogen.

Thanks to the studies of Pooriya Dastranjy Nezhadfar et al, 2018, “Mechanical Properties of 17-4 PH Stainless Steel Additively Manufactured under Ar and N2 Shielding Gas”, we can say after their mathematical simulations that the specific heat capacities (isochoric and isobaric) of Argon, are almost half that of Nitrogen. Consequently, more thermal energy will be absorbed via convection when Nitrogen is used inside the L-PBF chamber. When Argon is used inside the chamber, the peak temperature is ~100 ºC higher than the condition in which Nitrogen is used. The peak temperature gradient when using Argon is 11% (4.3 ºC/µm) higher than when using Nitrogen as the shielding gas.

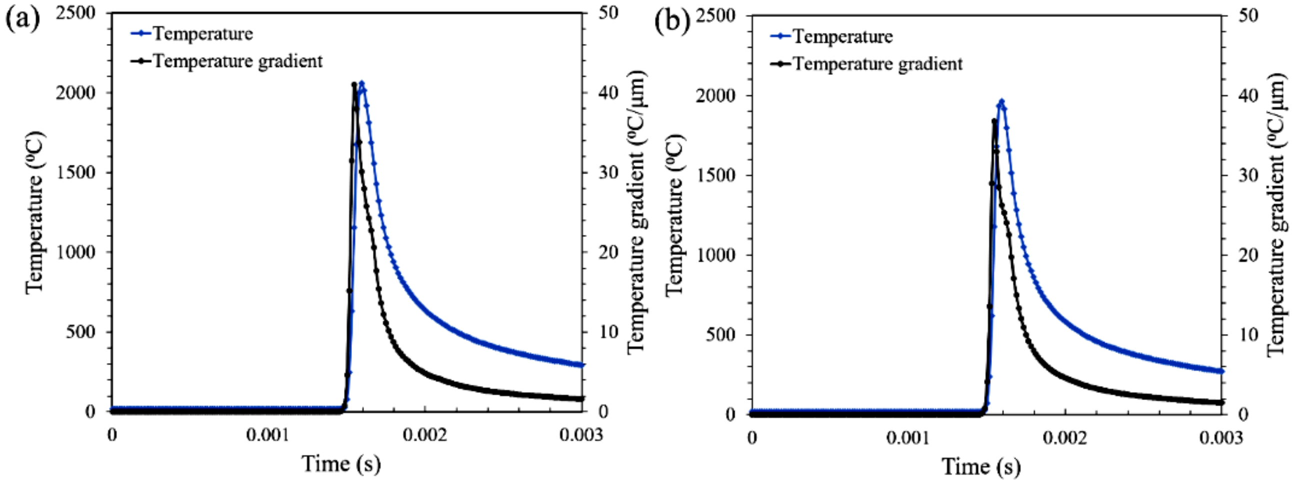

Figure 36: Temperature gradient at the middle of track under (a) Argon and (b) Nitrogen environment

It is observed in Figure 36 that the cooling rate at the middle point of the track, is ≈10% higher when Nitrogen is used as the shielding gas. Like the previous case, the difference in thermal properties of Argon and Nitrogen causes the change in cooling rate. From the results, it is observed that convective heat transfer is more important when Nitrogen is used as a shielding gas compared to when Argon is used. This means that more energy will be dissipated by the environment when Nitrogen is used as the shielding gas (see Figure 37). [33]

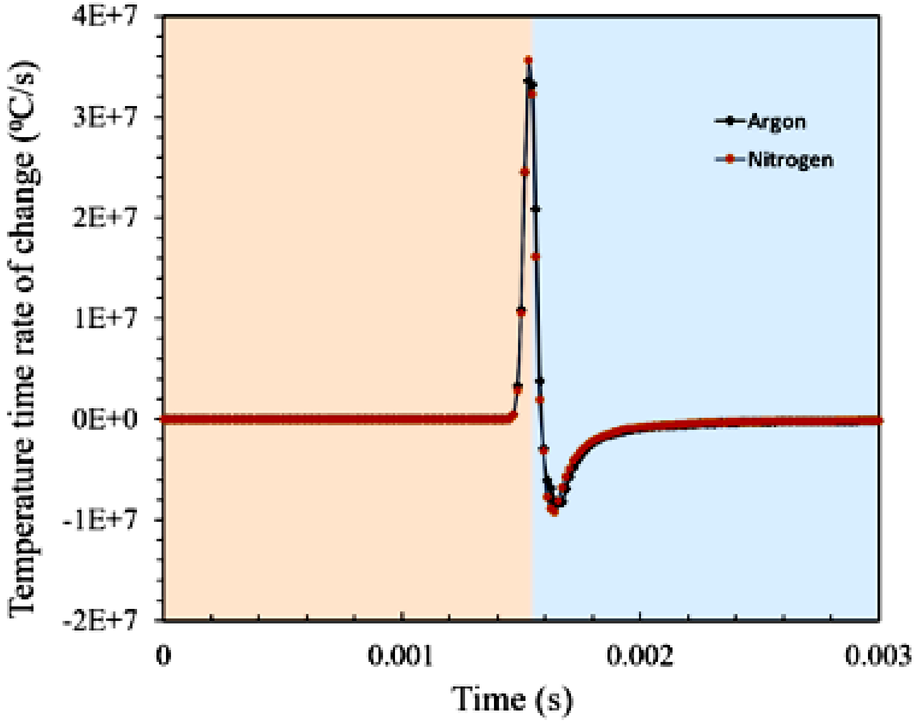

Figure 37: Cooling rate at the middle of track under Argon and Nitrogen atmosphere

Argon is an inert gas but depending on the grade of the industrial gas quality used it will contain impurities such as oxygen. In addition to this, the build chambers in most L-PBF setups are not fully gas-tight, which means that oxidation will occur during the printing process; this implies enhanced oxygen levels in the finished parts. Besides the abovementioned oxygen contamination, nitrogen is not inert at elevated temperatures, and an appreciable amount of nitrogen can be dissolved in stainless steel.

Nitrogen "pick-up" is relevant for austenitic stainless steels above, say, 900 °C, where there is an appreciable capacity for nitrogen in the solid state (in the austenite and by formation of Cr-nitrides). At these temperatures molecular nitrogen gas can dissociate and can easily result in nitrogen contents of more than 1 wt % (at equilibrium) depending on temperature. Uptake of nitrogen during processing can result in higher strength without loss of ductility and improved corrosion resistance provided it resides in solid solution in the austenite. However, at too high nitrogen concentrations the material can suffer from formation of hard chromium nitrides and local sensitization at elevated temperatures, thereby – negatively – changing the mechanical and anti-corrosion properties of the steel. [34]

Since the analysis of the recirculation system on the machine is not fully accessible, a test system see Figure 38 has been set up to study its flows and load losses. The circuit consists of all the main parts:

- Recirculation pump (1)
- Printing room (2)
- Cyclone Filter (3)
- Coarse filter (4)
- Fine Filter (5)

- Pressure Sockets (P)
- Valves for adjusting load losses (V)

In order to have greater clarity of the phenomena that are generated in the room, it was decided to replicate the printing chamber through Polymethyl 2-methylpropenoate) sheets with a thickness of 10 mm. For greater robustness, a fastening with screws as well as gluing was opted. A silicone sealant was used to prevent possible escapes from the chamber.

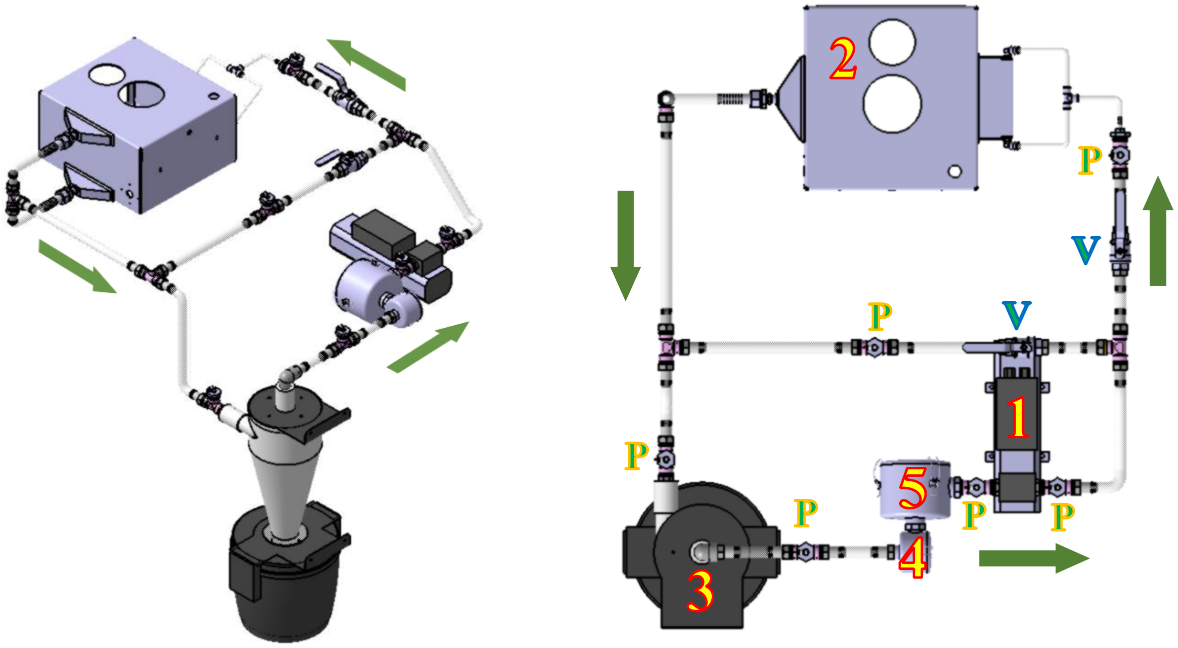

Figure 38: layout of the test plant

The test circuit was equipped with 6 pressure sockets (indicated with 'P' in Figure 38 and numbered according to the scheme of Figure 39) so that load losses could be measured in each section.

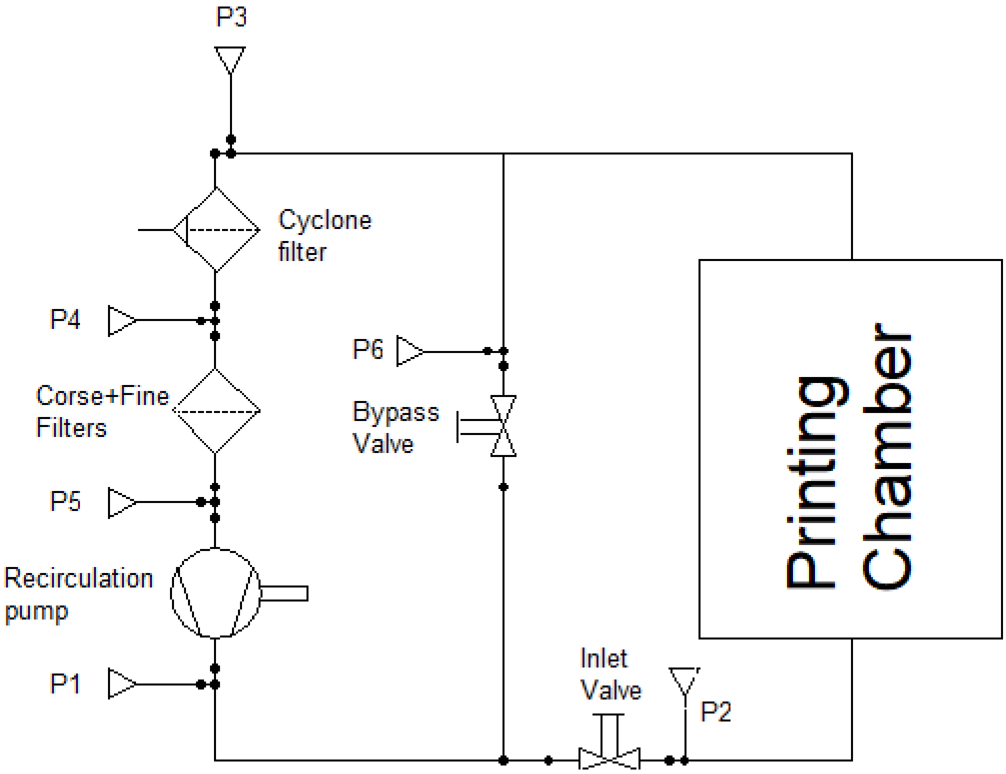

Figure 39: numbering of the manometer connections

The analysis of the flow in the room was addressed using two experimental methods: the first method with the help of a smoke machine, analysing the smoke lines coming out of the send mouth. Unfortunately, this system does not allow an overall analysis in the entire section of interest, but only allows us a local analysis (in our case only near the send mouth). The second method considers the possibility of placing thin wires with which the global speed field could be analysed. In particular, these indicators were placed on the lower surface respectively in order to analyse the speeds near the printing plate, on the upper wall, to get a clear picture of the degree of shuffling in the gas chamber (and consequently the spatter). To insert additional indicators that covered the free volume between the ceiling and base of the room, some supports composed of thin nylon wire were used, so as not to have major interference on the indicators themselves. This type of arrangement allowed us to have a complete overview of the speed fields in the entire volume of the print room (see Figure 40).

The characteristic curve of the pump was used as a reference for determining the actual range of the circuit by crossing it with the circuit curve.

The characteristic curve is provided by the manufacturer for the maximum power of the pump.

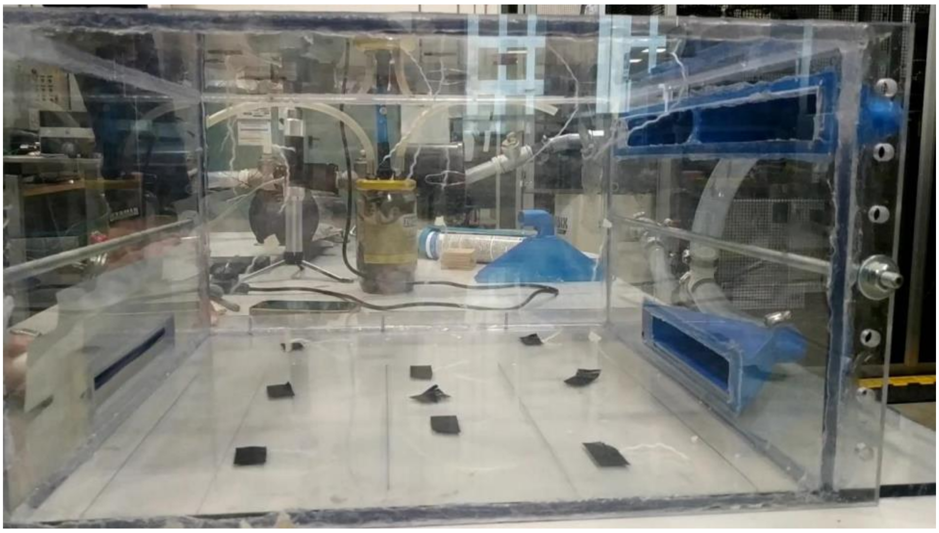

Figure 40: configuration of the flags inside the chamber

The pump's prevalence curve is provided by the manufacturer. Load losses of the systems mounted on the machines were measured as the pump's power increased with the insertion of rapid attacks upstream and downstream of the pump (see Figure 39, P1 → P5). The instrument to measure is a digital differential gauge (see Figure 41A). In the graph in Figure 41B you can see the prevalence curve of the pump with the points relative to the pump power values with a 10% voltage increase at each step.

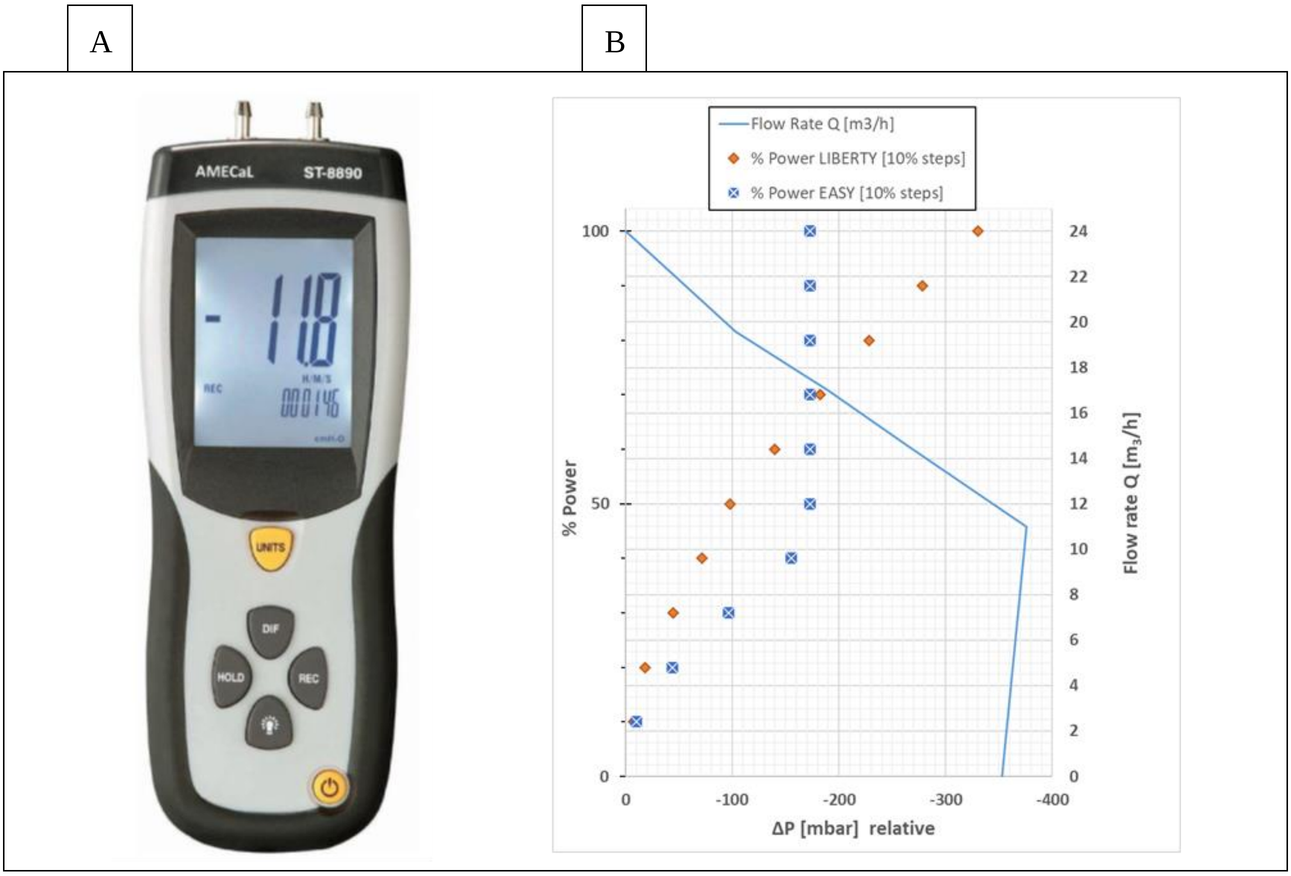

Figure 41: [A] differential manometer and [B] prevalence curve and power steps of pumps

Once the test circuit was mounted, the load leaks were measured along the various sections of the circuit so that there was a margin of gain to be able to increase the range of the inert gas.

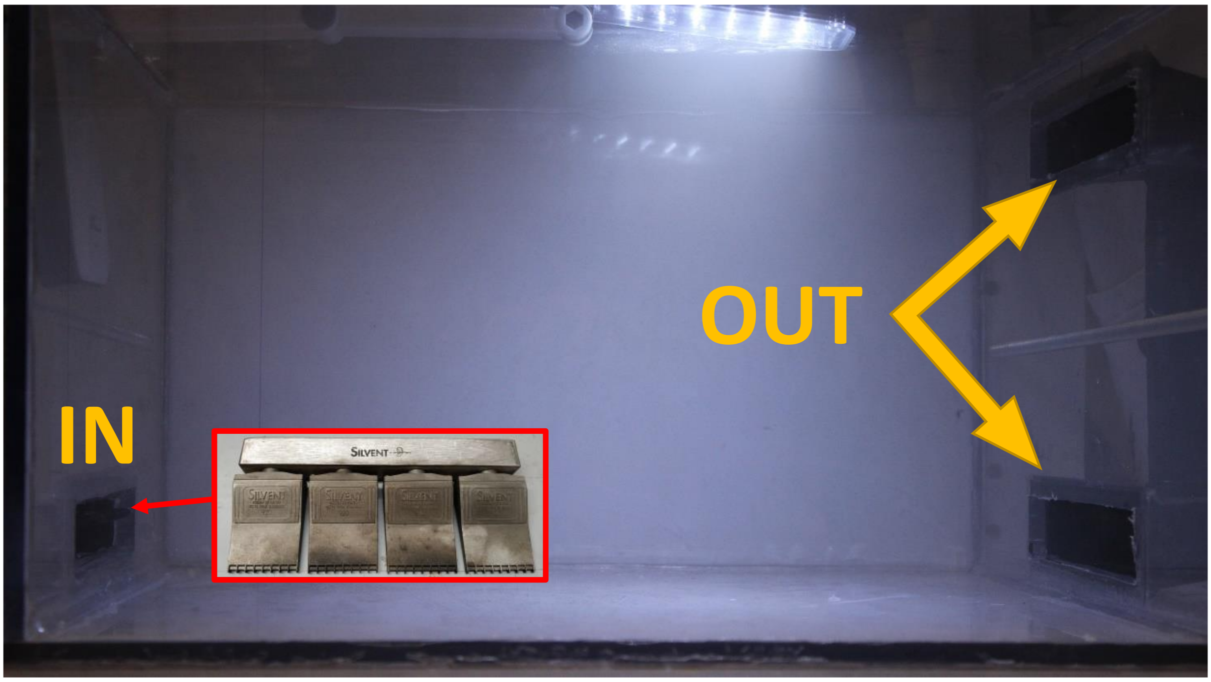

Figure 42: inside the printing chamber prototype. In the red frame the particular of the air knives

The work chamber has 1 send mouth (IN) and two suction vents (OUT), in the send mouth there is a flat nozzle usually used for blowing blades (see Figure 30). Measurements were made along all segments (Input Valve, Print Room, Cyclone Filter, Fine Filter, Pump) and by voltage step of 10% of the input signal that controls the pump, to replicate the normal functionality of the machine.

% Power (V)	**ΔP_{tubes} [mbar]**	**ΔP_{2-3} [mbar]**	**ΔP_{3-4} [mbar]**	**ΔP_{4-5} [mbar]**	**ΔP_{5-1} [mbar]**
10 - (1V)	0	0	0	0	0
20 - (2V)	0.8	14.5	0.1	1.6	17
30 - (3V)	3.4	31.2	0.2	3.2	38
40 - (4V)	5.7	53.5	0.4	5.4	65
50 - (5V)	6.4	85.2	0.6	7.8	100
60 - (6V)	9.5	115	0.9	10.6	136
70 - (7V)	5.2	159	1.2	14.6	180
80 - (8V)	6.6	202.4	1.5	18.5	229
90 - (9V)	5.8	253	2	23.2	284
100 - (10V)	7.4	304	2.3	28.3	342

Table 6: pressure drops of the components forming the pipeline of the 3d printing machine.

It is seen that the values shown for the pump are a summation of the individual measurements made on the individual strokes. In addition, the power supply corresponds to a unit voltage variation, as the pump is powered by a control over the supply of electrical potential; for each step of 1voltage you have an increase of 10% of the power delivered by the pump. By intersecting the load leak values with the pump's prevalence curve, it is possible to determine the volumetric range of gas that the pump can provide. In our case it corresponds to 12 m^3/h; therefore, the maximum value payable is halved.

With these first tests we have established that the inlet gas flow mouth presents a series of critical issues resolved then in the next machine model. The first obstacle to a good cleaning of the chamber from spattering lies in the presence of a step between the lower plate of the chamber and the lower profile of the intake nozzle (see Figure 43).

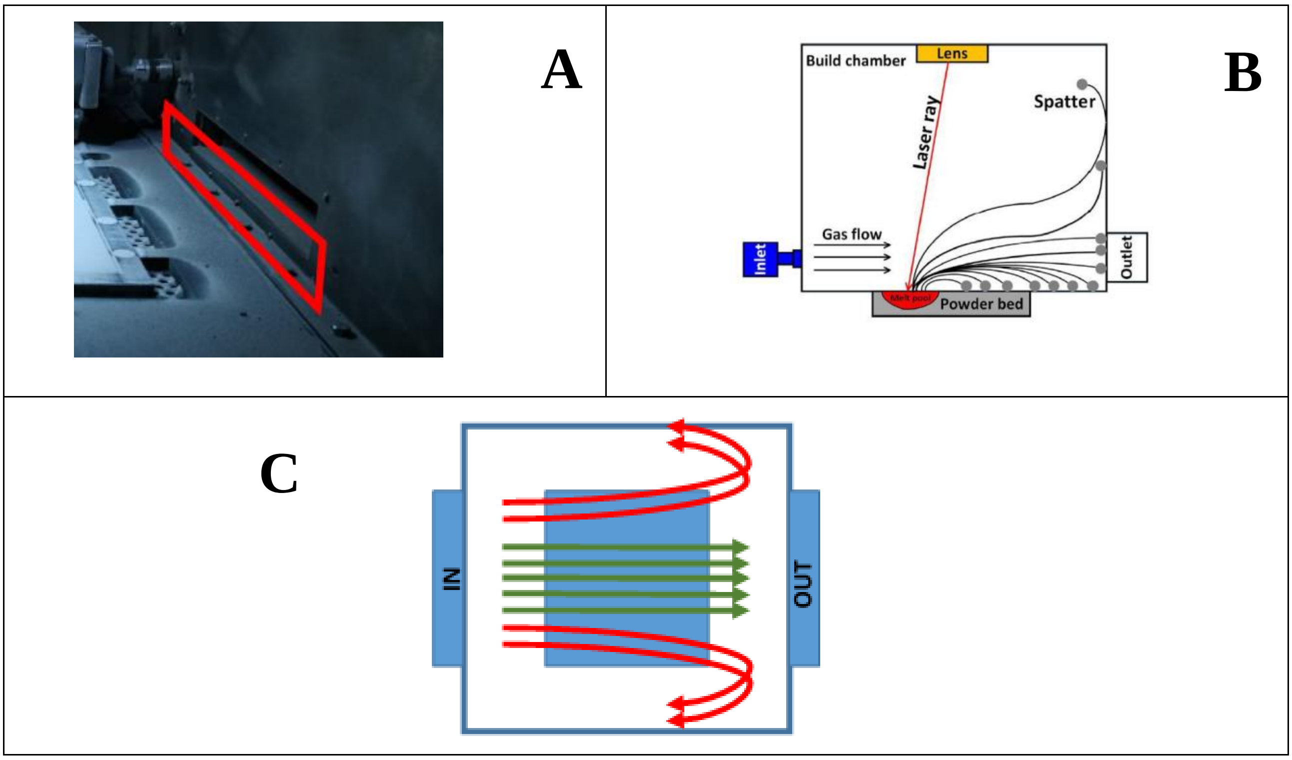

Figure 43: A - outlet flow mouth and particular (red square) of the small step. B and C spattering and gas direction on the final zone before the outlet mouth.

In this area (see Figure 43A) heavier particles cannot be ejected because the suction force is not high enough to allow the particles to fly in the dumping gas flow mouth. In addition, to the step, it has been shown by the wire analysis method that the dumping section limited to the size of the printing plate alone and not to the entire wall (see Figure 43C) is accentuating the formation of return vortexes. The return vortexes, in addition to making the smoke-saturated environment that defocuses the LASER beam, carry with them the residual spattering, which loses the kinetic energy falls on the printing plate, deleting the function of cleaning of the gas flow (see Figure 43 B and C). [35]

After further tests related to the flow in the chamber, the solution reconsiders the size of the outlet mouth and eliminates the step described above. These improvements are also confirmed in the studies of Xiaobing Zhang et al (2020, 'Simulation study of the spatter removal process and optimization design of gas flow system in LASER powder bed fusion').

With the development of the printing parameters for new materials discussed in Chapter 3, we have been faced with the serious problem of the substantial production of black powder, i.e., all the dust that is expelled either because of the spattering effect or because of submicrometric particle size, which is therefore particularly volatile. The solution studied and then subsequently implemented in the machine was the design and manufacture of a cyclonic filter. This type of filter guarantees, with an appropriate sizing, the elimination of the largest particulate matter, with an increase in the duration of the filters. [35]

Cyclone separators provide a method of removing particulate matter from air or other gas streams at low cost and low maintenance. Cyclones are somewhat more complicated in design than simple gravity settling systems, and their removal efficiency is much better than that of settling chamber. Cyclones are basically centrifugal separators, consists of an upper cylindrical part referred to as the barrel and a lower conical part referred to as cone (see Figure 44).

They simply transform the inertia force of gas particle flows to a centrifugal force by means of a vortex generated in the cyclone body. The particle laden air stream enters tangentially at the top of the barrel and travels downward into the cone forming an outer vortex. The increasing air velocity in the outer vortex results in a centrifugal force on the particles separating them from the air stream. When the air reaches the bottom of the cone, it begins to flow radially inwards and out the top as clean air/gas while the particulates fall into the dust collection chamber attached to the bottom of the cyclone. [35]

Figure 44: Cyclone particles/gas trajectory and cyclone sizes

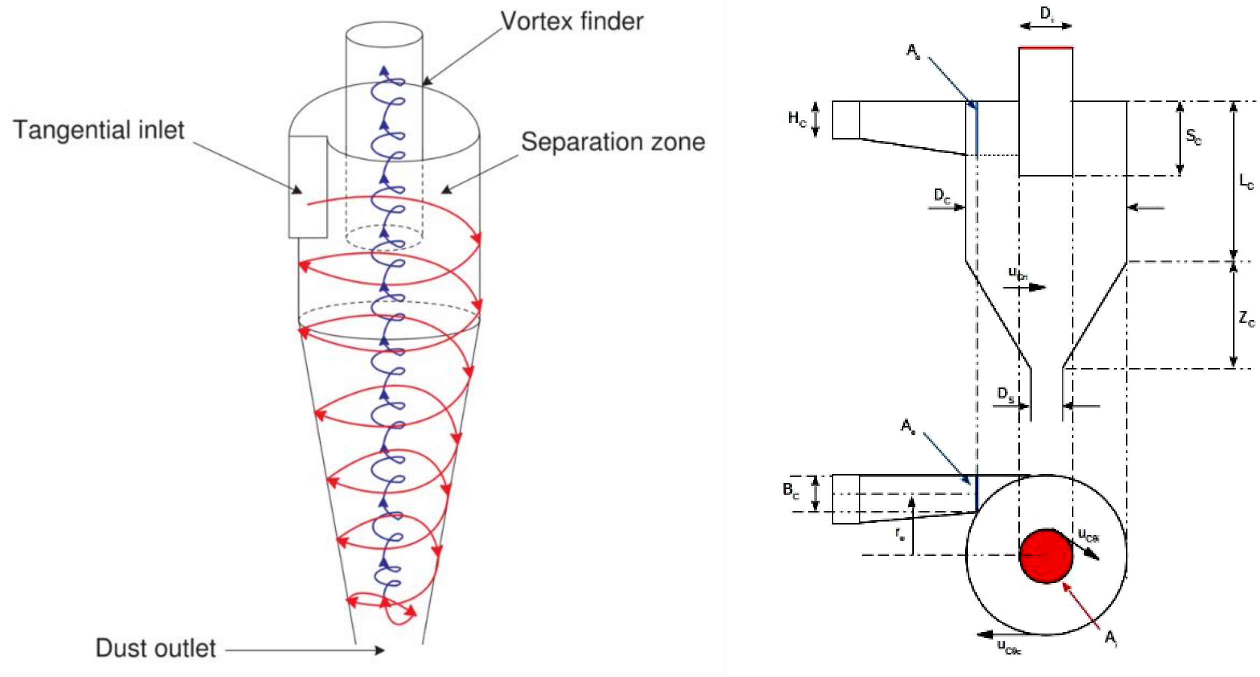

Cyclone efficiency will decrease with increases in the parameters such as gas viscosity; cyclone body diameter; gas exit diameter; gas inlet duct area; gas density; leakage of air into the dust outlet. The efficiency of a cyclone collector is related to the pressure drop across the collector. This is an indirect measure of the energy required to move the gas through the system. The pressure drop is a function of the inlet velocity and cyclone diameter.

The efficiency of a cyclonic filter is inversely proportional to:

- Viscosity and density of the gas,
- Diameter of the cyclone body,

- Area of the inlet mouth.

In addition, the efficiency of the cyclone is directly attributable to the loss of flow load, because it represents the energy required for the flow to be able to cross it. In turn, pressure loss is a function of the flow rate and cyclone diameter, so small cyclones have greater efficiency than large cyclones. [35]

Specifically, it was decided to size the cyclone according to the Stairdman method that allows to have a high efficiency cyclone, that is, able to separate small particles.

The parameters driving the design of a cyclone are the diameter of the cyclone body, and the available volumetric flow (see Table 7). These two parameters are the key points on which all the geometric parameters for the sizing of the cyclone depend, for this reason in the literature the geometric dimensions of the cyclone are all referring to the diameter of the body. [35]

Flow Characteristics			
Volumetric Flow Rate	**Q**	**24**	**m^3/h**
Powder	**MAX 10**	**10**	**g/m^3**
Viscosity	**μc**	**1.78E-05**	**Pa*s**
Density	**a 25°C**	**1.13**	**kg/m^3**
Bulk Density	**7700**		**kg/m^3**

Table 7: Cyclone Inlet gas flow characteristics

The fundamental output parameter is the cut-off diameter, that is, the equivalent diameter of the smallest particle that the cyclone can filter. The loss of load generated by the cyclone itself also falls within the parameters of choice and sizing.

The maximum volume of the cyclone depends on its insertion inside the machine's crankcase; for this reason, you are bound to a maximum diameter of 150 mm.

For the calculus of the size of the cyclone, 3 different diameter values are taken that could meet this constraint and then the cut-off diameter and load loss occur (see Table 8).

Parameters to check					
Cyclone Diam. Dc (m)		**Cyclone Diam. Dc (m)**		**Cyclone Diam. Dc (m)**	
0.1	**m**	**0.12**	**m**	**0.15**	**m**
Cut-Off Diameter (microns)		**Cut-Off Diameter (microns)**		**Cut-Off Diameter (microns)**	
1.6	**microns**	**2.2**	**microns**	**3.4**	**microns**
Pressure Lost		**Pressure Lost**		**Pressure Lost**	
90.5	**Pa**	**41.9**	**Pa**	**16.2**	**Pa**

Table 8: Types of cyclones depending on the cut-off diameter.

For the realization of the cyclone the diameter of 120mm was chosen because it is an excellent compromise between cut-off diameter and load losses. The first option was discarded due to high load losses in relation to the dimensional gain of the filtered particles, and the second because the vertical footprint of the cyclone would have been excessive.

Having chosen the diameter of 120 mm, the cyclone dimensions are shown in Figure 45.

Stairdman		**Size calculation**	
Characteristic Ratio		**Dimension**	**[m]**
$H_c/D_c = K_H$	**0.5**	**H_c**	**0.06**
$B_c/D_c = K_B$	**0.2**	**B_c**	**0.02**
$S_c/D_c = K_S$	**0.5**	**S_c**	**0.06**
$D_i/D_c = K_i$	**0.5**	**D_i**	**0.06**
$L_c/D_c = K_L$	**1.5**	**L_c**	**0.18**
$Z_c/D_c = K_Z$	**2.5**	**Z_c**	**0.30**
$D_S/D_c = K_D$	**0.375**	**D_S**	**0.05**

Figure 45: sizes of the cyclone of 120 mm diameter

With the insertion of the cyclone, we had an increase in the lifecycle of the filtering group. This upgrade pays off in terms of costs (see Figure 46) but also reduces the downtime due to their replacement.

BEFORE CYCLONE INSTALLATION				
FILTERS REPLACEMENT			TOTAL COSTS	
C67	24 h	300 pieces/year	C67	4500 €
CuZn42	16 h	550 pieces/year	CuZn42	8250 €
AFTER CYCLONE INSTALLATION				
FILTERS REPLACEMENT			TOTAL COSTS	
C67	72 h	100 pieces/year	C67	1500 €
CuZn42	48 h	184 pieces/year	CuZn42	2760 €

Figure 46: total costs of filter's substitution before and after cyclone installation

2.3: Optimization of the powder distributor

The powder's dispenser inside the machine plays an important role to obtain a good printing process, in terms of reducing printing time, quality of powder's distribution and consequently the powder bed on which the melting process takes place.

Unlike other companies that take advantage of a lifting system, in our case the powder falls from above, so falling by gravity helps the filling of the charger. Through the rotation of a screw-cylinder system, the powder then falls into a conveyor with a lip; the linear movement of the sled on which the conveyor is mounted allows the distribution of powder on the printing plate.

The starting system consists mainly of a spring inserted in a cylinder with break-in on which a perforated cylinder is then inserted that allows powder to fall inside the distributor. The large deficit found in this mechanism is the poor homogeneity with which the powder falls into the dispenser, because on several occasions the powder pulls from the inlet duct to the bearing seat, packing it. Due to the fine particle size of the powder, the sealing and protection systems on the bearings are insufficient to ensure acceptable sealing standards to prevent grip (see Figure 47).

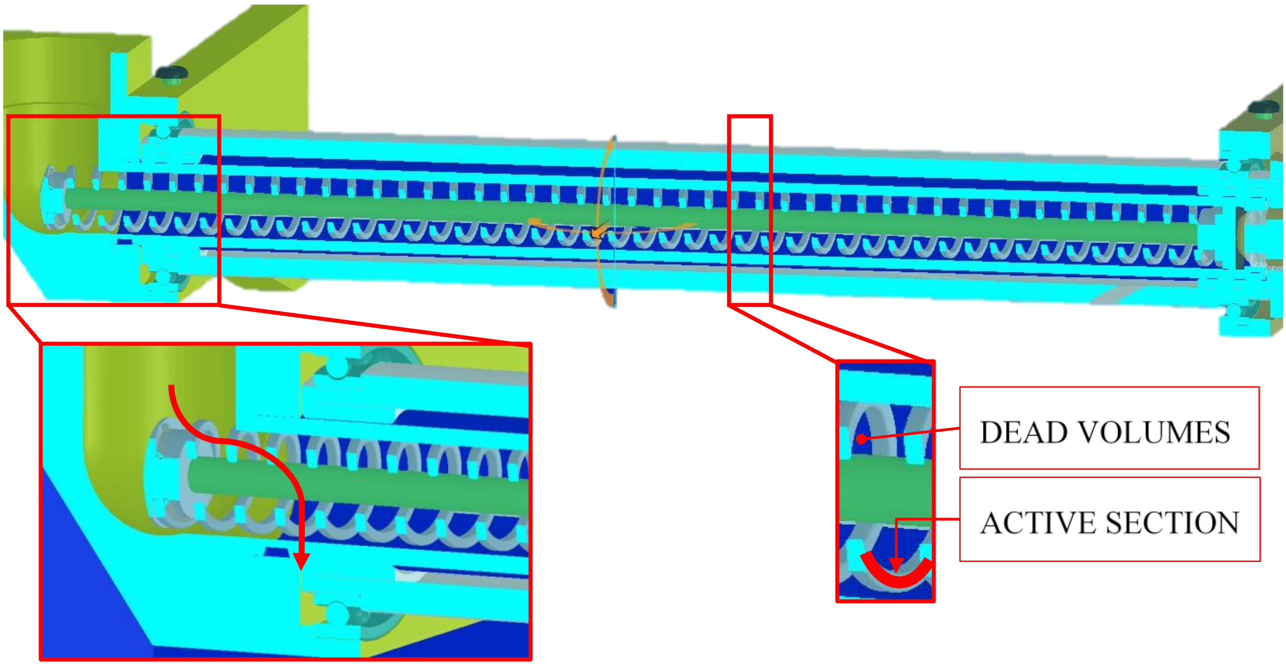

Figure 47: first powder-distribution's system

The spring profile is the only surface that actively participates in the sliding of dust, while the dead volume between the support rod and the spring is not affected by any motion.

Starting from the initial condition of the exhaust distributor, up to normal operation of the machine, some measurements were made of the number of rotations necessary to obtain a homogeneous layer of dust; the data collected are given in Table 7. The experimental plan started during the optimization parameters of the stainless steel 316L powder and ended with the setting up of the Brass CuZn42 powder. For the C67 Spring Steel, the geometry of the doser adopted is the result of the mechanical innovations founded to reduce the recoating time.

Table 7: measures of rounds with the empty doser and after the complete powder filling

TRIES	STAINLESS STEEL 316L		BRASS ALLOY CUZN42	
	Starting point	During process	Starting point	During process
01	47	14	45	12
02	45	15	48	13
03	42	16	40+10	15
04	50	15	50	15
05	50	15	50	15
06	52	17	50	15
07	48	15	50	18
08	50	15	50	15
09	50	15	50	15
10	50	13	50	17
MEAN	**48**	**15**	**49**	**15**

The values obtained are not acceptable because a lot of powder is delivered both at the initial stage and during the process, at the risk of reaching the condition where there is no more powder in the upper tank and that the sieve is overloaded. This configuration does not allow a precise measurement of the amount of powder dispensed, a necessary characteristic to avoid loading the machine with excessive powder and then risking polluting the virgin powder with sub-micrometric spattering that pulls from the sieve mesh.

With coarse spattering the vibrating system with eccentric motor has no effect if the mesh is loaded with an excessive amount of powder, because the weight caused by the powder on the metal’s spider completely dampens the vibrations, rendering the work of the electric motor out of order. For this reason, an ultrasonic sieve was chosen.

One solution adopted without making too many mechanical changes to the doser was the replacement of the spring with a screw also called Archimede’s Screw.

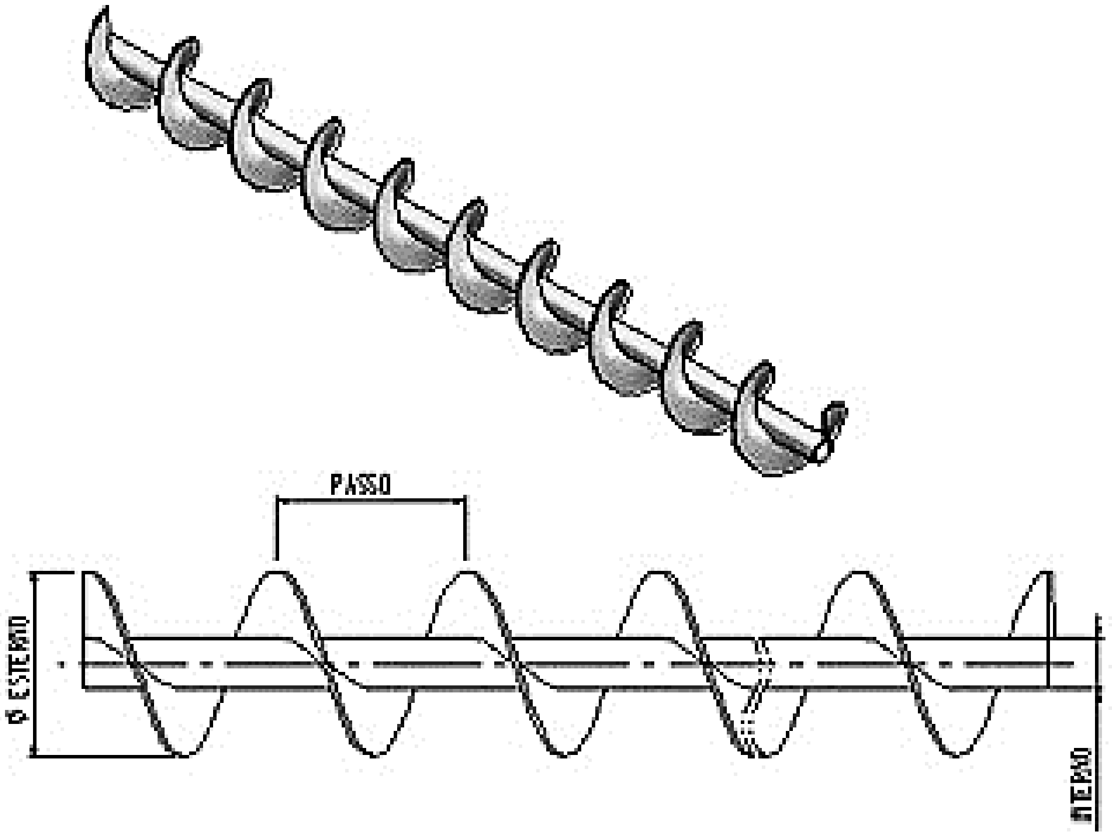

Figure 48: example of an Archimede's screw

The principle of operation is very simple: through the rotation of the screw a certain amount of powder is collected from the supply duct that for each turn advances a certain distance equal to the step of the screw. The powder is discharged by means of a duly drilled outer cylinder. The rotation of the screw and the outer cylinder are in solidarity with each other, so the rotation of one generates a simultaneous rotation of the other. This synchrony allows you to reconsider the support system, which now is a rolling bearing equipped with a dust-proof, with a PTFE bushing (see Figure 49).

This solution for both the supply side and the opposite side solved bearing grip problems due to excessively fine powder, which managed to penetrate inside the cage with the balls.

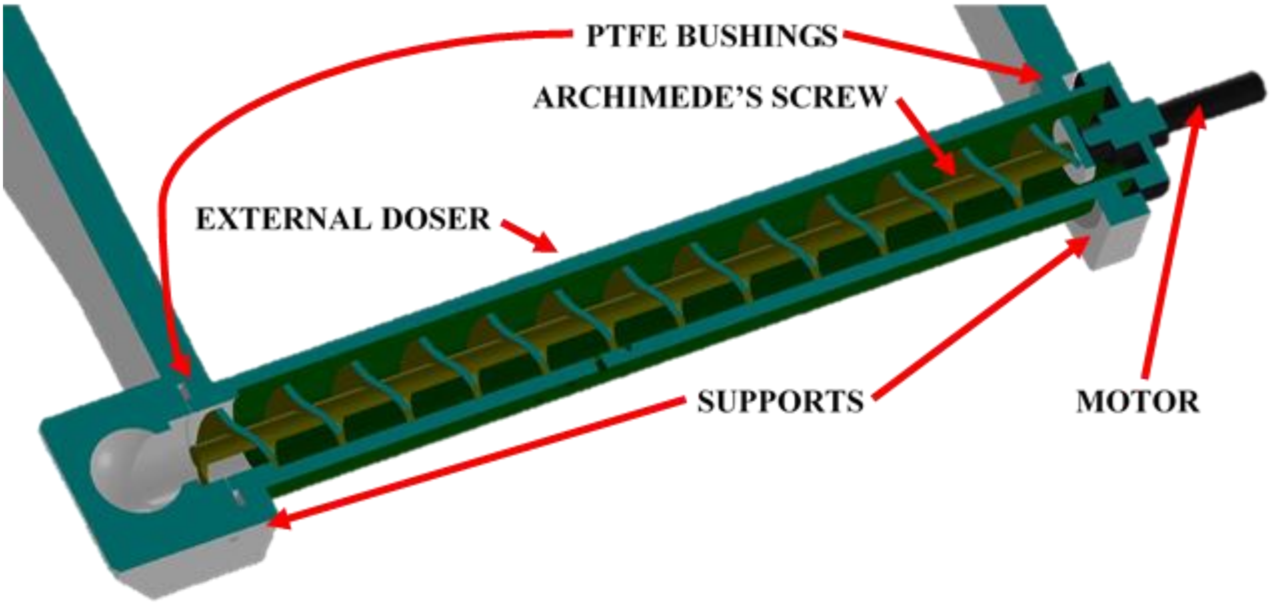

Figure 49: section of the doser with the position of the single parts

With the new configuration the distribution is much more homogeneous, so the amount of dust dispensed much more regular. It is therefore possible to have a quantitative measure of the powder that is used for each printing layer of the machine. The measurement allows you to know with a minimum deviation, how much dust is needed to obtain a component, knowing as given simply the number of total layers extrapolated from the slicing software. The tests were carried out for both 316L stainless steel and CuZn42 brass alloy. The difference in dust by weight depends on the fact that the densities of the two materials are different, respectively 7.9 g/cm^3 and 8.4 g/cm^3 (see Figure 50).

Figure 50: dosing tests with the Archimede's screw

Tries	Stainless Steel 316L		Brass alloy CuZn42	
	Starting point	During process	Starting point	During process
1	10+5	2	15	1
2	15	1	15	1
3	15	1	15	1
4	15	1	15	1
5	15	1	15	1
MEAN	**15**	**1**	**15**	**1**

Thanks to the excellent repeatability of the tests it was possible to quantify the dust weight that is used for each printing layer (7.5 g/cm^3 for 316L Stainless Steel and 8.4 g/cm^3 for CuZn42 brass alloy).

3: Material development and characterization methods

The implementation of new material in the AM systems required more attention and involves more problem that those may be observed in conventional technologies Switching from molten to powder could result in a change in the concentration of the elements that make up the alloy; subsequent consolidation by means of the LASER source could in turn lead to a substantial change in the crystalline structure of the solid-state alloy. Finally, this change implies different mechanical properties. As discussed in paragraph 1.4.1 there are various dust production systems; from the fastest and least expensive (wide particle size range - irregular morphology - low smoothness) to more complex but more expensive systems (fine particle size - extremely regular morphology - high smoothness). For this reason, it is always necessary in case of development of new materials to have a characterization plan.

The first step of a new material evaluation requires the SEM scanning electron microscope analysis of the material. Scanning Electron Microscopy (SEM) allows to obtain, from an appropriate sample, high-resolution three-dimensional images (~100 A) by scanning an electron beam in a small area of the test sample. All the effects that are produced at the point of impact of the beam can be used, through special detectors, to produce contrast, then the image. In addition, the analysis of the X-rays produced allows to carry out compositional analysis at high spatial resolution (microanalysis). With appropriate X – EDS probes it is possible to obtain a chemical analysis of the powders to quantify the family of elements of which it is composed.

The operation and scheme of an SEM with X - EDS probe is shown in Figures 51.

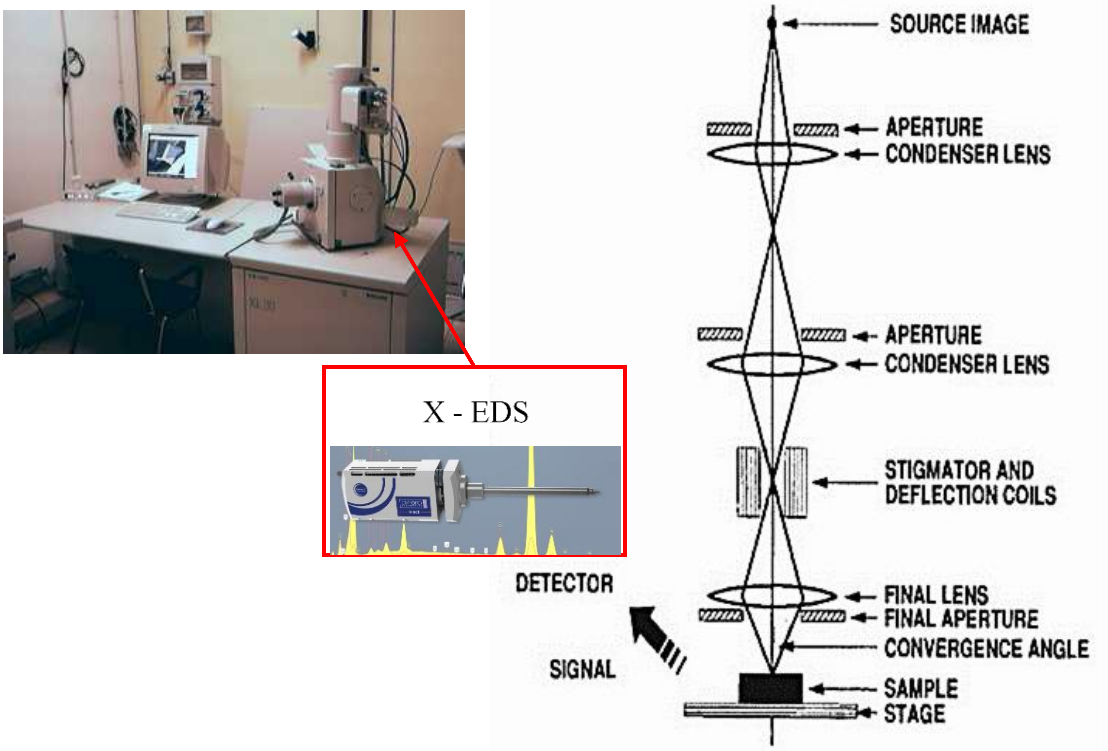

Figure 51: SEM and X - EDS. Courtesy of University of Modena and Reggio Emilia - CIGS

Regarding the analysis of the piece obtained by additive manufacturing, the procedure is more articulated, because the determination of the optimal parameters passes through the development of an experimental plan with which the process parameters are correlated. In the case of additive manufacturing the process parameters are the power of the LASER, the scanning speed, and the distance between the LASER passes. The latter parameter is most often a negligible variable because it is defined from the beginning after having determined the width of the melting pool. Since the excessive overlap between LASER passes would generate a recast of the newly established area, the percentage value on which one stands to ensure a planar continuity of the molten material is 44%. [36]

Once the finished piece has been obtained, the first analysis that is carried out is the determination of the relative volumetric density with the Archimedes method, which precisely exploits the principle of hydrostatic thrust of a body immersed in a liquid (see Figure 52).

The process is relatively simple; the sample is first weighed in the air, and after the tare is weighed in a liquid whose temperature and density are known. With the ratio of the two measurements, it is possible to determine the relative volumetric density of the sample. The percentage difference between the theoretical and relative value calculated determines the value of volumetric porosity. As the lower limit we consider the density of the acceptable component if it is greater than 99,5 %.

Figure 52: balance used for the density's analysis.

$$\rho = \left[\frac{m_a}{m_a - m_b} * (\rho_w - \rho_a)\right] + \rho_a with \begin{cases} \rho = sampledensity \\ \rho_w = 0{,}9987 \dfrac{g}{cm^3} waterdensity@20°C \\ \rho_a = 0{,}0012 \dfrac{g}{cm^3} airdensity@20°C \\ m_a = sample'smass \in air \\ m_b = sample'smass \in water \end{cases}$$

3.1: Brass powder CuZn42

Brass, among the engineering materials, is one of the most versatile used to make corrosion resistance and recyclable component. Moreover, brass give a substantial contribution to a more sustainable and safer planet.

With brass containing lead, we can obtain high pressure tightness and machinability, without electroplating needs. Brass components with a percentage of lead are cheaper than those, for example, of durable stainless-steel parts. Legislation on the lead content in brass has become more stringent in recent years pushing toward the development of new lead-free brass. Eco-friendly lead-free brass alloys called Ecobrass, are instigated by the restriction of lead usage and forthcoming health safety regulations [37]. These alloys can substitute the traditional leaded brasses especially for the applications that involve risk components, when they are continuously in contact, for example, with drinking water. In this case the acceptance and approval of new products requires the verification of the composition of the metallic materials that must be check for compliance with the list of accepted materials [38]. The procedure adopted by the 4MS Joint Management Committee (a group of European States) indicates that the materials are categorized in groups that have the same behaviour in contact with drinking water, the same field of applications and have restrictions regarding water composition and wet surface are of the component. The materials may only be used for certain products due to the restrictions with respect to the surface area:

A. the grouped components have 100% of the surface in contact with drink water (e.g., uncoated pipelines),
B. group B forecast components that have the 10% of the surface inn contact with drinking water, e.g., pump and valve bodies,
C. components of group B product with contact surface lower 10%,
D. water treatment components.

The CW510L (CuZn42) may be used only for components belonging to group B, C, and D [38]. The composition limitations for CW510L are showed in Table 8.

Table 8: CW510L component weight % limitation for B, C and D groups application

Constituents		Impurities					
Cu [%]	Zn [%]	Al [%]	Fe [%]	Ni [%]	Pb [%]	Sn [%]	other
57.0 - 59.0	balance	≤ 0.05	≤ 0.3	≤ 0.2	-	≤ 0.3	≤ 0.02

In USA potable water component manufacturers must demonstrate compliance with federal lead-free requirements by certifying products to NSF Standard 372 that is the standard method used to calculate the lead content in a potable water component with respect to the wetted surface area [39]. On September 1, 2020, the U.S. Environmental Protection Agency (EPA) published the final regulation "Use of Lead-Free Pipes, Fittings, Fixtures, Solder, and Flux for Drinking Water." In the final rule, EPA makes conforming changes to existing regulations based on the Reduction of Lead in Drinking Water Act (RLDWA).

The traditional valve production requires many steps. For example, consider the manufacturing process of the ball valve. It is a quarter turn valve which can be open or closed applying pressure on the hollow and pivoting ball inserted into void opening. Many components are produced by forging process: pipe fittings, valve bonnet and body, hose pipe fittings, beer dispensing body, vertical check valve body, pressure reducing valve parts etc. Brass must first be roughly shaped or preformed before the finished machining is done. The forging process starts from a rod cut into desired length and large enough for the valve body. For the next step, the red-hot rod is forged into desired shape. The forging process generally is preferred over casting process because forged products are tougher, have more strength and eliminates the occurrence of cavity even if casting process is cheaper than forging one (see Figure 53).

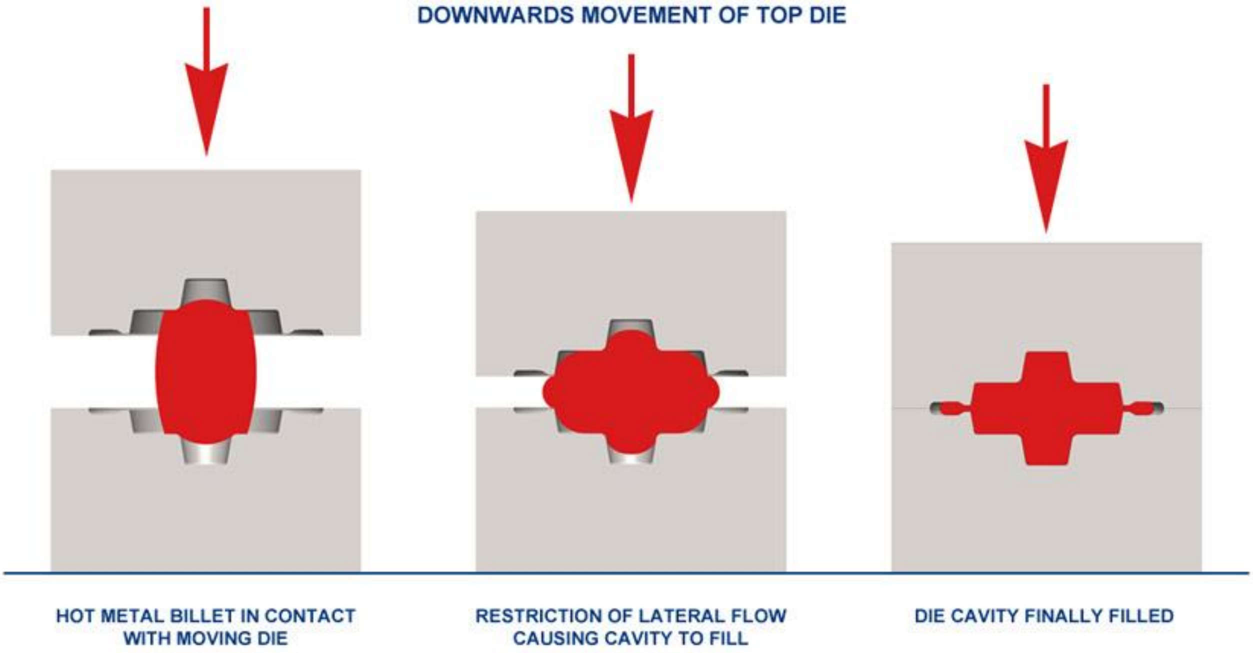

Figure 53: forging process

The forged component requires the trimming to remove the burr and shot blasting to smooth the surface. At last CNC multi axis machines work out the correct dimensions, threads, and stem holes. The valves are manufactured to order based on design and specifications. Typically, better valve can last up five years while the low-quality ones can only last up to three years. The described process guarantees an economical production but may result expensive when is applied to the production of a prototype or pre-series that cannot be followed by a high-volume production or can require further changes.

AM technologies allows the production of prototype and small series of a component without the time and financial source consuming of traditional sequential manufacturing cost. LASER-based powder bed fusion (L-PBF) is presently the most important additive manufacturing technique for metals. Nonetheless, the range of feedstock powders that are commercially available is still very limited and, among them, brass is a noteworthy absence.

There are few literature data regarding the additive manufacturing of brass with a high Zn percentage. Some authors investigated the solid-state powder deposition process by cold spray additive-manufacturing technique (CSAM) using a matrix with 36-42 Zn weight percentage [40]. The CSAM technology does not allow the production of hollow or complex component. Mechanical data of additive manufactured CuZn28 specimens are published but without data regarding technology and process parameters used [41]. In 2018, Yang et al. announced the production of Cu-12.5Zn-2.9Si silicon brass parts by SLM [42].

However, except for these seminal articles, almost nothing is known so far about the manufacturability of high zinc percentage brass by L-PBF. To fill this gap, the present contribution is dedicated to the fabrication of CuZn42 parts and to the optimization of the L-PBF parameters.

Many researchers focus on usability predicting of a new material for AM based on physical and chemical characteristics of material. Some authors define the materials suitable for the PBF technique [5] when they have:

- high LASER absorptivity,
- high boiling point element,
- low thermal conductivity.

The present study want to demonstrate that the obstacle to the production of full density component it is not due to the direct effect of low boiling point elements, as affirmed in some papers [42], or that it is necessary to increase LASER power in PBF devices to beyond the poor LASER power absorption of copper alloys [42]. Bourell et al. affirms that high reflectivity and high thermal conductivity alloys has difficulty to produce an effective melt pool and therefor it is necessary to increase the LASER power up to 1 kW [43][44]. The low density of low LASER absorptivity material (i.e., copper) and low melting boiling point material (i.e., zinc) is due to a complex collection of phenomena, such as sputtering and Rayleigh instability, that can prejudice the powder characteristics maintenance. It is known that unsuitable selection of LASER power and scan speed causes Rayleigh instability of the melt flow that results in the formation of pores: [28][29][30]. The absorbance of an alloy differs from that of pure component. Table 9 [45] compares the absorbance and reflectance of some alloys and commercial pure element for a wavelength close to that used on the 3D printing machine and at room temperature.

Table 9: absorbance and reflectance of some materials

Material	λ = 1053 nm		λ = 527 nm	
	Absorbance	Reflectance	Absorbance	Reflectance
Commercially pure Al	16 %	84 %	32 %	68 %
AA5251, AlMg (average)	24 %	76 %	48 %	52 %
AA6082, AlMgSi	24 %	76 %	39 %	61 %
Commercially pure Cu	6 %	94 %	58 %	42 %
Brass, CuZn37 (average)	12 %	88 %	38 %	62 %
Zinc coatings (average)	64 %	36 %	47 %	53 %

Results of the material development define an upper scanning speed limit beyond which melting pool became instable and there is a surface energy density that optimizes the material density.

3.1.1 Experimental Procedure

The CuZn42 feedstock powder is provided by AMP GmbH Advanced Metal Powders. Table 10 shows the particle size distribution: it is analysed by a LASER granulometer (Mastersizer 2000 Ver. 5.22, Malvern Instruments Ltd., Malvern, UK) according to ISO 13320:2009. The particle size distribution of the feedstock powder is monomodal. The powder is slightly coarser but still compatible with the size range (15-45 µm) typically required for L-PBF. The flow rate is measured through the Hall flowmeter funnel, according to ASTM B213-17, and through the Carney funnel, according to ASTM B964-16, both in static flow method. Prior to testing, the funnels and powders are dried at 80 °C for 24 hours.

Table 20: 10%, 50%, 90% volume fraction diameter

d (0.1) [µm]	d (0.5) [µm]	d (0.9) [µm]
22	39.3	64.6
Distribution data		
$d_{average}$ [µm]	Kurtosis	Skew
41.4	-0.129	0.558

The powder morphology is observed at SEM Tescan Vega 3 scanning electron microscope equipped with an EDAX Elements EDS system. Three cubes 12.5x12.5x12.5 mm^3 are built for each parameter combination.

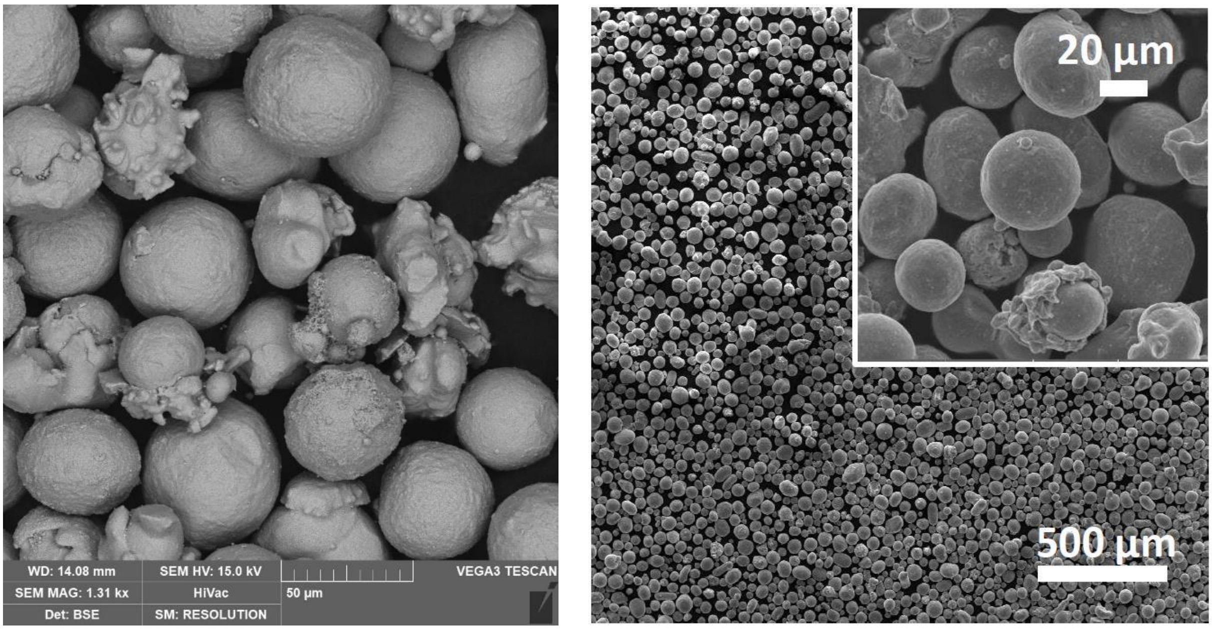

Figure 54: Powder's SEM-EDS analysis

The cubes density is measured by the Archimede’s technique and by optical microscope porosity measurements. This last is performed using the following procedure,

- one cube for each set of parameters was polished on a side (parallel to growth direction) until removing 2.5 mm of material and observed under an optical microscope (NIKON eclipse LV150N, Nikon, Japan),
- Three images were acquired on a diagonal and then analyzed using DIGIMIZER software (Digimizer Image Analysis Software, MedCalc Software bv, Belgium).

The density is obtained as difference between the whole surface observed and the percentage of porosity.

The values obtained using Archimedes technique and optical microscope methods are compared and expressed as percentage of full density CW519L component. As shown in Figure 54, the powder morphology is roundish but not perfectly spherical and some particles are strongly irregular.

The powder is processed on a modified 3D4steel L-PBF machine, mod. “Easy” (3d4mech S.r.l., Sasso Marconi, Bologna, Italy). The machine is modified to preserve specimen quality and the filters functionality that may be damage by the ultrafine powder with high percentage of Zn that is sputtered during the LASERing. To preserve the mirror of the galvanometer against the reflectance of the LASER during the melting process, we mounted a mirror-filter.

The machine uses 300 W Yb-fiber LASER operating in nitrogen atmosphere: the nitrogen is produced by a aboard local generator. To assess the manufacturability of CuZn42, a preliminary test followed by a full factorial design of experiment is performed (Figure 55). Preliminary tests, evidence that the hatch distance (h) had a minor effect with respect to beam power and scan velocity; therefore, it is kept constant to 0.1 mm. The layer thickness is fixed to 0.05 mm. Components are built on top of a steel baseplate and a scan of stripes strategy is used for the core (relative rotation between layers: 67°), while 2 contour passes are applied to the skin (distance: 80 µm).

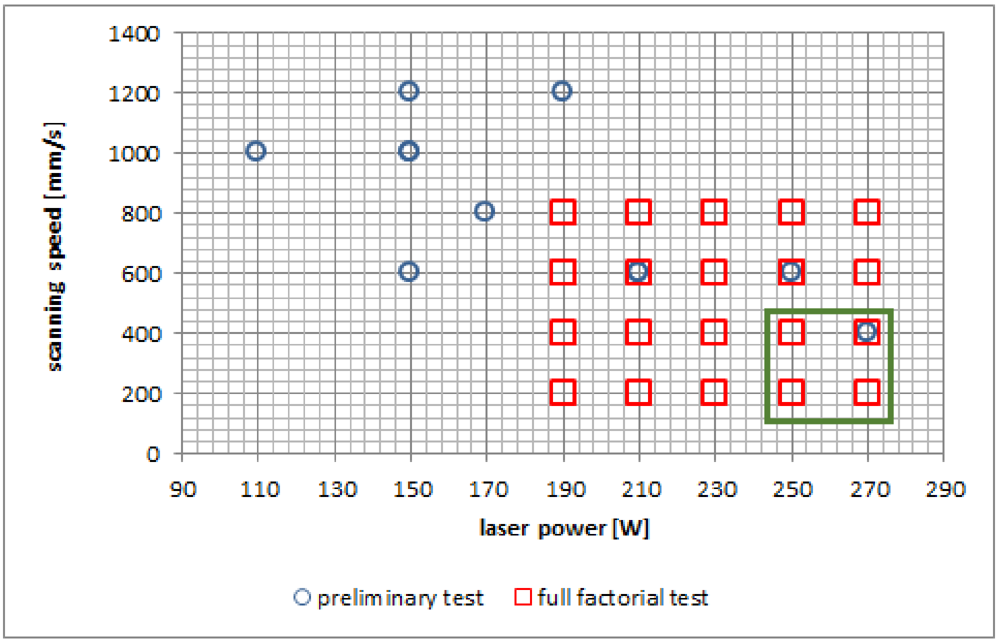

Figure 55: preliminary and full factorial test

The continuous search for the scanning speed and the power of the LASER to obtain a volumetric density value of more than 99.5% has pushed us to investigate in more detail speeds in the range 200 – 300 mm/s and LASER powers with values 250 Watts and 270 Watts. The volumetric density values obtained for the narrow series of power and speed parameter pairs allowed us to approach the target set (volumetric density > 99,5%). The possibility of further reducing the scanning speed was evaluated but immediately discarded since concentrating a high power of the LASER in a limited area equal to the LASER spot and for a limited time no longer involves a simple melting of the powder, but a complete sublimation of the material to be consolidated. For this reason, you have chosen the dual scan mode. Figure 56 shows the detail of the experimental plan (green box in Figure 55).

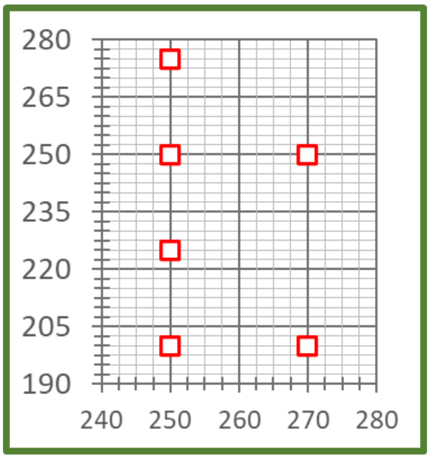

Figure 56: Green box of the Figure 55 - detail of the full factorial's design of the experiment

The results of the manufacturing process are expressed as function of surface energy density:

$$E_s = \frac{P}{vd}$$

Es = surface energy density [J/mm^2],

P = actual LASER power [W],

v = scanning speed [mm/s],

d = spot diameter [mm].

Some authors [46] prefer define results as function of volume energy density, Ed, which is the energy conveyed by the LASER per unit volume of material according to Equation:

$$E_d = \frac{P}{vht}$$

v = scanning speed [mm/s],

h = hatching space [mm],

t = thickness layer [mm].

But the volume energy density does not describe effectively the energy adsorbed for each volume unit [46]. After some single LASER scanning line, the tests defined the melting pool X-Y dimensions. The same tests also defined the melted height equal of five or six layers. Therefore, the layer thickness cannot represent a significant value to compare the data because the real melted depth changes with the power and scanning speed used. Moreover, it is known from LASER welding studies that for each material there is a critical value of surface energy density that determines the transition from conduction regime to keyhole one (see Figure 57). [47]

Figure 57: Keyhole (a) vs Conduction regime (b)

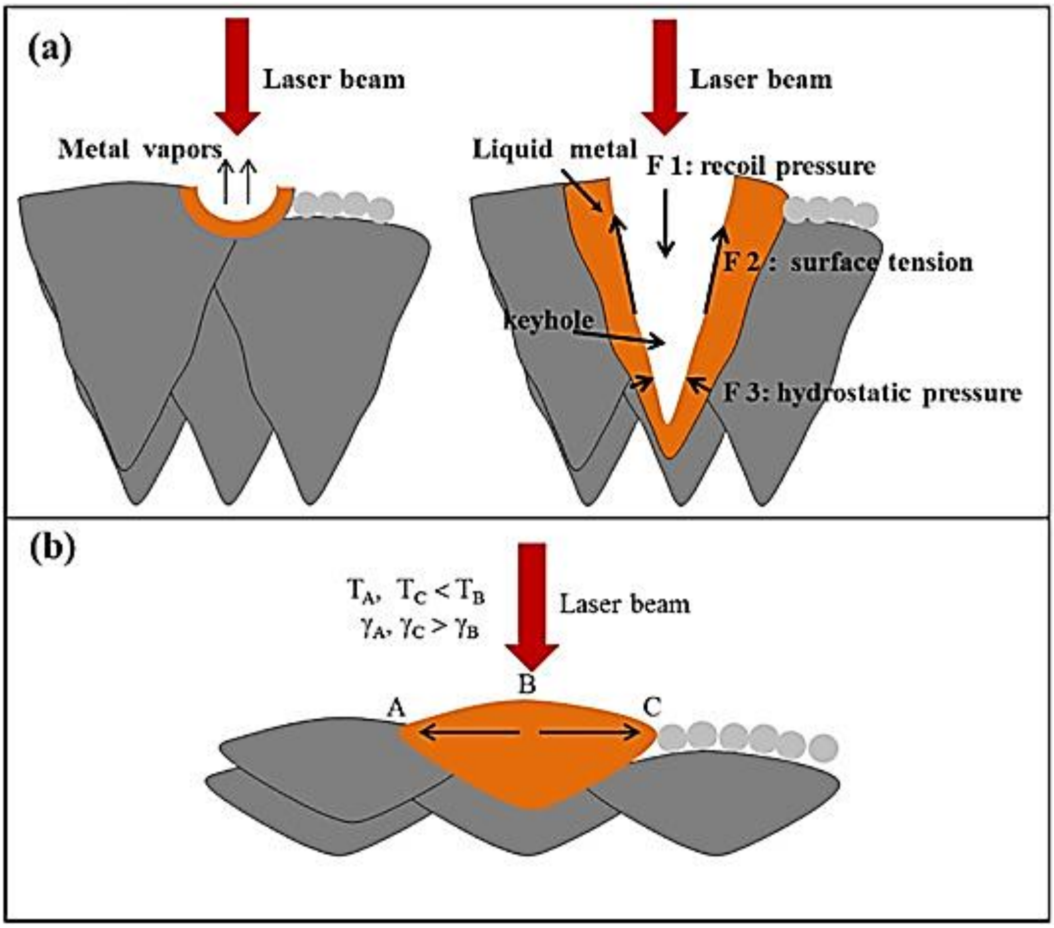

In all AM LASER Powder Bed Fusion processes one of the downsides is the production of dusty waste, which originates during the fusion of the material, which is called Black Powder. Black powder produced during spattering can affect two aspects of the AM LASER Powder Bed Fusion process.

The first aspect concerns the quality in terms of volumetric density: spattering with mass and dimensionally greater than virgin powder tends to fall on the dust bed to be consolidated, polluting what could later become part of a manufactured component (for this reason an attempt is always made to consolidate against the direction of the gas flow used for the removal of spattering). The second aspect concerns the duration of the filtering group: excessive production of black powder captured by the intake vent causes a reduction in life and continuous maintenance /replacement of the filtering group, with relative downtime. For this reason, as already discussed in paragraph 2.2, a cyclonic filter has been implemented.

In Figure 58())you can see a sample of powder worn and polluted by black powder and in Figure 58(b) a magnification carried out under a scanning electron microscope, with which it was possible to verify the excessive degradation of the dust in morphological terms to verify a possible influence in the flow of dust.

The preliminary tests evidence the production of sputtered sub-micrometer black powder with high percentage of Zn (up to 65%), the black powder is shown in Figure 58.

Figure 58: (a) Black powder bin, (b) black powder SEM images

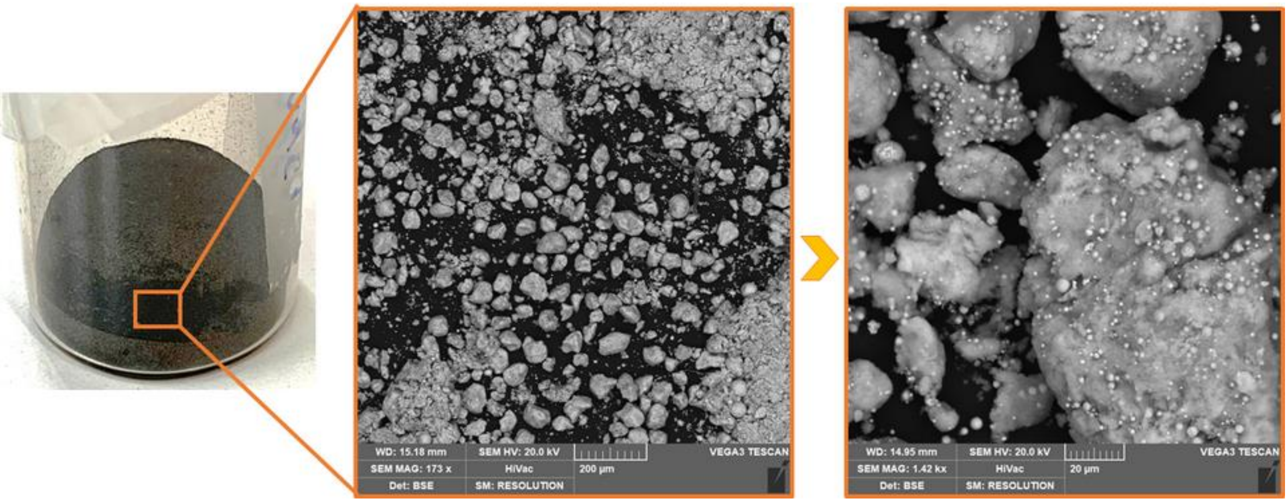

Figure 59: Brass virgin powder flowability tests

flow rate ASTM B213		flow rate ASTM B964	
[g/s]	**[s/50g]**	**[g/s]**	**[s/150g]**
2.41(0.04)	21	19.3(0.1)	7.8
Static flow method		Static flow method	

Klages et al. evidence the presence of the production of small Zn rich particle during seam welding process. The phenomenon is described as fumigation of Zn, it causes the reduction of aesthetical and mechanical properties of the component. [48]

In the case of processed brass, a surface was analysed through an EDS probe using a scanning electron microscope to check if the zinc fumigation effect is present, because this element, as seen in Figure 60, has a lower melting temperature than the copper melting temperature and therefore zinc is the element that undergoes repeated melting processes with energy density far above that necessary to melt this Element.

Figure 60: State diagram Cu - Zn

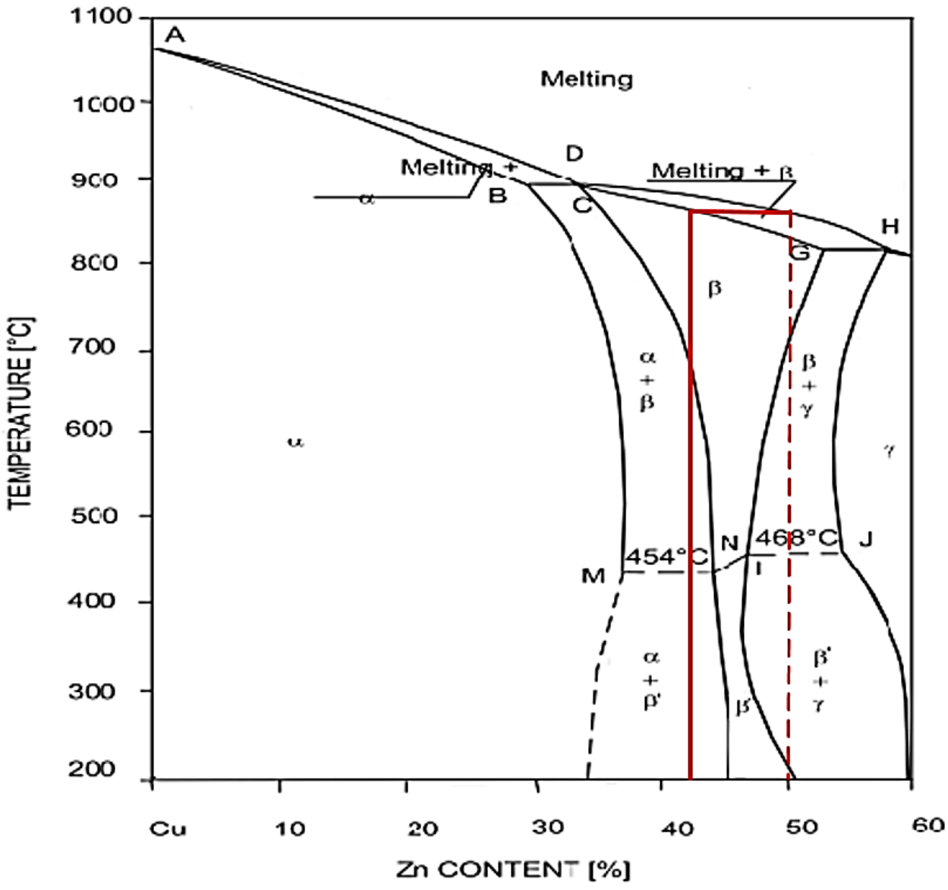

The phenomenon of zinc fumigation has been verified by taking some specimens of the experimental campaign, to confirm that zinc fumigation occurs not only superficially as found on black powders (see Figure 61), also in the inner layers of the component.

A further experimental campaign on LASER gun cleaning was carried out on samples taken from the experimental campaign. Four cleaning tests were carried out: as built, 50%, 75% and 100% emitted power. The tests also serve to determine whether there is the possibility of using the LASER finish to improve surface roughness.

Figure 61: EDS analysis of black powder

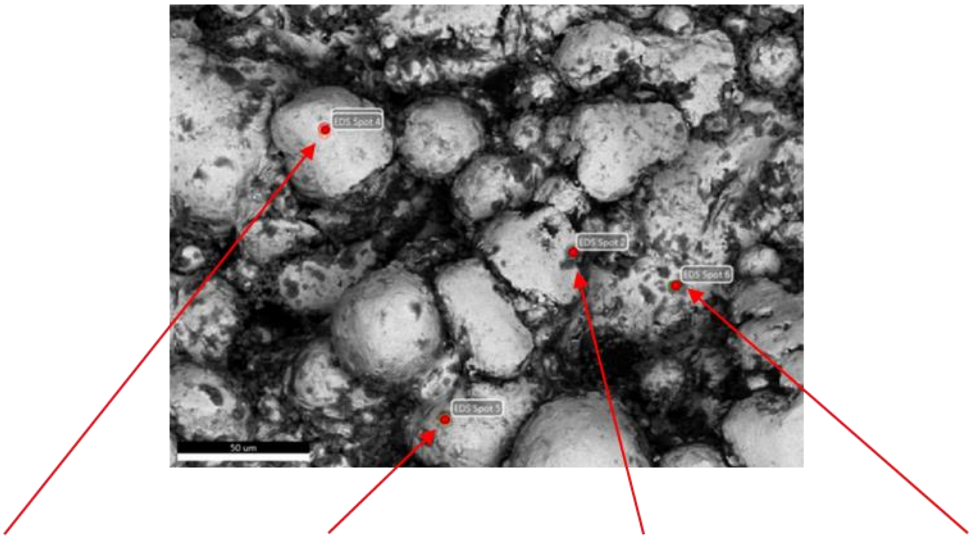

Spot 4		Spot 5		Spot 2		Spot 6	
Element	Weight %	Element	Weight %	Element	Weight %	Element	Weight %
ZnK	38.91	ZnK	40.76	ZnK	35.23	ZnK	41.17

The system works thanks to LASER pulses, this does not damage the surface but only removes the top layer and is vaporized.

A powerful focused LASER beam hits the surface for a few seconds by scanning the surface side by side; the surface absorbs most of the energy of the LASER beam, which is directly transformed into thermal energy, and removes (vaporizes) contamination. The base material is cleaned without direct mechanical action, without damage and with low and limited radiation without the need for chemical agents harmful to the environment. The higher the absorption – the ability to absorb LASER energy – by the element/contaminant to be removed more easily this is removed.

Bulk material, unlike the surface patina, does not absorb but reflects the radius. Metal materials are particularly suitable for cleaning with this technology for their high reflection factor.

With a precise dosage of LASER pulses and with the insertion of suitable parameters, the base material is not damaged. Figure 62 shows the results for calculating the percentage weight of zinc within the material with its trend curves, depending on the power of the LASER used. Below are the images containing the zinc percentage values for each individual test, normalized to the value obtained from the as built surface and its SEM images (from Figure 63 to Figure 72).

Figure 62: Graph of Zn [wt.%] relative of LASER Power polishing

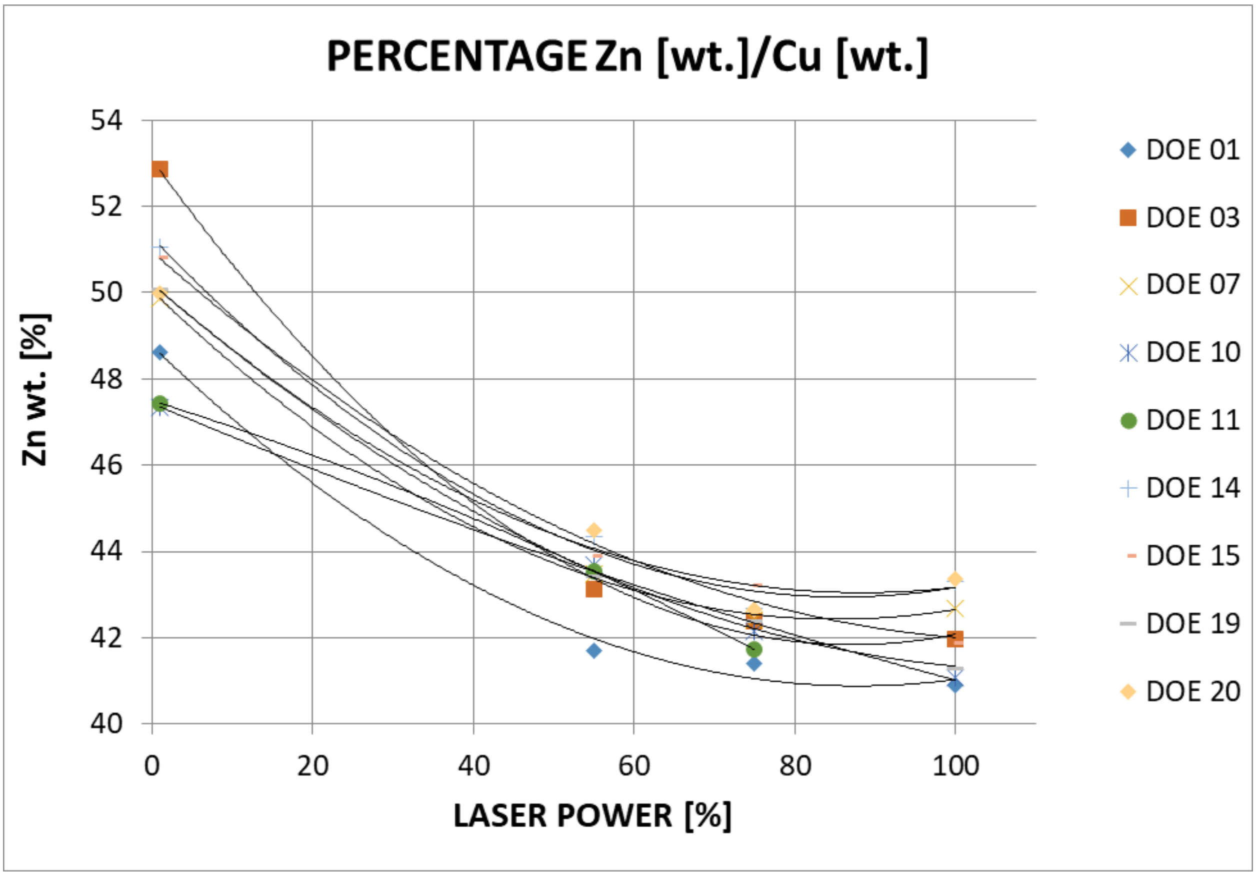

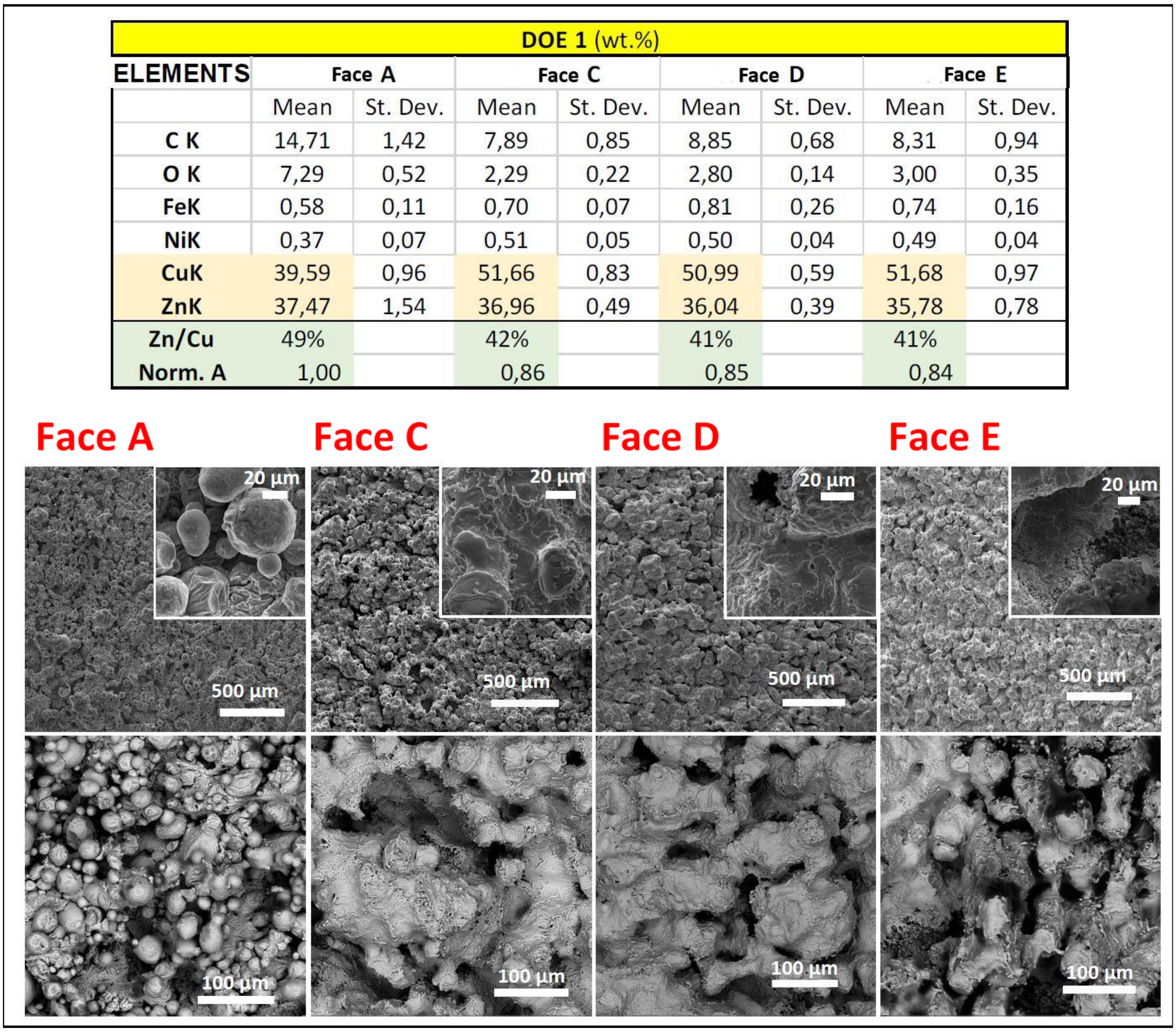

DOE 1 (wt.%)								
ELEMENTS	**Face A**		**Face C**		**Face D**		**Face E**	
	Mean	St. Dev.	Mean	St. Dev.	Mean	St. Dev.	Mean	St. Dev.
C K	14,71	1,42	7,89	0,85	8,85	0,68	8,31	0,94
O K	7,29	0,52	2,29	0,22	2,80	0,14	3,00	0,35
FeK	0,58	0,11	0,70	0,07	0,81	0,26	0,74	0,16
NiK	0,37	0,07	0,51	0,05	0,50	0,04	0,49	0,04
CuK	39,59	0,96	51,66	0,83	50,99	0,59	51,68	0,97
ZnK	37,47	1,54	36,96	0,49	36,04	0,39	35,78	0,78
Zn/Cu	49%		42%		41%		41%	
Norm. A	1,00		0,86		0,85		0,84	

Figure 63: SEM and EDS analysis of sample 1

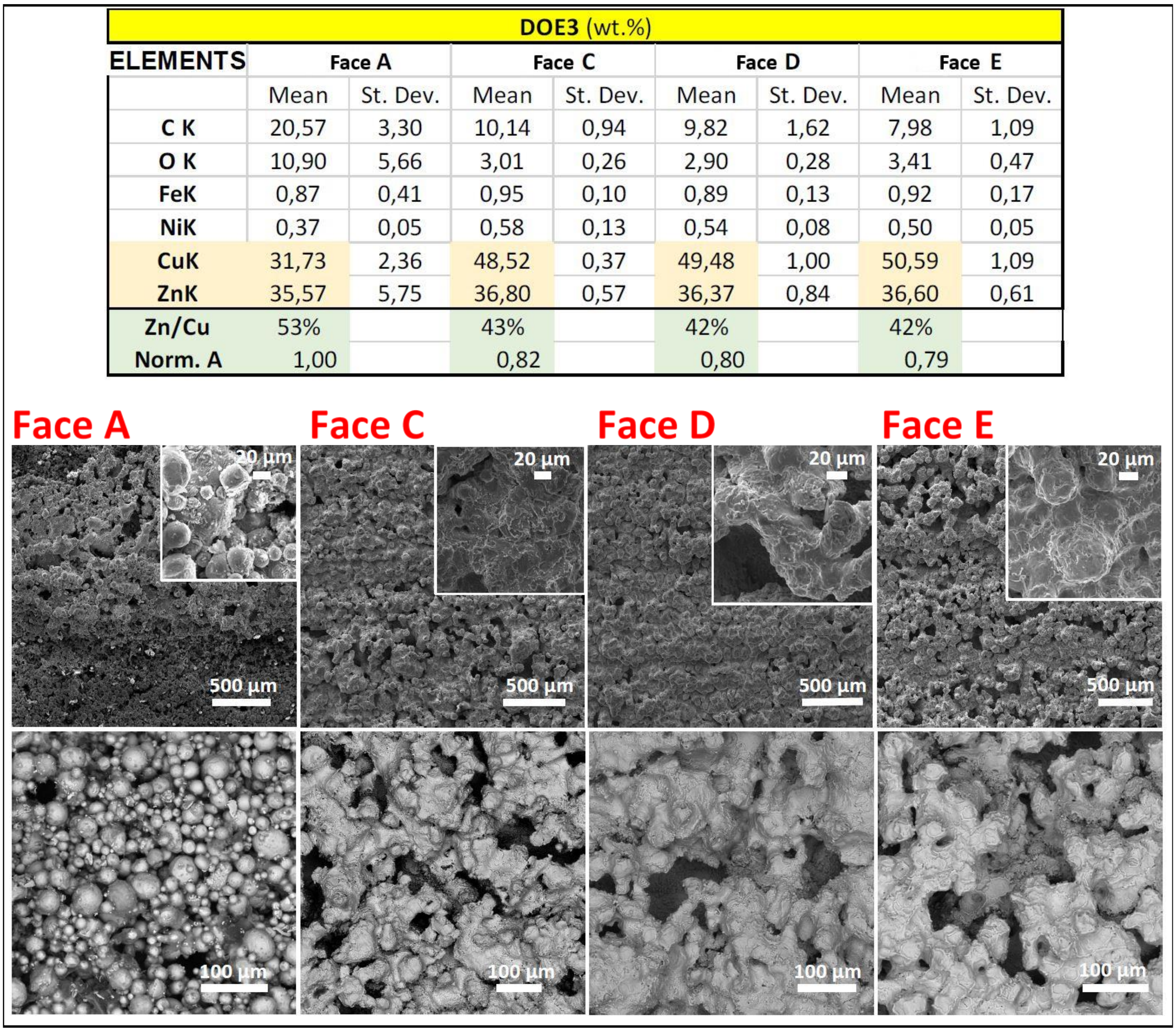

DOE3 (wt.%)								
ELEMENTS	**Face A**		**Face C**		**Face D**		**Face E**	
	Mean	St. Dev.	Mean	St. Dev.	Mean	St. Dev.	Mean	St. Dev.
C K	20,57	3,30	10,14	0,94	9,82	1,62	7,98	1,09
O K	10,90	5,66	3,01	0,26	2,90	0,28	3,41	0,47
FeK	0,87	0,41	0,95	0,10	0,89	0,13	0,92	0,17
NiK	0,37	0,05	0,58	0,13	0,54	0,08	0,50	0,05
CuK	31,73	2,36	48,52	0,37	49,48	1,00	50,59	1,09
ZnK	35,57	5,75	36,80	0,57	36,37	0,84	36,60	0,61
Zn/Cu	53%		43%		42%		42%	
Norm. A	1,00		0,82		0,80		0,79	

Figure 64: SEM and EDS analysis of sample 3

DOE7 (wt.%)								
ELEMENTS	**Face A**		**Face C**		**Face D**		**Face E**	
	Mean	St. Dev.	Mean	St. Dev.	Mean	St. Dev.	Mean	St. Dev.
C K	19,55	2,29	8,78	0,83	9,76	1,71	8,65	0,85
O K	11,01	0,51	3,05	0,32	2,85	0,15	3,18	0,09
FeK	0,82	0,11	0,76	0,17	1,10	0,20	0,94	0,12
NiK	0,44	0,03	0,47	0,06	0,59	0,10	0,53	0,04
CuK	34,18	0,98	49,14	0,75	49,34	0,93	49,69	0,42
ZnK	33,98	1,68	37,79	0,41	36,36	0,91	37,01	0,37
Zn/Cu	50%		43%		42%		43%	
Norm. A	1,00		0,87		0,85		0,86	

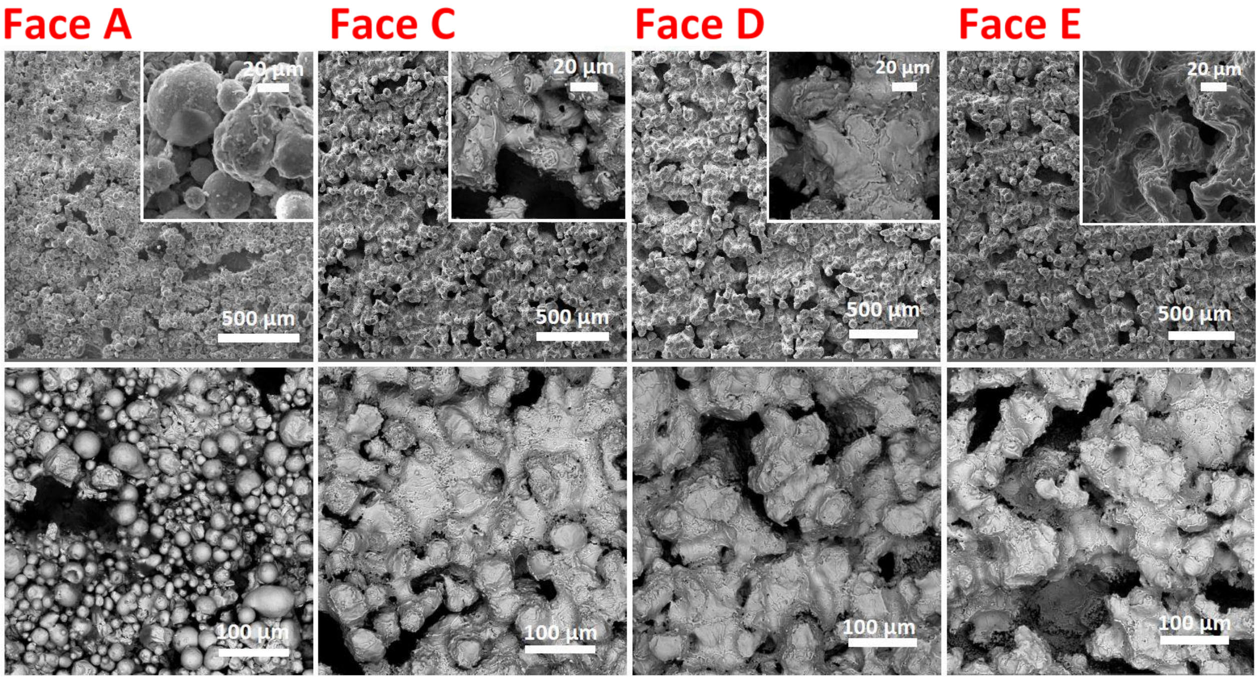

Figure 65: SEM and EDS analysis of sample 7

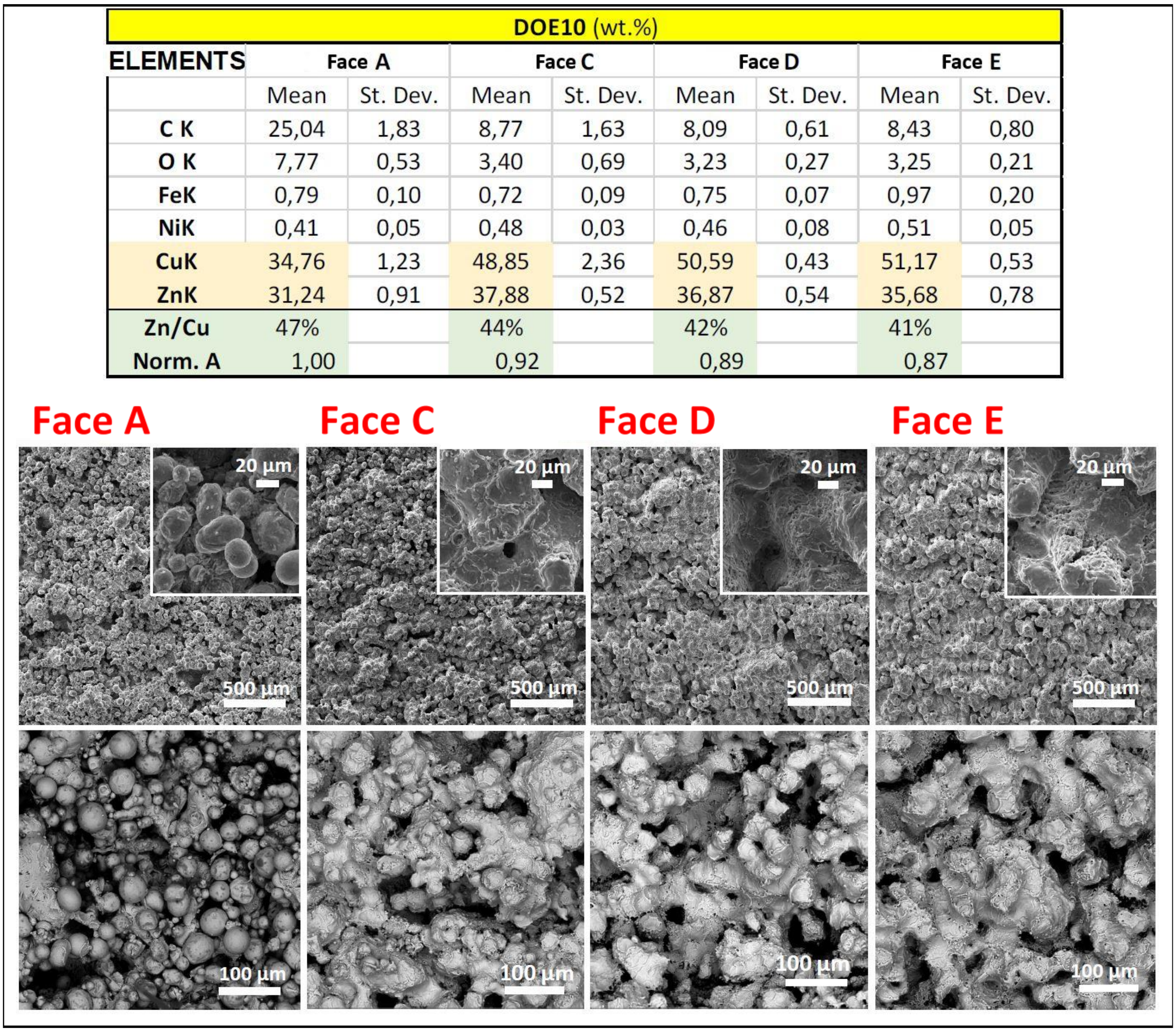

DOE10 (wt.%)

ELEMENTS	Face A		Face C		Face D		Face E	
	Mean	St. Dev.	Mean	St. Dev.	Mean	St. Dev.	Mean	St. Dev.
C K	25,04	1,83	8,77	1,63	8,09	0,61	8,43	0,80
O K	7,77	0,53	3,40	0,69	3,23	0,27	3,25	0,21
FeK	0,79	0,10	0,72	0,09	0,75	0,07	0,97	0,20
NiK	0,41	0,05	0,48	0,03	0,46	0,08	0,51	0,05
CuK	34,76	1,23	48,85	2,36	50,59	0,43	51,17	0,53
ZnK	31,24	0,91	37,88	0,52	36,87	0,54	35,68	0,78
Zn/Cu	47%		44%		42%		41%	
Norm. A	1,00		0,92		0,89		0,87	

Figure 66: SEM and EDS analysis of sample 10

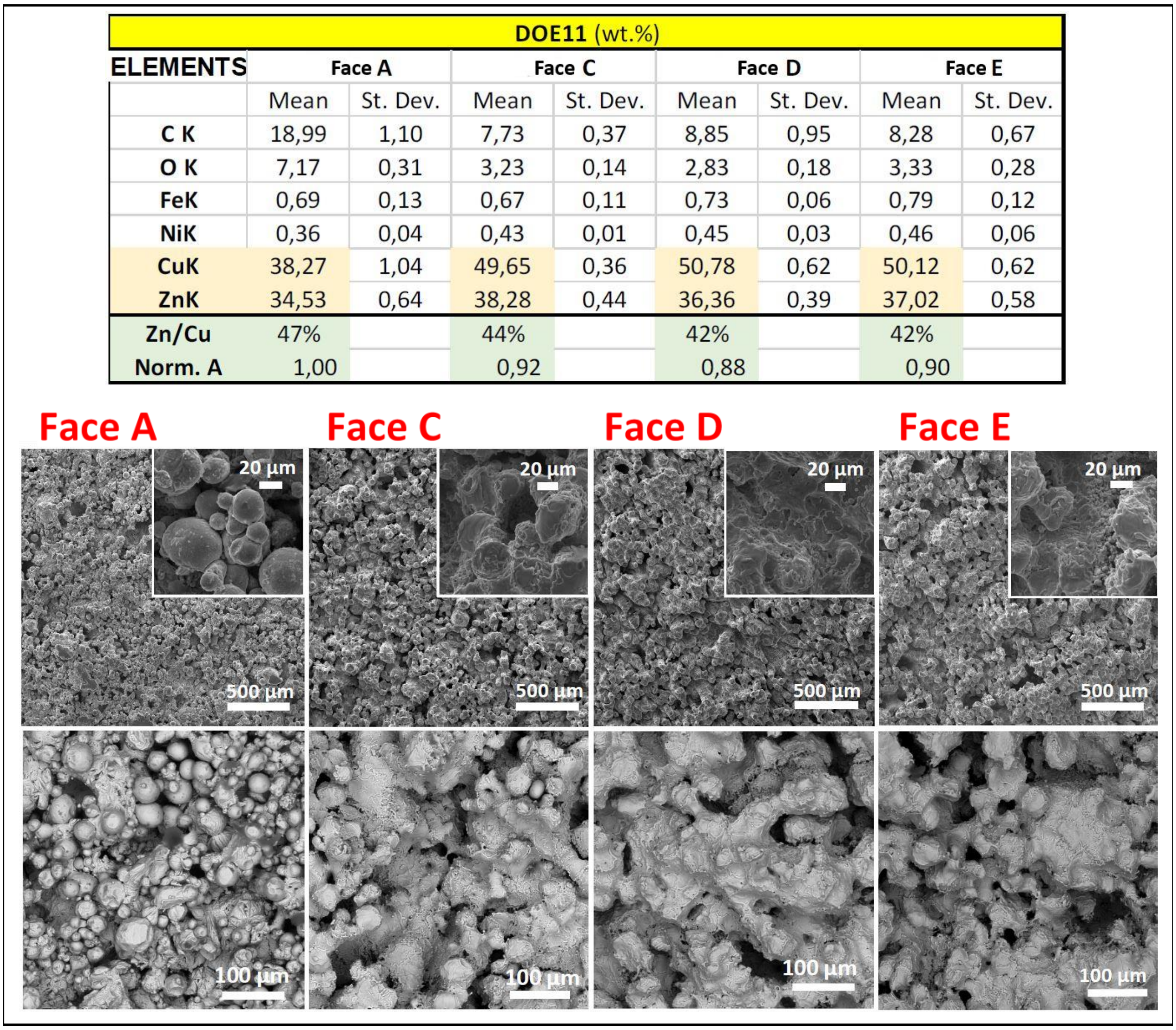

DOE11 (wt.%)								
ELEMENTS	**Face A**		**Face C**		**Face D**		**Face E**	
	Mean	St. Dev.	Mean	St. Dev.	Mean	St. Dev.	Mean	St. Dev.
C K	18,99	1,10	7,73	0,37	8,85	0,95	8,28	0,67
O K	7,17	0,31	3,23	0,14	2,83	0,18	3,33	0,28
FeK	0,69	0,13	0,67	0,11	0,73	0,06	0,79	0,12
NiK	0,36	0,04	0,43	0,01	0,45	0,03	0,46	0,06
CuK	38,27	1,04	49,65	0,36	50,78	0,62	50,12	0,62
ZnK	34,53	0,64	38,28	0,44	36,36	0,39	37,02	0,58
Zn/Cu	47%		44%		42%		42%	
Norm. A	1,00		0,92		0,88		0,90	

Figure 67: SEM and EDS analysis of sample 11

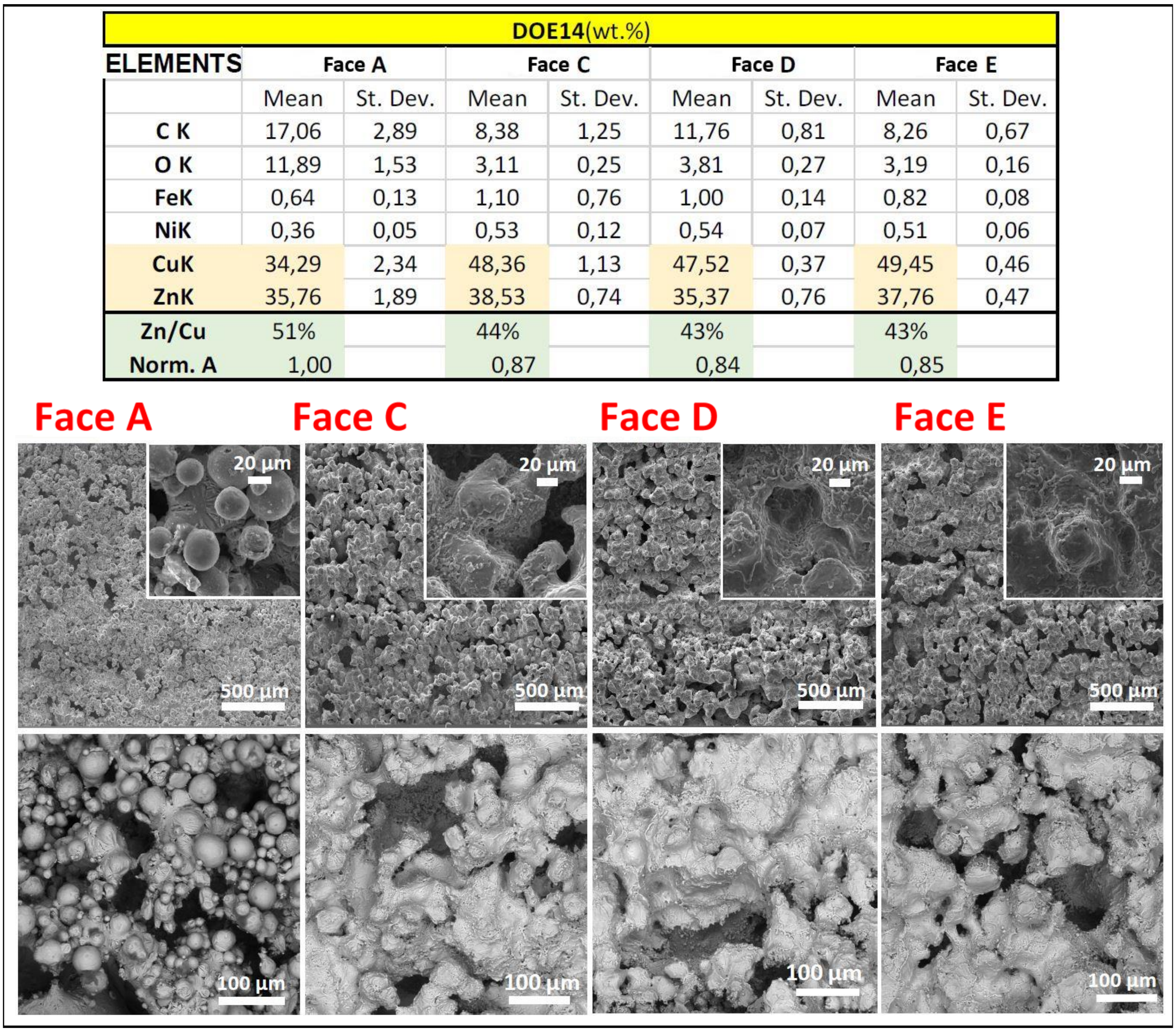

DOE14(wt.%)								
ELEMENTS	Face A		Face C		Face D		Face E	
	Mean	St. Dev.	Mean	St. Dev.	Mean	St. Dev.	Mean	St. Dev.
C K	17,06	2,89	8,38	1,25	11,76	0,81	8,26	0,67
O K	11,89	1,53	3,11	0,25	3,81	0,27	3,19	0,16
FeK	0,64	0,13	1,10	0,76	1,00	0,14	0,82	0,08
NiK	0,36	0,05	0,53	0,12	0,54	0,07	0,51	0,06
CuK	34,29	2,34	48,36	1,13	47,52	0,37	49,45	0,46
ZnK	35,76	1,89	38,53	0,74	35,37	0,76	37,76	0,47
Zn/Cu	51%		44%		43%		43%	
Norm. A	1,00		0,87		0,84		0,85	

Figure 68: SEM and EDS analysis of sample 14

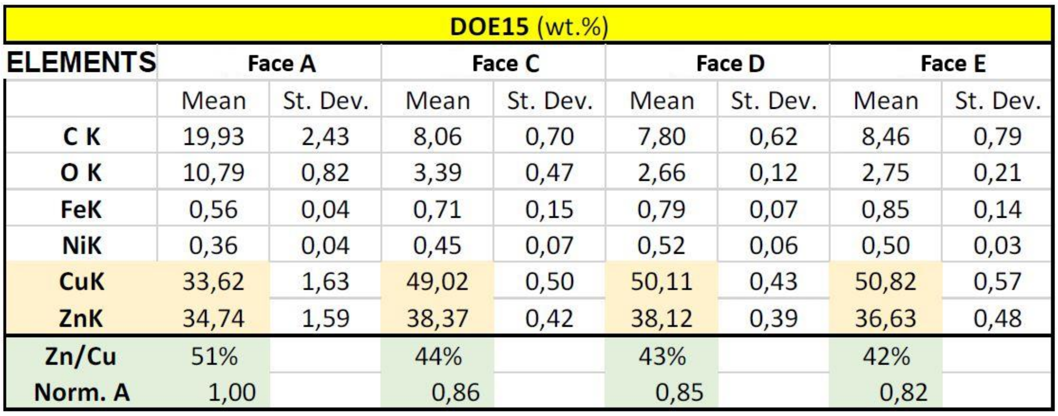

DOE15 (wt.%)

ELEMENTS	**Face A**		**Face C**		**Face D**		**Face E**	
	Mean	St. Dev.	Mean	St. Dev.	Mean	St. Dev.	Mean	St. Dev.
C K	19,93	2,43	8,06	0,70	7,80	0,62	8,46	0,79
O K	10,79	0,82	3,39	0,47	2,66	0,12	2,75	0,21
FeK	0,56	0,04	0,71	0,15	0,79	0,07	0,85	0,14
NiK	0,36	0,04	0,45	0,07	0,52	0,06	0,50	0,03
CuK	33,62	1,63	49,02	0,50	50,11	0,43	50,82	0,57
ZnK	34,74	1,59	38,37	0,42	38,12	0,39	36,63	0,48
Zn/Cu	51%		44%		43%		42%	
Norm. A	1,00		0,86		0,85		0,82	

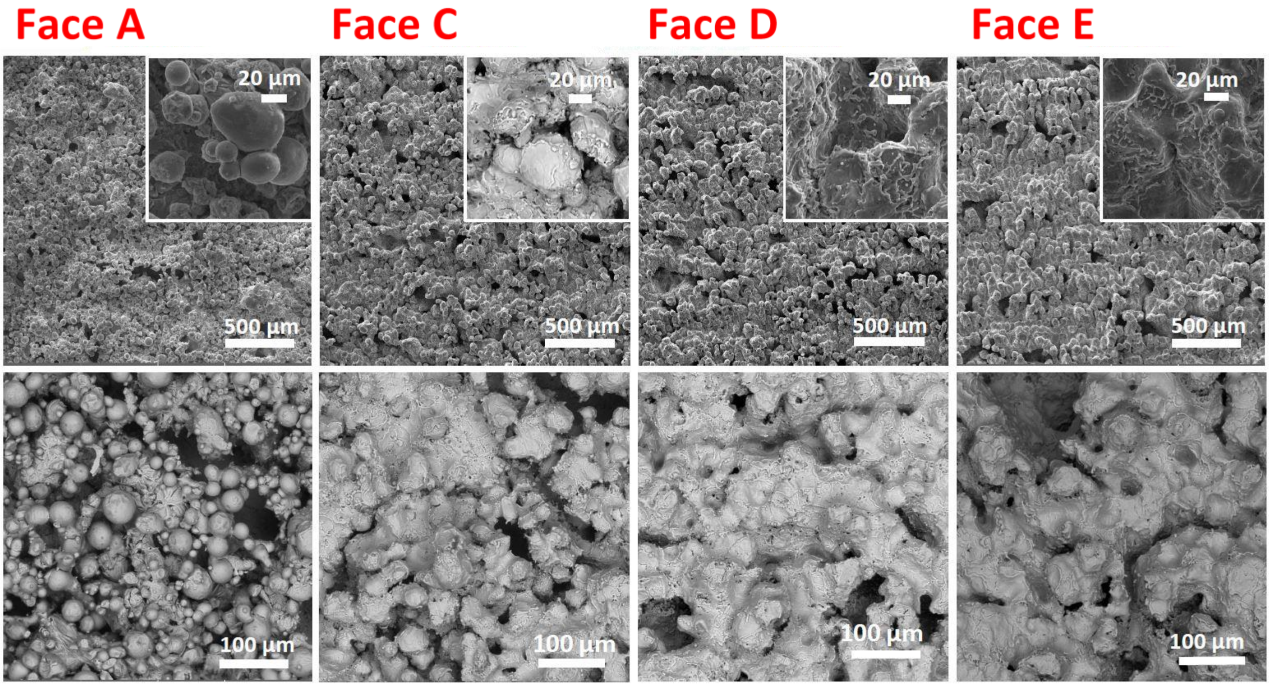

Figure 69: SEM and EDS analysis of sample 15

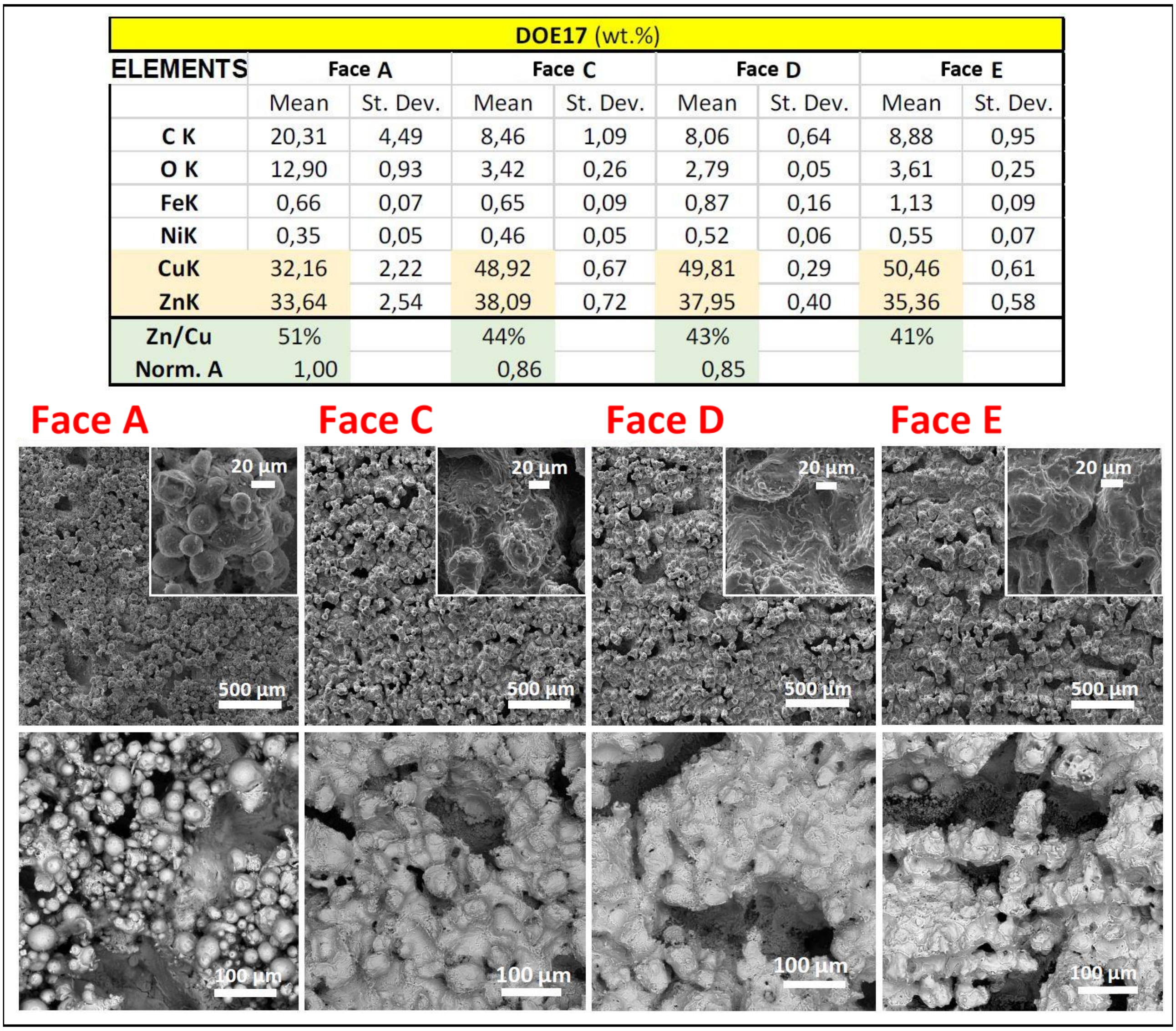

DOE17 (wt.%)

ELEMENTS	Face A		Face C		Face D		Face E	
	Mean	St. Dev.	Mean	St. Dev.	Mean	St. Dev.	Mean	St. Dev.
C K	20,31	4,49	8,46	1,09	8,06	0,64	8,88	0,95
O K	12,90	0,93	3,42	0,26	2,79	0,05	3,61	0,25
FeK	0,66	0,07	0,65	0,09	0,87	0,16	1,13	0,09
NiK	0,35	0,05	0,46	0,05	0,52	0,06	0,55	0,07
CuK	32,16	2,22	48,92	0,67	49,81	0,29	50,46	0,61
ZnK	33,64	2,54	38,09	0,72	37,95	0,40	35,36	0,58
Zn/Cu	51%		44%		43%		41%	
Norm. A	1,00		0,86		0,85			

Figure 70: SEM and EDS analysis of sample 17

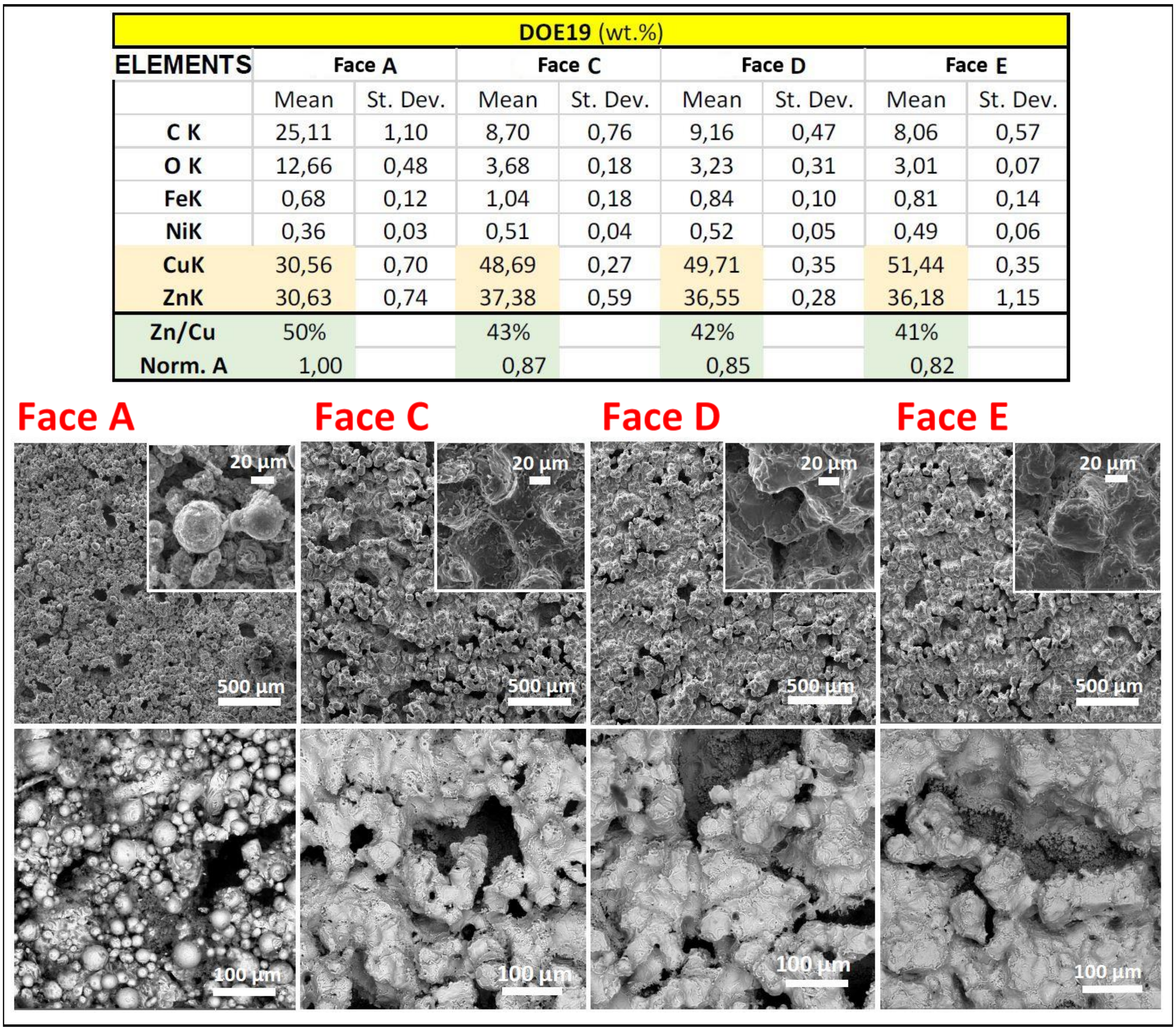

DOE19 (wt.%)								
ELEMENTS	**Face A**		**Face C**		**Face D**		**Face E**	
	Mean	St. Dev.	Mean	St. Dev.	Mean	St. Dev.	Mean	St. Dev.
C K	25,11	1,10	8,70	0,76	9,16	0,47	8,06	0,57
O K	12,66	0,48	3,68	0,18	3,23	0,31	3,01	0,07
FeK	0,68	0,12	1,04	0,18	0,84	0,10	0,81	0,14
NiK	0,36	0,03	0,51	0,04	0,52	0,05	0,49	0,06
CuK	30,56	0,70	48,69	0,27	49,71	0,35	51,44	0,35
ZnK	30,63	0,74	37,38	0,59	36,55	0,28	36,18	1,15
Zn/Cu	50%		43%		42%		41%	
Norm. A	1,00		0,87		0,85		0,82	

Figure 71: SEM and EDS analysis of sample 19

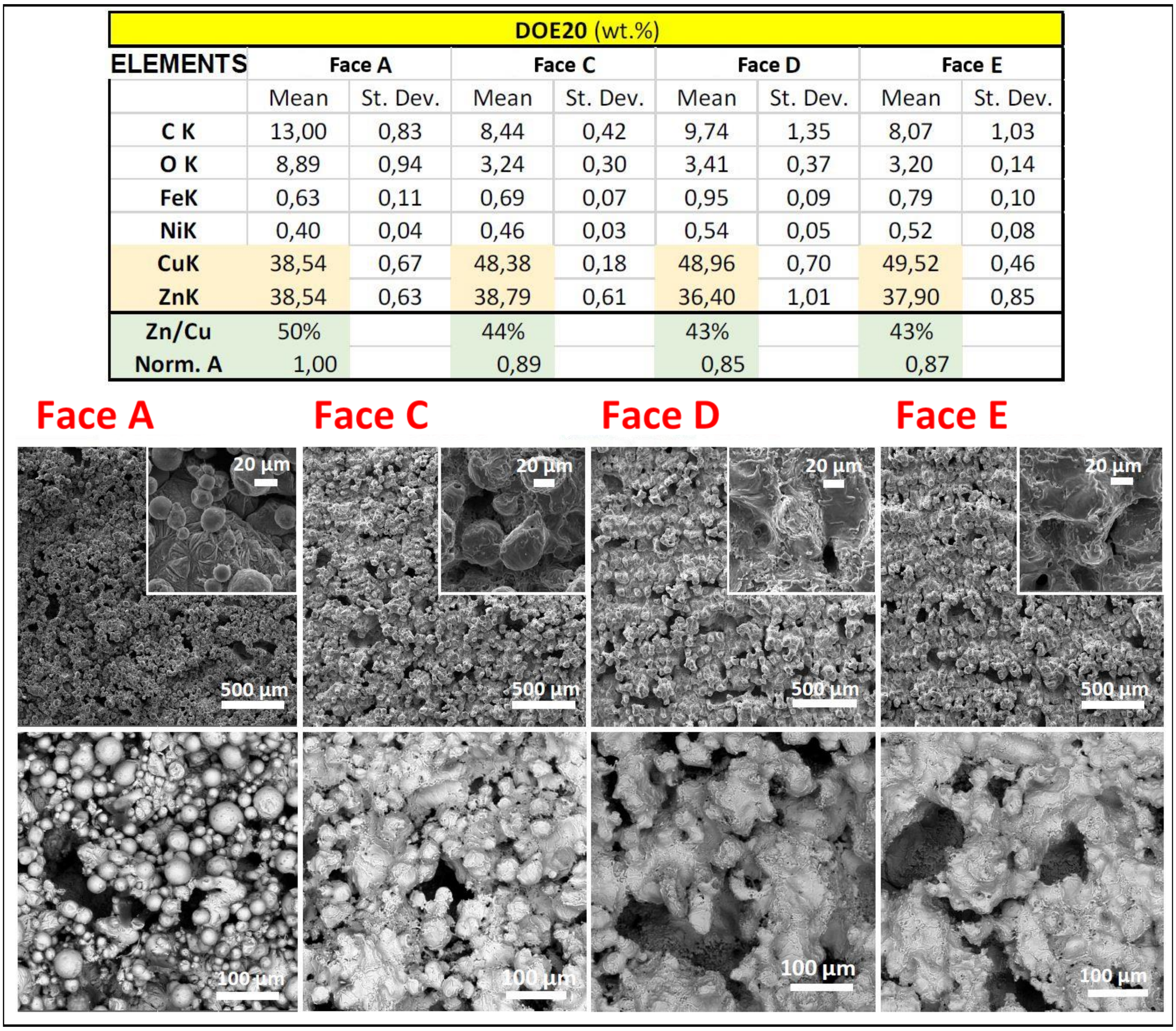

DOE20 (wt.%)

ELEMENTS	Face A		Face C		Face D		Face E	
	Mean	St. Dev.	Mean	St. Dev.	Mean	St. Dev.	Mean	St. Dev.
C K	13,00	0,83	8,44	0,42	9,74	1,35	8,07	1,03
O K	8,89	0,94	3,24	0,30	3,41	0,37	3,20	0,14
FeK	0,63	0,11	0,69	0,07	0,95	0,09	0,79	0,10
NiK	0,40	0,04	0,46	0,03	0,54	0,05	0,52	0,08
CuK	38,54	0,67	48,38	0,18	48,96	0,70	49,52	0,46
ZnK	38,54	0,63	38,79	0,61	36,40	1,01	37,90	0,85
Zn/Cu	50%		44%		43%		43%	
Norm. A	1,00		0,89		0,85		0,87	

Figure 72: SEM and EDS analysis of sample 20

Using the printing parameters to obtain over the 99% of volumetric density we produced 10 samples to do characteristic tensile tests.

The test machine is an INSTRON 5567, mounting a cell load of 30kN MAX LOAD and an analogic extensometer INSTRON GL25mm EX2630-107. The instrument is located to the Engineering Department of the University of Modena and Reggio Emilia, under the supervision of Professor Andrea Gatto, Professor Elena Bassoli and Professor Lucia Denti, chiefs of the research group of mechanical technologies and production technologies.

The normative used is the UNI EN ISO6892-1 with a cross head speed of 0.5 mm/min.

About 10 samples:

- Samples 1, 2, 3, 4, 5, 6, 7, 8 were tested,
- Sample 9 was broken during the turning process,

- Sample 10 did not finish the printing process, perhaps due to an uneven distribution of the powder on the building plate.

In Figure 73 are represented the Stress – Strain curves of the 8 samples tested.

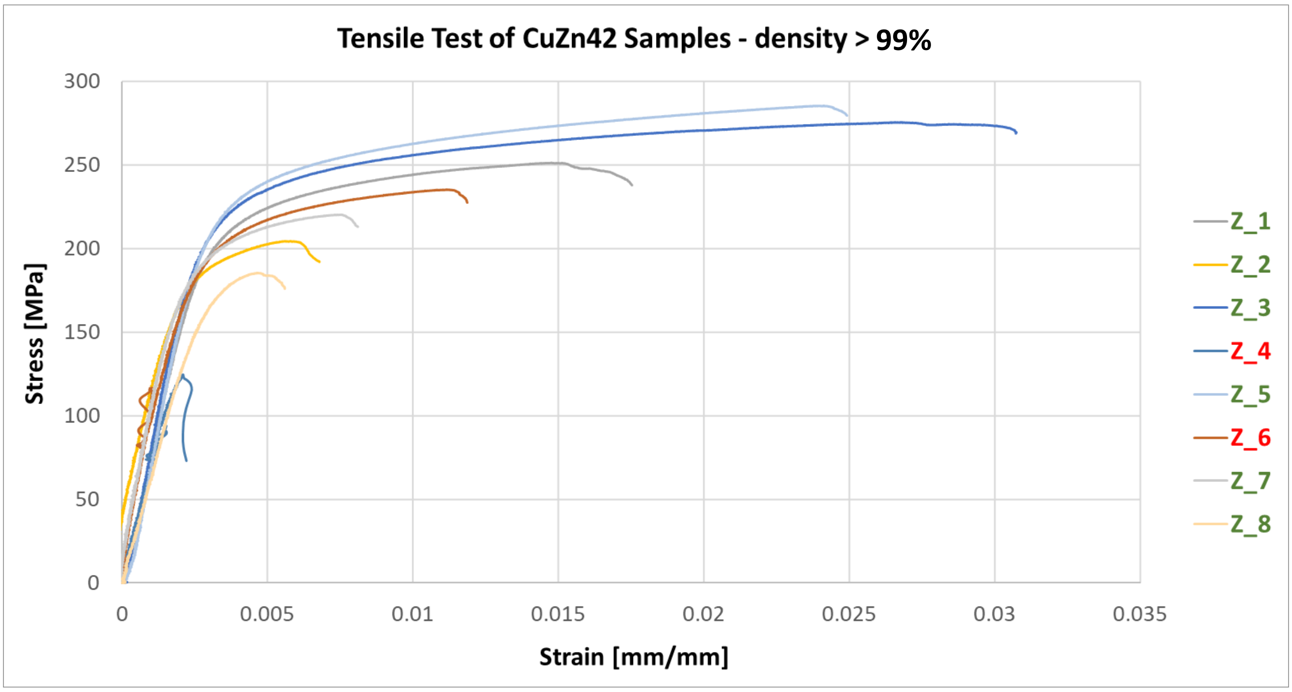

Figure 73: curves Stress - Strain of the 8 samples of CuZn42

During the tests, on sample named Z_6 and Z_4 the grips of the extensometer were slipped from their relative position, so the curves are not usable, if not trough appropriate graphical corrections.

On Figure 74 and Figure 75 are represented individually respectively the Z_6 curve and Z_4 curve with the relative corrections. From the curves it is presumed that the return section of the extensometer is due to a slippage of the grips (blue circle).

Figure 74: Stress - Strain curve of sample Z_6 before and after the correction (blue circle)

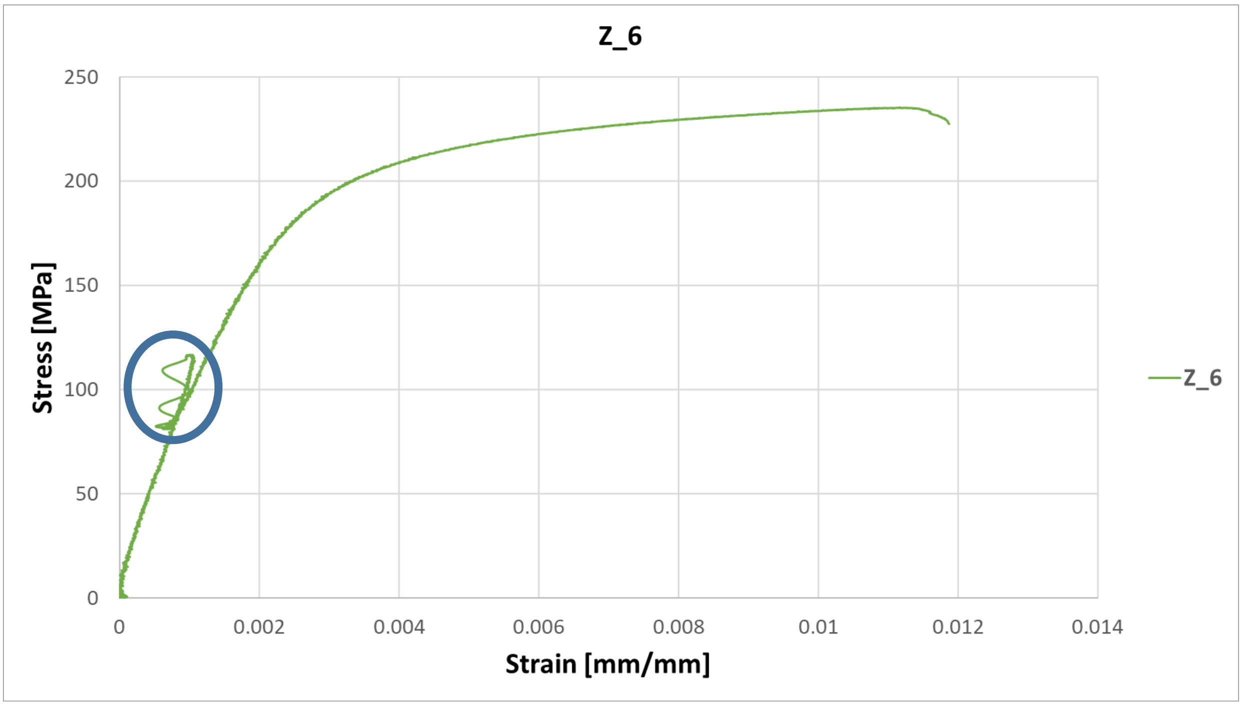

Figure 75 : Stress - Strain curve of sample Z_4 before and after the correction (blue circle)

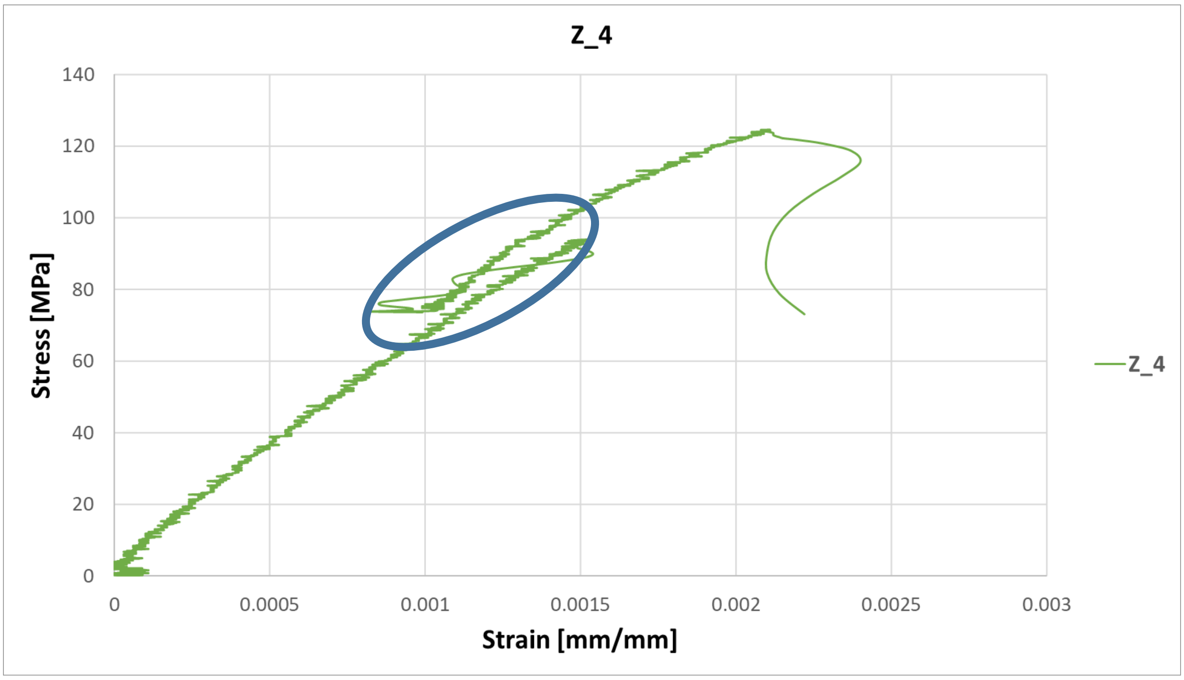

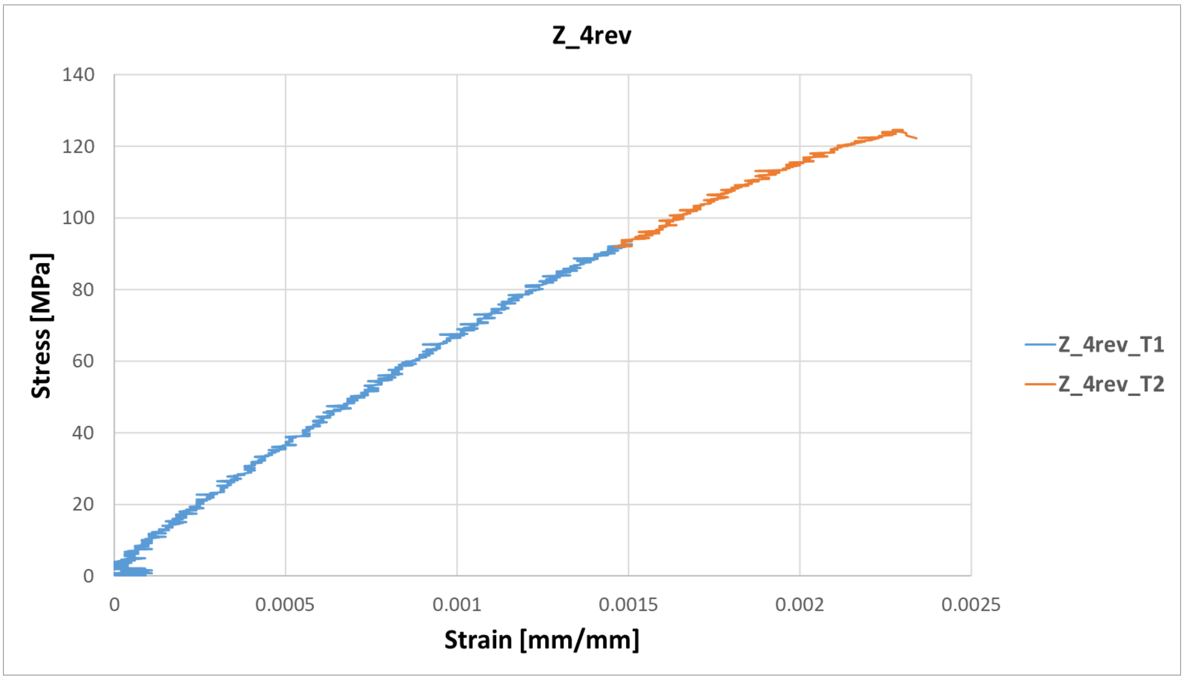

The following tables show the experimental values of Young's modulus, yield strength, mechanical strength and percentage elongation.

Table 3: Results of the tensile tests

Sample	**Young Modulus**	**$R_{p\,0,2}$**	**R_m**	**A_t**
	(GPa)	**(MPa)**	**(MPa)**	**(%)**
Z_1	81	223	251	1.7
Z_2	97	194	204	1.4
Z_3	88	233	276	3.1
Z_5	92	238	285	3.9
Z_7	92	207	220	1.4
Z_8	63	184	185	0.6
MEAN	**86**	**213**	**237**	**2.0**
STD. DEV.	**12.2**	**21.7**	**40.3**	**1.2**
Sample	**Young Modulus**	**$R_{p\,0,2}$**	**R_m**	**A_t**
	(GPa)	**(MPa)**	**(MPa)**	**(%)**
Z_6	97	209	235	1.4
Z_4	63	-	125	0.2

Compared with values obtained from literature, Young's modulus can vary from a minimum of 85 GPa to a maximum of 110 GPa. As indicative values of $R_{p\,0,2}$ and R_m we consider the ranges 310-380 MPa and 430-480 MPa respectively. The values are to be understood as entirely indicative.

Given the significant dispersion of the curves relating to the tensile tests, some fracture surfaces were analysed to better understand the possible cause of failure.

Sample Z_5:

The specimen called Z_5 is the one that returned the highest values in the tensile test for this reason it was taken as a means of comparison for the surfaces of the specimens Z_4 and Z_6, which for various reasons gave non-catalogable results.

The surface of the specimen Z_5 is homogeneous on the whole, indicating the typical plastic deformation of ductile material. The contour of the fracture surface does not present anomalies, from which it is possible to deduce possible fracture grafts.

Figure 76: fracture surface of the sample Z_5

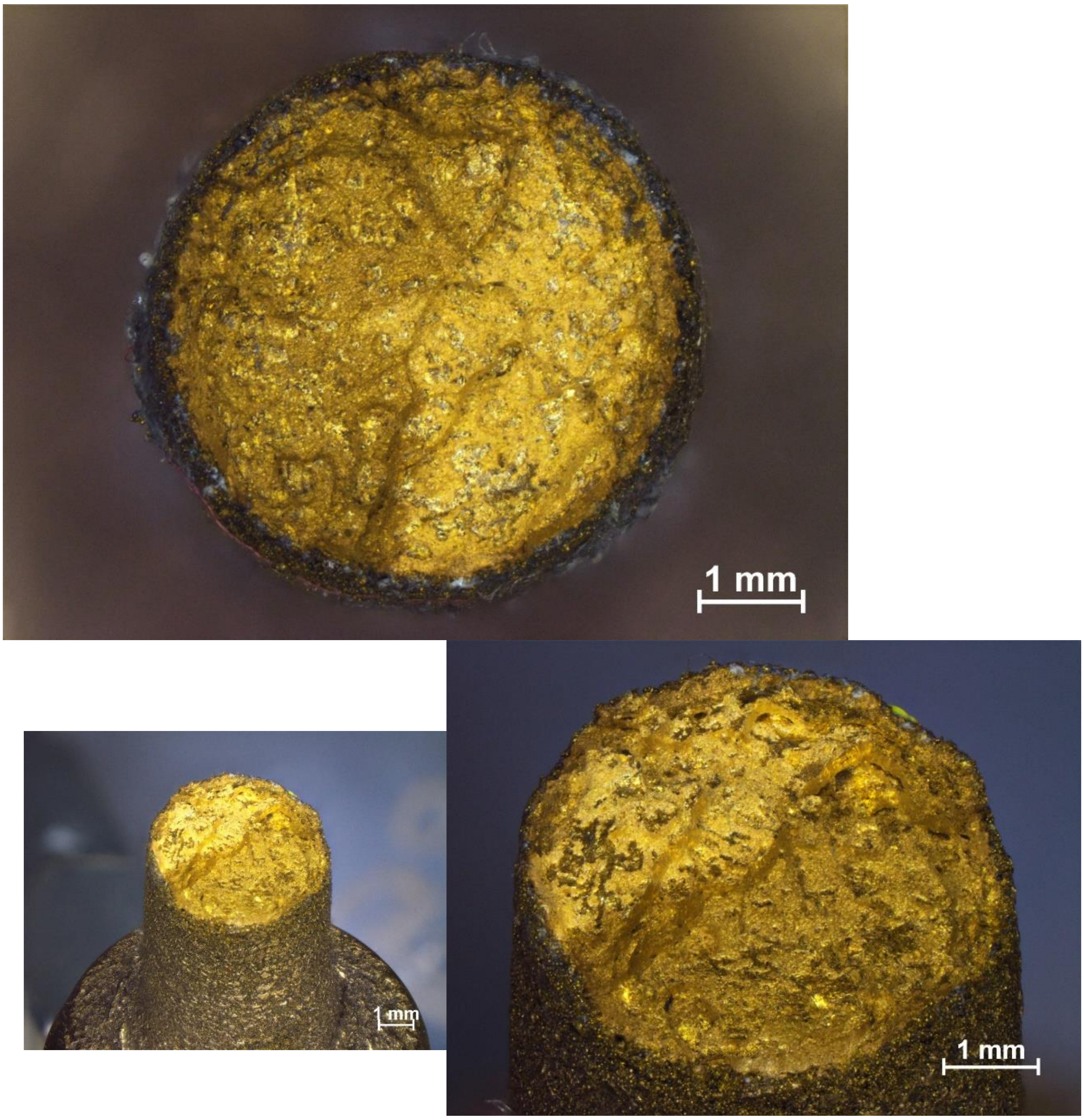

Figure 77: detailed images of sample Z_5

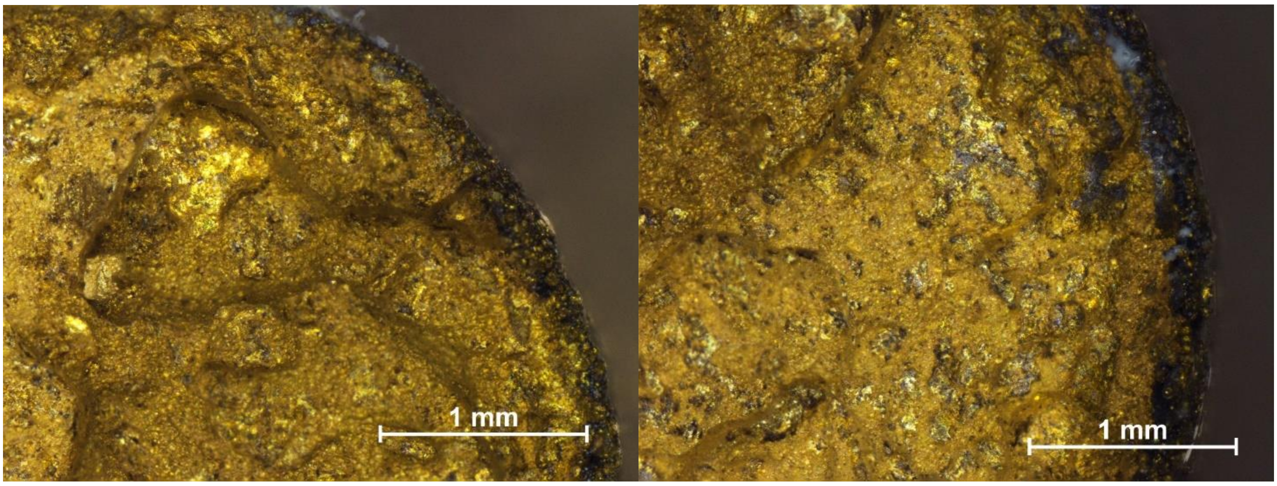

In figure 77 some detailed images of the surface are shown. In both images the contours of the specimen are homogeneous and do not present relevant discontinuity points.

Sample Z_6:

Figure 78: external fractures of sample Z_6

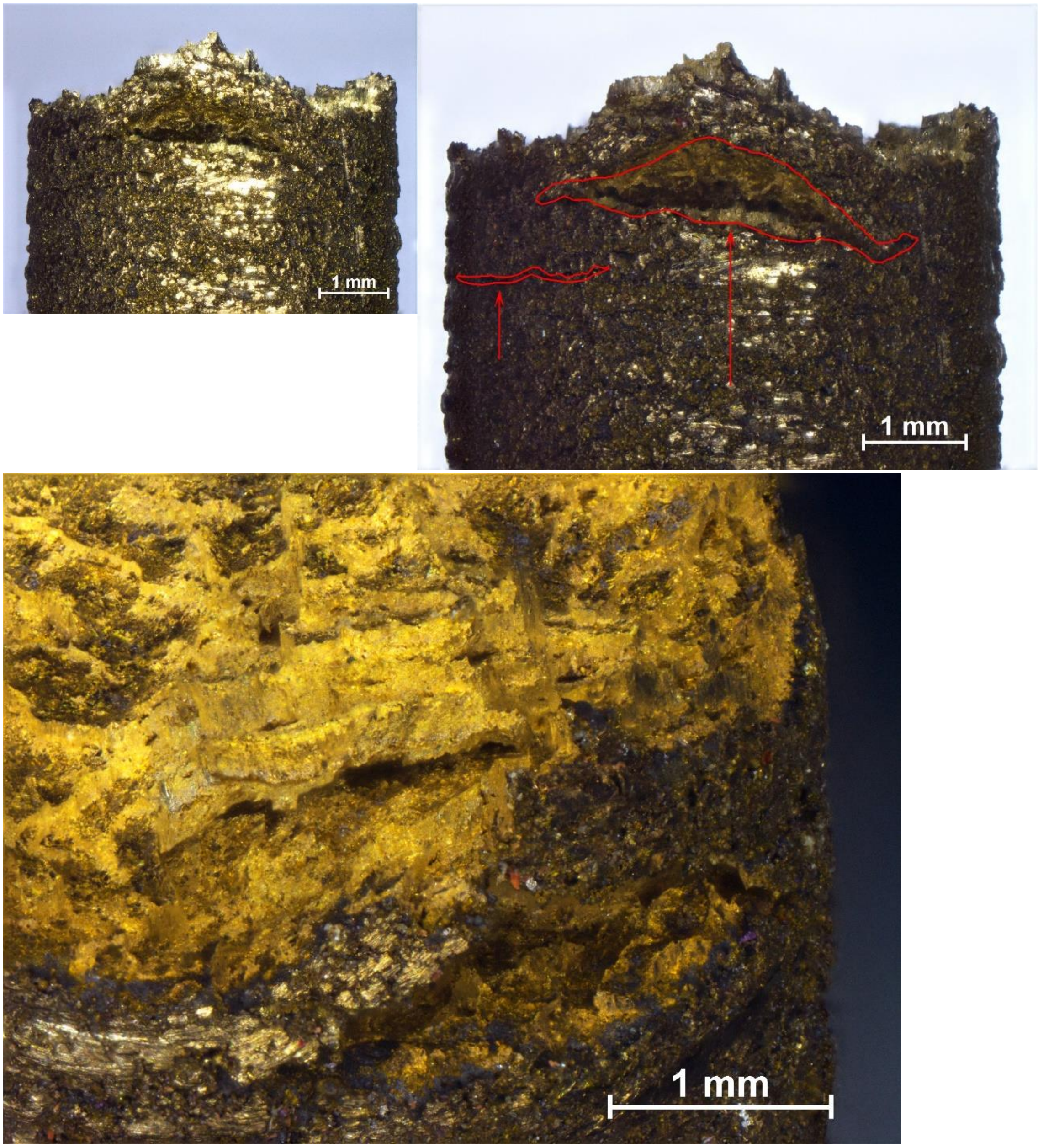

Z_6 is the specimen that returned results that were not in line with the other specimens. The characteristic curve presents a slippage of the extensometer grips. From a first correction it is clear that in reality this shift did not produce singularities on the overall curve.

Analysing the fracture area, visible delamination effects between various areas can be seen, indicating a possible erroneous distribution of the powder bed. Another possible reason is the presence of a significant porosity near the external contour of the component. On the respective counterpart, it is also noted that the delamination effect is not localized along the outer skin, but this effect was also possible in the consolidated part of the 'Infill' scan type (see Figure 78 and Figure 79).

Figure 79: internal fractures of sample Z_6

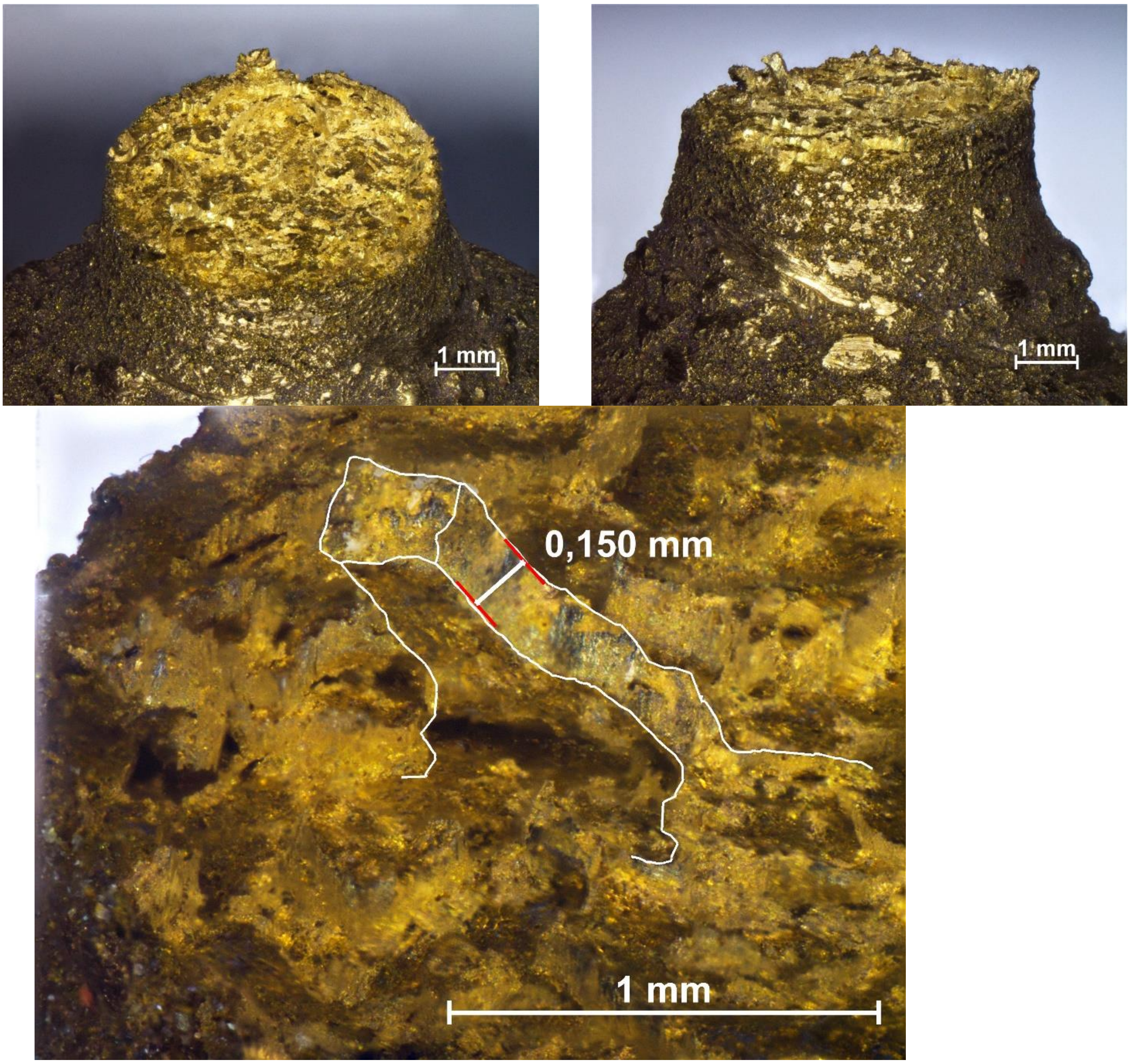

Sample Z_4:

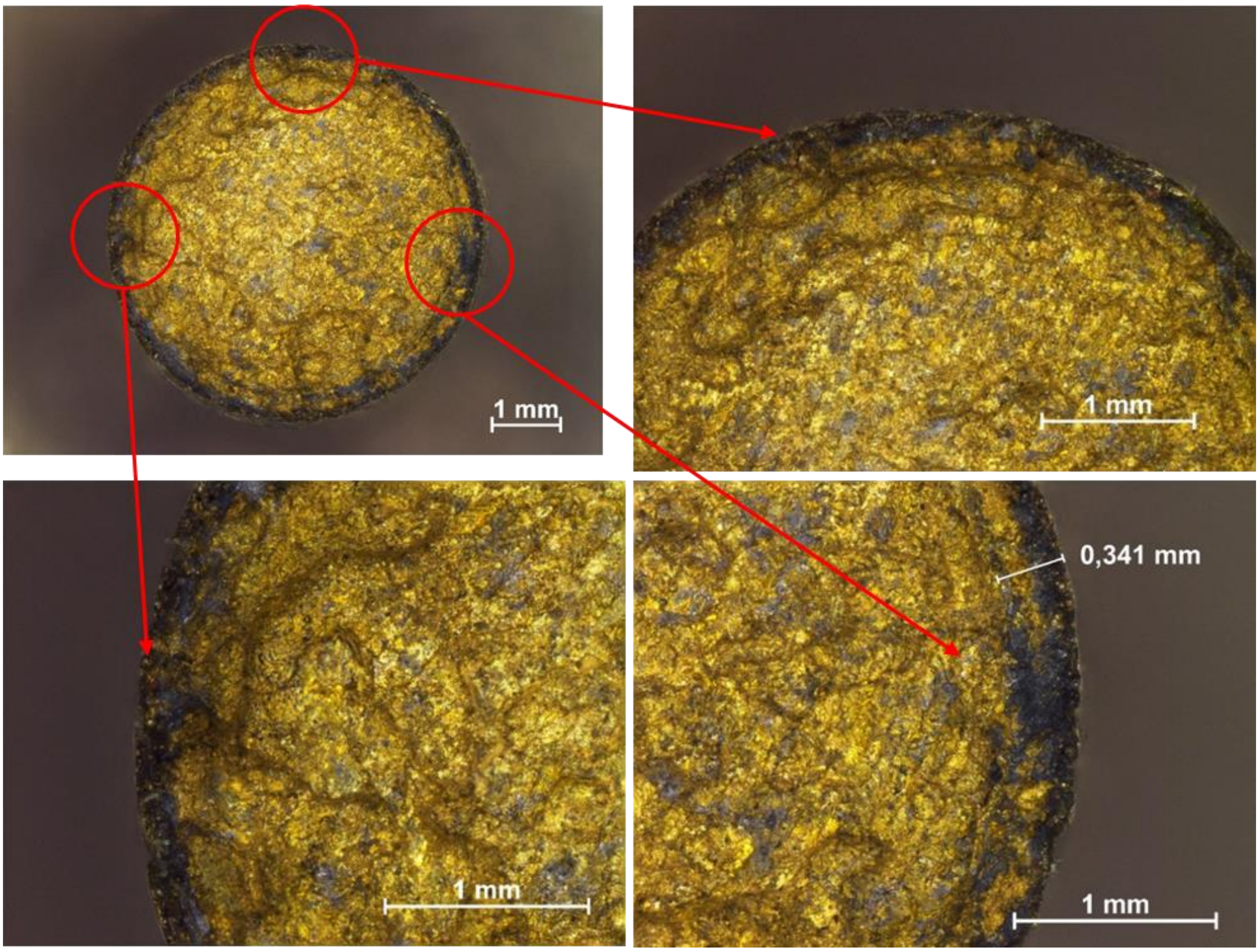

Figure 80: sample 4 and three possible cracking zones

At a first analysis, the specimen Z_4 has a more homogeneous fracture surface than the specimen Z_6. Also, for this specimen we found a slip in the grips of the extensometer, consequently also for this test the data extrapolated from the curve are not representative. In any case, a more detailed analysis of the surface was carried out and this allowed us to identify more trigger points. The concomitance of many trigger points has probably weakened the useful section in a short time interval leading to a sudden failure of the material (see Figure 80).

3.2: Brass roughness measures

As a last step we wanted to quantify the surface roughness, to have a complete picture of the entire additive process for this type of material with this specific particle size.

The instrument used to capture images is a NIKON Eclipse LV150N optical microscope equipped with a LASER source; through an image processing software it was possible to extrapolate the individual roughness profiles and their numerical values.

Since precise print parameters other than those used to produce the bulk part have been implemented for up-skin surfaces, roughness maps concern a lateral surface of the specimen and the upper surface, respectively.

LATERAL SURFACE MAP:

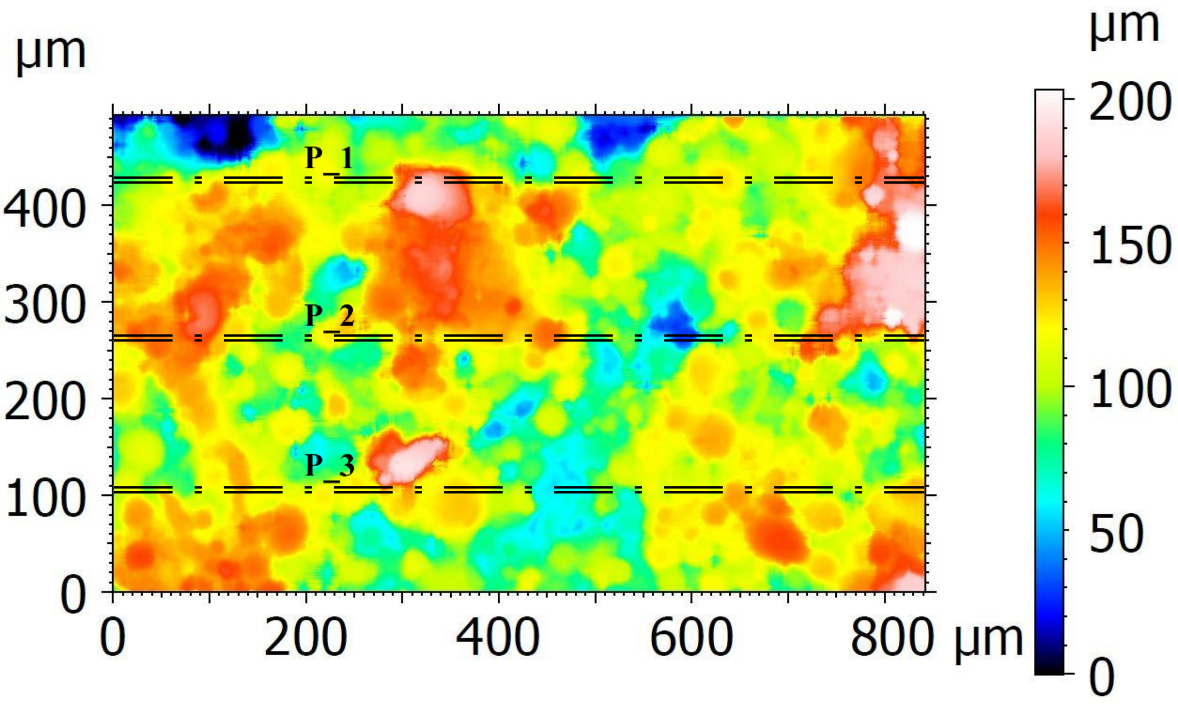

PROFILE_1:

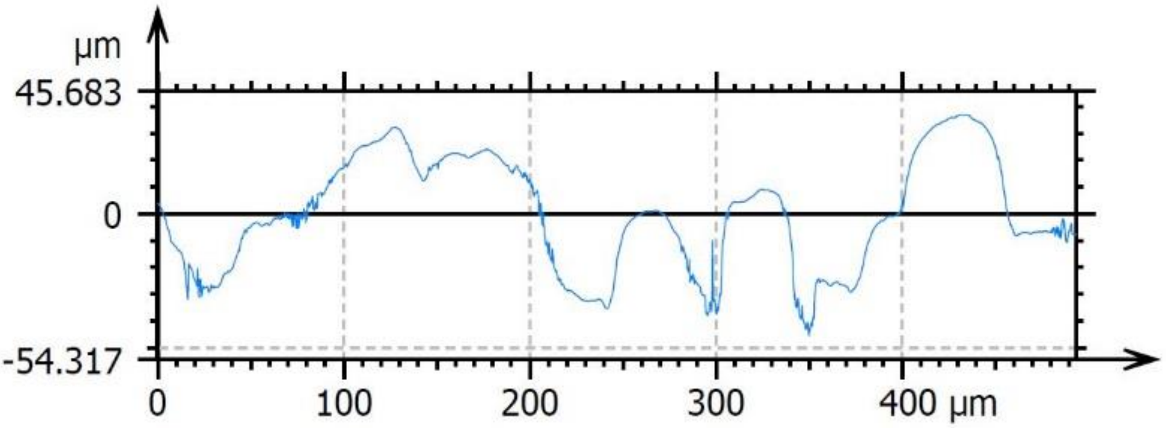

PROFILE_2:

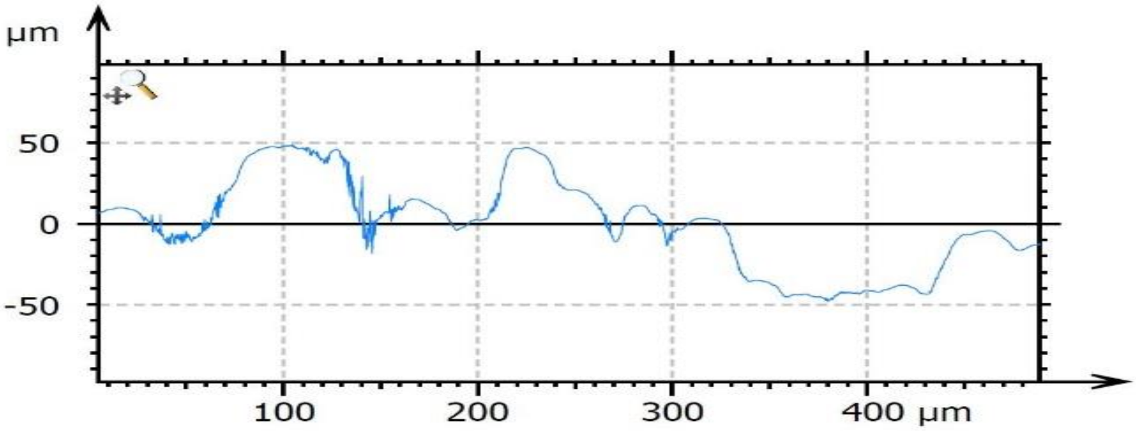

PROFILE_3:

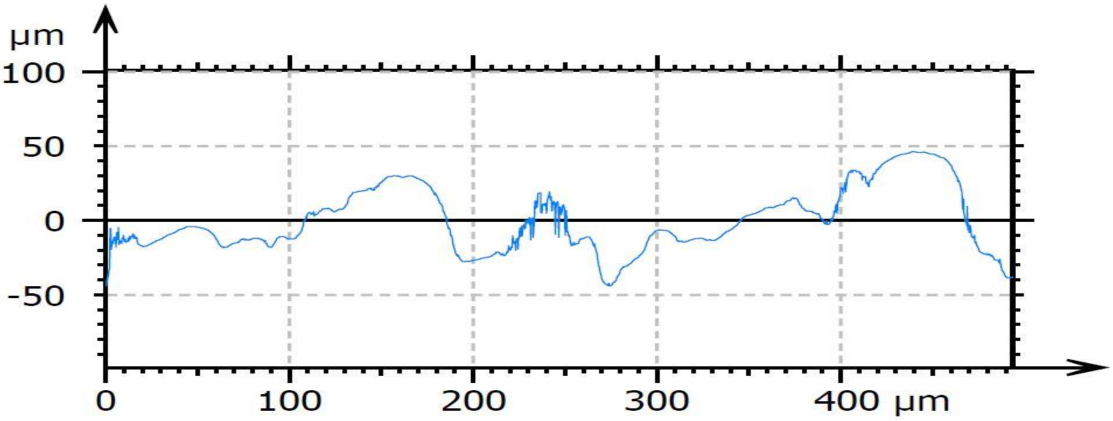

UPSKIN SURFACE MAP:

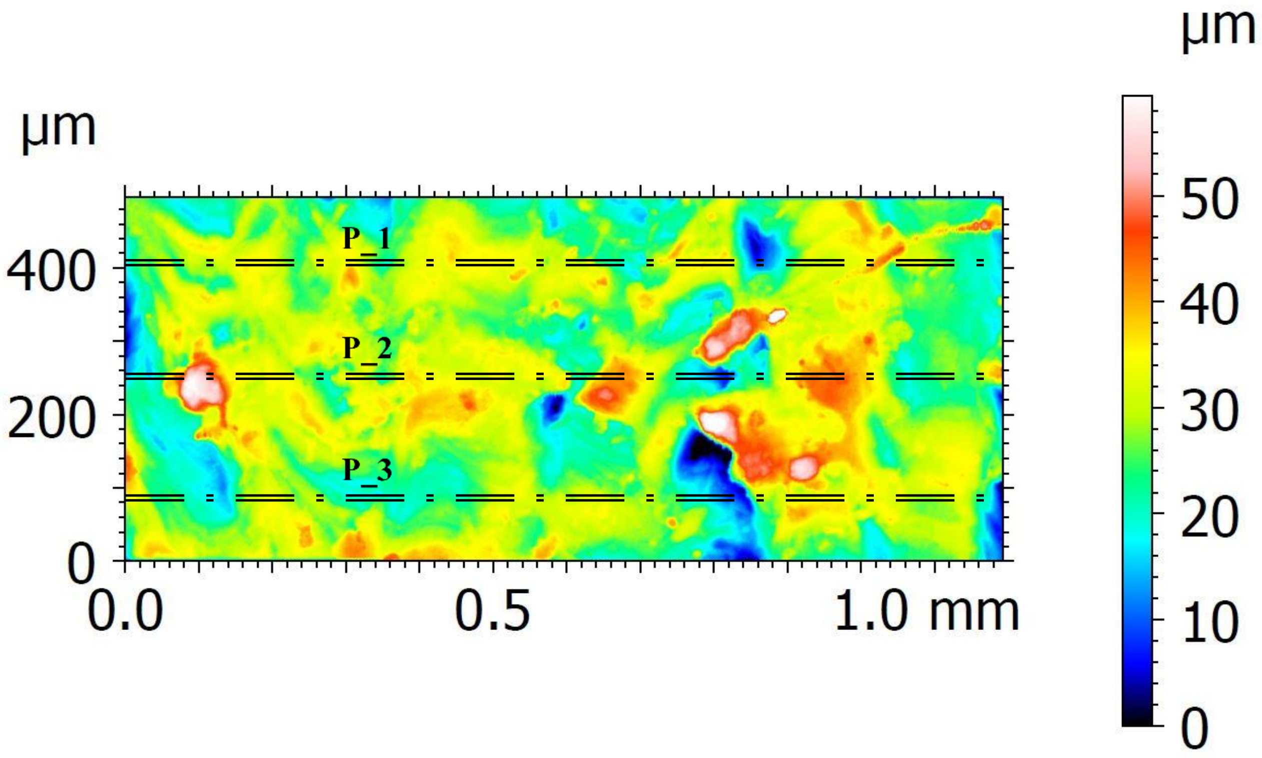

PROFILE_1:

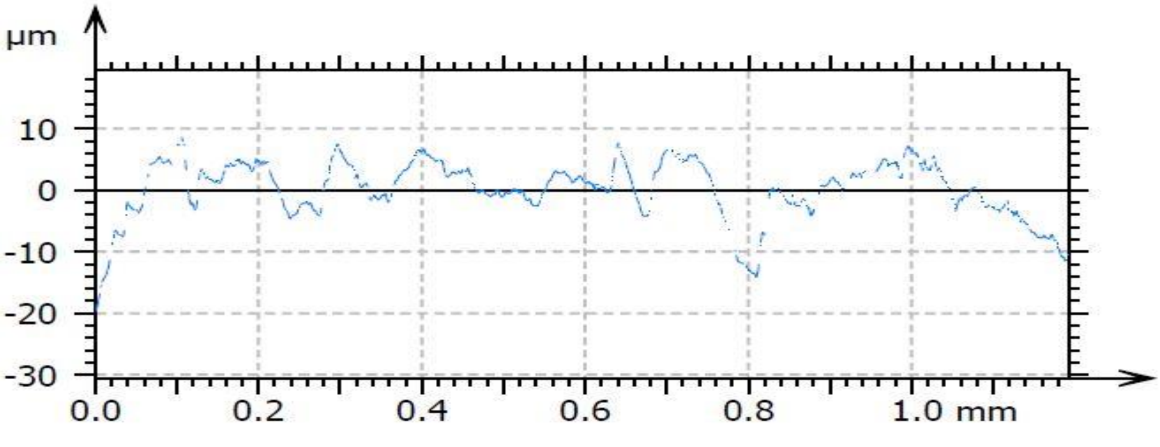

PROFILE_2:

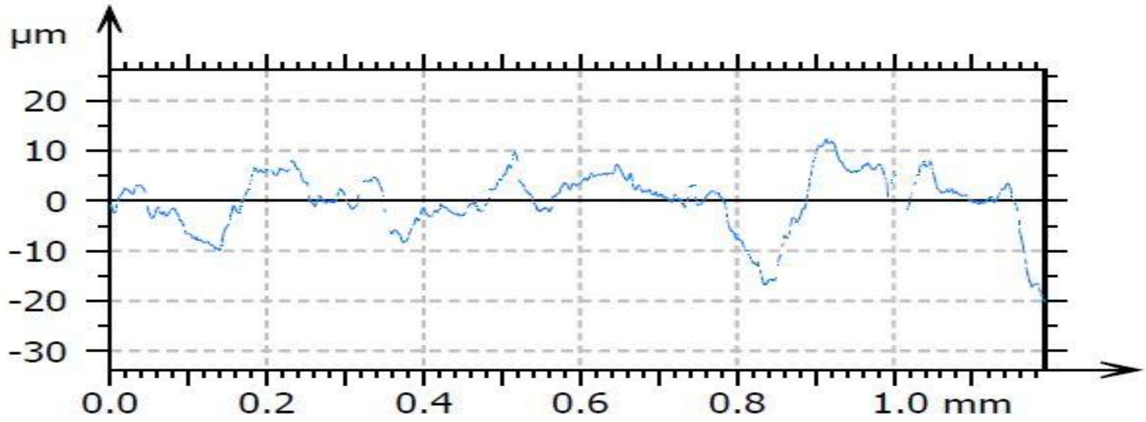

PROFILE_3:

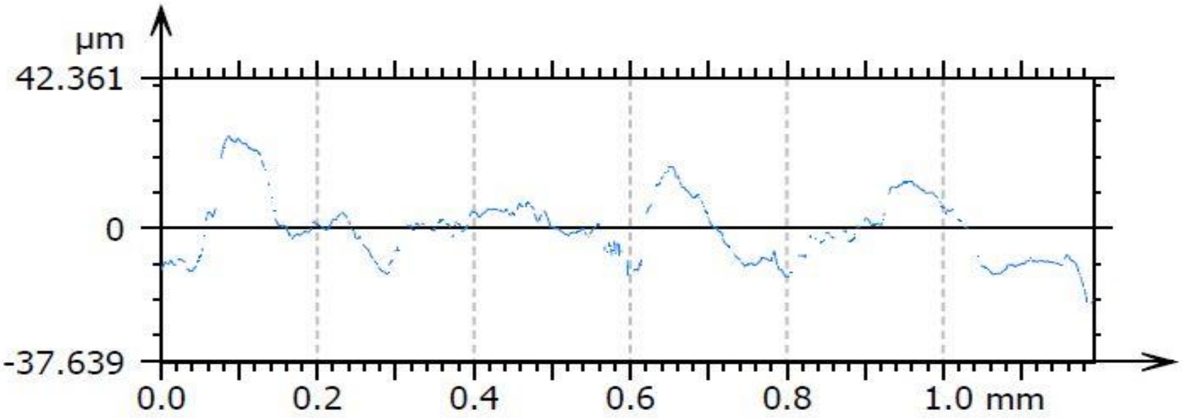

3.3: C67 – tempered steel for spring production

The spring is an elastic object, generally made of steel, used, and optimized to accumulate mechanical energy. In classical mechanics, the ideal spring is adopted for the study of the harmonic oscillator.

The microscopic physical reason why the spring accumulates potential energy is the stretching of intermolecular bonds, while its macroscopic behaviour is defined for many materials by Hooke's law; Hooke's law is the simplest constitutive relationship of elastic material behaviour, which states that the deformation that a body that an elastic body undergoes is directly proportional to the effort applied.

Starting from the utterance originally provided by Hooke, the equation expressing the elastic force exerted by a longitudinally pressed spring, in traction or compression, along an x-axis is:

$$F = -k_E \triangle l * \hat{x}$$

therefore, the force F with which the spring reacts to the stress is directly proportional to the elongation $\triangle l$. The constant k_E represents the longitudinal elastic constant of the spring, expressed in $[N*m^{-1}]$.

In a very similar way, we derive the equation that expresses the elastic moment, directed along an orthogonal $\hat{z}$-axis to the torsion plane, exerted by a tangentially solicited torsional spring:

$$M = -k_0 \triangle \alpha * \hat{z}$$

Therefore, the mechanical moment M with which the spring reacts to the stress is directly proportional to the variation of the angle $\triangle\alpha$. The constant k_0 represents the tangential elastic constant of the body, expressed in $[N*m]$.

However, today's formulation of Hooke's law uses two vector quantities, the σ voltage and the ε deformation, bound together by a tensor relationship.

In the one-dimensional case the longitudinal relation becomes:

$$\sigma = E * \epsilon \begin{cases} \epsilon = \dfrac{l_{end} - l_{start}}{l_{start}} \\ E = YoungModulus \end{cases}$$

The inverse relationship is:

$$\epsilon = C * \sigma$$

where the inverse of Young's modulus is called the longitudinal Cedevolence module $C = E^{-1}$.

The above applies within the elastic deformation limit, defined as the maximum force limit applied, within which the released elastic body returns to its dimensions prior to the application of force; beyond this limit, the atomic bonds break and reconfigure differently: the spring therefore remains deformed. In various materials this limit is not precisely defined, and deformation phenomena occur with repeated use (aging): in these case Hooke's law is not respected.

The spring, depending on its construction characteristics, can have a different behaviour, exactly as depicted in the image. This is because depending on the use the characteristics of the spring must be different. In spring watches or barbell watches, this must have a high constancy of its strength, which is achieved with a spiral spring, which for most of its intermediate compression has an almost constant force.

In other applications such as suspension, there is a linear feature thanks to helical or torsion springs, or progressive thanks to conical or cylindrical helical springs with variable pitch (progressive gradual) or cylindrical helical double pitch (progressive multi-linearity). These characteristics, in addition to being intrinsic to the spring, can be recreated or modified by means of levers or special systems. Some applications, on the other hand, require a degressive feature, such as the tightening of bolts or the tensioning of a bearing, for this reason cup springs are used that can have this characteristic, in addition to having a small footprint, but can also have an exponential, linear, degressive-exponential, degressive-constant-exponential, or degressive-regressive-exponential characteristic depending on the construction of the same, the height and thickness.

Some springs, as in the case of wave springs (or Wave Spring), have as their peculiarities the small footprint: in many cases they are used to replace helical springs.

In Figure 81 are represented some schematic load responses of different spring’s types.

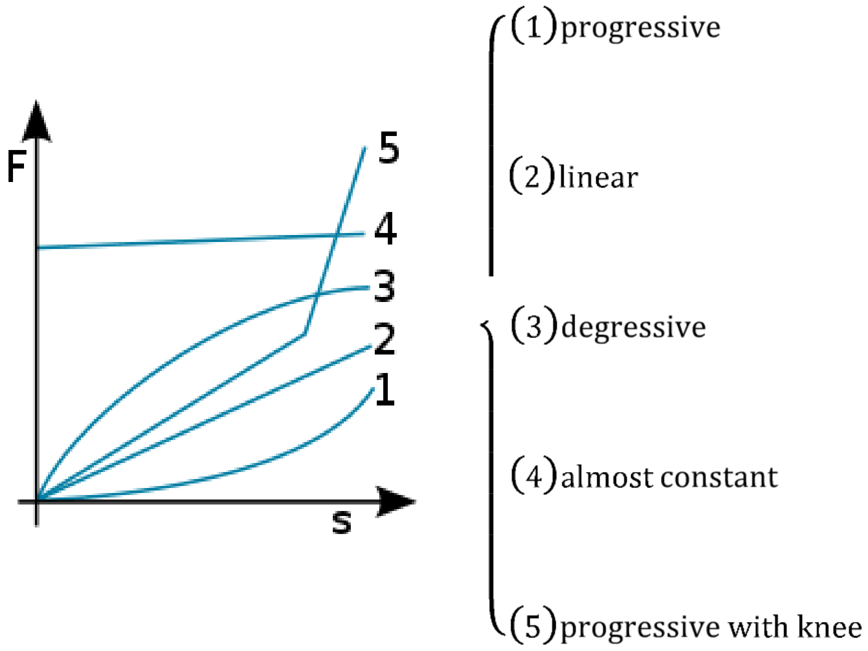

Figure 81: Load response of different spring's types

Research on non-linear springs has led, for example, to the production of air springs that show exponential behaviour. In the automotive sector from a design point of view, there are suspension springs with linear and progressive feature. With linear springs, the spring strength increases in proportion to the extent to which they are crushed. Progressive springs start with a soft characteristic curve and become stiffer as they move away from the equilibrium condition.

Depending on the specifications of the vehicle manufacturer, suspension springs are produced from constant wire (same diameter of the wire for the entire length of the spring) or non-constant wire (variable diameter with the length of the spring). This effect (dual behaviours) can also be achieved with a spring like the one shown in Figure 1 F). There are two springs in one: one soft and the other strong. The progressive mini-block springs, for example, offer high levels of driving comfort at levels of low dynamic load and low arrow, so the spring is "soft" with low vehicle load and "strong" at full load.

This study aims to evaluate and develop springs with a geometry that provides a non-linear response. The theory developed starts from the analysis of the problem seen as a series system of springs, for which the overall elastic constant is:

$$k_0 = \frac{\prod_{i=1}^{n} k_i}{\sum_j \left(\frac{\prod_{i=1}^{n} k_i}{k_j}\right)}.$$

The spring studied in this thesis is a conical and telescopic spring with variable wire section. Telescopic is the feature that allows the spring to go completely compaction. The diameter of the spring wire has a continuous section variation from the start to the end point of the spring.

The variation in the diameter of the wire allows to have a spring that at the largest diameter of the coil has the smallest diameter of the wire and, consequently, where the diameter of the coil is less the diameter of the wire is greater. In the literature there are few documents and articles on progressive springs and even less on telescopic conical progressive springs. For the proposed form, in literature, there is no reference because the original spring in its form is not producible with traditional systems. Regarding the characteristics of the machinery to produce springs, the only feasible solution to produce a variable wire section spring is to obtain a larger wire diameter at the diameter of the major coil and therefore a smaller wire diameter at the diameter of the major coil to have the need for forces for bending about constant. However, the design adopted in the spring proposed in this thesis would imply a noticeable change in force and a force for bending the smallest coil (corresponding to the largest wire diameter) too high. All this has led to the need to use innovative construction solutions (additive production) for the construction of the piece.

Regarding the articles found, they analyse the behaviour of nonlinear springs or springs for which the trend of the force curve as a function of displacement is not linear. These springs are also called progressive springs and are of different types as it is possible to obtain a non-linear function through various designs. In particular, the most used are construction solutions of the type: conical springs, double conical or barrel springs, springs with a variable pitch and springs with variable wire diameter, although the latter solution, due to construction difficulties is rarely used.

The articles that analyse the behaviour of progressive springs are mainly based on how to determine the nonlinear behaviour of the spring from a mathematical point of view through algorithms or FEM analysis. In the 1970s a particular push to find innovative patent solutions was provided to solve problems of elastic response.

A variable circular section helical spring with hyper-elastic behaviour has been produced. To determine the functionality tests and the F=F(x) relationship a series of compression tests were performed. The starting point for which it was decided to experiment on this spring is very intuitive: the characteristic of the progressive spring R increases with the increase in the diameter of the section; therefore, a performance tending towards an exponential model, as for example in air springs, is obtained by increasing the diameter of the wire as the diameter of the coil decreases. The combined effect of wire coil-diameter for traditional conical progressive springs on the value of R is less sensitive, as can be seen from the formula below.

As mentioned above to determine feature tests and the F=F(x) relationship, a series of compression tests were performed on an INSTRON 5567 30 kN machine using a 1 kN load cell. Tests of the loading and unloading cycle were carried out progressively increasing the stroke this involved a sequential loading of the various coils according to the following mode: in the first stroke the first coil was loaded and discharged, in the second stroke the first and second coils were loaded; the process was repeated until all coils were compressed until the entire spring was compacted. The tests were carried out with a crossbar movement speed of 10 mm/min.

The results obtained from the various tests are perfectly repeatable for the running part that reproduces the behaviour of the single coil. In other words, in the compaction test the curve F=F(x) involves a path that subsequently engages the individual coils: the stroke that affects for example the coils "1" corresponds exactly to the reduced stroke used in the first test.

It should be noted that the curve never has singular points or discontinuity points, the curve F=F(x) is continuous throughout the useful stroke and this is attributable to the continuous change in diameter throughout the extension of the spring.

Figure 82 shows the geometric characteristics of the coil radius and wire diameter as the angle of development of the propeller changes. The spring was made of AISI 316L Stainless Steel.

Figure 82: geometric characteristics of the printed spring

n	A_a [mm^2]	A_b [mm^2]	a [mm]	b [mm]
1	26.06	28.27	2.88	3
2	23.24	24.81	2.72	2.81
3	15.90	22.40	2.25	2.67
4	15.62	17.50	2.23	2.36
5	11.70	13.59	1.93	2.08

n	R_a [mm]	R_b [mm]
1	15.88	12.68
2	22.42	19.19
3	28.86	25.43
4	35.33	31.93
5	39.83	38.4

Below in Figure 83 is reported the trend of the Force vs Displacement curve for the proposed spring. Two different speed were performed of the crosshead to verify possible differences about the answer of the spring under a different working load speed. As reported graphically it is not a substantial variation.

The first stroke is approximated as a linear trend but as crushing progresses the behaviour changes radically. Figure 84 shows the spring made in AISI 304 for powder bed fusion, in its first version of the survey.

Figure 83: trend of Force vs Displacement with two crosshead speeds

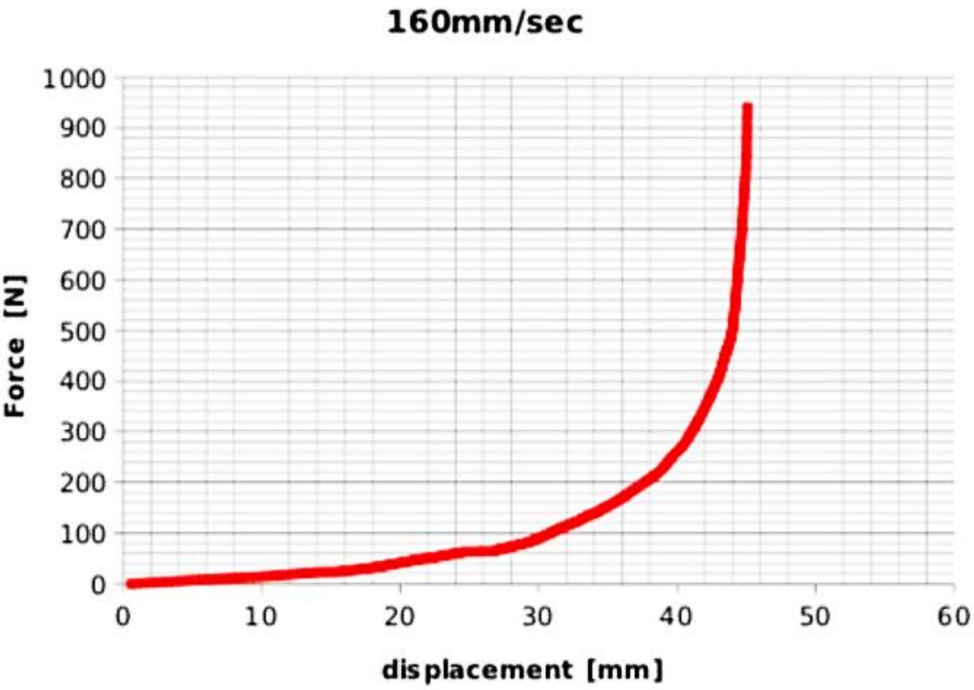

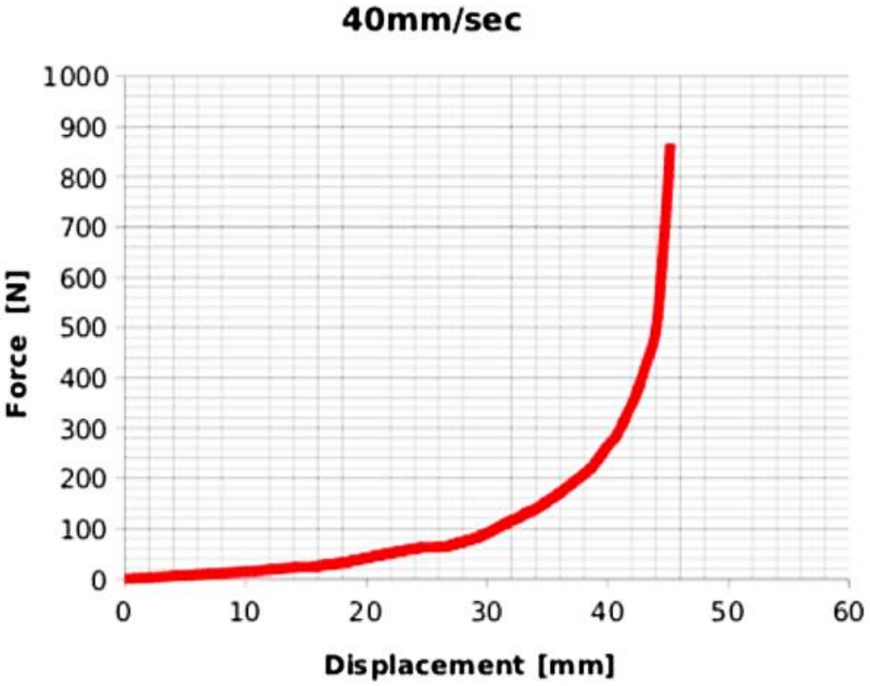

Figure 84: printed spring

Steel suitable to produce springs or more generally suitable to produce bodies capable of stretching if a certain force is applied to it, and then return to its natural shape, is generally high-performance steel, stainless steel or 17-7PH or X7CrNiAl, suitable for flat springs with a complex shape.

The thermal processes shown in Figure 85 where the component undergoes to obtain the required elastic characteristic is a remediation cycle, which includes respectively a hardening phase with subsequent tempering cycle. The aim of the quenching is to obtain the martensite structure, the hardest constituent of steel.

Figure 85: quenching and tempering cycles

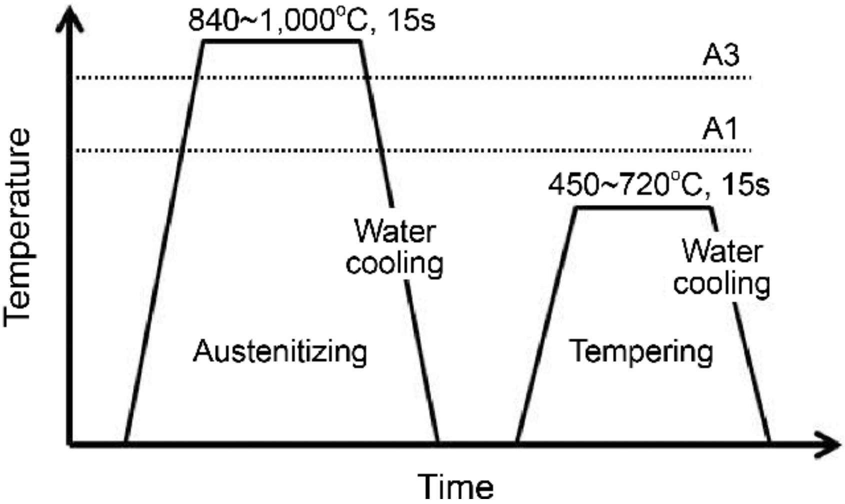

Martensite is also the most fragile constituent, which is why tempering must always be followed by a tempering phase, designed to hold the hardened component from the tensions induced for the microstructural transformation that has just taken place.

As far as quenching is concerned, two basic conditions must best be met:

1. have a complete austenitic phase conversion, to ensure homogeneity of temperature throughout the section of the treated component
2. have a cooling fast enough to exceed the "critical processing speed" of each steel.

There are different means of quenching, which are chosen based on the steel being treated, the geometry of the component, the characteristics required by the designer.

Such means can be water, polymeric aqueous solutions, oil, fused salts, pressure gas (nitrogen, helium, argon), air.

Tempering is that heat treatment carried out at a temperature below the processing point A1 (500÷680 °C) designed to hold the newly hardened material, the structure of which tends to consist of martensite, and to give it the mechanical characteristics defined at the design stage. The post-hardening temper turns martensite into an aggregate called sorbite which is the structure with the best hardness – toughness compromise.

Figure 86: martensite formation after quenching and tempering.

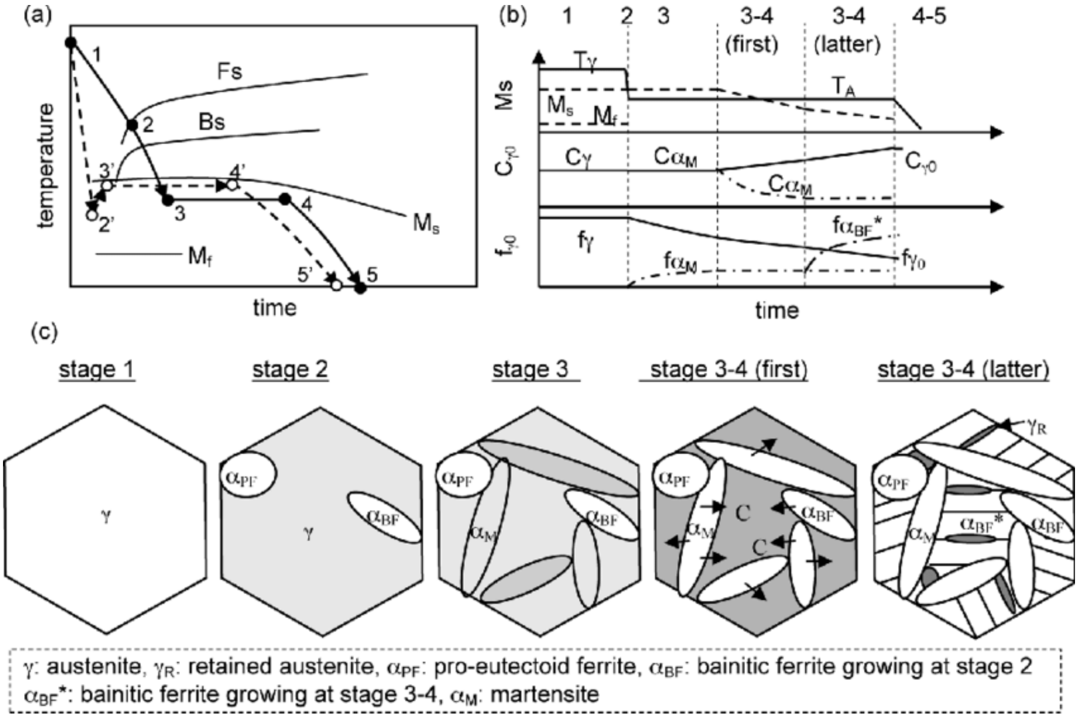

The hardness value of martensite drops as the tempering temperature increases. Tempering can be followed by slow cooling (oven or air) or fast cooling (water or oil); rapid cooling is recommended for steels to the Mn, Ni, Cr to avoid fragility from tempering (see Figure 86).

Some steels, such as hot and cold tool steels, require multiple tempering – interspersed with slow cooling to room temperature – to better develop secondary hardening, transform any residual austenite, ensure complete microstructural and geometric stability.

The development of process parameters for additive construction LASER Powder Bed Fusion begins with particle size analysis of virgin powder and a semi-quantitative analysis of the elements that make it up. Through a scanning microscope equipped with an EDS probe it is possible to determine the chemical composition of the powder to compare the composition of the powder with the chemical composition of a reference sample.

As can be seen in Figure 4, dust has many satellites which often affect sphericity. This situation may involve risks on the regularity of the distribution of the layers and therefore on the dimensional tolerance. By way of comparison, Figure 5 shows the morphology of the AISI 316L powder used in point 1.

Figure 87: powder's comparison between C67 and AISI 316L

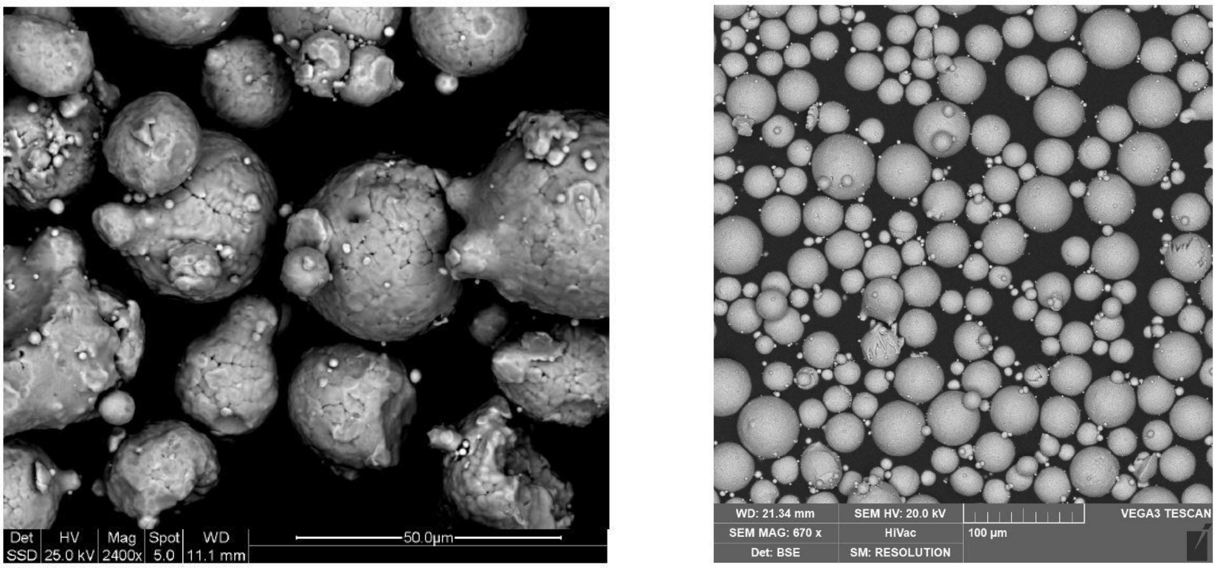

To optimize the production process and then set a correct up-skin and down-skin policy, thus minimizing roughness, 5 different positioning conditions of the element to be produced were evaluated. At the same time there are cubes to be used for measuring the actual density of the material (expected around 99,4 - 99,8 %). Figure 87, which shows the springs made of 316L material, allow you to appreciate the different roughness values obtainable according to the orientation: this preliminary analysis is essential and preparatory to the launch of the actual realization phase to be carried out with definitive material, whose process parameters are still to be optimized.

The initial choice behind the design of experiment was to start from the process data for AISI 316L. However, evaluated the surface defects and characteristics of the samples produced for v=1600 mm/s and v=1800 mm/s for powers of 170, 190 and 210 W, it was decided to move at speeds of an order of magnitude lower by increasing production time by almost twice as much.

In the literature, data on non-bound steels indicate that as the carbon content increases, the specific power required to melt steel particles decreases (due to the increased fluidity of the spindle).

However, these data indicate a considerably higher energy density than stainless steel. The data of the tests carried out confirm these observations, so that future development will proceed in the direction of the increase in specific energy.

This is contrary to the normal way of feeling in traditional processes of carbon steels compared to stainless steel that "kneads" in mu processing, in PBF the opposite happens, carbon steel has a much more complex behaviour than 316L. The literature shows that the optimum conditions for LASER irradiation of high-density carbon steel depend on the carbon content in steel dusts. The energy required for full densification decreases as the carbon content increases. This is due to the increased wettability of the FeC alloys fuse due to the higher carbon content. The residual microhardness and tension values for fully dense samples tend to increase as the carbon content in steel dust increases.

Interestingly, however, when a mixture of iron powders and graphite is used, the density of parts obtained for PBF Powder Bed Fusion increases as the carbon content increases This suggests that if the energy imposed during the process is high enough, full densification is more easily achieved as the carbon content increases. However, the data in the literature do not consider the smoothness of the dust and its characteristics.

Since the density trend is not linear with power and speed, it is preferred to express it in fiction of surface power density. Figure 88 shows this trend and, except for the sample obtained for 21 J/mm^2, there is a tendency to increase the density of the material as the energy density increases. However, this asymptotic trend is sometimes reversed suddenly because of some specific phenomena.

The experimentation will continue to obtain maximum density before the occurrence of these phenomena and then will focus on optimizing the transition from the skin to the massive part (in-filler).

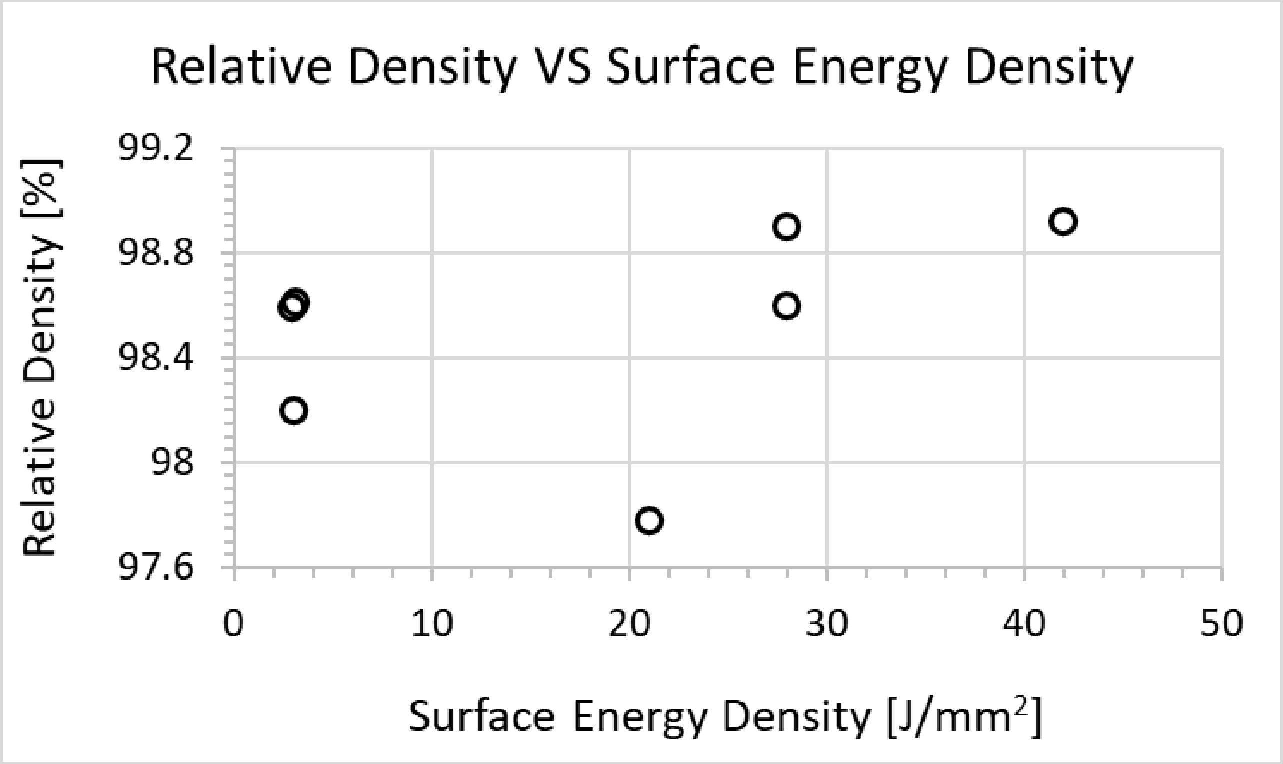

Figure 88: Material Development of C67

To validate the structure of the material, two separate samples were provided: one to a private laboratory and another to the Laboratory of Mechanical Technology and Processing Systems of the "Enzo Ferrari" Engineering Department of the University of Modena and Reggio Emilia (which coordinates a Research contract on additive construction with the company). The two laboratories came to the same conclusion.

The process parameters used for the construction of the cube and specimens for tensile tests are:

- power of the LASER 190 W and scanning speed 150 mm/s.
- Hatching space is 0,14 mm.

The cube, in both cases, has been dissected. The outer surface and that of the section facing the heart of the specimen were then prepared metallographically and attached with Nital 2% then observed both under an optical microscope and at SEM. A dissected sample is shown in Figure 89.

Figure 89: dissected sample

Figure 90 shows some images of the microstructure in a central and internal position, while Figure 91 shows an area near the edge.

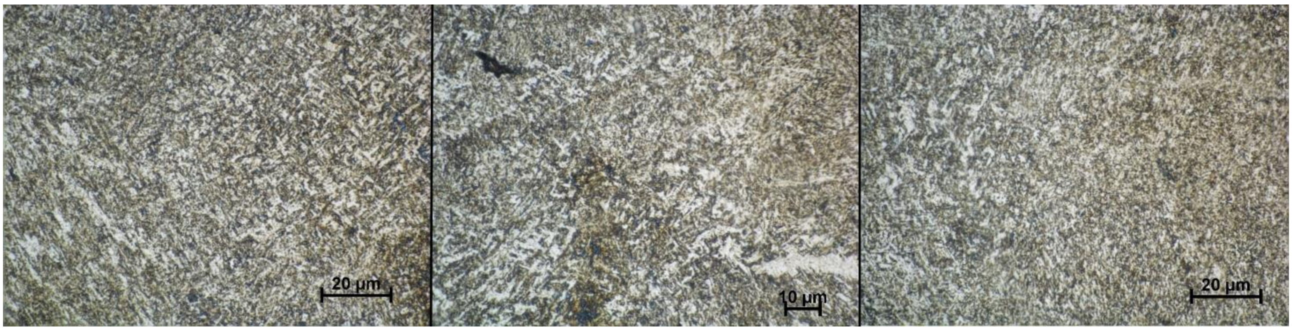

Figure 90: microstructure images captured with an optical microscope in central position of the specimen.

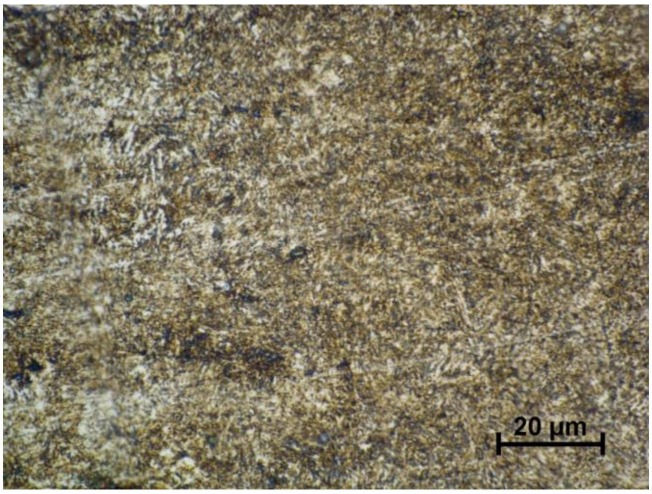

Figure 91: image near the border of the specimen.

Figure 92 shows porosity present for a density of 99%. This value is physiological and considerably lower than that of a component obtained by fusion. The 99% value, however, corresponds to what is identified, according to international literature as full density.

Figure 92: image of residual porosity

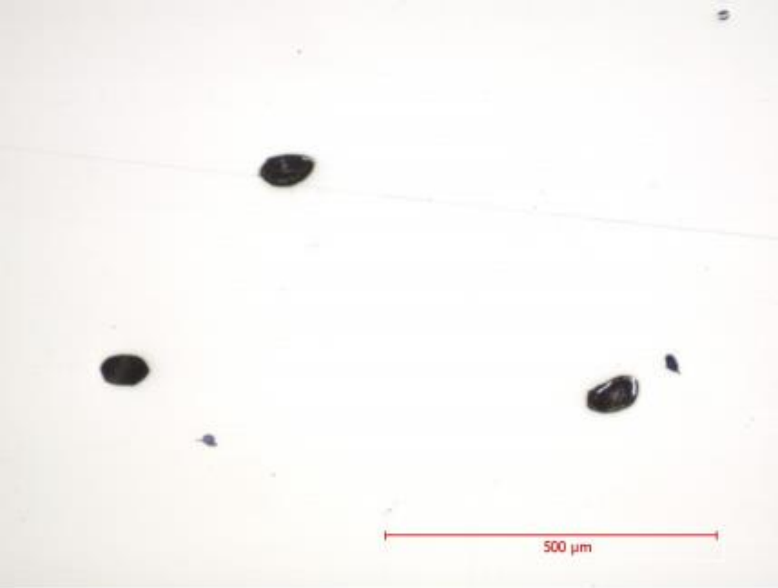

Figure 93 shows the image obtained at the Scanning Electron Microscope (SEM) of the inner section of the sample, which should be compared with Figure 94 which shows the image of a microstructure found in literature and obtained in the same way for an ASM 1070 steel equivalent to C67. From the images one can appreciate the analogy of the structures of which one is obtained by additive construction the other by a traditional process of normalization treatment.

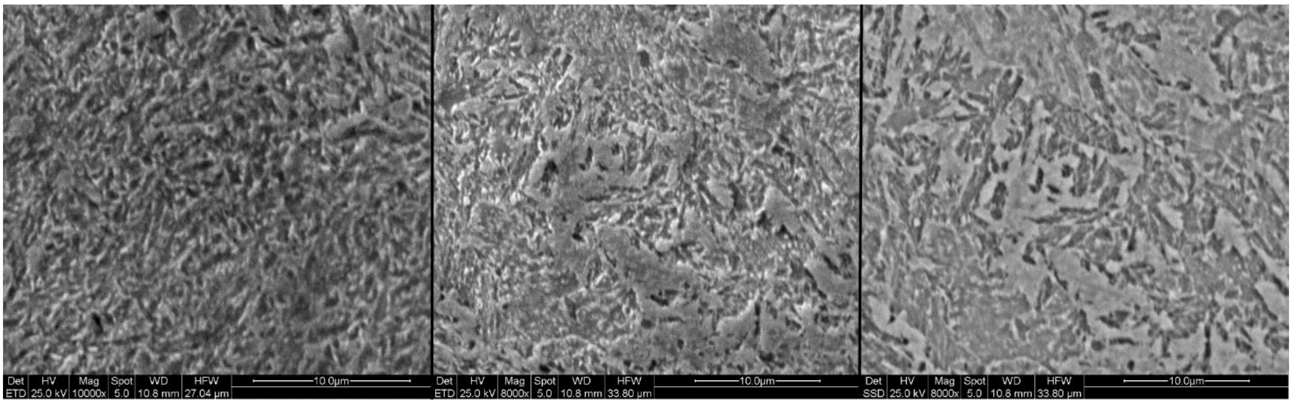

Figure 93: SEM image took on the centre surface of a C67 sample.

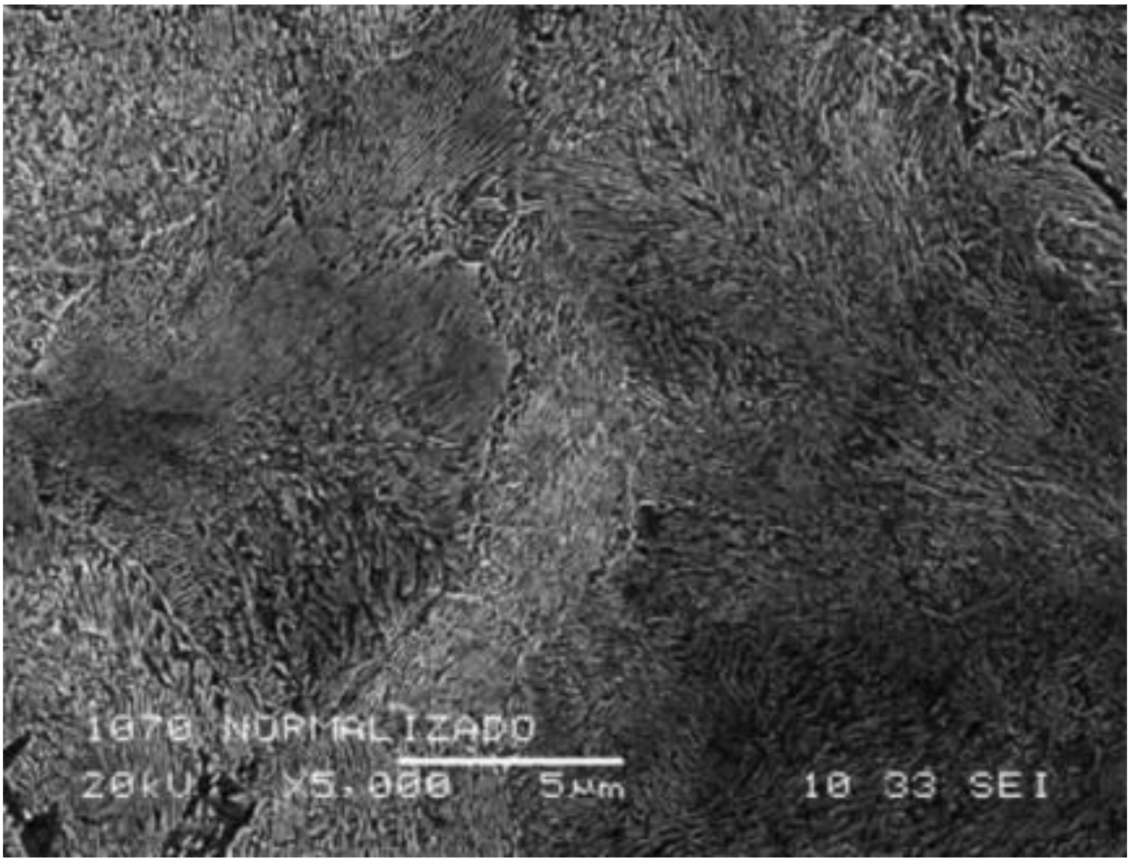

Figure 94: surface micro-structure of a normalized ANSI 1070 steel. [49]

Subsequently, tensile test specimens built along the Z-direction were produced to determine the mechanical properties of the material. The disposition of the samples on the building platform is shown in Figure 95 b):

Figure 95: figure (a) represent the geometry and figure (b) is a screenshot of the parts disposition on the building plate.

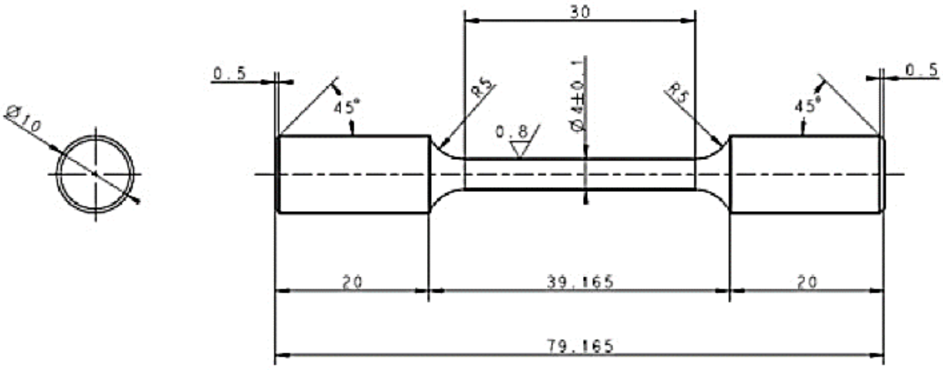

(a)

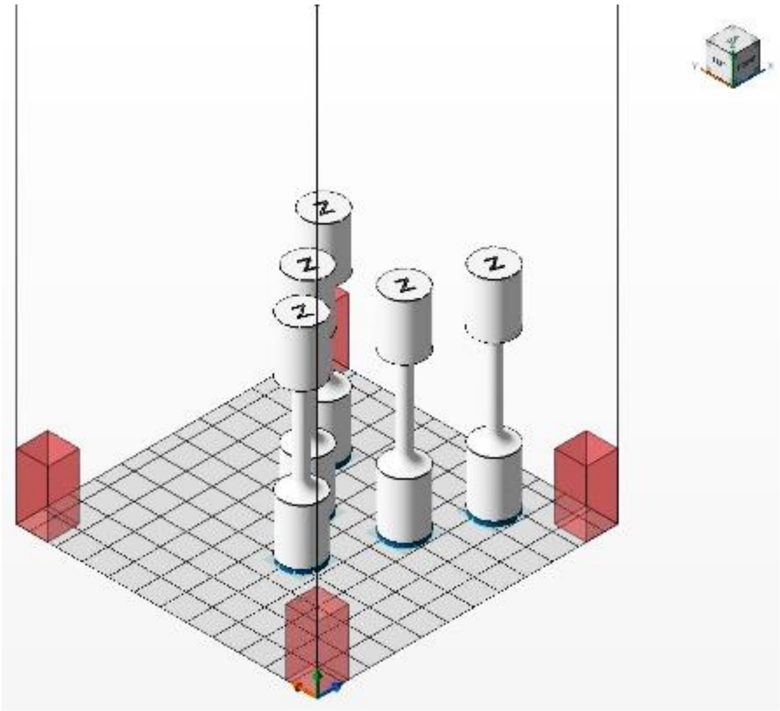

(b)

The tensile tests were carried out on the machine INSTRO 5567, using a crossbar displacement speed of 0.5 mm/min with elastic stretch strain rate of 2.5*10-4 ± 5*10-5 s^{-1} and an active extensometer over useful length of 25 mm (UNI EN ISO 6892-1). The results are reported in Figure 93.

The samples named with the ‘As_x’ index are the samples ‘As Built’, so called because the samples did not receive any kind of surface after treatment. The samples called with the ‘HT_x’ index are the samples with a Heat Treatment. For this material we used the same heat treatment as a conventional component produced with an ANSI 1070 steel. The heat treatment is composed from quenching and tempering cycles.

Given the excellent results achieved with the as-built specimens, it was decided to proceed with the heat treatment cycles that the company normally provides for its components. The thermal cycles are hardened according to UNI ISO 1099:2002 regulations and after quenching a tempering cycle is carried out (see Figure 96).

Figure 96: values of Hardness Test on C67.

Hardness test – required values			
Type of Scale	n. pieces	From	To
Rockwell C	**-**	**43,00**	**47,00**
Hardness test – measured values			
Type of Scale	n. pieces	From	To
Rockwell C	**3**	**46,00**	**47,00**
▨			
Heat treatments			
1. QUENCHING UNI ISO 1099:2002 **2.** TEMPERING			

As with brass alloy, C67 steel has also assessed the surface roughness that the additive manufacturing process generates on the product component. In this first phase, given the functionality of the component, it was not necessary to search for optimized upskin and downskin parameters, which will still be the topic of research scheduled at a future stage.

LATERAL SURFACE MAP:

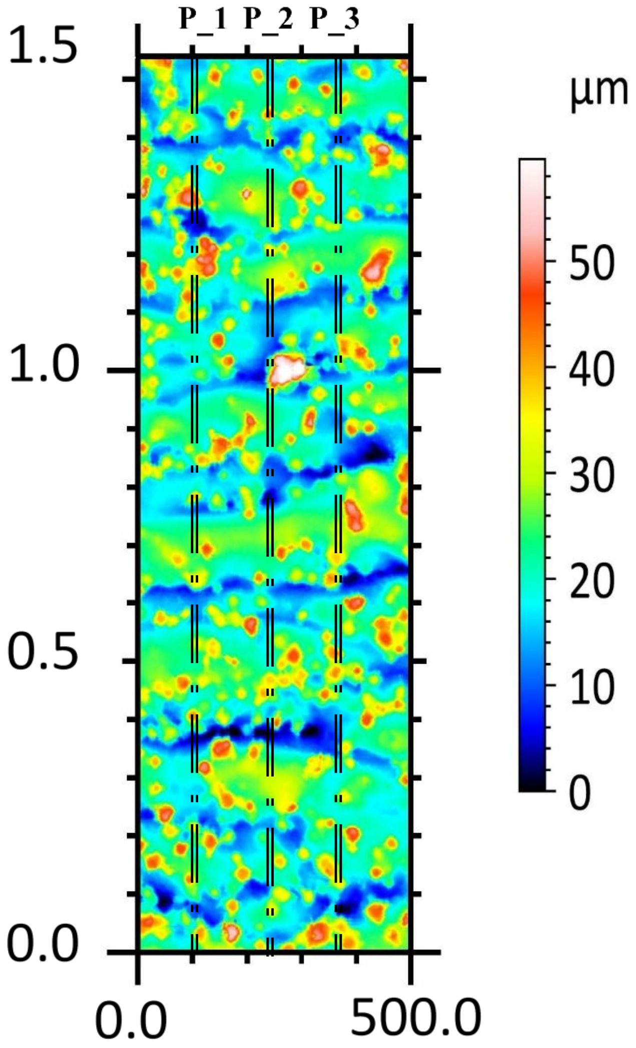

PROFILE_1:

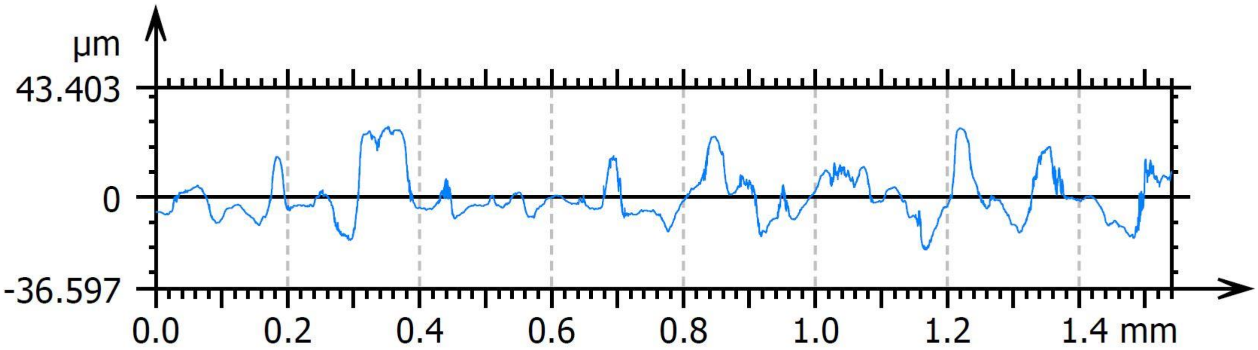

PROFILE_2:

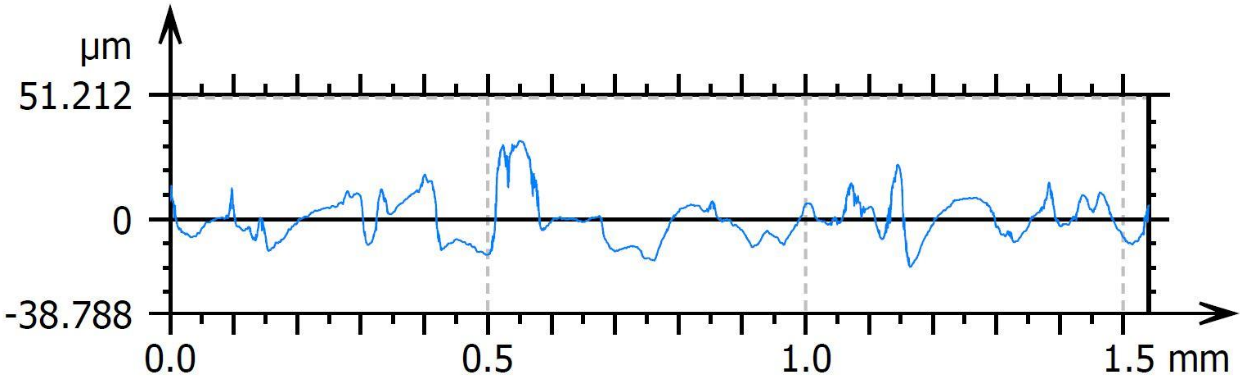

PROFILE_3:

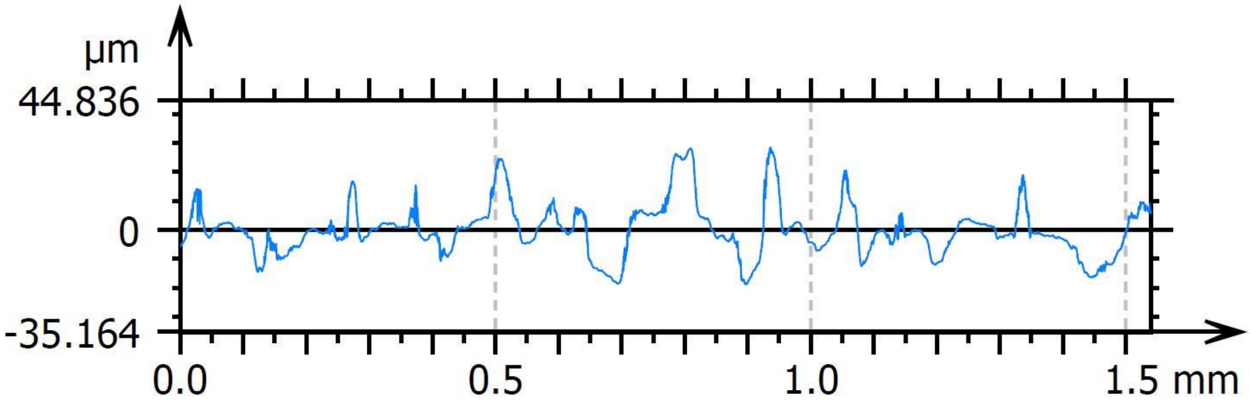

4: Results and Data analysis

In this chapter, the numerical values derived from the experimental tests are reported and discussed. Starting from the measurements of the relative volumetric densities, obtained through the Archimedes method, it is evident that the specimen one grows in agreement with the value growth of the surface energy density (Figure 97), however the values for which the maximum density is obtained differ slightly. Using the optical microscope measurement method, the maximum density value (99.9%) is obtained for surface energy density of 13.9 and 22.5 J/mm^2: de facto a full density value. When the Archimedes method is used the maximum (99.2%) is obtained for a surface energy density of 31.7.5 J/mm^2 even if value of 99% are obtained at the 13.9 and 22.5 J/mm^2. The density value obtained by L-PBF technique is higher than that reported in literature [50] as maximum value for Al alloy component produced by pressure dies casting process minimum shrinkage porosity 1.6725%. Using industrial criterion for the acceptance of aluminum alloy structural component, it is evident that a very low porosity component is equated to a full density component. NCAP (Nissan Casting Australian Plant) classifies the porosity at a given location into four grades according to its severity [51]:

- grade 1 denotes nil or little porosity,
- grade 2 denotes some porosity,
- grade 3 indicates considerable or just acceptable porosity,
- grade 4 evidence not acceptable porosity.

If analogously to the casting process the relationship between fatigue life and porosity is considered, the acceptance criteria as well as the fatigue life limit to the casting defects is established. Some authors indicate as 4% the porosity fraction to be considered as a mean value [51]. Therefore, the CuZn42 component produced by L-PBF can reach stricter limits of porosity than those indicated in the acceptance criteria of components obtained by melting processes.

Figures 4 demonstrates that, despite the high reflectance of Cu alloys, several sets of parameters result into a material density exceeding 99%.

However, if the energy density is increased further, the material density decreases, which is consistent with the trend observed by Yang et al. for silicon brass [42].

It must be noted that the differences between the density measurement methods are not due to the data scattering but depend on the process parameters used. Figure 5 and 6 show the absolute value of the difference between the density evaluated by optical microscope and Archimedes method. The difference increases when the scanning speed increases (Figure 98) while decreases in accordance with the decrease of surface energy density (Figure 99).

Figure 97: Both density measurement methods used evidence that the specimen density grows in agreement with the value growth of the surface energy density.

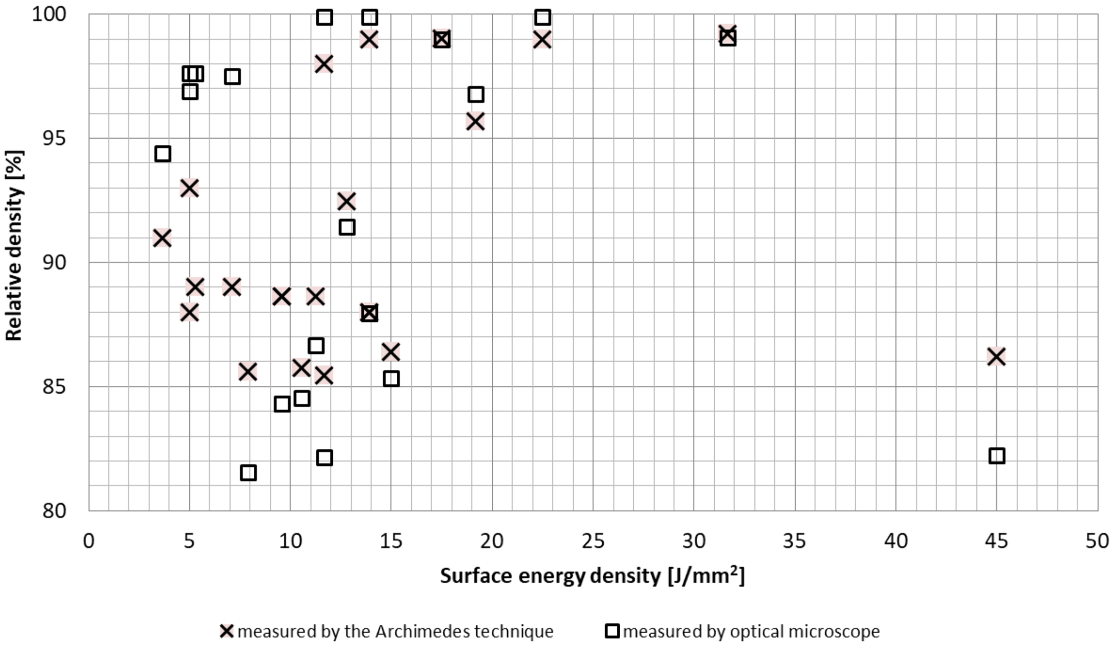

Figure 98 can be explained based on the following assertion:

1) the observed section is a plane parallel to the specimen growth direction,
2) if the defect is anisotropic and has an elongated shape in a direction lying on the XY plane, the section on the plane parallel to the Z axis will return a smaller pore than that observed with a section perpendicular to the Z axis,
3) The Rayleigh instability grows with the scanning speed. The melted pool may be approximated by a melted cylinder and when the cutting speed increases the length of the cylinder increases. It is subject to cooling stress and can break up into tiny droplets.

Therefore, the density measurement by optical microscope can underestimate the anisotropic shape porosity i.e., overestimate the density. Under these conditions, the difference between density measured on a section parallel to direction growth by means of the optical microscope and density measured with Archimedes' method can be used as an indicator of the onset of Rayleigh instability.

Figure 98 allows to affirm that the scanning speed=800 mm/s is the limit beyond that the instability may arise and it is evident at a scanning speed of 1000 mm/s. Zhenga et al [52] indicate that a AISI 304 LASER track (machined by L-PBF) became instable at the same value.

The difference between the density values measured using the two methods decreases when the surface energy increases until the maximum value used. Figure 100 shows the section of the specimens with a density of 92.5%. The hardness value shows a linear dependence with the relative density value (Figure 101).

Figure 98: Difference of density percentage value evaluated by OM method and Archimedes one VS scanning speed. The line indicates the zone where the difference may be due to the Rayleigh instability.

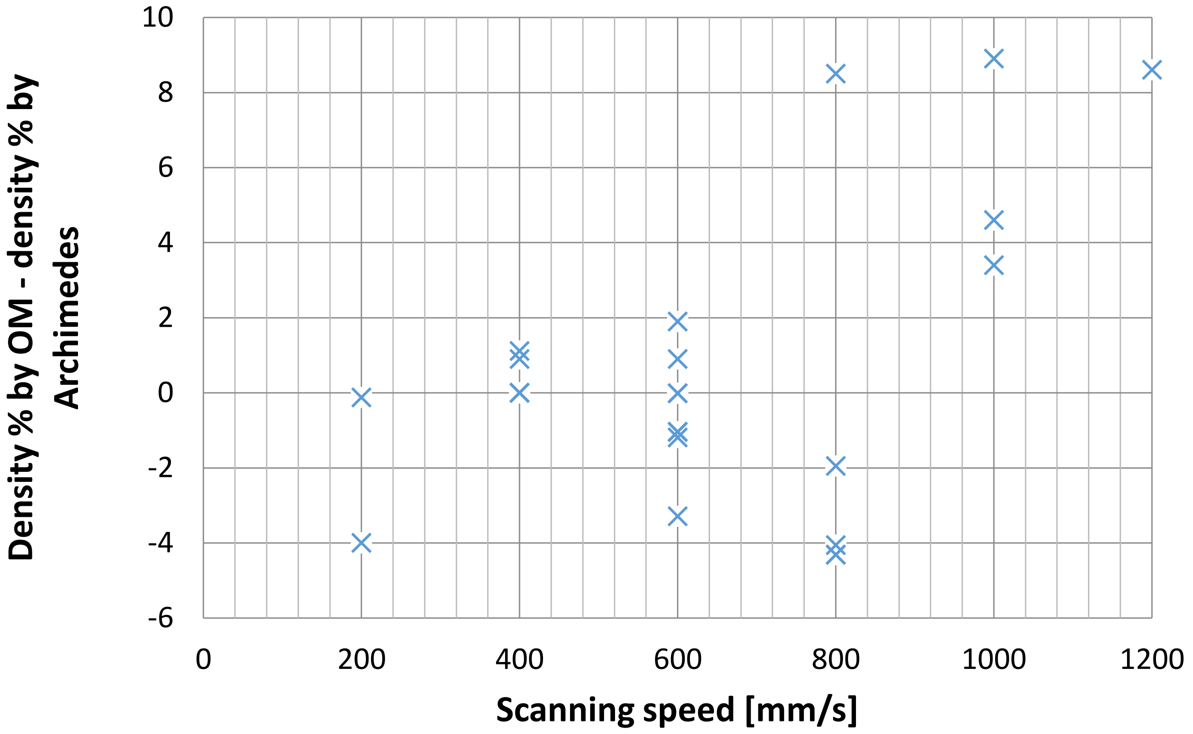

Figure 99: Difference of density percentage value evaluated by OM method and Archimedes one VS surface energy density.

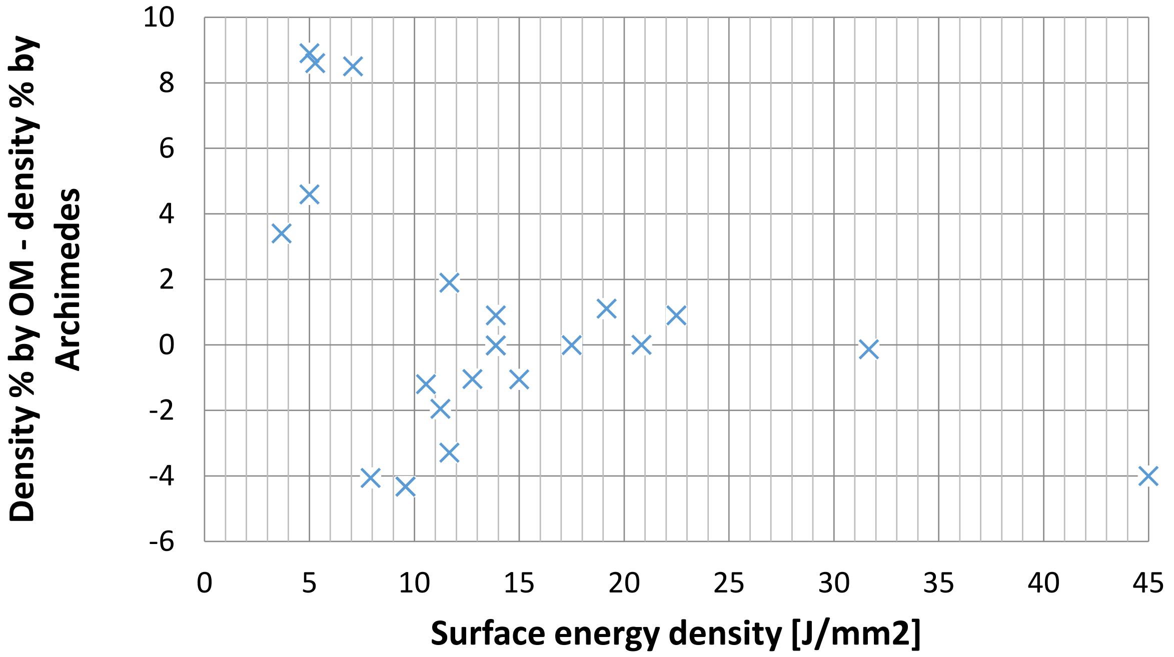

Figure 100: Specimen obtained using the following process parameters: P=230 W, v= 600 mm/s.

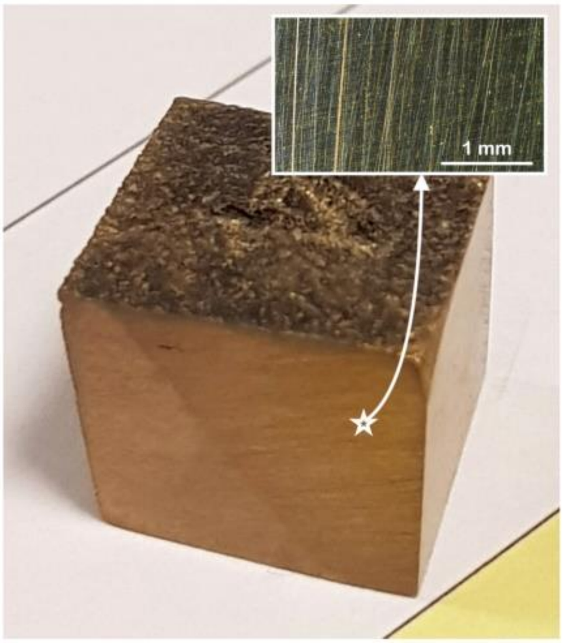

Figure 101: The hardness value shows a linear dependence with the relative density value.

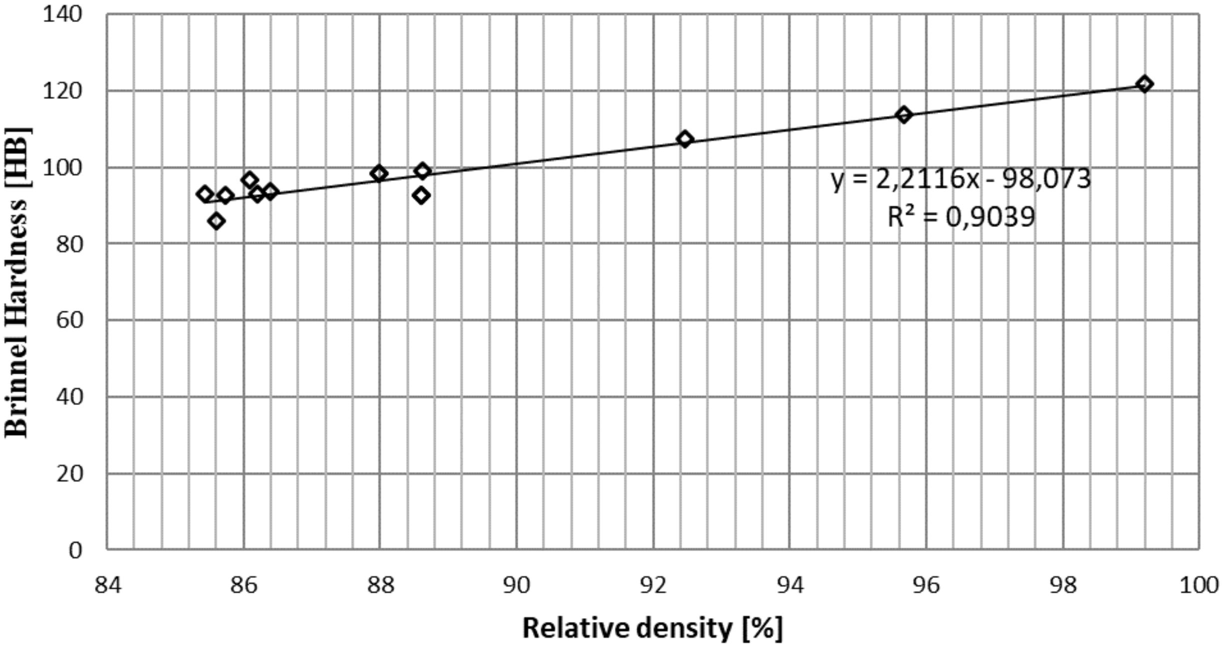

One of the aspects required during validation is the evaluation of surface quality obtained through LASER Powder Bed Fusion technology. As reported in numerous mechanical technology articles and manuals, LASER Based additive manufacturing technology produces surfaces with a linear roughness in a range between 10 µm and 30 µm. [53], [54]

This range, however, is strongly dependent on the value of the thickness layer that is used to build the component but also on the particle size of the starting powder with which you want to print. In our case, for both brass and C67, particle size is smaller than that normally used by other industries for the same technology (20-30 µm versus 50 µm), as a result you have the possibility of obtaining lower roughness. [14], [17], [18], [55]

Table 3 and Table 4 show the values of some linear roughness profiles, respectively. It can be seen that thanks to a considered choice of printing parameters for the upskin surface it has been possible to reduce roughness by 53,3%, from a value of 6 µm to a value of 2,8 µm.

Table 4: values of the roughness measured on lateral surface.

LATERAL ROUGHNESS – ISO 4287 [µm]							
PROFILE	R_a	R_q	R_c	R_z	R_t	R_p	R_v
P_1	6.2	7.0	23.7	22.9	39.3	8.9	14.0
P_2	6.0	7.4	16.7	29.0	49.4	11.3	17.7
P_3	5.6	6.8	15.5	26.2	42.8	11.7	14.5
AVERAGE	**6.0**	**7.1**	**18.6**	**26.0**	**43.8**	**10.6**	**15.4**
STD. DEV.	**0.3**	**0.3**	**4.4**	**3.1**	**5.1**	**1.5**	**2.0**

Table 5: values of the roughness measured on up-skin surface.

UPSKIN ROUGHNESS – ISO 4287 [µm]							
PROFILE	R_a	R_q	R_c	R_z	R_t	R_p	R_v
P_1	2.41	3.04	6.99	11.5	16.4	5.43	6.05
P_2	2.57	3.34	7.61	14.1	19.8	.6.03	8.1
P_3	3.55	4.68	9.75	19.3	26	9.34	9.98
AVERAGE	**2.8**	**3.7**	**8.1**	**15.0**	**20.7**	**4.9**	**8.0**
STD. DEV.	**0.6**	**0.9**	**1.4**	**4.0**	**4.9**	**4.7**	**2.0**

Regarding C67 reclaimed steel (AISI 1070), Figure 102 gives the forecast curve for the experimental plan to determine the surface energy density value which allows a relative density greater than 99,5% to be guaranteed. it can also be noted that the non-asymptotic trend of the forecast curve does not respect the simple concept that the higher the energy density provided to the process, the higher the relative density value of the product component. This fact is widely discussed and analysed in the literature and almost certainly the relative drop in density is attributed to the key-hole effect [47] that the dust bed undergoes if the LASER beam that impacts on it has a concentration of energy greater than the energy that the material to be melted can absorb.

Also, in Figure 102 it is noted that for an around 20-30 J/mm^2 the number of tests with the highest relative density value is relevant, an indication that this energy density range is the most correct.

Figure 102: C67 material development with the trend line

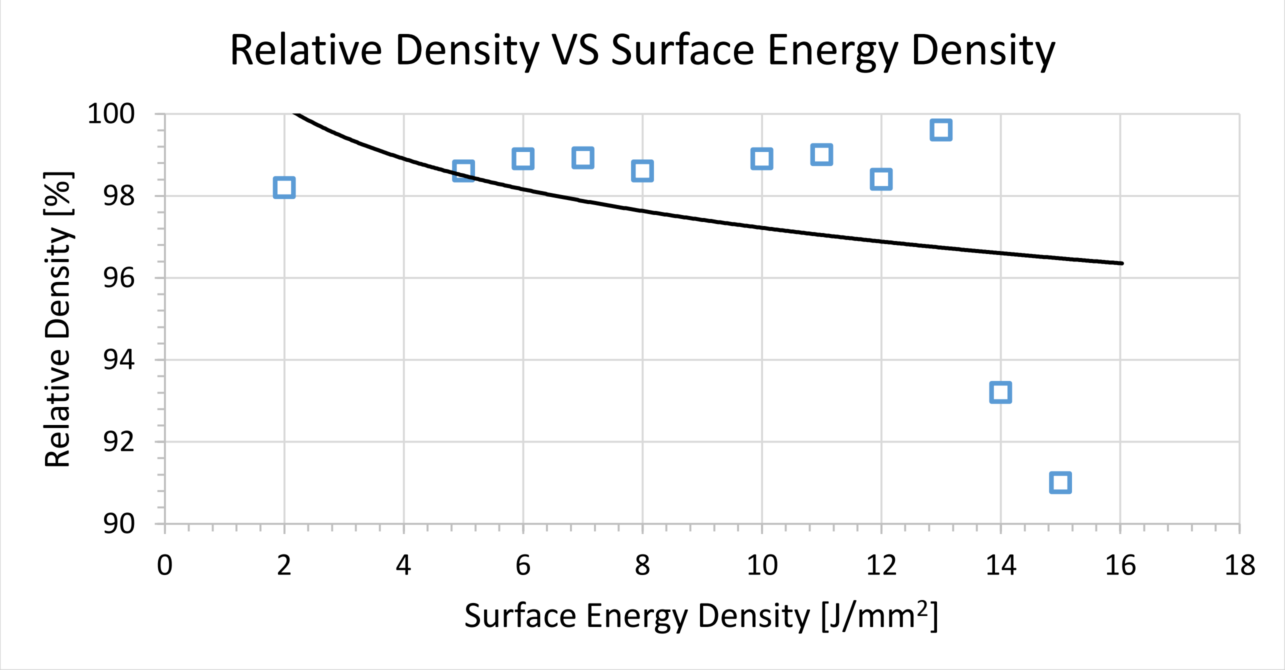

Looking instead at the process from the thermal point of view and the formation of some mineral elements we can say that, given the proximity of the TTT and CCT curve of the C67 (ASM 1070) to the eutettoid (where the two noses of the curve disappear into one) it can be said that the cooling curve intercepts the transformation start curve but does not complete it (CCT curve in Figure 103). The structure appears to be a bainitic structure. In continuous cooling, the cooling rate to form bainite is greater than that required for perlite, but lower than for martensite, for steels with the same composition. Since the LASER melts up to 5-6 layers and the ultimate melting, which determines the structure of the material is surrounded by a hot zone. Therefore, a cooling curve is conceivable which progressively decreases its slope or a dT/dt which decreases as t increases.

Figure 104 shows the outer surface of a second sample and Figure 105 shows its internal structure.

In conclusion, it can be said that:

- the structural difference between the outer surface and the heart of the sample is not substantial. However, the outer surface has a finer structure indication of a higher cooling rate:
- the structure is bainitic with troostites zones.

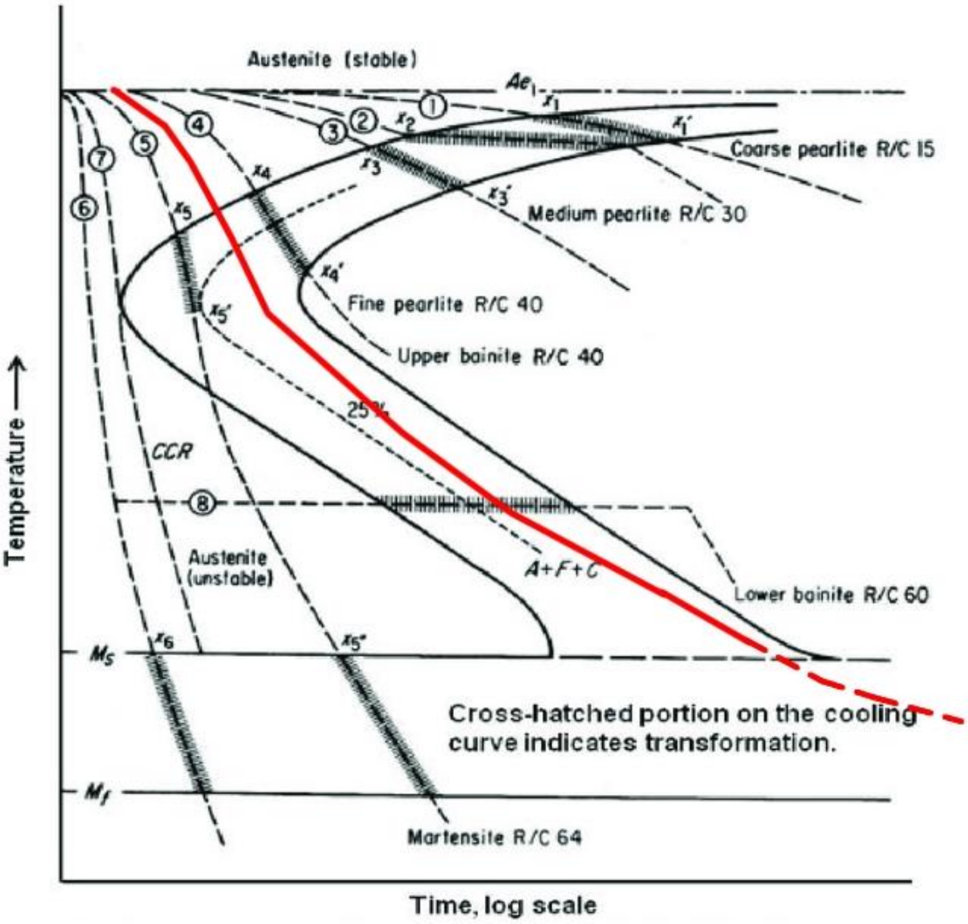

Figure 103: TTT curve for ANSI 1070 steel

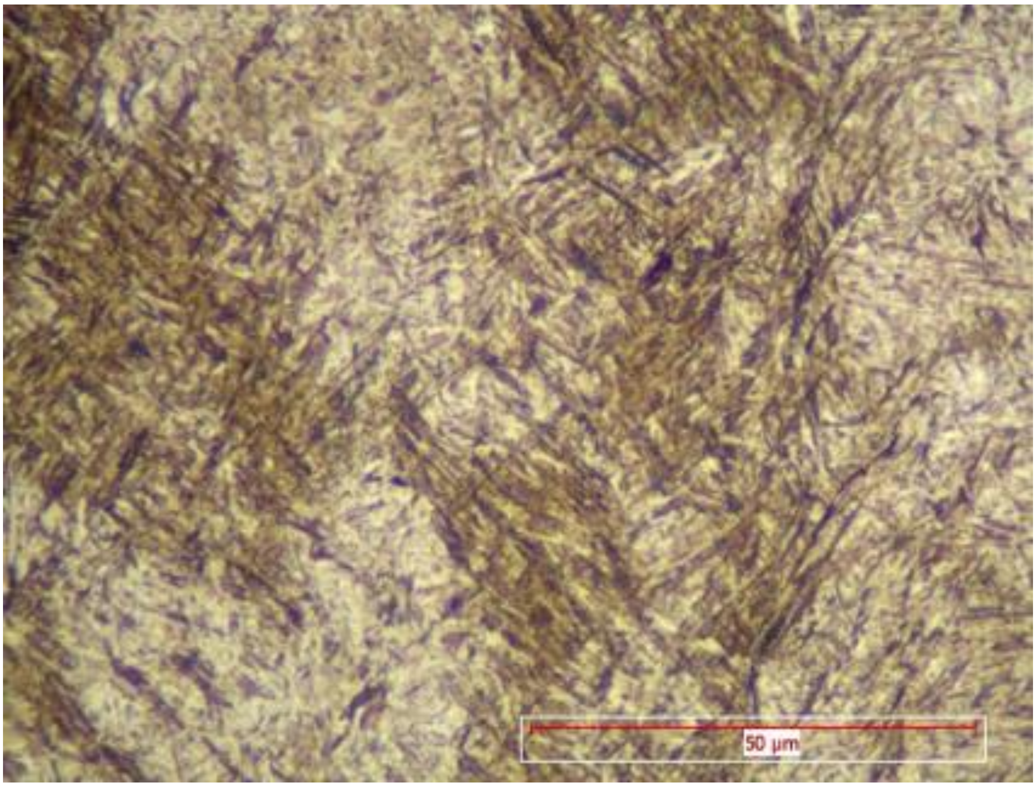

Figure 104: outer surface after chemical attack (NITAL 2% - 1000x)

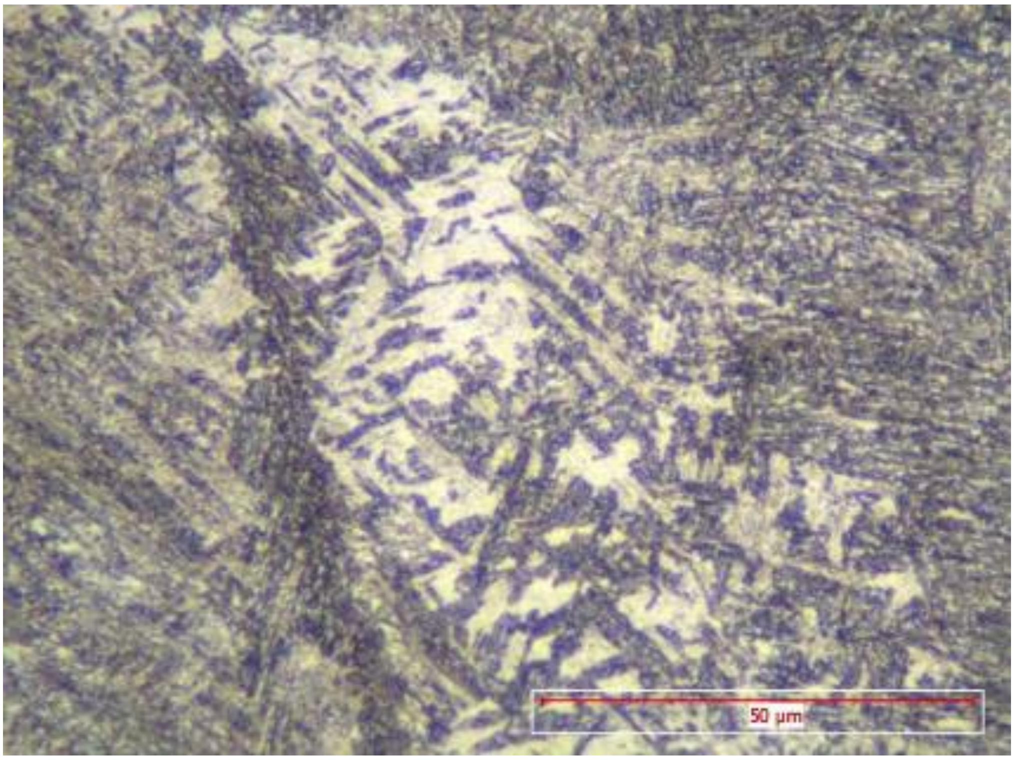

Figure 105: internal surface after chemical attack (NITAL 2% - 1000x)

Figure 106: example of bainitic structure

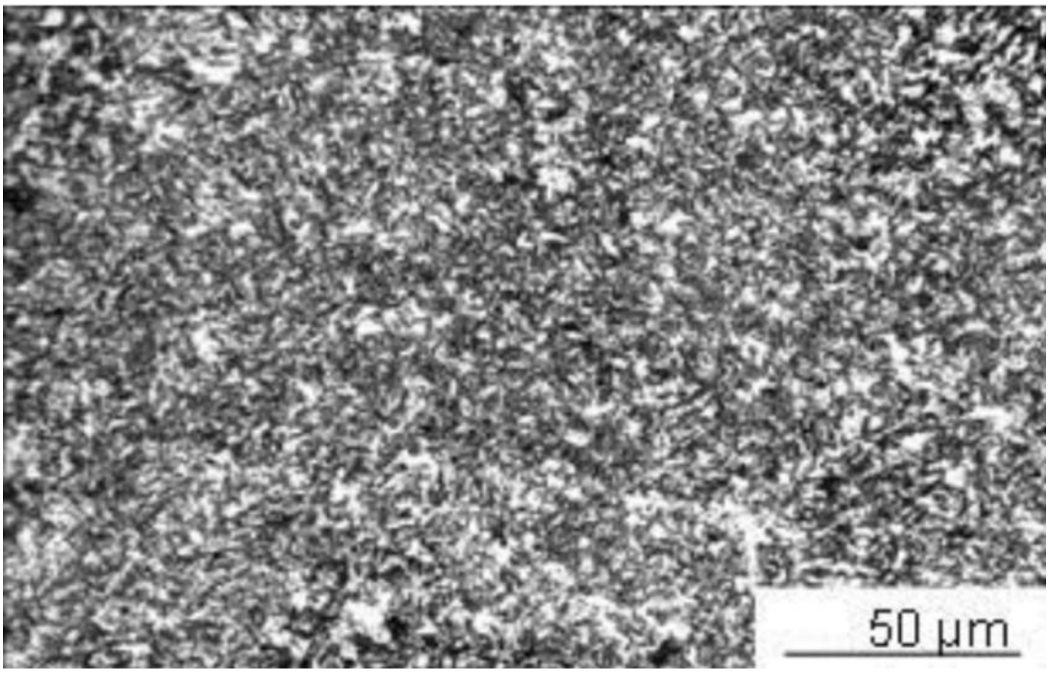

The EDAX semi-quantitative analysis carried out during observation at SEM showed the composition for the characteristic components reported in figure 107:

Figure 107: characteristic element carried out from EDAX analysis.

Si %	Mn %	P %	S %
0.2	0.52	0.01	0.01

The probe used was not suitable for C detection, which will be carried out with other technology.

In figure 109 are reported the curves obtained during the tensile tests. It is visible the difference of the as built group by the heat treatment group.

The heat treatment to which the specimens are placed has increased some mechanical properties, first R_m and $R_{p\ 0.2}$.

As far as Young's module and elongation are concerned, there is a 10 % decrease compared to the condition as built.

Figure 108: results of the tensile tests

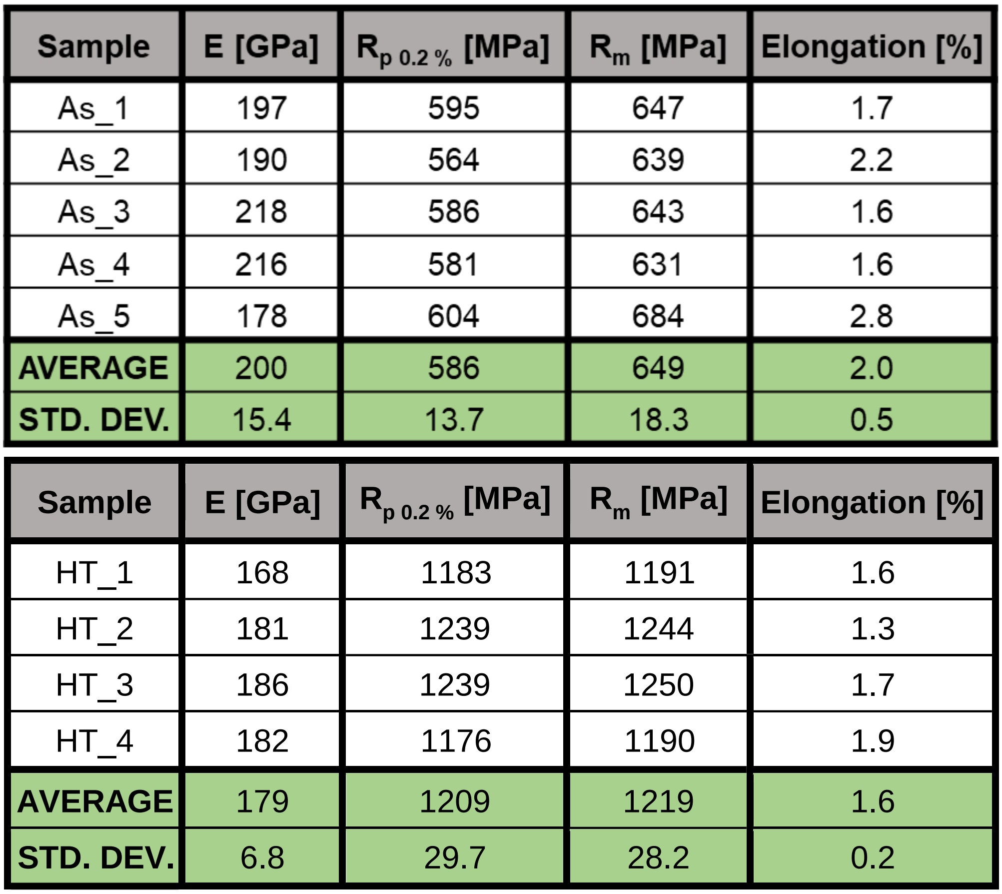

Sample	E [GPa]	$R_{p\,0.2\,\%}$ [MPa]	R_m [MPa]	Elongation [%]
As_1	197	595	647	1.7
As_2	190	564	639	2.2
As_3	218	586	643	1.6
As_4	216	581	631	1.6
As_5	178	604	684	2.8
AVERAGE	200	586	649	2.0
STD. DEV.	15.4	13.7	18.3	0.5

Sample	E [GPa]	$R_{p\,0.2\,\%}$ [MPa]	R_m [MPa]	Elongation [%]
HT_1	168	1183	1191	1.6
HT_2	181	1239	1244	1.3
HT_3	186	1239	1250	1.7
HT_4	182	1176	1190	1.9
AVERAGE	179	1209	1219	1.6
STD. DEV.	6.8	29.7	28.2	0.2

Figure 109: C67 curves of the tensile test

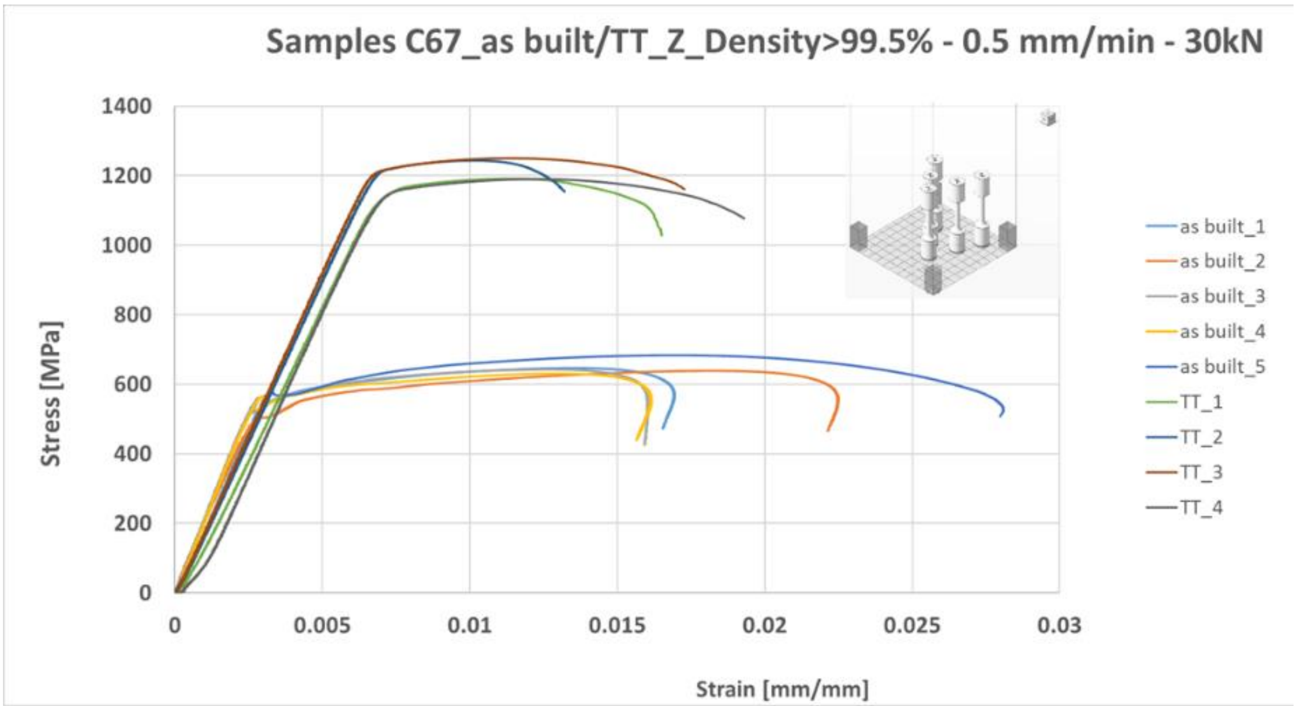

Figure 110 – A) shows an image of an audition before the test and figure 103 – B) shows the test specimens after the tensile test. It should be noted that the specimen named Z2 has a surface partially machined to machine tools (see Figure 111).

Figure 110: picture of the sample. A) sample before the test - B) samples after tensile tes

Figure 111: specimen Z2 and specimen Z1. A macroscale of the surfaces: Z2 has a pre-machined surface and Z1 has an As Built surface

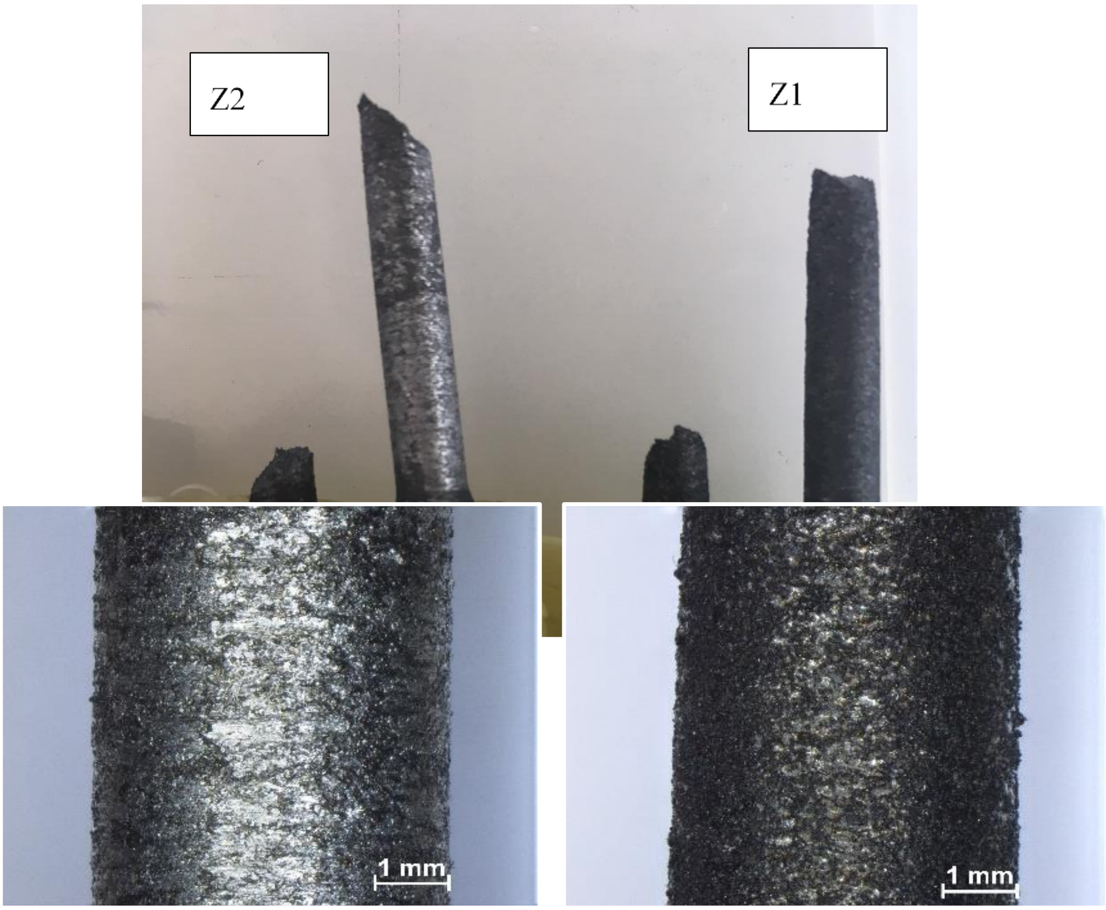

Rockwell hardness tests were carried out according to UNI EN ISO 6508-1:99 with diamond indenter at an angle of 120° and a total load of 100 kgf.

Table 5 shows the measurements for both an XY surface (parallel to the printing direction) and an XZ/YZ plane (orthogonal surface to the printing direction).

Table 6: HRD tests on XY and XZ - YZ surfaces

ROCKWELL HARDNESS D - UNI EN ISO 6508-1:99 C67				
	TESTS		MEAN	STD. DEV.
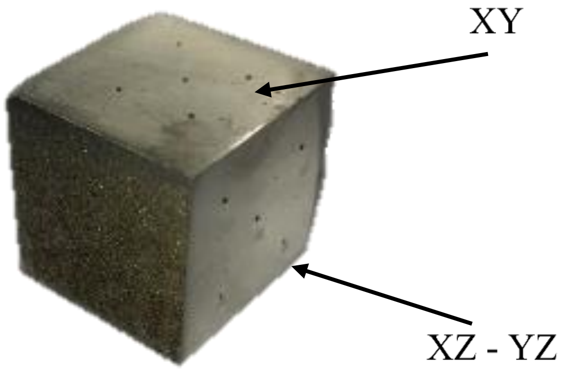	XY	63	62	1,2
		63		
		60		
		62		
		62		
	XZ/YZ	42	54	7,3
		55		
		59		
		55		
		59		

The hardness tests have been divided to show that the relative density value reached by the printed component is likely to differentiate the measured values if the tests are conducted with respect to the construction plane or if they are carried out along one of the orthogonal planes. In fact, it can be seen in table 5 that the hardness tests carried out compared to the XY plane are 10% higher than the hardness tests carried out along the XZ or YZ plane. This feature probably depends on whether in the first case (the XY one), the axial load of the durometer is applied orthogonally to the printing layers, rather than in the XZ-YZ case where the durometer exerts interlaminar pressure between the printing layers (see Figure 112).

Figure 112: LOAD application of the durometer

Following the hardness tests, linear roughness measurements were carried out using NIKON LV150N optical microscope to quantify the quality of the surfaces obtained. Table 6 shows the values obtained. The average value of roughness is lower than the values found in the literature; this ensures better as built conditions than the conditions to which you are normally accustomed in the additive manufacturing field.

Table 7: roughness values of three different profiles

Surface ROUGHNESS – ISO 4287 [µm]							
PROFILE	**R_a**	**R_q**	**R_c**	**R_z**	**R_t**	**R_p**	**R_v**
P_1	6.34	8.07	18.8	33	47.1	17.3	15.7
P_2	5.86	7.03	16	28.9	41.8	14.8	14.1
P_3	5.19	7	14.9	32.5	45.8	19.9	12.6
AVERAGE	**5.8**	**7.4**	**16.6**	**31.5**	**44.9**	**17.3**	**14.1**
STD. DEV.	**0.6**	**0.6**	**2.0**	**2.2**	**2.8**	**2.6**	**1.6**

5: Conclusions

With the data collected through the numerous experimental tests we can say that thanks to the improvements applied to the machine regarding the distribution of dust it has been possible to optimize the use of virgin powder during the entire printing process, going from recoating times of 15/20 seconds to only 4 seconds.

The closed circuit of the protective gas (nitrogen) in the chamber has been optimized and implemented by adding to the system a cyclonic filter, which has allowed to increase the yield of the entire filtering system; this, in turn, has led to a saving in the consumption of filter cartridges, going from an annual expense of about 8000 euros to only 1800 euros.

The simulation with the prototypal printing chamber booth allowed to analyse the flows generated in the chamber, therefore, to have clear criticalities present in the real model; from these tests it was then possible to make the relevant changes, verify their actual effectiveness or make further changes if the tests were not satisfactory.

The synergy with all the various mechanical improvements, the new dust loading and distribution system, together with the entire gas filtration system in the closed circuit, have in fact led to a general reduction in printing times, as well as an increase in the quality of the printed component, both in terms of relative density and in terms of surface quality.

Regarding to the development of the printing parameters of the materials studied here we can say that their applicability in the additive manufacturing field can be considered innovative as materials still little or not at all present in the scientific literature. Brass alloy for its high concentration of zinc and for a low concentration of lead has an applicability in the food field or in any case for uses in which there may be present or contact with foodstuffs.

Also, with regarding brass alloy we can say that the phenomenon called zinc fumigation has not been found, and that thanks to the LASER gun cleaning technique the phenomenon is completely removed, bringing the zinc concentration values back to the standard values.

The use of surface cleaning by LASER gun has also made it possible to insert and validate as a cleaning technique a brass alloy printed component the use of a smart dynamic system, much more pocket-sized and less expensive than a numerically control machine or a more aggressive manual process such as blasting processes, sandblasting.

Regarding C67 dust, we can say that, although it is a material with a medium-concentration carbon content, it can still be processed by additive construction technology in an atmosphere with a controlled atmosphere saturated with nitrogen and not argon, a gas that is known to be much more harmful and dangerous in the event of abnormal losses.

In general, it can be said that regarding the use of this technology in the pre-processing phases of a new mechanical component would lead to a serious reduction in lead times, as there would no longer be a need to develop expensive molds (in the case of forging processes or punching processes). On average for the development of a new component they pass on average from 6 to 8 weeks, only for the design of the mold that would then lead to the realization of a pre-series. Thanks to Additive Manufacturing, the time is greatly reduced to having a first functional pre-series in a few days.

In conclusion, it can be said that, as a technological development, additive manufacturing has made great strides compared to 10 years ago, so that only demonstration and non-functional components could be obtained from this type of technology. However, it can still be done both in terms of the development of new materials (steels with high concentrations of carbon or additional brass alloys for electrical applications), and in terms of the development of new technologies (types of LASER sources with ever greater yields and perhaps at an increasingly low cost).

Bibliography

[1] T. Gornet, ‘History of Additive Manufacturing’, pp. 1–24, 2017.

[2] M. Baumers, C. Tuck, R. Wildman, I. Ashcroft, and E. Rosamond, ‘Transparency Built-in Manufacturing’, vol. 17, no. 3, 2012.

[3] ‘me3d’, 2017. [Online]. Available: http://me3d.com.au.

[4] C. J. D. B. K. Foster, E. W. Reutzel1, A.R. Nassar, B. T. Hall, S.W. Brown, *Optical, layerwise monitoring of powder bed fusion*. 2015.

[5] B. S. Ian Gibson, David Rosen, ‘Additive Manufacturing Technologies’, in *Additive Manufacturing Technologies*, Second edi., 2015, p. 511.

[6] S. Vock, B. Klöden, A. Kirchner, T. Weißgärber, and B. Kieback, ‘Powders for powder bed fusion: a review’, *Prog. Addit. Manuf.*, vol. 4, no. 4, pp. 383–397, 2019.

[7] A. Petik, ‘Some aspects of using STL file format in CAE systems’, *Int Work. CA Syst Technol*, pp. 80–86, 2000.

[8] T. Funkhouser, ‘Design, Representation and Processing for Additive Manufacturing’.

[9] H. Lee, C. H. J. Lim, M. J. Low, N. Tham, V. M. Murukeshan, and Y. J. Kim, ‘LASERs in additive manufacturing: A review’, *Int. J. Precis. Eng. Manuf. - Green Technol.*, vol. 4, no. 3, pp. 307–322, 2017.

[10] Lee Kwok-san and Tong Shiu-sing, ‘What is a LASER?’ [Online]. Available: http://www.hk-phy.org/articles/LASER/LASER_e.html.

[11] V. Ter-Mikirtychev, *Springer Series in Optical Sciences: Fundamentals of Fiber LASERs and Fiber Amplifiers*. 2014.

[12] 3D Natives, ‘3D Natives’, 2017. [Online]. Available: https://www.3dnatives.com/en/electron-beam-melting100420174/.

[13] V. Gunenthiram *et al.*, ‘Analysis of LASER – melt pool – powder bed interaction during the selective LASER melting of a stainless steel to cite this version: HAL Id: hal-01664637’, 2017.

[14] Renishaw, ‘Renishaw’, 2020. [Online]. Available: https://www.renishaw.it/it/sistemi-per-la-produzione-additiva-in-metallo-stampa-3d--37011.

[15] 3D Systems, ‘3D Systems’, 2020. [Online]. Available: https://www.3dsystems.com/3d-printers/metal.

[16] G. Electric, ‘General Electric Additive’, 2020.

[17] EOS, ‘EOS’, 2019. [Online]. Available: https://www.eos.info/systems_solutions/metal/systems_equipment.

[18] SLM Solutions, ‘SLM Solutions’, 2018. [Online]. Available: https://www.slm-solutions.com/en/products/machines/.

[19] 3D Systems Corporation, ‘Metal Additive Manufacturing with the DMP printer series’, p. 2018, 2018.

[20] M. S. I. N. Kamariah, W. S. W. Harun, N. Z. Khalil, F. Ahmad, M. H. Ismail, and S. Sharif,

‘Effect of heat treatment on mechanical properties and microstructure of selective LASER melting 316L stainless steel’, *IOP Conf. Ser. Mater. Sci. Eng.*, vol. 257, no. 1, 2017.

[21] P. Aggarangsi and J. L. Beuth, ‘Localized preheating approaches for reducing residual stress in additive manufacturing’, *17th Solid Free. Fabr. Symp. SFF 2006*, pp. 709–720, 2006.

[22] L. C. Wei, L. E. Ehrlich, M. J. Powell-Palm, C. Montgomery, J. Beuth, and J. A. Malen, ‘Thermal conductivity of metal powders for powder bed additive manufacturing’, *Addit. Manuf.*, vol. 21, no. December 2017, pp. 201–208, 2018.

[23] R. Emilia, R. Prof, and A. Gatto, ‘Ottimizzazione dei flussi in camera e dei parametri di processo di una macchina per costruzione additiva L-PBF Indice ’:, 2020.

[24] S. E. Brika, M. Letenneur, C. A. Dion, and V. Brailovski, ‘Influence of particle morphology and size distribution on the powder flowability and LASER powder bed fusion manufacturability of Ti-6Al-4V alloy’, *Addit. Manuf.*, vol. 31, no. November 2019, p. 100929, 2020.

[25] M. Rackl, F. E. Grötsch, and W. A. Günthner, ‘Angle of repose revisited: When is a heap a cone?’, *EPJ Web Conf.*, vol. 140, pp. 1–4, 2017.

[26] R. Hebert, ‘Effects of Environmental Conditions on Powder Mechanics’, *Met. Powder Dyn. Symp.*, pp. 2–26, 2017.

[27] C. Pauzon, E. Hryha, P. Forêt, and L. Nyborg, ‘Effect of argon and nitrogen atmospheres on the properties of stainless steel 316 L parts produced by LASER-powder bed fusion’, *Mater. Des.*, vol. 179, 2019.

[28] T. DebRoy *et al.*, ‘Additive manufacturing of metallic components – Process, structure and properties’, *Prog. Mater. Sci.*, vol. 92, pp. 112–224, 2018.

[29] T. F. Kuech, ‘Integration of Dissimilar Materials’, *Compr. Semicond. Sci. Technol.*, vol. 1–6, pp. 1–24, 2011.

[30] B. Aldo, ‘Sviluppo di un nuovo modello LBM ibrido per una miscela binaria in presenza di surfattante’, 2014.

[31] T. N. Le and Y. L. Lo, ‘Effects of sulfur concentration and Marangoni convection on melt-pool formation in transition mode of selective LASER melting process’, *Mater. Des.*, vol. 179, p. 107866, 2019.

[32] C. L. A. Leung *et al.*, ‘LASER-matter interactions in additive manufacturing of stainless steel SS316L and 13-93 bioactive glass revealed by in situ X-ray imaging’, *Addit. Manuf.*, vol. 24, no. May, pp. 647–657, 2018.

[33] B. K. Post *et al.*, ‘Solid Freeform Fabrication 2018: Proceedings of the 29th Annual International Solid Freeform Fabrication Symposium – An Additive Manufacturing Conference Reviewed Paper’, *Solid Free. Fabr. Symp.*, pp. 2430–2446, 2018.

[34] E. H. Valente, V. K. Nadimpalli, S. A. Andersen, D. B. Pedersen, T. L. Christiansen, and M. A. J. Somers, ‘Influence of atmosphere on microstructure and nitrogen content in AISI 316L fabricated by LASER-based powder bed fusion’, *Eur. Soc. Precis. Eng. Nanotechnology, Conf. Proc. - 19th Int. Conf. Exhib. EUSPEN 2019*, pp. 244–247, 2019.

[35] Kashan Bashir, ‘Design and fabrication of cyclone separator’, *ResearchGate*, no. January 2015.

[36] S. P. Narra, ‘Melt Pool Geometry and Microstructure Control Across Alloys in Metal Based Additive Manufacturing Processes’, *Dissertations*, 2017.

[37] ‘U.S Food and Drug Administration’. [Online]. Available: https://www.fda.gov/home.

[38] J. Baron, ‘Materials in Contact with Drinking Water’, *Anal. Methods Drink. Water Adv. Sampl. Anal.*, pp. 115–173, 2006.

[39] A. Standard, ‘and Lead Content’, no. December 2008, pp. 0–1, 2013.

[40] C. J. Huang *et al.*, ‘Advanced brass-based composites via cold-spray additive-manufacturing and its potential in component repairing’, *Surf. Coatings Technol.*, vol. 371, no. February, pp. 211–223, 2019.

[41] Z. Szakál, A. Kári-Horváth, T. Pataki, and M. Odrobina, ‘The Mechanical Properties of 3D Printed CuZn28 Brass Specimens with Different Orientations’, *Int. J. Eng. Manag. Sci.*, vol. 4, no. 1, pp. 253–259, 2019.

[42] C. Yang, Y. J. Zhao, L. M. Kang, D. D. Li, W. W. Zhang, and L. C. Zhang, ‘High-strength silicon brass manufactured by selective LASER melting’, *Mater. Lett.*, vol. 210, pp. 169–172, 2018.

[43] S. A. Khairallah, A. Rubenchik, A. T. Anderson, A. Anderson, and S. Rubenchik, ‘LASER powder-bed fusion additive manufacturing: Effects of main physical processes on dynamical melt flow and pore formation from mesoscopic powder simulation’, no. December 2015.

[44] J. Yin *et al.*, ‘High-power LASER-matter interaction during LASER powder bed fusion’, *Addit. Manuf.*, vol. 29, no. June, p. 100778, 2019.

[45] D. Bergström, J. Powell, and A. F. H. Kaplan, ‘Absorptance of nonferrous alloys to Nd:YLF and Nd:YAG LASER light at room temperature’, *Appl. Opt.*, vol. 46, no. 8, pp. 1290–1301, 2007.

[46] U. Scipioni Bertoli, A. J. Wolfer, M. J. Matthews, J. P. R. Delplanque, and J. M. Schoenung, ‘On the limitations of Volumetric Energy Density as a design parameter for Selective LASER Melting’, *Mater. Des.*, vol. 113, pp. 331–340, 2017.

[47] E. M. Stanciu, A. C. Pävälache, G. M. Dumitru, O. G. Dontu, D. Besnea, and I. M. Vasile, ‘Mechanism of keyhole formation in LASER welding’, *Rom. Rev. Precis. Mech. Opt. Mechatronics*, no. 38, pp. 171–176, 2010.

[48] A. S. Kilian Klages, Arnold Gillner, Alexander Olowinsky, Sandra Fronczek, ‘LASER Beam Micro Welding of Dissimilar Metals’, in *International Congress on Applications of LASERs & Electro-Optics*, 2003.

[49] A. T. C.C. Viafara, M.I. Castro, J.M. V ´ elez, *Unlubricated sliding wear of pearlitic and bainitic steels*. 2005.

[50] Q. C. Hsu and A. T. Do, ‘Minimum porosity formation in pressure die casting by taguchi method’, *Math. Probl. Eng.*, vol. 2013, 2013.

[51] C. Tian *et al.*, ‘Effect of melt cleanliness on the formation of porosity defects in automotive aluminium high pressure die castings’, *J. Mater. Process. Technol.*, vol. 122, no. 1, pp. 82–93, 2002.

[52] Y. G. Hang Zhenga, Huaixue Lib, Lihui Langa, Shuili Gongb, ‘Effects of scan speed on vapor plume behavior and spatter generation in LASER powder bed fusion additive

manufacturing', *J. Manuf. Process.*, vol. 36, pp. 60–67, 2018.

[53] W. E. Frazier, 'Metal additive manufacturing: A review', *J. Mater. Eng. Perform.*, vol. 23, no. 6, pp. 1917–1928, 2014.

[54] B. S. Ian Gibson, David Rosen, *Additive Manufacturing Technologies*, First., vol. 1. 2010.

[55] hoganas, 'https://www.hoganas.com/'.